Buoyancy-Driven Two-Phase Flows of Liquid Metal contributing to the Generation of Electricity from a Fusion Reactor by Magnetohydrodynamic Energy Conversion

A Thesis Submitted to the University of London for the Degree of Doctor of Philosophy

by

Charles Edwin Wood

School of Engineering and Materials Science

Queen Mary University of London

Mile End

E1 4NS

October 2015

Declaration

I, Charles Edwin Wood, confirm that the research included within this thesis is my own work or that where it has been carried out in collaboration with, or supported by others, that this is duly acknowledged below and my contribution indicated.

I attest that I have exercised reasonable care to ensure that the work is original, and does not to the best of my knowledge break any UK law, infringe any third party's copyright or other Intellectual Property Right, or contain any confidential material.

I accept that the College has the right to use plagiarism detection software to check the electronic version of the thesis.

I confirm that this thesis has not been previously submitted for the award of a degree by this or any other university.

The copyright of this thesis rests with the author and no quotation from it or information derived from it may be published without the prior written consent of the author.

Signature: Charles E. Wood

Date: October, 2015

Abstract

Fusion is desirable for providing the world's future base-load power capacity due to its lack of greenhouse gas emissions, low environmental and safety risk, and large, secure fuel reserves. Fusion power plants are not expected to deliver electricity commercially until 2050, when it is expected that most fossil-fuelled power plants will have been removed from the global electricity generating mix. However, for fusion power plants to remain competitive with other forms of primary energy sources, the unit cost of electricity should be kept as low as possible. The objective of this work has therefore been to examine and compare a range of conversion methods for the purpose of increasing overall fusion plant efficiency.

Model C of the Power Plant Conceptual Study provided a benchmark against which a proposed power cycle could be compared. The power cycle associated with model C, using a thermal input of 3991 MW_t and neglecting cycle pressure losses, delivers 1780 MW_e with a cycle efficiency of 44.6%. Allowing for blanket gain, but after deducting plant power requirements, an overall plant efficiency of 45.9% is achieved.

The proposed power cycle uses a primary Brayton cycle, which takes helium directly from the blanket, to deliver 1688 MW_e. A topping cycle, which uses two-phase liquid metal magnetohydrodynamic energy conversion, delivers 22 MW_e. Three water-based bottoming Rankine cycles are used to extract heat rejected by the Brayton cycle to deliver 409 MW_e. Small-scale experimental work was undertaken to verify the performance of the topping cycle and observe the circulation of a dense liquid metal by using buoyancy, thereby removing the need to pump liquid metal through a blanket. The proposed power cycle, without cycle pressure losses, delivers a total of 2119 MW_e with a combined cycle efficiency of 53.1%. An overall plant efficiency of 56 % is achieved, an improvement of 10.1% over PPCS model C.

Acknowledgements

I would like to thank my primary supervisor Emeritus Professor Chris Lawn, Queen Mary University of London, for his support and patience. The feedback he has provided throughout my study has been invaluable in enabling this thesis to be completed. I would also like to thank Dr. Tom Barrett, Culham Centre for Fusion Energy, and Dr. Huasheng Wang, Queen Mary University of London, for their support.

I would like to acknowledge Mr. Roger Nelson, Queen Mary University of London, for providing technical assistance during experimental testing. I would especially like to thank Mr. John Cowley, University College London, for his invaluable technical support, without which the experimental work could not have been undertaken. I would also like to acknowledge the following staff at Queen Mary University of London for their support: Jonathon Hills, Rajesh Chadha and Wei Zhang.

This research was funded by a CASE Award from the Engineering and Physical Sciences Research Council (Grant No. EP/J502157/1) and a Russell Studentship from the Culham Science Centre of the UK Atomic Energy Authority (Contract No. 30000165044). Their support is gratefully acknowledged

Finally, I would like to acknowledge the support of my family, to whom I dedicate this work.

Contents

List of Figures

List of Tables

Nomenclature

Latin symbols

A	cross-sectional area
A_e	electrode surface area
A_G	modified Richardson constant
A_0	Richardson constant
AGR	advanced gas-cooled reactor
B	boiler; heater; blanket; magnetic field strength
BIC	bleed inter-cooler
b	channel width, distance between MHD electrodes
C	compressor
C_D	drag coefficient
C_f	friction factor
CCS	carbon capture storage
CECV	continuous electrode constant velocity
CGGT	combined cycle gas turbine
c	specific heat
D	deuterium; divertor; diameter, draught
DCLL	dual-cooled lithium lead
DEC	direct energy conversion
DEMO	demonstration power plant
d	distance

E	electric field; non-dimensional CISE correlation parameter
E’	electric field experienced by any charged particle moving with the fluid
EHD	electrohydrodynamic
EIA	Energy Information Authority
e	electron charge; entrainment fraction
F	Friedel correlation parameter; force
Fr	Froude number
F_T	fluid thrust
FW	first wall
G	total mass flux
GCV	gross calorific value
GHG	greenhouse gas
g	gravity
H	Friedel correlation parameter; hysteresis
Ha	Hartmann number
He	helium
HCLL	helium-cooled lithium lead
HCPB	helium-cooled pebble bed
HHF	high heat flux
HP	high pressure
h	Planck’s constant; height; enthalpy; convective heat transfer coefficient
I	inter-cooler; magnetic interaction number
ID	internal diameter
IEC	inertial electrostatic confinement

IHX	indirect heat exchange
ITER	International Thermonuclear Experimental Reactor
i	ratio of partial pressure of seed vapour to partial pressure of carrier gas
J	current density
J_e	electron current density
JET	Joint European Torus
K	fluid flow loss coefficient
k	Boltzmann constant
k_1	non-dimensional EHD loss coefficient
L	Length; channel length; perimeter
LM136	low-melt 136
LP	low pressure
LWR	light water reactor
M	Mach number
M_w	molecular weight
MCF	magnetic confinement fusion
MHD	magnetohydrodynamic
MIC	main inter-cooler
$\dot{m}$	mass flow rate
m_e	electron mass
N	number of thermoelectric modules; Avogadro number
Nu	Nusselt number
n	neutron; number of compressors
n_e	electron number density
n_v	number of valence electrons per atom

ODS	oxygen dispersed strengthened
P	pressure
Pr	Prandtl number
PF	plasma facing
PPCS	power plant conceptual study
PPM	parts per million
PTFE	polytetrafluoroethylene
PWR	pressurised water reactor
PV	photovoltaic
PVC	polyvinylchloride
p	coil pitch
$\dot{Q}$	thermal power
Q_C	electron-atom collision cross-section
Q_F	total fusion energy
R	reheat; electrical resistance; gas constant; thermal resistance
Re	Reynolds number
RAF	reduced activation ferritic
r	radius
r_p	cycle pressure ratio
r_{pi}	optimum pressure ratio per stage between inter-coolers
S	slip ratio
SECV	segmented electrode constant velocity
SSC	specific steam capacity
s	entropy
T	tritium; temperature; turbine

TBR	tritium breeding ratio
TEG	thermoelectric generator
U	overall heat transfer coefficient
u	phase velocity
V	voltage
V_0	voltage across external load
$\dot{V}$	volumetric flow rate
v	flow velocity
v_d	drift velocity
v_{d0}	drift velocity at channel entry
v_e	electron drift velocity
v_f	specific density
v_x	neutral gas velocity
W	work
$\dot{W}$	power
$\dot{W}_d$	power density
We	Weber number
WEC	World Energy Council
WCLL	water-cooled lithium lead
$\dot{w}$	non-dimensional power density
X	exhaust gas heat exchanger
X_1	distance from the peak of the potential barrier to the cathode
X_2	distance from the peak of the potential barrier to the anode
x	two-phase flow quality; dryness fraction
Y	non-dimensional El-Boher correlation parameter

y	non-dimensional CISE correlation parameter
Z	thermoelectric figure of merit
Z^*	thermoelectric figure of merit for any combination of p-type and n-type materials
z	vertical direction

Greek Symbols

α	Seebeck coefficient; cross-sectional void fraction
β	beta decay; thermionic non-dimensional performance parameter' volumetric void fraction
β_e	Hall coefficient
Γ	two-phase adiabatic index
γ	surface tension; adiabatic index
γ_L	non-dimensional electric field along channel length#
Δ	change; difference; loss
δ	MHD generator coefficient
ε	emissivity
ε_0	permittivity of free space
η	efficiency
θ	angle; contact angle
θ_a	approaching contact angle
θ_r	receding contact angle
θ_y	Young's contact angle
κ	thermal conductivity
λ_R	material correction factor
Λ	ion slip

μ	ion mobility; electron mobility; dynamic viscosity
ρ	density; electrical resistivity
ρ_e	space charge density
σ	electrical conductivity; Stefan-Boltzmann constant
σ_0	electrical conductivity of slightly ionised gas or seeded gas
τ	collision frequency; wall shear stress
ϕ	two-phase multiplier
φ	work function
ω	cyclotron frequency

Latin subscripts

a	anode
b	breakdown
C	cold; compressor/s
CGGT	combined cycle gas turbine
c	cathode
div	divertor
e	electron; electrical
ef	external film
est	estimated
fgo	gas-only friction factor
flo	liquid-only friction factor
fric	frictional
g	gas
go	gas-only

grav	gravitational
H	hot
h	homogeneous
IHX	indirect heat exchange
i	ionisation potential
if	internal film
in	input; inlet; inside
isen	isentropic
L	load
LM	liquid metal
l	liquid
lim	limit
ln	natural log
lo	liquid only
lv	liquid-vapour
m	mixture
max	maximum
mom	momentum
NTP	Normal temperature and pressure
n	n-based semiconductor
out	output; outlet; outside
p	p-based semiconductor; anode space charge; at constant pressure; feed pump
R	Rankine
res	reservoir
rot	rotameter

s	specific; isentropic
sl	solid-liquid
sv	solid-vapour
T	turbine/s
t	thermal; throat
targ	target
tp	two-phase
v	at constant volume
wc	wall conduction
x	x-direction
y	y-direction
z	z-direction

Greek subscripts

γ	surface tension

Numerical subscripts

0	channel entry; open**;** stagnation condition

Latin superscripts

n	number of compressors used in the multi-stage compression process
–	average/mean

Chapter 1: Introduction

The aim of this research is to examine a broad range of methods for generating electrical power from a fusion reactor, with the subsequent evaluation of these methods from an efficiency perspective, with some consideration for cost. This will lead to the identification of a novel energy conversion proposal that is feasible using the known physics and engineering constraints associated with power plants. This brief introduction will discuss why electrical energy is sought, before evaluating the existing electricity generation methods and their associated problems. This chapter will serve to illustrate the benefit nuclear fusion has to offer and the need for continued support in developing the technology required for achieving the first commercial fusion power plant capable of delivering electricity to the end user.

1.1 Conversion to Electrical Energy

Large-scale electricity generation is most often achieved through the conversion of chemical energy to thermal energy through the burning of bio-fuels and fossil-fuels such as coal, oil, natural gas or through the heat generated by nuclear fission processes. Thermal energy sources, with the inclusion of geothermal, are converted to electrical energy via heat engines, which transmit the mechanical energy via rotating shafts to electrical generators, where the relative motion of a solid conductor inside a magnetic field produces electrical energy via electromagnetic induction.

Other energy conversion routes that deliver electrical energy to national grids are found alongside renewable sources. Wind turbines convert the local kinetic energy of the atmosphere into mechanical energy via the blades of the turbine.

Hydroelectric power plants utilise gravitational potential to convert the local kinetic energy of falling water into electrical energy, whilst marine power is achieved by converting the kinetic energy carried by ocean waves and tidal rivers into either rotational or linear motion with the subsequent generation of electric power via induction.

What the aforementioned energy conversion methods have in common is that despite their primary energy sources, the penultimate energy conversion process to electricity, which is consumed by the end user, involves the conversion to mechanical energy, with the notable exception of solar photovoltaics.

Compared to thermal energy, electrical energy is a high-quality energy form. It is our most desired form of energy because with our technology it is the most versatile. For an energy source to be deemed useful, or versatile, it must be relatively easy to convert, transmit, and control. When one considers the other energy forms such as thermal, mechanical, electromagnetic, chemical, gravitational and nuclear, electrical energy better meets our criteria for versatility [Soo, 1968].

1.2 Electricity Consumption

The graph in figure 1.1 shows the global trend of electrical energy consumption between 1980 and 2012 [U.S Energy Information Administration], with the contributions from continental and sub-continental groups also shown. North America and Europe have been the largest consumers of electricity, particularly the USA and Canada in North America, and the UK, Italy, France and Germany in Europe. However, contributions from Asia & Oceania are now the highest of all groups, exceeding levels of consumption in Europe in 1994 and North America in 2004.

Japan has been a large consumer of electricity for some time. In 1980 their national electricity consumption was 521 TWh, almost 50% of the total electricity consumption of Asia & Oceania. In 2012 this increased to 921 TWh, but accounted

for only 11% of the total electricity consumption. Countries such as China and India, where 1980 levels were 261 TWh and 98 TWh, respectively, in 2012 consumed 4467 TWh and 865 TWh, respectively, which represents a significant increase in electrical consumption. Other countries of the same group such as Bangladesh, Bhutan, Indonesia, South Korea, Laos, Malaysia, the Maldives and Nepal have seen a steep rise in consumption. In 1980 Bhutan consumed a mere 0.02 TWh, but in 2012 this figure increased to 1.6 TWh; a rather paltry figure by comparison with the aforementioned figures, but this represents an increase in consumption of over 8000%.

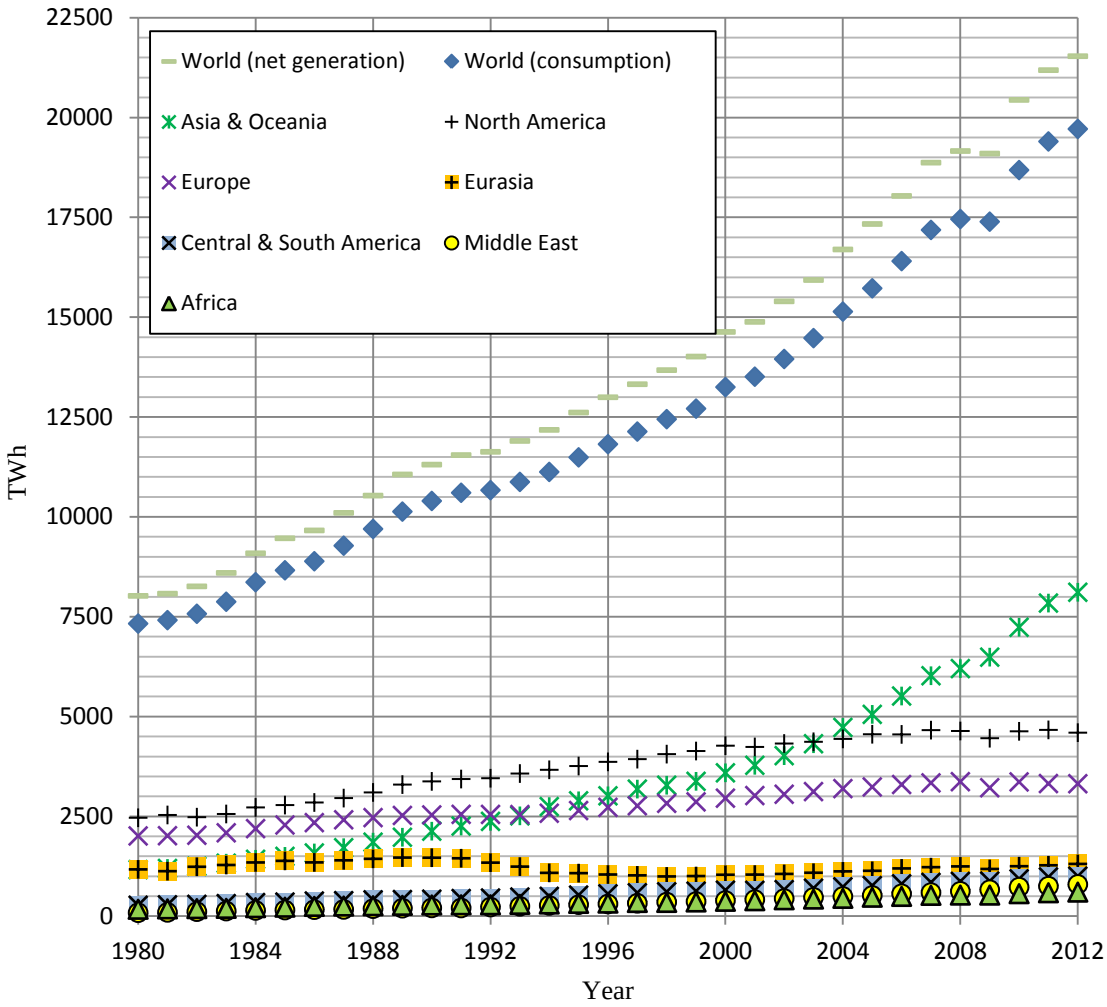

Figure 1.1 Global electricity consumption between 1980 and 2012 showing contributions from grouped nations, reproduced using data [U.S Energy Information Administration]

One could presume that these changes are due to the development in access to electricity. Figure 1.2 uses data [The World Bank] to show the averaged percentage for the populations of grouped nations between 1990 and 2010 which had access to electricity. The sub-division of Africa into North and sub-Saharan highlights the divide in electricity access between these regions. In 1990 the average percentage of the population of sub-Saharan Africa with access to electricity was the lowest of all groups: 22.4%, with countries such as Mauritius, Gabon and South Africa providing 97%, 73% and 65% access, respectively. In contrast to this, however, only 0.1% of the populations of Chad, Liberia and, what is now, South Sudan, had access to electricity. In 2010 levels of electricity access had increased, with the entire population of Mauritius having full access, Gabon offering 82% access and South Africa 83% access. There were marginal improvements in Chad, Liberia and nowadays South Sudan, but access to electricity was still low: 3.5%, 4.1% and 1.5%, respectively. It is certainly reasonable to surmise that with increasing access to electricity in sub-Saharan Africa electricity demand could soar and consumption would follow.

In figure 1.3 the same data [The World Bank] that helped to generate figure 1.2 is used to show the total population of the grouped nations, along with the sub-population that had access to electricity. For the purposes of consistency with figure 1.2 the division of the Africa group has remained. The graph in figure 1.3 is intended to highlight the immense population of the Asia & Oceania group, 3.8 billion in 2010, which when considered jointly with figure 1.2 shows how electricity consumption within this group has managed to surpass all others. Much like for the sub-Saharan Africa group, where in 2010 nearly 274 million out of a total population of 865 million still lacked access to electricity, one could surmise that with the remaining 1.2 billion in the Asia & Oceania group potentially receiving access to electricity in the near future that the level of global electricity consumption is likely to grow at an alarming rate.

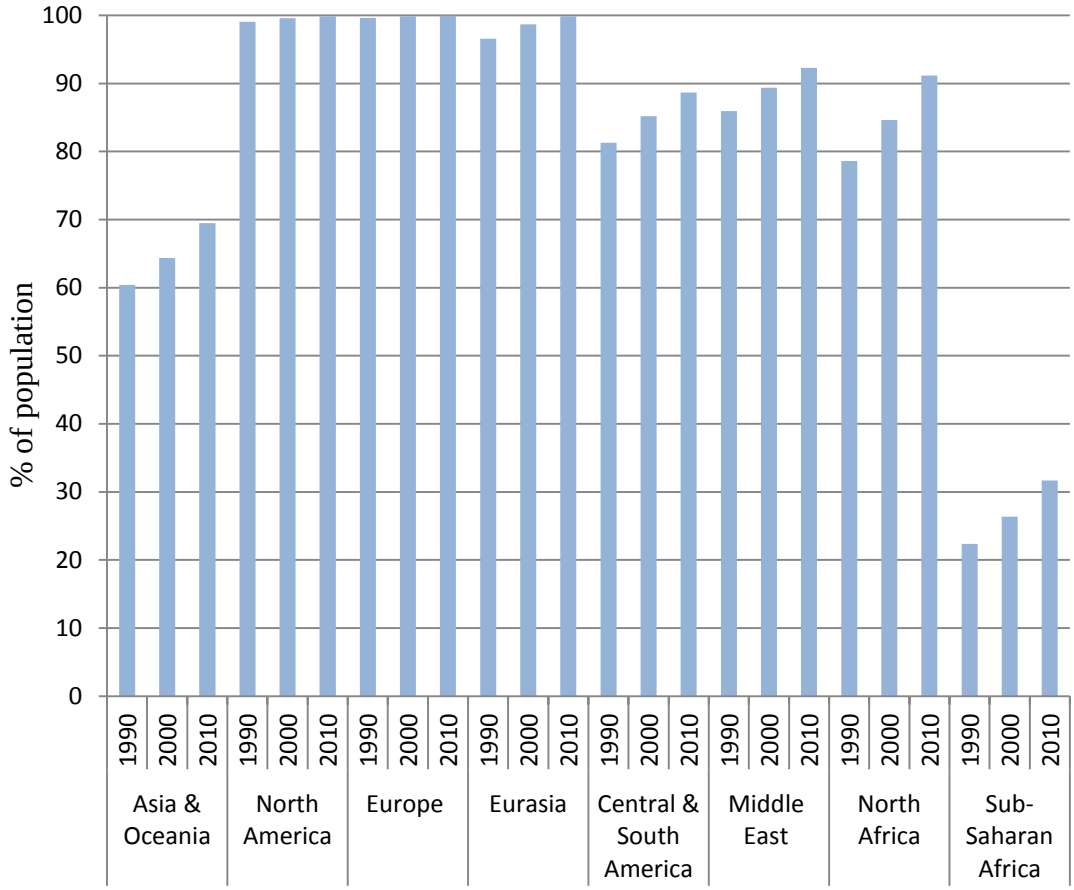

Figure 1.2 Averaged percentage of population by group with access to electricity, reproduced using data [The World Bank]

In North Africa, the Middle East and Central & South America the average access to electricity was relatively high between 1990 and 2010. However, by looking at the graph in figure 1.1 it can be seen that these groups account for three of the lowest consumers of electricity. The population of Eurasia had 99.8% access to electricity in 2010, but was the fourth lowest electricity consumer. Furthermore, figure 1.1 shows a brief decline in electricity consumption for Eurasia after 1989, before slowly increasing again. It would seem that the combination of either a relatively small population with high access to electricity, or a relatively large population with low access to electricity, is the reason for the low electricity consumption of these nations.

However, despite their current low impact upon global electricity consumption, with growing populations and increasing access to electricity it is perhaps evident that the contributions from these groups will be higher in the future.

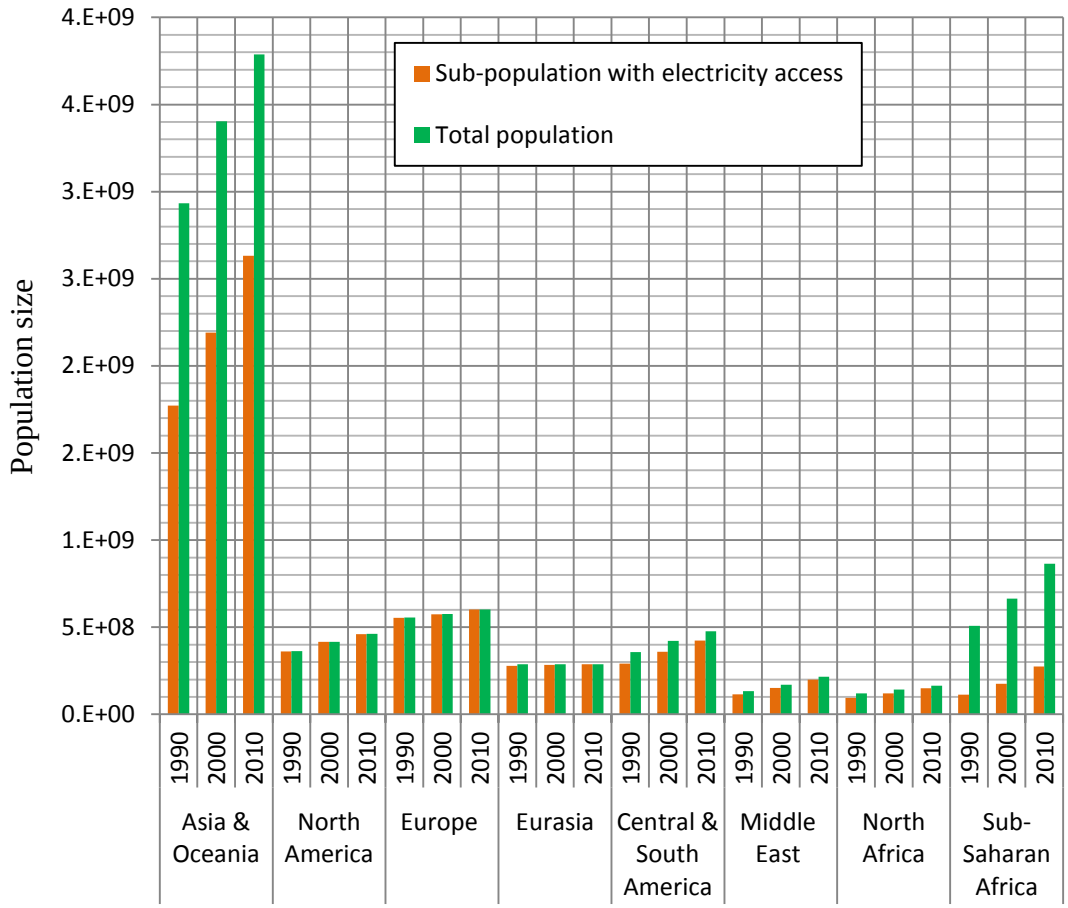

Figure 1.3 Population of grouped nations with sub-population that have access to electricity, reproduced using data [The World Bank]

Access to electricity within North America and Europe has been above 99% since 1990. In 2010 North America and Europe provided electricity access to 99.85% and 99.97% to their respective populations. Between 1990 and 2010 both groups experienced population growth, but in this period the population of North America has remained smaller than Europe. In 1990 the population of North America and Europe was 364 million and 555 million, respectively, whilst in 2010 it was 461 million and 602 million, respectively.

The graph of figure 1.4 uses data [The World Bank] to show the electricity consumption per capita for the grouped nations, where the contributions from North America and Europe, which are the highest, supports the notion that whilst electricity access and population growth are significant factors, they are not alone in contributing towards electricity consumption. In 1990 the global averaged electricity consumption per capita was just under 3130 kWh/y. This had risen to almost 3550 kWh/y in 2000 and around 4200 kWh/y in 2010.

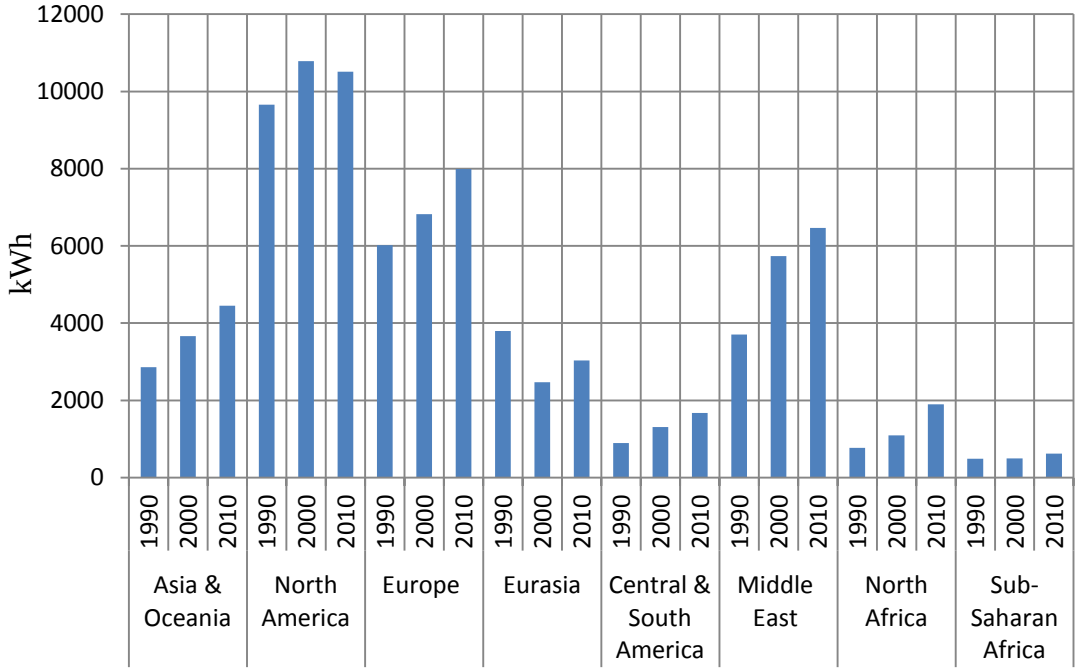

Figure 1.4 Electricity consumption per capita in kWh, reproduced using data [The World Bank]

1.3 Primary Fuel Consumption

Energy scenarios for the future are usually given as a contrast between two outcomes; their uncertainty is proportional to time. The first typically involves a scenario where energy efficiency and GHG emissions are not tightly controlled by policymakers, resulting in fuel insecurity and climate issues. A second scenario is envisaged in which GHG emissions are regulated with monetary emphasis on lower emissions.

This provides an impetus which leads to the development of cleaner, more energy efficient technologies. Fuel security is higher because nations openly collaborate to support developing economies instead of securing fuel for their own populations.

A report by the World Energy Council [WEC, 2013] gives the world electricity generation in 2010 as 21476 TWh. Comparing this with figure 1.1, for which the EIA gave the world electricity consumption as just under 18700 TWh in 2010, shows that supply could meet the demand for electricity in 2010. The graph in figure 1.5 provides a breakdown of primary fuels used for electricity generation in 2010.

Using WEC [2013] data the graphs in figures 1.6 and 1.7 show the electricity generation in 2050 for two WEC scenarios, respectively: Jazz, a scenario where policymakers do not put emphasis upon GHG emissions and energy efficiency, and Symphony, a scenario that emphasises clean, efficient energy technologies and a reduction in GHG emission through monetary impetus. CCS represents carbon capture storage.

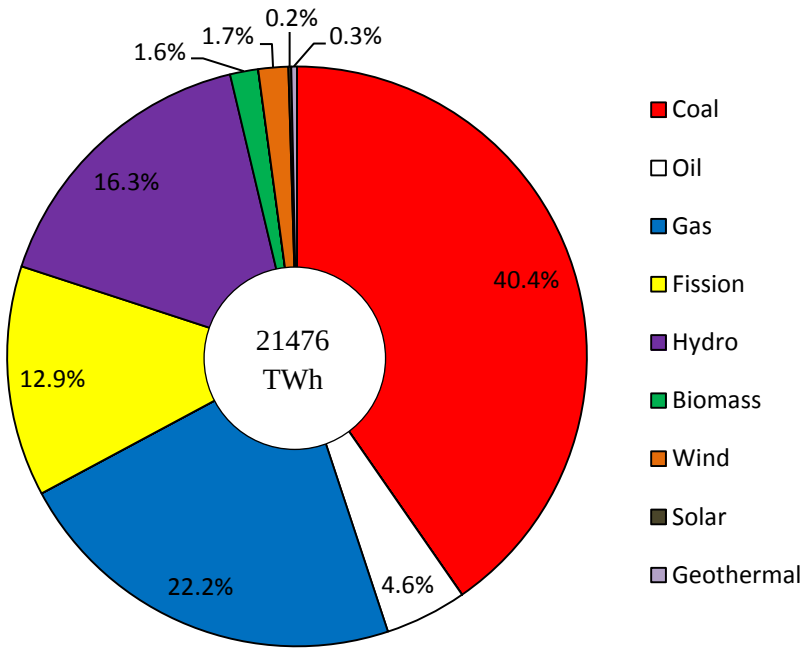

Figure 1.5 Electricity generation in 2010 reproduced using data from the World Energy Council [WEC, 2013]

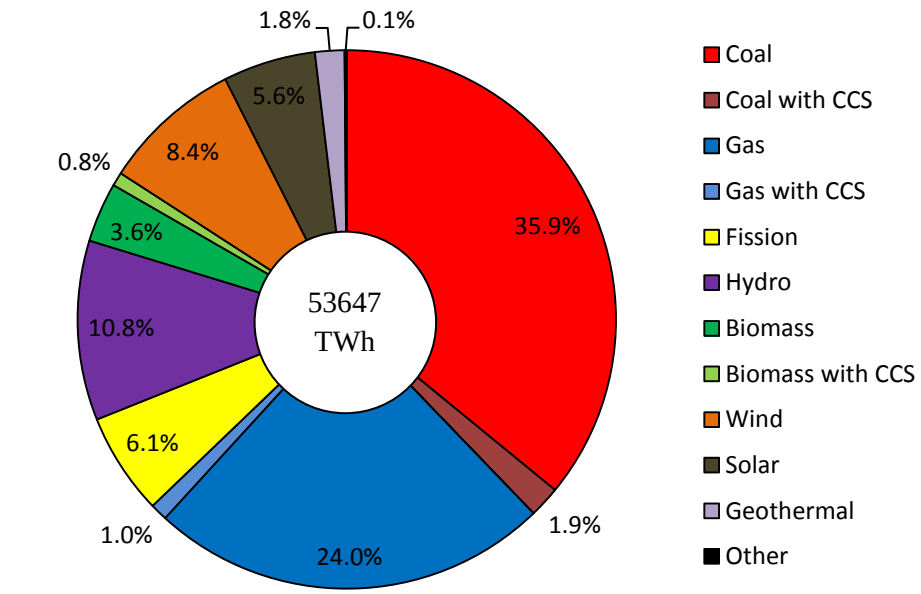

Figure 1.6 Projected electricity generation in 2050 for Jazz scenario reproduced using data from the World Energy Council [WEC, 2013]

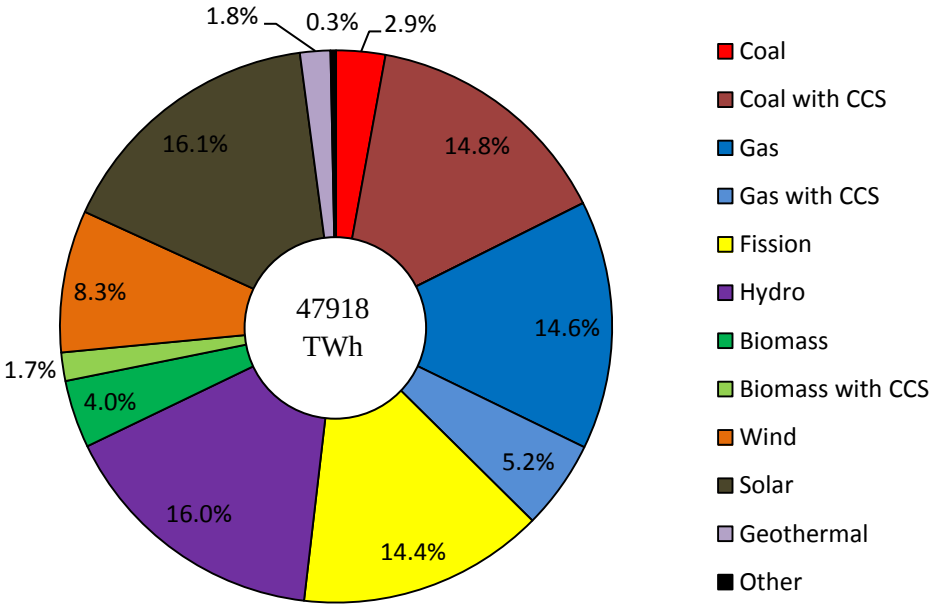

Figure 1.7 Projected electricity generation in 2050 for Symphony scenario reproduced using data from the World Energy Council [WEC, 2013]

The graph in figure 1.5 shows that coal-fired power stations dominated global electricity generation in 2010, generating 8666 TWh. Due to its relatively low price coal is widely used for generating electricity. In 2013 approximately 42% [DECC] of the electricity generated in the UK was through the use of coal. After the closure of Didcot A in early 2013, and the due closure of several other UK coal-fired power stations in late 2015, this figure should fall further. The trade association for the UK energy industry currently, 2015, puts the percentage of electricity generated by coal as 28% [Energy UK].

The drive to reduce the amount of electricity generated by the combustion of coal is due to its carbon content. Greenhouse gas emissions from coal, natural gas and oil-fired power stations consist mostly of CO_2, with small amounts of CH_4 and NO_2 contributing to the greenhouse effect. Coal-fired power stations were estimated to account for 39% of global CO_2 emissions in 2011 [National Geographic Society, 2014]. In 2008 CO_2 emissions from coal-fired power stations contributed 20% to global GHG emissions [National Geographic Society]. In 2050 the global amount of electricity generated by coal is expected to increase to just over 19272 TWh under the Jazz scenario. This represents an increase of just over 122%. Under the Symphony scenario, however, the contribution from coal drops to 1383 TWh, a reduction of 84%. Carbon capture storage (CCS) is lower in Jazz, only 1007 TWh, whilst in Symphony CCS is 7100 TWh.

Gas-fired power stations contributed just over 4777 TWh in 2010, whilst oil-fired power stations accounted for 980 TWh. Oil is more often, nowadays, used in the transportation sector or for residential heating, instead of being used for generating electricity. In 2050 contributions from oil-fired power stations are expected to fall to zero under both Jazz and Symphony. Natural gas contributions are expected to rise in 2050 to approximately 12869 TWh under Jazz and 7012 TWh under Symphony.

Gas-fired electricity generation with CCS is expected to be 558 TWh and 2505 TWh under Jazz and Symphony, respectively. There remains, however, uncertainty over the relative benefit of reduced CO_2 emissions from gas-fired power stations in

relation to the associated methane emissions from the supply and subsequent burning of natural gas [National Geographic Society].

Hydro remains the largest renewable electricity source, contributing close to 3491 TWh in 2010, just over 16% of the global electricity generation. Under Jazz, the contribution from hydro is expected to rise to 5789 TWh in 2050, but other primary energy sources are predicted to takeover, so the global contribution from hydro is actually reduced. Even under the Symphony scenario global contributions from hydro are expected to fall slightly to 16%, with a contribution of 7701 TWh. Hydro has the advantage of not producing any GHG emissions, but social concerns relating to the forced relocation of people and the environmental impact of hydroelectric plants remain an issue.

Electricity from nuclear fission is also expected to increase. Fission does not produce any GHG emissions, but, as mentioned at the start of this chapter, there is still public concern over safety. In 2010 contributions from fission amounted to just over 2763 TWh, and are expected to increase to almost 3279 TWh by 2050 under Jazz, representing a smaller percentage of the global electricity mix. Under Symphony the contribution from fission is expected to increase to 6950 TWh by 2050.

The traditional use for biomass has been for heating and cooking, but an increasing number of electricity generating plants are being built to burn wood, biodegradable waste, food waste or animal manure. It is a useful method of generating electricity from waste that would otherwise be destined for landfill, but it can also be used to produce methane for subsequent utilisation in natural gas power plants. In 2010 biomass plants contributed 337 TWh to the global electricity mix, whilst in 2050 this is expected to increase to 1923 TWh and 1913 TWh under the Jazz and Symphony scenarios, respectively. Biomass contributions utilising CCS are estimated to be 441 TWh under Jazz and 800 TWh under Symphony by 2050. In 2004 the Drax power station was partially converted to co-fire biomass, becoming the first UK-based power station generating electricity by burning willow. Drax also burns other biomass such as wood pellets, sunflower pellets and peanut shell husk. Most of the biomass fuels that Drax burns are imported [Drax Power Ltd, 2007].

In 2010 the renewable sources of wind, solar and geothermal were the lowest contributors, providing 358 TWh, 34 TWh, and 68 TWh, respectively, to the global electricity mix. Wind capacity is the fastest growing renewable source of electricity in the world, with the current annual growth close to 20% [National Geographic Society]. One of the concerns surrounding wind turbines is their aesthetic impact, but there is also the potential for environmental issues such as the damage to wildlife populations through turbine blade impact. In 2008 contributions from wind in the UK were approximately 7 TWh, but this had increased to nearly 30 TWh in 2013 [DECC]. In 2050 the global contribution from wind turbines is expected to be 4513 TWh under Jazz, but is lower under Symphony: 4003 TWh. An issue that is often raised about renewable energy sources is a problem related to intermittency. For wind power the supply can vary between summer and winter, even between day and night. Cloud cover can cause solar output to drop, whilst high temperatures during warmer months reduce the efficiency of solar panels. In 2010 grid-connected solar contributed just 34 TWh to the global electricity mix, but by 2050 this is expected to reach 2979 TWh and 7741 TWh for Jazz and Symphony, respectively. If the output of renewable sources cannot be matched to the demand then the result could be grid instability. However, storage solutions such as batteries could offer a way of providing ‘smoothing’ to compensate for any short-term variation in electricity generation.

Geothermal plants contributed a mere 69 TWh to the global electricity mix in 2010 and are only expected by 2050 to offer 949 TWh and 854 TWh under the Jazz and Symphony scenarios, respectively. Despite offering fewer intermittency issues than wind and solar, since sources of geothermal energy are consistent, the expected contribution to the future global electricity mix by geothermal is low. This might be due to the high capital cost of developing geothermal plants, where the locations are often far from large cities. Despite this, countries such as Indonesia, Kenya and Turkey are currently drilling rift zones [National Geographic Society].

1.4 Primary Fuel Comparison

Comparing the different energy densities of the fuels currently used for generating electricity is a simple way of highlighting the advantages of some electrical power generating methods over others. The gross calorific value, or energy density, of coal varies. High-quality coal such as anthracite has a GCV of 30 MJ/kg, whilst mid-quality bituminous coal falls in the range 20-25 MJ/kg. The lowest coal quality, lignite, has a GCV of only 8 MJ/kg. Crude oil has a slightly higher GCV of around 40-42 MJ.kg [Smil, 2010], whilst natural gas has a GCV of just below 53 MJ/kg [ISO 6967:1995]. The typical net calorific value of wood or wood-based products used in biomass plants is in the range 13-19 MJ/kg [Biomass Energy Centre]. The above values are only realised, however, if complete combustion occurs.

Evaluating the energy density is somewhat more complicated for fission. Uranium-235 has an energy density of 79.4 TJ/kg, but ^{235}U only accounts for approximately 1-4% of the fuel, depending upon the amount of enrichment. The majority of the fuel consists of ^{238}U which is converted to plutonium-239 with fast neutrons. Some fission reactors use a batch process, where the fuel is present within the reactor and not continuously fed into a combustion chamber, as is done for coal, gas, oil, biomass plants or even subcritical fission reactors. The fuel must be slowly burnt and therefore batch-process fission reactors have associated burn-up rates, measured in MWd/t, depending upon their design. A light water fission reactor, LWR, operating with uranium enriched to 3.5% and with a burn-up rate of 45 GWd/t, typical of second generation fission reactors, has an energy density of 3.9 TJ/kg [World Nuclear Association].

The above GCV values do not take into account the energy required for their production, such as mining, or for fission ore extraction and enrichment, but what the above figures do highlight is the advantage of nuclear energy processes over those of a chemical nature when evaluated from an energy and fuel weight perspective.

A further factor that must be mentioned when comparing energy processes for electrical power generation is thermal efficiency. Despite the superior energy density of fission, material constraints within LWRs limit the top steam temperatures to around 325°C for pressurised water reactors and 285°C for boiling water reactors [World Nuclear Association]. A similar limitation exists for Magnox reactors, but steam outlet temperatures are higher for Advanced Gas-cooled Reactors. There are currently nine operational fission reactors in the UK: seven AGR, one PWR and one Magnox, providing an average thermal efficiency of 39.6% in 2014. This is still higher than the average thermal efficiency of coal-fired power stations in the UK, which was 35.9% in 2014 [DECC, 2014].

Making a comparison between non-renewable and renewable energy sources must be done on a power density basis. Mackay [2009] makes the comparison between renewable sources and nuclear fission, using units of power per unit area, where the area is taken to represent the area occupied by a power-generating device or entire power plant. These values, given in table 1.1, highlight the diffuse nature of renewable energy sources and the necessarily larger land areas that would be required to generate similar electricity outputs as those power stations operating with non-renewable energy sources. Despite their relatively low power densities, they have the advantage of emitting zero GHG emissions. Moreover, on a volumetric basis both wind and solar PV have a further advantage. The base of a wind turbine is not solely occupied for the purpose of generating electricity; it can continue to be used for a variety of uses. Solar PV often occupies rooftops, a place where one would not find a coal-fired power station.

One further factor when assessing non-renewable energy sources is the amount of available fuel reserves. The BP statistical review of 2014 estimates that based on 2013 extraction rates there are 113 years of proven coal reserves remaining, whilst there are only 53 years of proven oil and 55 years of proven natural gas reserves. It should be noted, however, that oil is not reserved solely for the energy sector, oil is widely used in the transport sector, and therefore the estimated 53 years of proven oil reserves does not apply to electricity generation.

Power Source	Power Density (W/m^2)
Fission/Coal/Other non-renewable	1000
Solar PV	5-20
Hydro	11
Off-shore Wind	3
On-shore Wind	2
Biomass	0.5
Geothermal	0.017

Table 1.1 Comparison of renewable power densities with fission, reproduced from Mackay [2009]

1.5 Summary

The purpose of this chapter is not to undertake the complex task of analysing all the factors affecting the global upwards trend in electricity consumption. Rather it is to enlighten the reader as to where increased consumption is likely to occur and which primary energy sources will be required, depending upon energy policy, to meet demands.

The graph of figure 1.1 clearly shows the upward trend in global electricity consumption exists, and a qualitative argument has been made for the sustained upward trend in electricity consumption based on factors relating to population growth and increasing access to electricity within developing economies.

To meet the increasing global electricity demand, the global generating capacity will necessarily increase, where an important factor will be the primary energy source used to generate electricity. With the reduction in the use of fossil-fuelled power stations, driven by energy policies for reducing GHG emissions, the role of the major base-load contributor could fall to fission, despite environmental issues concerning waste products and safety.

Renewable energy sources are favourable because they do not produce any GHG emissions and possess a low operational environmental impact. Hydro plants have the ability to operate in base-load, load-following or peak-load modes, depending, however, on the supply of water. Biomass is suited to base-load operations, as is geothermal, despite its low power density. The drawback to wind and solar PV is that they are intermittent and present reliability issues, but their variability in output can be smoothed by employing forms of energy storage. Furthermore, on a volumetric basis, wind and solar PV have an advantage that the land, or surface area, they occupy can be used for alternative purposes, i.e., rooftops for solar PV or farming for wind. The large-scale adoption of solar PV and wind offers the ability for national grids to use them in a decentralised power generating role.

It seems a foregone conclusion that electrical energy is needed to sustain our modern existence. As economies grow, and the global electricity consumption increases, fuel reserves will be at risk of depletion unless new sources are found. Dependency upon fossil-fuels is expected to lessen in favour of renewable energy sources and nuclear power from fission, but whether this change will come soon enough is uncertain. As fuel reserves run low the risk of fuel security also becomes a concern. The development of technologies that are more efficient at using electrical energy will help, but what's required is a primary energy source that can provide adequate base-load capacity without producing GHG emissions, which possesses a low environmental and safety risk, and has large, secure fuel reserves.

Chapter 2: Nuclear Fusion

Nuclear fusion is the process whereby light atomic elements are fused together to yield a release of energy. The resulting fused product has less mass than that of its individual constituents and by the mass-energy equivalence large amounts of energy are released. The advantage of nuclear reactions over chemical reactions has already been highlighted in the previous chapter, but the advantage of fusion over fission can be highlighted by considering the following energy equivalency given by Freidberg [2010]: 0.8 tonnes of uranium has the same energy equivalence as one million tonnes of oil, however, only 0.14 tonnes of deuterium is required to match the energy equivalency for the same amount of oil. Of course, things are not so straightforward, as will be explained in this chapter.

The main application of nuclear fusion will be the large-scale terrestrial production of electricity, where Freidberg [2010] gives the three main advantages of fusion power as safety, environmental impact and fuel reserves. The main public concern attributed to nuclear power is due to incidents involving fission power stations, such as those at Three Mile Island in 1979, Chernobyl in 1986 and more recently Fukushima in 2011. However, a nuclear fusion power station will not depend upon sustaining a chain reaction within the reactor core, but instead require fuel to be continuously supplied at a rate chosen to maintain the fusion reaction. This means that there is a very small instantaneous concentration of fuel in the reactor core of a fusion reactor, thus making a meltdown impossible. To avoid such uncontrollable conditions, experienced in the aforementioned fission events, a fusion reactor will not be allowed to reach ignition: a self-sustaining state whereby the heating of the plasma by the fusion process maintains the plasma temperature without any external input.

2.1 Fusion Fuel Cycles

To gain an appreciation of the environmental impact of fusion, and the necessary fuel reserves for viable fusion power plants, the fusion fuel cycles must be considered. Nuclear fusion reactions do not produce CO_2 or any other GHG emissions. Nor are any harmful chemicals released into the environment under normal operation.

Furthermore, one component of the fuel, deuterium (D), an isotope of hydrogen, is readily available and extractable at low cost from sea water, where it exists on average as 0.0153% in sea water. The other fuel sources of interest for terrestrial fusion are the radioactive hydrogen isotope tritium (T) and the non-radioactive isotope helium-3 (^{3}He). These are used together in what are known as fusion fuel cycles. The D-T fusion fuel cycle produces α-particles, ionised ^{4}He, and high-energy neutrons, where Q_F is the total fusion energy.

$$ {}_1^2D + {}_1^3T \rightarrow {}_2^4He + {}_0^1n \quad [Q_F = 17.6\ MeV] $$

Tritium does not occur naturally on earth and must be produced within the reactor itself. This is achieved by using, what is termed, a 'breeder' that consists of the isotope lithium-6 and is present in a modular structure called the blanket which surrounds the reactor core. When ^{6}Li captures a neutron the following exothermic reaction occurs

$$ n + {}_3^6Li \rightarrow {}_1^3T + {}_2^4He + 4.78\ MeV $$

The technology required to breed tritium has not yet been fully tested, but will be developed during the ITER (International Thermonuclear Experimental Reactor) project. Assuming the present rate of world energy consumption geological estimates put 'inexpensive' reserves of ^{6}Li at around 20000 years [Freidberg, 2010]. Tritium undergoes β-decay with a half-life of 12.5 years [Stacey, 2010] and therefore due to its low-level radiation does not pose a significant safety risk. However, its transport and storage would require the observation of certain safety protocols. Perhaps the greater concern with the D-T reaction is the production of high-energy neutrons.

The blanket captures most of the neutrons, with the shield designed to capture the rest. This, therefore, does not pose a risk to the public; however, the high-energy neutrons cause structural materials to become activated, albeit mildly with an expected safe storage time of the order of 100 years [Freidberg, 2010].

The D-D fuel cycle has two outcomes of approximately equal probability.

$$ {}_1^2D + {}_1^2D \rightarrow \begin{matrix} {}_2^3He + {}_0^1n & [Q_F = 3.2\ MeV] \\ {}_1^3T + {}_1^1p & [Q_F = 4\ MeV] \end{matrix} $$

This fusion reaction is the most sought after since the fuel source is so abundant it is considered to be nearly inexhaustible. Furthermore, no breeding is required. At the present rate of energy consumption, and utilising conventional steam cycles, it is estimated that all the deuterium present in sea water could be used to power fusion reactors for two billion years [Freidberg, 2010]. Moreover, the neutrons that are produced are of much lower-energy, thus causing less damage to structural materials.

The final fusion fuel cycle of terrestrial interest is described by the following reaction and produces the most energy. However, ^{3}He has a natural abundance, on average, of only 0.00013% on earth [Kaye & Laby, 1973]

$$ {}_1^2D + {}_2^3He \rightarrow {}_2^4He + {}_1^1p \quad (Q_F = 18.2\ MeV) $$

The aforementioned fusion cycles have an associated fusion reactivity that determines the temperature at which a cubic metre of fuel is ignited, or reacts, per second. For the D-D cycle a fusion reactivity of approximately 0.1 x 10^{-22} m^3/s occurs at ion temperatures close to 50 keV. This equates to a temperature in excess of 580 x 10^6 K. The D-^{3}He reaction has a similar fusion reactivity rate, albeit at a slightly lower electron temperature of approximately 45 keV [Stacey, 2010]. These values are too low to initiate a significant fusion rate capable of delivering electricity on a large-scale. The ion temperatures necessary to achieve the reactivity conditions are also beyond current technological capabilities. At temperatures close to 15 x 10^6 K, ion temperatures of approximately 13-15 keV, the reactivity rate for the D-T fusion cycle is higher, just over 1 x 10^{-22} m^3/s, and is the reason why the D-T cycle is currently the mainstay of current fusion research [Stacey, 2010].

2.2 Fusion Confinement

In all current fusion power plant designs the reactor core is surrounded by a modular blanket, where circulating fluids receive heat generated through elastic and inelastic collisions between the high-energy 14.1 MeV neutrons of the D-T reaction and the blanket materials, and the exothermic reaction due to neutron capture by ^{6}Li. The neutrons account for approximately 80% of the D-T reaction and constitute a volumetric heating source. The remaining energy leaves the plasma in the form of either energetic charged particles or as radiant energy and is incident upon the first wall: the front face of the blanket module. These volumetric and surface heat sources increase the enthalpy of fluids circulating within the blanket which are subsequently used to drive an external gas, or steam, turbine to generate electricity.

The other purpose of the blanket is to breed the tritium through the interaction of the neutrons and a breeder containing ^{6}Li. The bred tritium is subsequently extracted from the breeder material and fed into the reaction chamber to sustain the D-T cycle, but to achieve a tritium breeding ratio, TBR, defined as the ratio of tritium generated per unit time to the tritium burnt per unit time, greater than unity the neutrons must undergo multiplication and moderation. To feasibly achieve TBR conditions greater than unity, parasitic neutron loss must be countered through neutron multiplication.

Since the neutrons do not interact with the plasma, they exit without any preferred direction. The breeder material, though occupying a significant volume of the blanket, cannot occupy the entire blanket and therefore some of these neutrons interact with structural materials, or coolant, instead of the breeder.

Fortunately, lithium occurs naturally, and abundantly, in the approximate form ^{6}Li 7.5 wt% and ^{7}Li 92.5 wt% [Stacey, 2010], where the latter undergoes the following endothermic reaction

$$n + {}^{7}_{3}Li \rightarrow {}^{3}_{1}T + {}^{4}_{2}He + n - 2.75\ MeV$$

This reaction is more probable with fast neutrons [Stacey, 2010], i.e., those with energies between 1 and 20 MeV, and therefore could provide good neutron

multiplication, but produces only a small amount of tritium and a loss of energy [Freidberg, 2010]. Naturally occurring lead also has good neutron multiplication properties for 14.1 MeV neutrons [Ricapito, 2010]. Moreover, lead is also a good neutron moderator, thus reducing fast neutrons to thermal neutrons, approximately 1-10 eV, where the n + ^{6}Li reaction is more probable [Stacey, 2010]. It is therefore hoped that lithium-lead alloys can perform the multiplication, moderation and breeding functions in one, though it will require the ITER project to determine whether this will work as predicted.

There are several ways in which terrestrial fusion can be obtained. The inertial electrostatic confinement (IEC) method is most often achieved with simple devices called fusors, where a voltage difference between two spherically concentric grids inside a vacuum concentrates ions into a dense core. The fuel, most often deuterium, is introduced and ionized by the voltage difference between the grids. The inner cage has a negative voltage relative to the outer cage and therefore the positive ions accelerate towards it, reaching energies where fusion conditions apply. If the ions collide fusion can occur.

The inertial confinement fusion (ICF) method most commonly utilises high-power lasers to heat the outer shell of a small fuel pellet consisting of deuterium and tritium. The heating process causes the outer shell of the pellet to explode creating an inward force which compresses the remainder of the fuel pellet to temperatures where fusion is initiated. The D-T plasmas that are achieved are of relatively high particle density, 10^{26} per cm^{3}, but short-lived: 10^{-11} seconds. This is in contrast to the relatively low particle density, 10^{14} per cm^{3}, long-lived, 10-second, D-T plasmas that are achieved in what is the most successful and perhaps best-funded method to date: magnetic confinement fusion [Pfalzner, 2006].

2.2.1 Magnetic Confinement Fusion

Magnetic confinement fusion is most often demonstrated using a torus-shaped device called a tokamak, a reactor design developed in the 1960s in the former Soviet Union and adopted worldwide largely for its successful results [CCFE]. The Joint European

Torus (JET) shown in figure 2.1, located at the Culham Centre for Fusion Energy (CCFE), requires temperatures of 100 million degrees Celsius to produce 16 MW_t of power from a D-T reaction using an input power of 24 MW_t, a record set in 1997 [CCFE].

JET's successor, ITER, is expected to produce its first plasma in November 2020, and generate 500 MW_t of power from an input power of 50 MW_t [ITER]. The deuterium and tritium in ITER, which will only have a total weight of a few grams, will be injected into the reaction chamber and heated to over 150 million degrees Celsius. A terrestrial-based prototype of a commercial fusion power station called DEMO is then expected to build on the projected success of ITER and deliver 2-5 GW_t [Stork, 2012], where 1-2 kg of tritium may be present [Stacey, 2010].

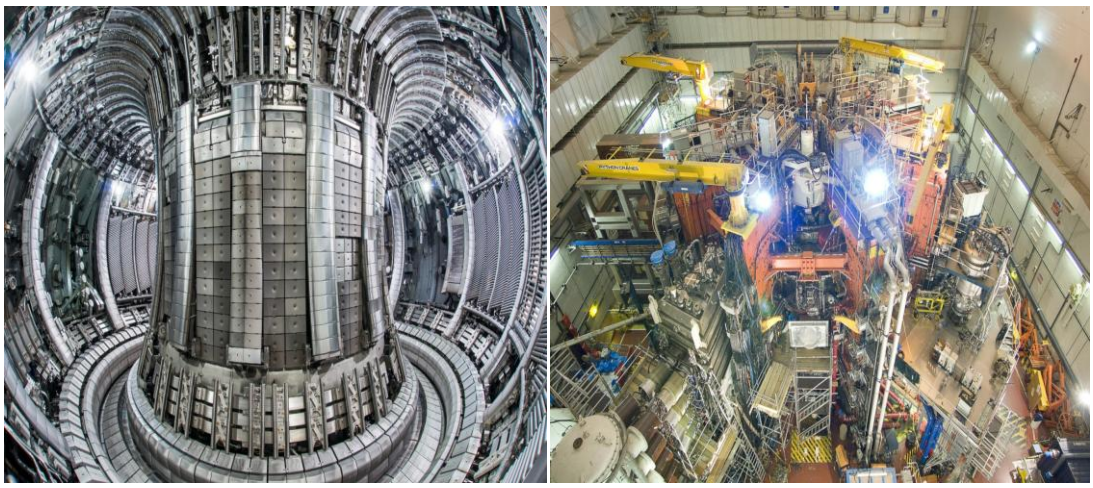

Figure 2.1 Internal and external views of JET, courtesy of [EUROfusion]

In a tokamak a small amount of deuterium and tritium fuel is heated in a reaction chamber to form plasma under vacuum conditions, where a complex configuration of magnetic fields are then used to confine the plasma in an attempt to keep it from contacting the walls of the reaction chamber, which would otherwise quickly erode and allow impurities to enter the plasma and subsequently cause it to cool. There are two types of magnetic field system present in a tokamak: poloidal and toroidal, and these may be ohmic or superconducting.

A current is induced in the plasma through the transformer action produced by an alternating current in a central solenoid, or inner poloidal field coil. A set of external poloidal field coils, otherwise called the equilibrium field coils, serve to both elongate the plasma in the vertical direction, to provide better energy confinement, and to force the plasma inwards against the outwards force of the plasma. The central solenoid and equilibrium coils constitute the poloidal magnet system. A further set of coils are used to provide an extra stabilising force and constitute the toroidal magnet system. The result is a helical magnetic field, which in practice is not always perfect and a variety of charged particles escape confinement and are incident upon the wall of the reaction chamber.

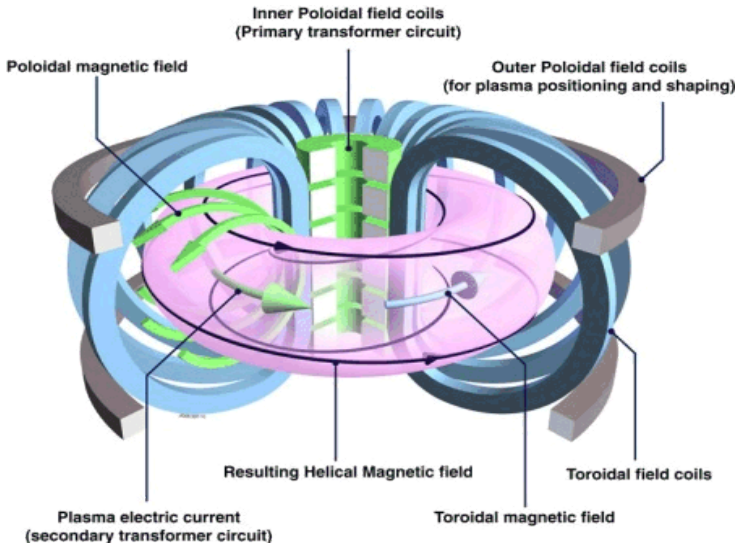

Figure 2.2 Tokamak magnetic confinement system, courtesy of [CCFE]

The role of the blanket has already been described, where its modular approach, visible in figure 2.4, allows for ease of extraction, repair and modification or replacement. The rear wall of the blanket constitutes the shield, which has the role of absorbing any neutrons not captured by the blanket and any subsidiary nuclear reactions that generate gamma rays. Freidberg [2010] notes that the shield must perform this function extremely well, since the superconducting magnets that lie just beyond the shield can only tolerate heat loads within the capacity of the cryogenic cooling system.

A simple cross-sectional representation of this arrangement is shown in figure 2.3, whilst a more detailed view is presented of ITER in figure 2.4.

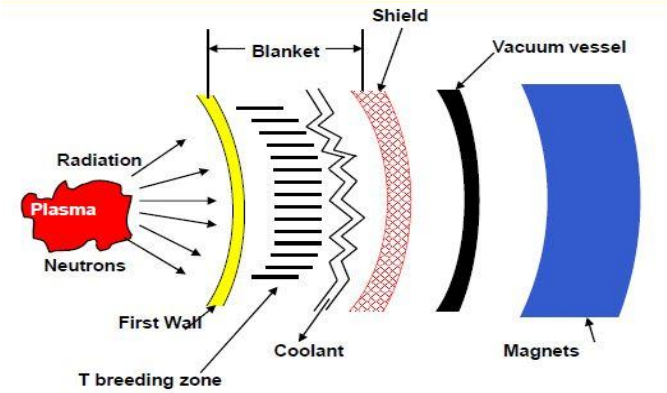

Figure 2.3 Cross-section showing tokamak zones, reproduced from Ricapito [2010]

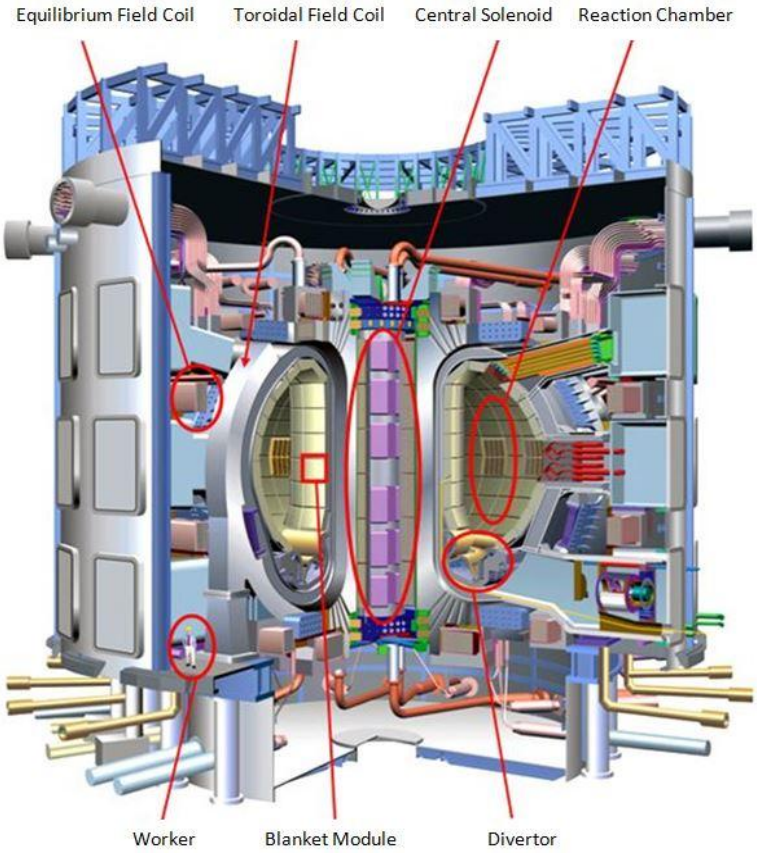

Figure 2.4 Overview of ITER tokamak, with introduced highlighted components. Original image courtesy of [ITER]

Also present in the MCF concept is a component called the divertor, which is essentially a complex exhaust used to rid the plasma of waste material. A view of the divertor in JET is shown in figure 2.5, where it can be seen that a modular design has also been adopted for the same reasons as for the blanket. Magnetic field lines divert heavier ions near the plasma edge, which if left in the plasma would lower its temperature, into a separate chamber where they are incident upon collection plates and their energy converted into heat. A small percentage of the incident particles that are reflected from the collection plates are removed from the reactor via a vacuum duct, whilst the rest remain in the divertor chamber and act as a thermal insulating buffer between the collection plates and the particle fluxes coming from the main plasma. Atoms ejected into the plasma by the erosion of the first wall also find their way into the divertor chamber, where they are prevented from returning to the main plasma by the insulating buffer of partially-ionised gas. Stacey [2010] writes that divertor experiments have successfully demonstrated this plasma impurity control method, which has also resulted in an increase in energy confinement that is not fully understood.

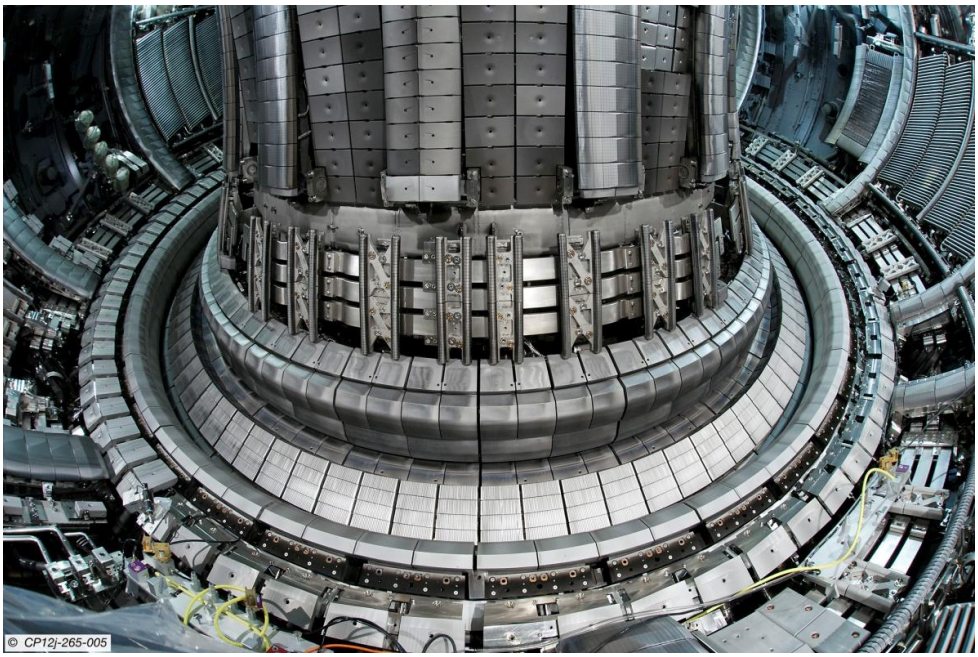

Figure 2.5 Internal close-up view of modular divertor concept in JET, courtesy of [EUROfusion]

2.3 Fusion Plant Models

The power plant conceptual study (PPCS) was born from studies carried out in Europe between 1990 and 2000, which focussed on environmental, economic and safety factors of commercial fusion reactors. These studies concluded that fusion had the potential to provide reasonably-priced electricity, compared with other sources that were considered to be of an environmentally-responsible nature, without any GHG emissions and by using an "inexhaustible energy source" [Maisonnier et al., 2005]. For first-generation reactors operating under the D-T fusion cycle "inexhaustible" is only true to the extent of the deuterium supply from sea water and the success of tritium breeding within the blanket. In 2005, after a three-year study, the PPCS [Maisonnier et al., 2005] was published. It focussed on four fusion power plant models, ranging from the near-term models A and B, to the intermediate model C and the advanced model D. In 2007 an addendum to the PPCS was added in the form of model AB, based upon a new near-term blanket solution [Maisonnier et al., 2007]. The PPCS allows the clarification of the European DEMO concept: the intermediate fusion power plant intended to build upon the expected success of ITER and lead to the first fusion power plant capable of delivering electricity to the end user. DEMO models A, B and AB are based upon plasma physics approximately 30% better than those designed for ITER, whilst models C and D are based upon an assumed rate of plasma physics development. However, the models are also differentiated by the blanket concepts used to convert the fusion power to electrical power output.

2.3.1 Model A

This fusion plant model is based upon a water-cooled lithium-lead (WCLL) blanket, where a lithium-lead alloy, Pb-17Li, is used to moderate and multiply the neutrons, and to breed the tritium. Figure 2.6 shows a single WCLL module, one of many that comprise the modular blanket, as depicted in figure 2.4. Water in the blanket operates under PWR conditions: 15.5 MPa, with inlet and outlet temperatures of 285°C and 325°C, respectively.

The structural material for the blanket is composed of low-activation, low-impurity, ferritic-martensitic steel called EUROFER. A water-cooled divertor also features in this plant model and is expected to also operate under PWR conditions, however, there are two concepts being investigated. The first is based upon the limited extrapolation from the ITER divertor concept, where CuCrZr is used for the high heat flux, HHF, zone. This limits the maximum water temperature to 167°C.

The alternative approach uses stainless steel for the HHF zone to achieve maximum water temperatures of 325°C. EUROFER is still used as the main structural material and tungsten tiles are used for the plasma facing, PF, armour.

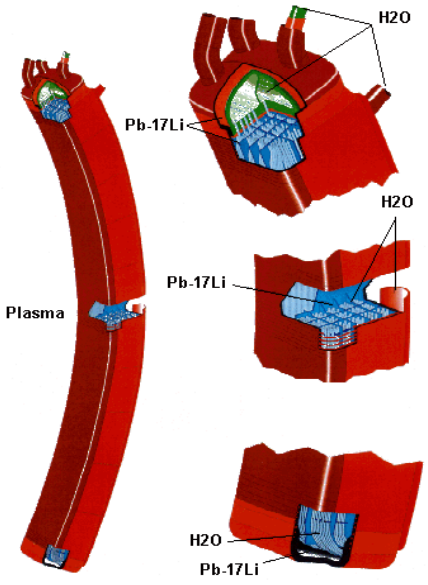

Figure 2.6 WCLL blanket module, reproduced from [CEA]

The fusion power available from this plant model is 5000 MW_t, where 894 MW_t is deposited in the divertor. There is a blanket gain ratio of 1.18, caused by the exothermic reaction of D-T neutrons with ^6Li, which yields a blanket power of 4845 MW_t. The power conversion system yields a gross electrical power output of 2066 MW_e and a Rankine cycle efficiency close to 36%. This is increased slightly to approximately 37% by the adoption of the advanced water-cooled divertor concept.

After taking into account the electrical input power required for plasma heating, breeder heating and coolant pumping the net electric power is 1546 MW_e; approximately 1650 MW_e if the more advanced water-cooled divertor concept is used. The overall plant efficiency is defined as the ratio of the net electric power to the fusion power. For model A this is 31% for the case using the limited divertor, whilst for the advanced divertor it is 33%.

2.3.2 Model B

Model B is based upon a helium-cooled pebble bed (HCPB) blanket with EUROFER used as the structural material. Lithium-based ceramic pebbles such as lithium metasilicate, Li_2SiO_3, and lithium orthosilicate, Li_4SiO_4, are used to perform the breeding function, whilst the neutron multiplier is composed of beryllium or beryllium titanate. The moderation is achieved jointly by the lithium-based ceramic pebbles and beryllium. A diagram of a single HCPB blanket module is given in figure 2.7. Helium operating at 8 MPa is used as the blanket coolant, where inlet and outlet temperatures for the blanket are 300°C and 500°C, respectively. The shield zone is also cooled with helium, where inlet and outlet temperatures are 240°C and 280°C, respectively.

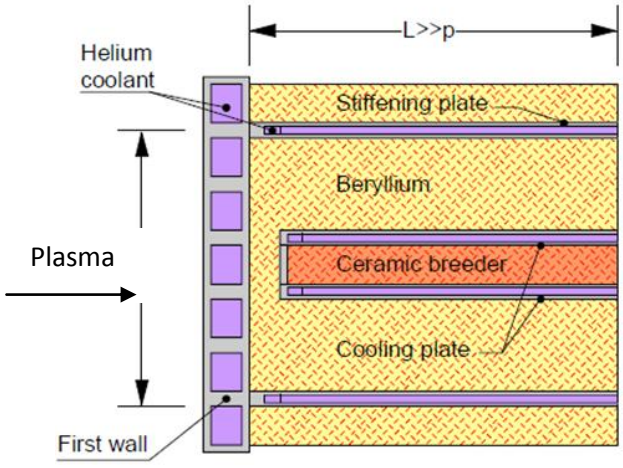

Figure 2.7 Cross-section of HCPB blanket module, reproduced from Kleefeldt [2003]

The divertor operates using helium at 10 MPa, where inlet and outlet temperatures are 500°C and 740°C, respectively. The HHF zone uses a tungsten alloy and tungsten as the PF armour, whilst the structural material is oxide dispersion strengthened, ODS, reduced activation ferritic, RAF, steel.

The fusion power for model A is 3600 MW_t, where 685 MW_t is deposited in the divertor and 4319 MW_t in the blanket and shield through a blanket gain of 1.39. The power conversion system uses indirect heat exchangers to supply heat to a superheat Rankine cycle featuring reheat, with a net cycle efficiency of 41.5% [Maisonnier et al., 2005]. The gross electrical power output for a model B fusion plant is 2157 MW_e, but the plant net electrical power is lower: 1332 MW_e. This is partly due to the extra pumping power required to circulate helium through the blanket, however, the helium-cooled divertor yields a couple of extra percentage points with an overall plant efficiency at 37%.

2.3.3 Model AB

The blanket for model AB has the same characteristics as the model B concept, with the exception that the ceramic pebbles are replaced with a lithium-lead breeder: Pb-17Li, where the inlet and outlet temperatures are 300°C and 480°C, respectively. The diverter for model AB is the same as that for model B. Figure 2.8 shows a single helium-cooled lithium-lead (HCLL) blanket module.

The fusion power for this addendum to the PPCS is 4290 MW_t, with 981 MW_t being deposited in the divertor and 4470 MW_t deposited in the blanket, giving a blanket gain of 1.18. Indirect heat exchangers supply heat to a superheat Rankine cycle featuring reheat, with a net cycle efficiency of around 40% [Wong, et al., 2007]. The gross electrical power output is 2385 MW_e and the plant net electric power is 1500 MW_e, however, there is a slightly lower overall plant efficiency of 35%. The reason for this is not explicitly given in the PPCS reports, though by comparing gross and net electric powers it is clear that there is some greater input power required for this model than for model B.

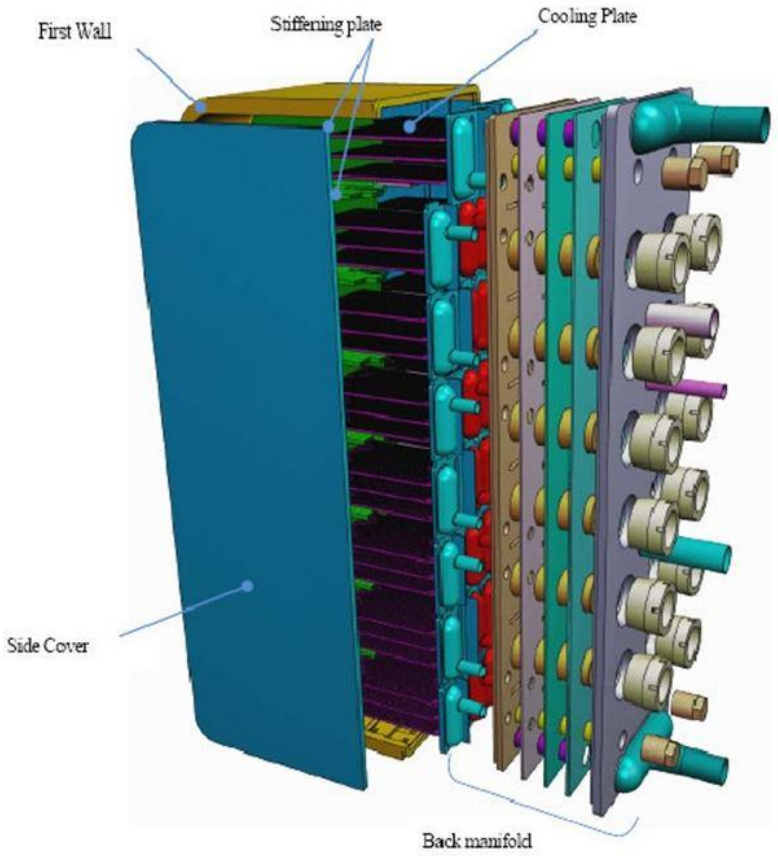

Figure 2.8 HCLL blanket module, reproduced from [Fusion for Energy]

2.3.4 Model C

This model uses the dual-cooled concept where both helium and the liquid metal breeder, Pb-17Li, are circulated to remove heat from the blanket. Helium operating at 8 MPa enters the blanket at 300°C and exits at 480°C after several passes through the module. The breeder meanwhile, flowing with average velocities in the cm/s range, as opposed to the mm/s range in the near-term A and AB models, enters the blanket at 480°C and exits at 700°C. A single dual-cooled lithium-lead (DCLL) blanket module is shown in figure 2.9.

The structural material of the blanket is EUROFER, with a range of materials proposed for the channel inserts: EUROFER, ODS-SiC, SiC. Two separate flows of helium, each at 10 MPa, are used to cool the ODS-RAF divertor structure, where

tungsten is used for the PF armour and tungsten alloy for the HHF zone. The first is called the divertor bulk helium flow and provides 335 MW_t with inlet and outlet temperatures of 480°C and 615°C, respectively. The second is the divertor target helium flow and provides 248 MW_t with inlet and outlet temperatures of 700°C and 800°C, respectively.

The fusion power for model C is 3410 MW_t, with 583 MW_t being deposited in the divertor and 3408 MW_t in the blanket due to a gain of 1.21. The power conversion system consists of four external loops, where a Brayton cycle operates with 'secondary' helium at 15 MPa. The secondary helium does not pass through the blanket, but receives heat from four indirect heat exchangers: IHX1 (blanket helium), IHX2 (divertor bulk), IHX3 (blanket breeder), IHX4 (divertor target). The four IHX processes give a gas turbine inlet temperature of 700°C and a net cycle efficiency of 42.5%. After conversion the external Brayton cycle delivers a plant gross electric power of 1696 MW_e and a plant net electric power of 1449 MW_e.

The pumping power for this reactor model is lower since helium is not the only coolant. An overall plant efficiency of 42% is achieved.

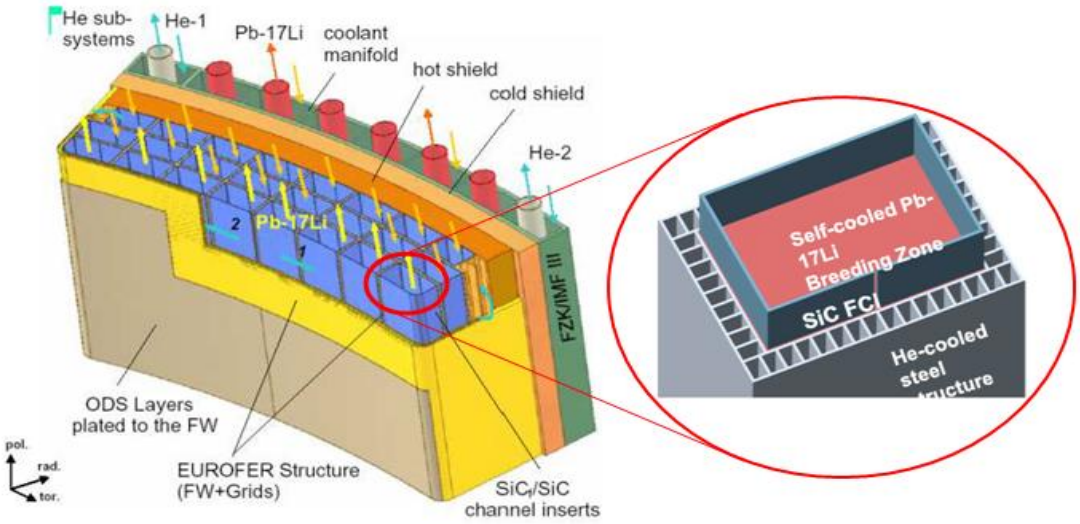

Figure 2.9 DCLL blanket module, reproduced from Ricapito [2010]

2.3.5 Model D

This relies upon the self-cooled concept, where the blanket and divertor, using silicon carbide as a structural material and tungsten as the PF armour, are cooled solely by the liquid metal breeder Pb-17Li. The liquid metal breeder velocities are in the m/s range with blanket inlet and outlet temperature of 700°C and 1100°C, respectively, whilst the divertor inlet and outlet temperature are 600°C and 900°C, respectively. A single self-cooled lithium-lead (SCLL) blanket module is given in figure 2.10.

The fusion power for model D is 2530 MW_t, with 607 MW_t being deposited in the divertor and 2164 MW_t being deposited in the blanket and shield due to a blanket gain of 1.32. The heat is rejected separately from the blanket and divertor to two external Brayton cycles generating a plant gross electric power of 1640 MW_e. The Brayton cycle associated with the divertor has a thermal efficiency close to 56%, whilst the Brayton cycle associated with the blanket has a thermal efficiency close to 60%. The plant net electric power is 1527 MW_e giving an overall plant efficiency of just over 60%.

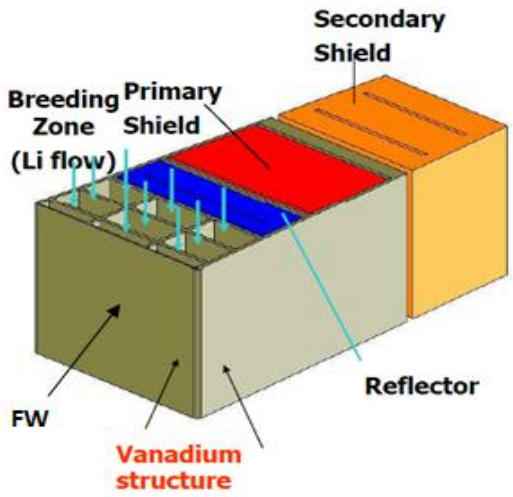

Figure 2.10 SCLL blanket module, reproduced from Ricapito [2010]

2.3.6 PPCS Summary

To summarise the performance of each PPCS model the main plant parameters are reproduced from data [Masonnier et al., 2005]. [Masonnier et al., 2007] and summarised in table 2.1. Supporting data from Wong et al. [2007] and Stork [2012] has been used to summarise the blanket and divertor parameters in table 2.2 and table 2.3, respectively.

Plant Parameter	**Model A (WCLL)**	**Model B (HCPB)**	**Model AB (HCLL)**	**Model C (DCLL)**	**Model D (SCLL)**
Fusion Power (MW_t)	5000	3600	4290	3410	2530
Blanket Gain	1.18	1.39	1.18	1.21	1.32
Blanket Power (MW_t)	4845	4319	4470	3408	2164
Divertor Power (MW_t)	894	685	981	583	607
Pumping Power (MW_e)	110	375	400	87	12
Heating Power (MW_e)	246	270	257	112	71
Gross Electric (MW_e)	2066	2157	2385	1696	1640
Net Electric (MW_e)	1546	1332	1500	1480	1527
Cycle Efficiency (%)	36/37	41.5	40	42.4	56/60
Plant Efficiency (%)	31/33	37	35	43.5	60

Table 2.1 PPCS plant model parameters, reproduced using data from Maisonnier et al. [2007]. Model C plant parameters taken from Norajitra et al. [2003]

Blanket Type	**WCLL (Model A)**	**HCPB (Model B)**	**HCLL (Model AB)**	**DCLL (Model C)**	**SCLL (Model D)**
Material (FW/ Channel inserts)	EURO-FER	EURO-FER	EUROFER	EUROFER (EUROFER/ ODS SIC/SIC)	SiC/SiC
Blanket Coolant	Water	Helium	Helium	He Pb-17Li	Pb-17Li
In/Out (ºC) (Shield zone)	265/325	300/500 (240/280)	300/500	He: 300/480 Pb-17Li: 480/700	700/1100
Pressure (MPa)	15.5	8	8	He: 8 Pb-17Li: 1 - 2	0.5 - 1
Power Cycle	Rankine	Rankine	Rankine	Brayton	Brayton
Breeder	Pb-17Li	Li_4SiO_4 Li_2SiO_3	Pb-17Li	Pb-17Li	Pb-17Li
In/Out (ºC)	~280/315	N/A	450/480	460/700	700/1100
TBR	1.06	1.12	1.13	1.15	1.12

Table 2.2 Summary of blanket parameters [Maisonnier et al., 2005] [Stork, 2012]

Blanket Type	**WCLL (Model A)**	**HCPB (Model B)**	**HCLL (Model AB)**	**DCLL (Model C)**	**SCLL (Model D)**
Structural material	EUROFER	ODS-RAF			SiC
HHF material	CuCrZr (Stainless steel)	Tungsten alloy			SiC/SiC
PF armour	Tungsten				
Coolant	Water	Helium			LiPb
In/Out (ºC)	140/167 (~140/325)	500/740	500/740	Bulk: 480/615 Target: 700/800	600/900
Pressure (MPa)	15.5	8	8	10	0.5 - 1

Table 2.3 Summary of divertor parameters [Maisonnier et al., 2005]

2.4 Fusion Constraints

The constraints relating to the successful development of fusion power plants are considerable, but can be divided into two parts: physics and engineering constraints, where the latter perhaps poses the greater challenge.

Freidberg [2010] concisely summarises the physics constraints in three parts: plasma pressure, neutron moderation and neutron capture. Plasma pressures for a given volume are determined from the statistical cross-section for a particular fusion cycle.

Maintaining this plasma pressure is critical for keeping the plasma at energies suitable for fusion conditions. Impurities in the plasma and confinement leakage contribute to plasma cooling and the loss of such conditions.

Neutron moderation and capture relate to the blanket. Sufficient levels of moderation must be achieved to allow neutron capture by ^{6}Li so that tritium can be bred. Once fast neutrons are slowed to thermal neutron energies the cross-section for their capture by ^{6}Li is quite large and should occur readily. The mean-free path for a range of neutron energies is dependent upon the moderating material and will determine the thickness of the blanket. Achieving the correct moderation is crucial for the sufficient breeding of tritium in the blanket.

The engineering constraints largely relate to materials. The first wall must cope with high heat fluxes due to energetic charged particles and radiant energy losses in the plasma. The high-energy D-T neutrons can also cause atom displacements in the first wall materials leading to embrittlement, erosion and sputtering: the ejection of material atoms into the reaction chamber. Plasma facing components like the first wall and divertor plates must cope with these extreme conditions over a protracted length of time to lower the maintenance and replacement costs, thus keeping the cost of electricity delivered by fusion power to the end user economical. It is expected that the divertor will be replaced every two full-power-years, whilst the blanket will be replaced every five full-power-years. For DEMO it has been suggested [Masonnier et al., 2006] that the modules be as large as possible, taking into account the magnet arrangement and the size of the equatorial ports through which the modules must pass, to minimise the total number of modules to between 150 and 200. Based upon this, and assuming suitable blanket handling devices, an availability of 75% could be reached.

Structural materials used in the blanket face the same issues with neutron loading, but can also suffer from tritium permeation. It is thought that since tritium has a high solubility and is readily extractable from liquid breeders that it will leach from the breeder into the surrounding structure [Stacey, 2010]. Tritium permeation barriers must be developed to maintain levels of tritium in the breeder, otherwise the tritium

rate entering the reaction chamber would fall, which would ultimately lead to the reduction in the D-T fusion reaction rate.

Materials that are irradiated by neutrons suffer from swelling and embrittlement, caused by the transmutation of elemental atoms and the subsequent production of hydrogen and helium. A variety of complex steels have been proposed for the near-term models, but research is still ongoing [Stacey, 2010].

Stainless steels suffer from transmutation effects caused by neutron radiation and these limit their maximum operating temperature to around 550°C. Titanium alloys have unacceptable tritium absorption properties, whilst high nickel-based alloys suffer in neutron environments. Refractory metal alloys using vanadium, niobium and molybdenum possess good strength properties, but suffer if impurities such as hydrogen, carbon dioxide or methane are present in the helium coolant. For the intermediate and advanced PPCS models silicon carbide has been suggested, which is thought to offer the promise of high-temperature helium conditions, leading to increased thermal cycle efficiency. Currently, the use of complex steels limit coolant outlet temperatures and therefore also thermal cycle efficiencies [Stacey, 2010].

2.5 Summary

Due to the high reactivity of the D-T fusion cycle, and the current technological limitations on reaching higher ion temperatures, D-T fusion is considered the most achievable form of terrestrial-based fusion. Several methods of achieving fusion conditions in plasmas are available, however, the MCF concept remains at present the most successful way to sustain plasmas at fusion conditions for the purpose of large-scale electricity production.

The ITER experiment will test several technologies necessary to prove the viability of MCF, particularly those relating to tritium breeding and its subsequent extraction, without which the D-T cycle could not be maintained. The PPCS reports outline several models for DEMO, the intermediary fusion plant that will build upon developments made in ITER and precede the first commercial-based fusion reactors

capable of delivering electrical power to the end user. The PPCS outlines the necessary improvements in plasma physics and blanket technology required to achieve certain DEMO plant parameters.

Several physics and engineering constraints must be overcome to enable viable fusion plants. Plasma pressures must be maintained to deliver a certain amount of power, whilst in the blanket neutron moderation and capture must be achieved to allow tritium breeding ratios greater than unity.

Materials capable of operating within a fusion environment for a protracted length of time must do so without significant embrittlement, erosion and sputtering. Tritium permeation must be dealt with to allow sufficient levels to reach the reaction chamber, whilst structural blanket materials capable of allowing high coolant outlet temperatures are crucial for increasing overall plant efficiency and lowering the cost of electricity to the end user.

Chapter 3: Electrical Power Generation

The previous chapter outlined the route being pursued in an attempt to build terrestrial-based fusion reactors capable of delivering electricity to a national grid. It also highlighted the physics and engineering challenges that need to be overcome in realising such fusion power plants. This chapter will look at how electrical power is currently expected to be generated from fusion reactors that utilise a blanket.

Rankine and Brayton power cycle configurations will be examined, noting current limitations on their efficiencies using the blanket outlet temperatures in table 2.3 of the previous chapter, with some extrapolation to higher temperatures for improved materials. A brief discussion will follow concerning the possibility of alternative conversion routes for generating electricity from a fusion reactor, before ending with the performance of several power conversion technologies that will be quantified in the context of fusion blanket designs.

3.1 Conventional Electricity Generation

As already mentioned, large-scale conventional electricity generation is achieved through the conversion of thermal energy to electrical energy using an intermediate mechanical step. In the context of fusion, the previous chapter explained how the blanket and divertor supply the thermal energy for the subsequent conversion to electrical energy.

The two thermal power cycles used for generating electricity are the Rankine and Brayton cycles, for which their configurations can range from the simple to the complex. The Rankine cycle operates using a two-phase fluid, typically water, but other binary substances such as ammonia or isobutene are viable. The Brayton cycle,

however, uses a single-phase gaseous fluid, which in the context of fusion is currently helium, but there is also interest in supercritical Brayton cycles using supercritical water [Sardain et al., 2007] and supercritical carbon dioxide [Linares et al, 2015].

The graphs in this subsection have been generated using the governing equations for power cycles (see chapter 5) to show the performance of a range of power cycle configurations under certain operating conditions.

3.1.1 Rankine Cycle

A simple Rankine cycle uses four basic components: boiler, steam turbine, condenser and feed pump. The steam entering the turbine is wet and causes the turbine blades to deteriorate over time. Heating steam past the dry saturation point brings it into the superheat region. This alteration to the simple Rankine cycle has the benefit of increasing both cycle efficiency and the net work output, but also reduces turbine blade erosion.

Taking the case where the boiler pressure is 155 bar, as in PWRs, the condenser pressure as 0.0563 bar and the isentropic efficiency of the steam turbine as 90%, the cycle efficiency and net work output of a simple and superheat Rankine cycle can be compared. Figure 3.1 shows the marked increase in efficiency and net work output by superheating the steam before it enters the turbine. The dry saturation point of steam at 155 bar is approximately 345 °C and marks the point at which the simple Rankine cycle ends and the superheat Rankine cycle begins.

For a Rankine cycle associated with PPCS models B and AB there must be an indirect heat exchange, IHX, process. Assuming ideal IHX conditions, neglecting any pressure drop and assuming a zero pinch-point, allows the turbine inlet temperature to be equal to the blanket outlet temperature. In reality, of course, this is impossible, but this approach has been adopted here to determine the best possible performance.

The divertor could be used to further increase the turbine inlet temperature to provide a boost in cycle efficiency and net power output, but only up to the maximum continuous operating temperature of the steam turbine, which can be up to 620°C [General Electric].

The divertor in PPCS models B and AB could instead be used to reheat the exhaust of the steam turbine, thus constituting a reheat Rankine cycle. There is an optimum pressure at which the turbine exhaust is reheated. For the graph in figure 3.2 this has been taken as 42 bar, the dry saturation point for an ideal expansion, i.e. where the isentropic efficiency is 100%. The optimum reheat pressure will be dependent upon the amount of divertor thermal power used and the heat capacity ratio of the two streams in the IHX process. Once again assuming an ideal IHX process, which would give a turbine inlet temperature of 500°C, the efficiency and net work output can be compared for a range of reheat temperatures.

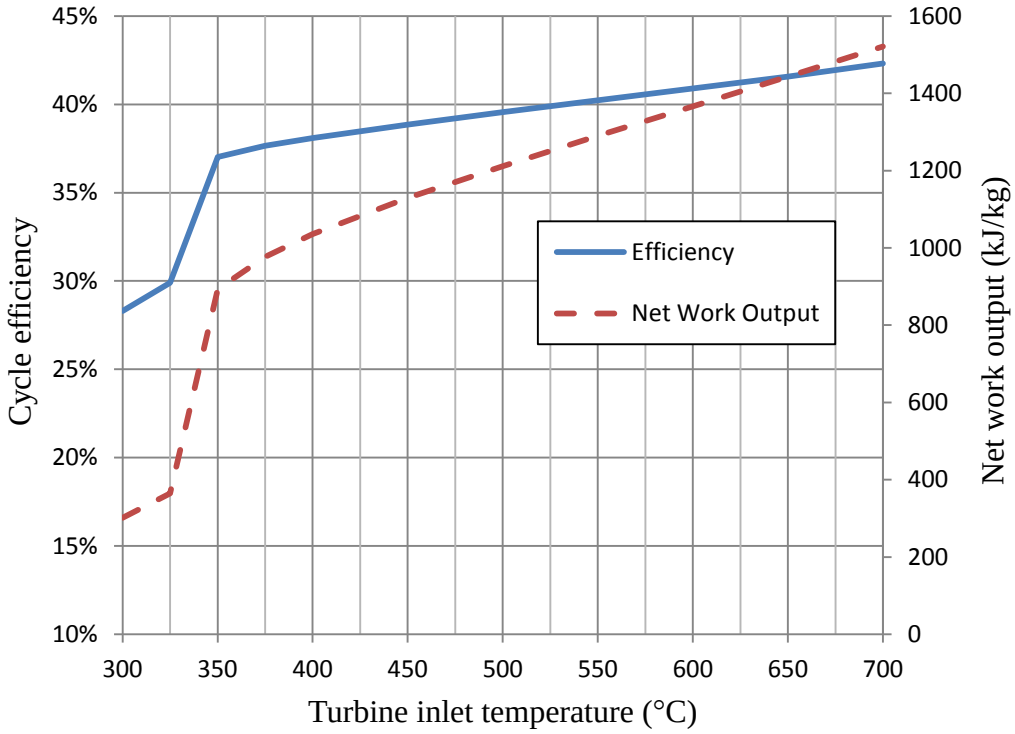

Figure 3.1 Cycle efficiency and net work output for a Rankine cycle transitioning from simple to superheat, where the boiler pressure is 155 bar, condenser pressure is 0.0563 bar and the turbine isentropic efficiency is 90%

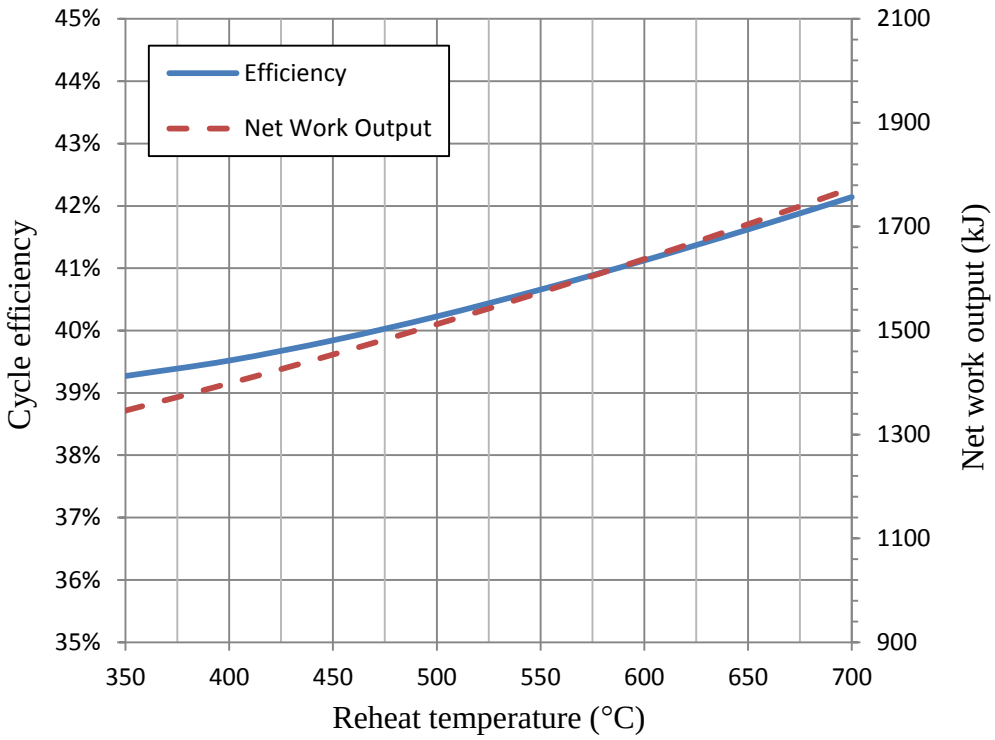

Figure 3.2 Rankine cycle for a range of reheat temperatures, using a boiler pressure of 155 bar, turbine inlet temperature of 500°C, turbine isentropic efficiency of 90%, reheat pressure of 42 bar and condenser pressure of 0.0563 bar

An alternative Rankine cycle arrangement involves regeneration, where a portion of the turbine exhaust is used to pre-heat the water entering the boiler. This can be done more than once, by bleeding-off steam at different pressures as the steam expands in the turbine, but for the purpose of a simple comparison the graph in Figure 3.3 shows a Rankine cycle with only one level of regeneration, where the steam has been bled at 13 bar, the optimal regeneration point. Varying the turbine inlet temperature between 350°C and 700°C produces a range of bleed fractions. At 350°C a 30% bleed is produced, whilst at 700°C a 22% bleed is produced, assuming bleeding occurs at the dry saturation point. The range of turbine inlet temperatures accommodates the use of the divertor in PPCS models B and AB.

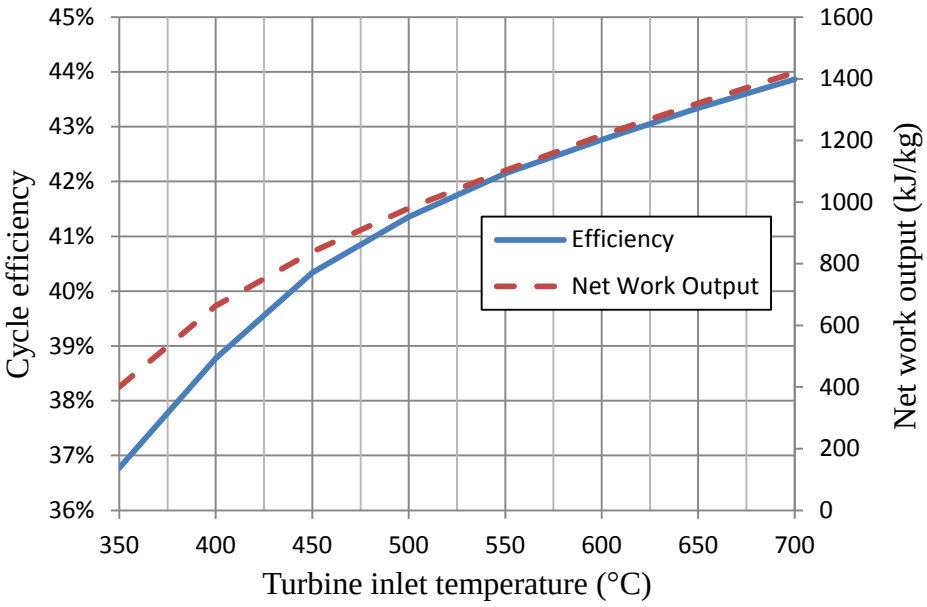

Figure 3.3 Rankine cycle with one level of regeneration for a range of turbine inlet temperatures, using a boiler pressure of 155 bar, condenser pressure of 0.0563 bar, optimal regeneration pressure of 13 bar and turbine isentropic efficiency of 90%. A range of turbine inlet temperature produces a range of bleed fractions

Of course, the aforementioned cycle modifications can be combined into one cycle, yielding a Rankine cycle with superheat, reheat and regeneration. Using the ideal IHX process, the graph in figure 3.4 shows the efficiency and net work output of such a cycle, where the initial turbine inlet temperature, boiler pressure and condenser pressure values are the same as in the other graphs. The reheat pressure is equal to the regeneration pressure and is optimised for reheat temperature efficiency.

By using the blanket and divertor thermal powers, given in table 2.1, the required steam mass flow can be found, which would give a steam turbine inlet equal to the blanket outlet temperature. For example, to achieve a steam turbine inlet temperature of 500°C at 155 bar, using the thermal power available from the blanket of PPCS model B, the required steam mass flow is 1375 kg/s. Using the available thermal power from the PPCS model B divertor, and a steam mass flow of 1375 kg/s, it is

found that, for the case of using the divertor to further superheat the steam, a turbine inlet temperature of 600°C is attainable.

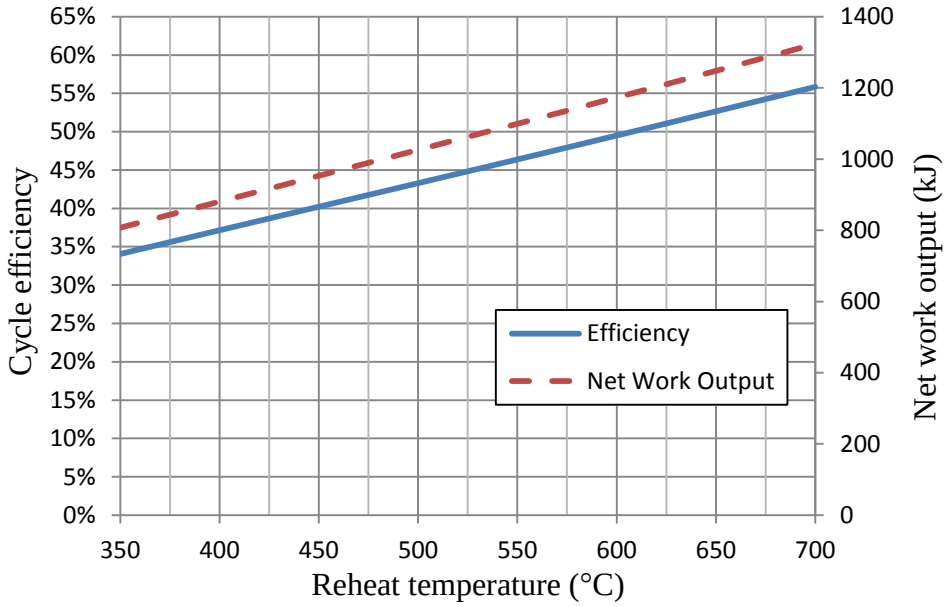

Figure 3.4 Rankine cycle with superheat, reheat and one level of regeneration, for a range of reheat temperatures, using a boiler pressure of 155 bar, turbine inlet temperature of 500°C, condenser pressure of 0.0563 bar, isentropic efficiency of 90%. Equal reheat and regeneration pressures optimised for cycle efficiency.

For the case where the divertor is instead used to reheat the steam at 21 bar, a reheat temperature of only 423°C is reached. However, for PPCS model AB, where the available thermal power from the divertor is higher, the reheat temperature at 21 bar is 510°C.

When reheat is used with regeneration there is a benefit because some of the steam is bled for feed-heating. The reduced mass flow of steam being reheated can reach a higher temperature than if reheat alone was used. Using PPCS model B parameters a bleed fraction close to 28% enables a reheat temperature of 512°C to be reached, whilst for PPCS model AB 600°C is easily attainable due to the larger thermal power available from the divertor.

The performance of the various Rankine cycle configurations are summarised in table 3.1, where the effect of using the divertor can be seen. Also included in the table is the specific steam capacity, SSC, a measure, in units of kg/kWh, of the required steam flow to generate unit power output. PPCS models C and D use a Brayton cycle operating with helium, due to the higher peak temperature permissible by a gas turbine, though model C could use a Rankine cycle if a continuous steam turbine inlet temperature of 700°C was permissible.

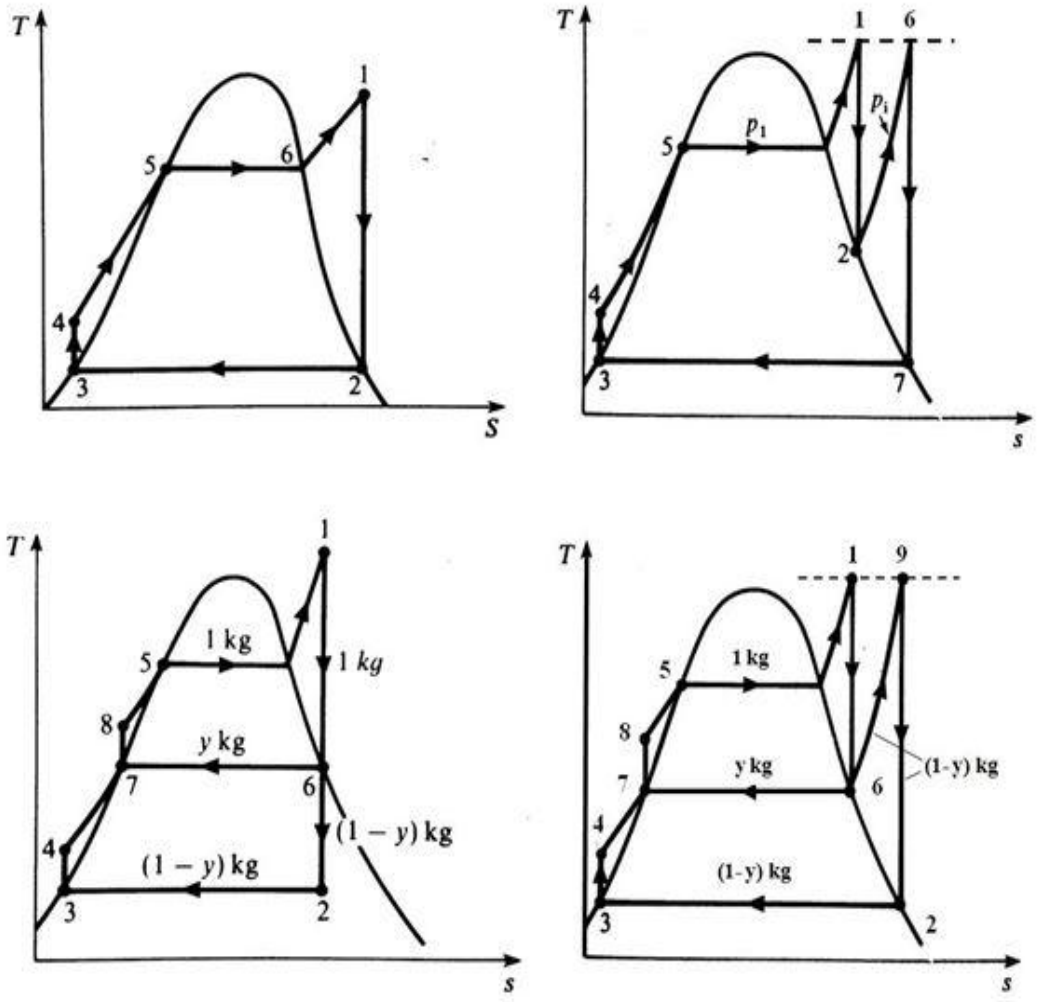

Figure 3.5 T-s diagrams for the simple (top left), reheat (top right), regenerative (bottom left) and reheat & regeneration (bottom right) Rankine cycle configurations, showing ideal expansions. Images reproduced from Eastop & McConkey [1993]

Rankine Cycle	HP Turbine inlet (°C)	LP Turbine inlet (°C)	Divertor Used	Cycle η (%)	Net Work Out (kJ/kg)	SSC (kg/kWh)
Simple (PPCS A)	325	N/A	No	29.9	364	9.88
Superheat (PPCS B & AB)	500	N/A	No	39.6	1211	2.97
Superheat (PPCS B & AB)	600	N/A	Yes	40.1	1366	2.64
Superheat with Reheat (PPCS B)	500	423	Yes	39.7	1424	2.53
Superheat with Reheat (PPCS AB)	500	510	Yes	40.3	1524	2.36
Superheat with Regeneration (PPCS B & AB)	500	N/A	No	41.4	980	3.67
Superheat with Regeneration (PPCS B & AB)	600	N/A	Yes	42.8	1216	2.96
Superheat Reheat and Regeneration (PPCS B)	500	512	Yes	44.0	1043	3.45
Superheat Reheat and Regeneration (PPCS AB)	500	600	Yes	49.5	1173	3.07

Table 3.1 Comparison of Rankine cycles using a boiler pressure of 155 bar, condenser pressure of 0.0563 bar, reheat and regeneration pressure of 2.1 bar, turbine isentropic efficiency of 90% and ideal IHX process

3.1.2 Brayton Cycle

Brayton cycles associated with PPCS models B and AB will now be examined. The simplest Brayton cycle is denoted as the CBT cycle, after the components from which the cycle is comprised: C – compressor, B – boiler/heater, T – turbine. In the context of fusion, B can also represent the blanket.

CBT cycles suffer from low cycle efficiency, much like simple Rankine cycles. To counter this, an exhaust gas heat exchanger, denoted by the letter X, is used to remove heat from the outlet of the gas turbine and use it to preheat the gas entering the heater. This regeneration has the effect of simultaneously lowering the mean temperature of heat rejection and raising the mean temperature of heat reception, thus increasing cycle efficiency. The CBT cycle then becomes a CBTX cycle. To approach a situation where all heat reception occurs at the highest temperature, reheat, R, is used. In conjunction with an exhaust gas heat exchanger such a configuration is denoted as a CBTRTX cycle. Likewise, to ensure all the heat rejection occurs at the lowest temperature, inter-cooling, I, is used and the configuration is a CICBTX cycle.

In theory, infinite reheating and infinite inter-cooling will allow all the heat reception and heat rejection to occur at the highest and lowest temperatures, respectively. In reality, however, this is of course impossible, but approachable if enough inter-cooling and reheating steps are performed, usually at extra cost for diminishing returns. If reheating and inter-cooling are used without an exhaust gas heat exchanger then the effect is a reduction in cycle efficiency, but an increase in net work output [Haywood, 1980]. The aforementioned Brayton cycle modifications can be combined to give the CICBTRTX cycle, where one stage of reheat and inter-cooling is used, as shown in figure 3.6.

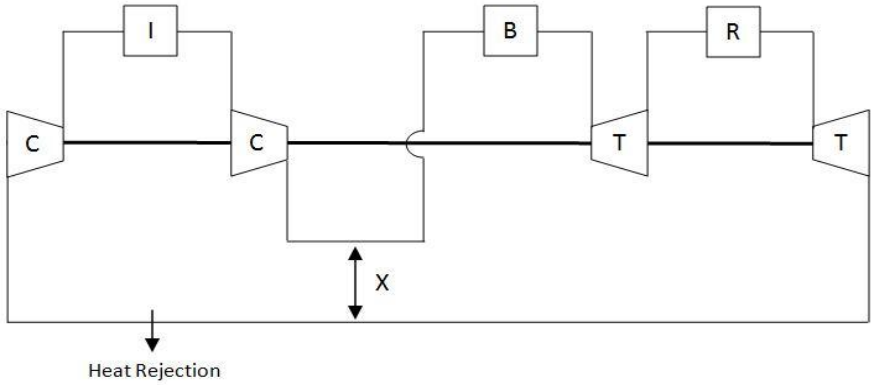

Figure 3.6 Cycle diagram showing a CICBTRTX configuration

3.1.2.1 Primary Brayton Cycles

In PPCS models B and AB the blanket helium could be used directly in a primary cycle, i.e. instead of transferring heat to an external power cycle, which for clarification purposes should be called a secondary cycle. The divertor helium operates at the same pressure as the blanket helium: 8 MPa. Moreover, the blanket outlet temperature is the same as the divertor inlet temperature. However, table 3.2 shows that the helium mass flows for the blanket and divertor are different.

PPCS Model	ṁ blanket helium (kg/s)	ṁ divertor helium (kg/s)
B	4156	549
AB	4301	787

Table 3.2 Summary of helium mass flow rates in blanket and divertor for PPCS models B and AB

For PPCS model B the total mass flow of helium in the blanket is 4156 kg/s, whilst in the divertor the total helium mass flow is 549 kg/s. To make a primary Brayton cycle viable, 549 kg/s must be bled from the main helium just after it has left the

blanket, where 4156 kg/s of helium receives 4319 MW_t. This is done so that the divertor in PPCS model B receives the specified amount of helium: 549 kg/s.

The first turbine receives 3607 kg/s of blanket helium at 500°C, whilst the bled helium passing through the divertor receives 685 MW_t before entering a second turbine at 740°C. After their respective expansion processes the separate helium streams are mixed before rejecting heat. Such a cycle can be denoted as a CBTDT and is shown in figure 3.7, where D represents the divertor and can replace R for any cycle using reheat, so long as the reheat is performed by the divertor.

To examine the performance of a CBTDT cycle a compressor inlet temperature of 35°C and an isentropic efficiency for both the compressor and turbine 90% can be assumed. On this basis, the CBTDT cycle would require a cycle pressure ratio of approximately 4.2 so that the outlet temperature of the compressor matches the required inlet temperature of the blanket: 300°C. The cycle efficiency at this pressure ratio is only 22%.

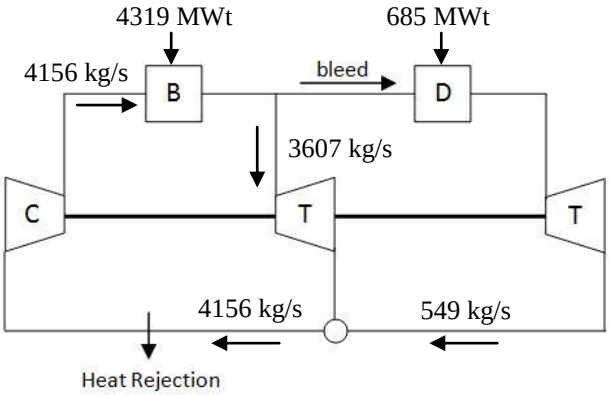

Figure 3.7 Cycle diagram of a CBTDT cycle, depicting mass flows of helium and heat inputs based on PPCS model B

The addition of an exhaust gas heat exchanger, with an effectiveness of 90%, turns the CBTDT cycle into a CBTDTX cycle and allows the cycle pressure ratio to be reduced from 4.2 to 2.6, an optimum for this cycle operating under the same conditions as for the CBTDT cycle. The cycle pressure ratio can be reduced because the outlet temperature of the compressor can be raised by the turbine exhaust to meet

the required blanket inlet temperature. The result is a lower compressor power input, which increases the cycle net power output and subsequently increases the cycle efficiency to 30.5%. The cycle diagram for this cycle, without annotation, is shown below in figure 3.8

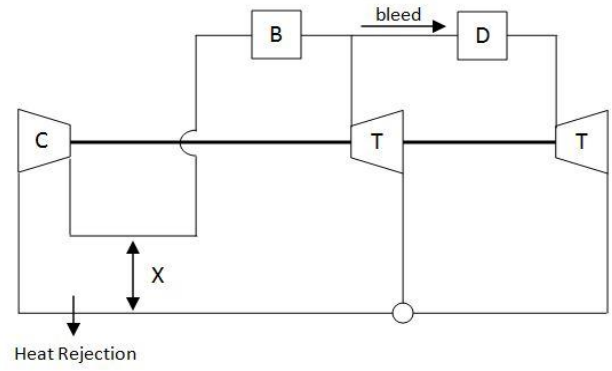

Figure 3.8 Cycle diagram for CBTDTX cycle

The introduction of inter-cooling produces a CICBTDTX cycle, where the optimum inter-cooling pressure is achieved by taking the square root of the cycle pressure ratio [Haywood, 1980], further lowers the outlet temperature of the compressor. The amount of regeneration from the turbine exhaust is therefore higher, but the compressor input power is reduced, leading to an increase in cycle efficiency. The optimum cycle pressure ratio is 3.5 and the cycle efficiency is increased to 39%. The cycle diagram is the same as in figure 3.6, but with the inclusion of the divertor as a reheater.

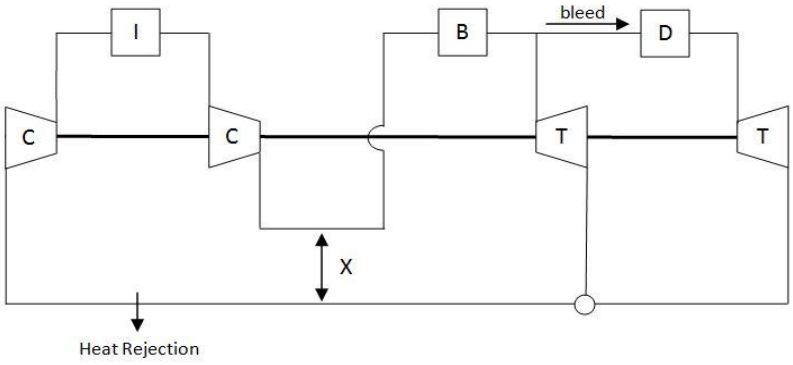

Figure 3.9 Cycle diagram for CICBTDTX cycle

An alternative arrangement for a primary Brayton cycle is to omit the reheat turbine and use the divertor to instead raise the temperature of the blanket helium, before entering the gas turbine, through direct contact heat exchange. This would be simpler, more cost effective and achieve the same level of performance. The cycles would then be denoted as CBDT, CBDTX and CICBDTX, respectively.

A summary of these results for PPCS model B are presented in table 3.3, including those for model AB using the same cycle conditions for the compressor, turbine and exhaust gas heat exchanger. In the above Brayton examples, however, it should be remembered that pressure losses in the blanket and divertor have been neglected, which would serve to lower the cycle efficiency. The figures in table 3.3 therefore represent the best possible performance for these primary Brayton cycles.

Brayton Cycle	**ṁ 1st turbine (kg/s)**	**ṁ 2nd turbine (kg/s)**	**Best Cycle η (%)**	**Cycle r_p**	**$\dot{W}_{C\_in}$ (MW)**	**$\dot{W}_{net}$ (MW)**
CBTDT (Model B)	3607	549	22	4.2	5717	1101
CBTDT (Model AB)	3515	787	22.9	4.2	5916	1246
CBTDTX (Model B)	3607	549	30.5	2.6	3439	1525
CBTDTX (Model AB)	3515	787	30.4	2.6	3560	1656
CICBTDTX (Model B)	3607	549	39	3.5	4208	1953
CICBTDTX (Model AB)	3515	787	39.3	3.6	4466	2118

Table 3.3 Comparison of primary Brayton cycles using a compressor inlet of 35°C, and isentropic compressor and turbine efficiencies of 90%

3.1.2.2 Secondary Brayton Cycles

After considering the primary Brayton cycles, the possible configurations of a secondary Brayton cycle should be examined, which avoid the issue of direct tritium contamination. The primary cycle now consists of two heaters: blanket and divertor.

There is no expansion process, only an IHX process that rejects heat to a secondary Brayton cycle. If pressure drops in the heaters and IHX of the primary cycle are assumed negligible, the external power input to the compressor will be small and can be neglected. After the blanket and divertor helium streams have mixed in the primary cycle, the temperature of the helium is 532°C. The thermal power available to the secondary cycle is the sum of the blanket and divertor thermal powers, but also the power input to the compressor, though this could be negligible.

Again, to present an ideal case let it be assumed that the effectiveness of the IHX process is unity, so that the pinch-point is zero. This would allow 5004 MW_t, the summation of the blanket power and divertor power in PPCS model B, to be received by the secondary cycle, remembering that in this case the compressor work has been neglected. This would also require that the helium mass flow in the secondary cycle is 4156 kg/s.

It has been shown that a Brayton cycle operating without an exhaust gas heat exchanger limits the cycle pressure ratio and reduces cycle efficiency. Any possible configurations for a secondary Brayton cycles should therefore include the CBTX and CICBTX cycle. The cycle diagrams for these cycles are shown in figures 3.10 and 3.11, respectively. Reheat does not appear to be possible, since the thermal power of the divertor has already been used in the primary cycle. Table 3.4 summarises the performance of a secondary CBTX and CICBTX cycle for PPCS models B and AB, whilst figures 3.12 and 3.13 provide a graphical representation of how the efficiency and net power output, respectively, varies, where applicable, with cycle pressure ratio for primary and secondary Brayton cycles that have been considered thus far.

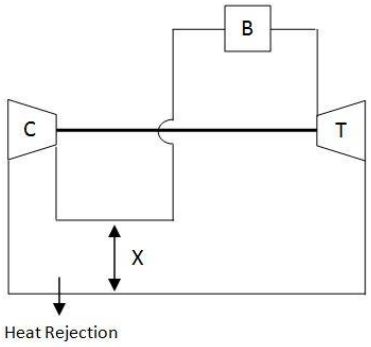

Figure 3.10 Cycle diagram of secondary CBTX cycle

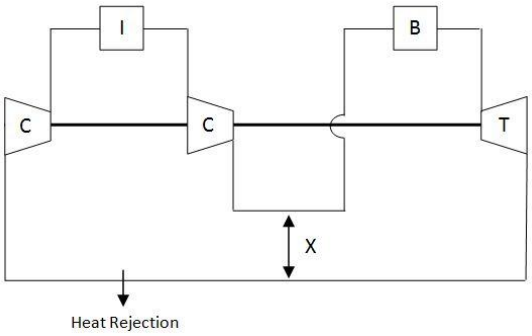

Figure 3.11 Cycle diagram of secondary CICBTX cycle

Brayton Cycle	**ṁ (kg/s)**	**Best η (%)**	**r_p**	**$\dot{W}_{C\_in}$ (MW)**	**$\dot{W}_{net}$ (MW)**
CBTX (Model B)	4156	30.5	2.6	3443	1527
CBTX (Model AB)	4301	30.4	2.6	3564	1580
CICBTX (Model B)	4156	39	3.5	4207	1953
CICBTX (Model AB)	4301	38.9	3.5	4354	2021

Table 3.4 Comparison of secondary Brayton cycles using compressor inlet temperature of 35°C and isentropic compressor and turbine efficiencies of 90%

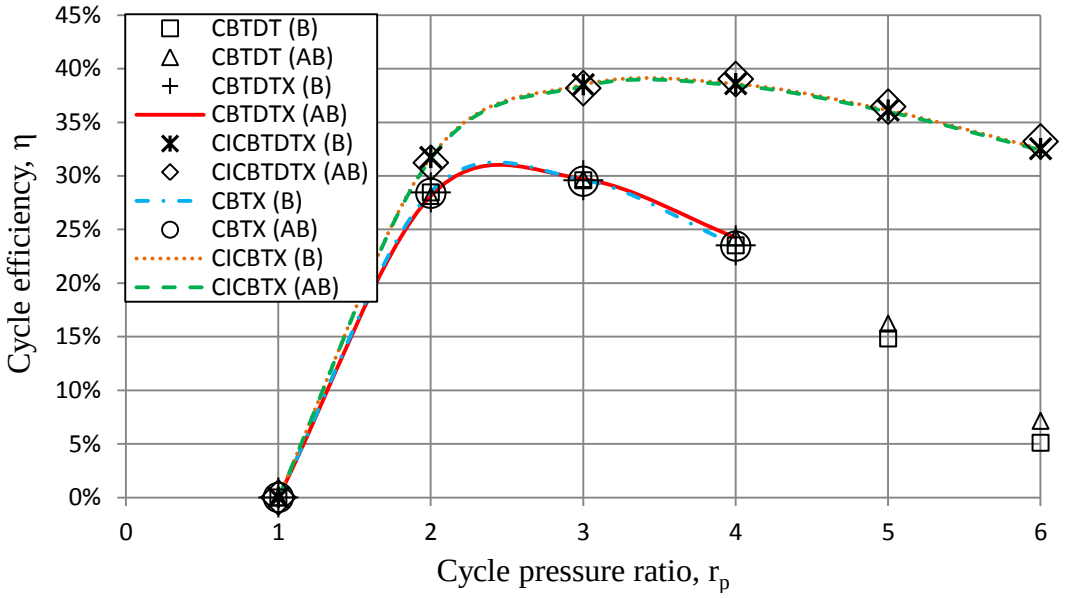

Figure 3.12 Graph showing variation of cycle efficiency with cycle pressure ratio for primary and secondary Brayton cycles using parameters from PPCS models B and AB

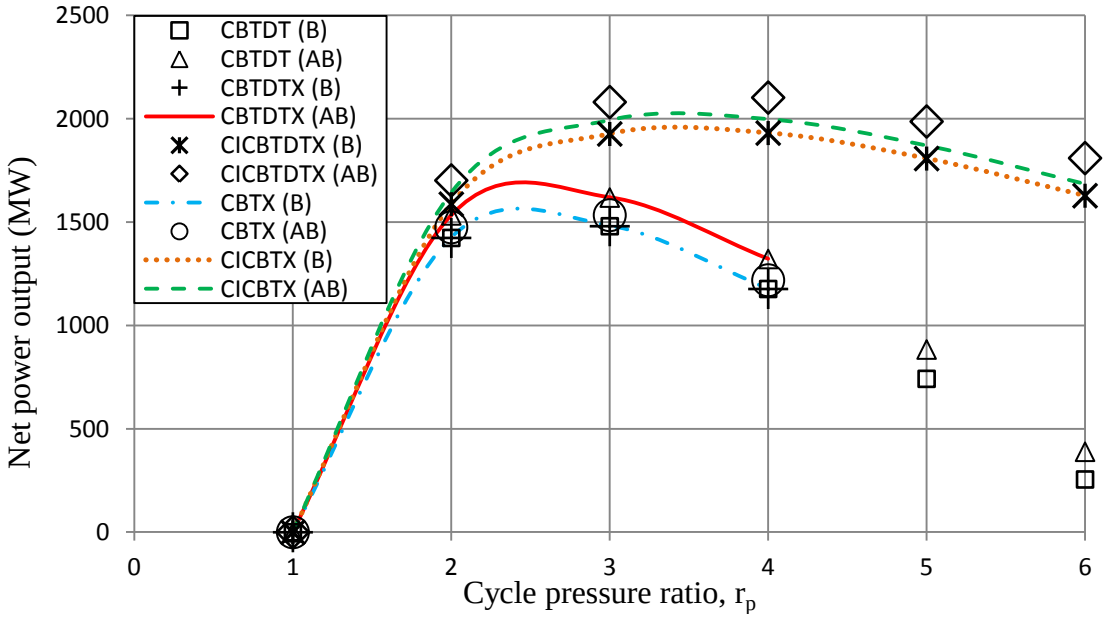

Figure 3.13 Graph showing variation of net power output with cycle pressure ratio for primary and secondary Brayton cycles using parameters from PPCS models B and AB

The advantage of the secondary Brayton cycle is that it is not constrained by the operating pressure of the blanket and divertor helium. The graph in figure 3.12, however, shows that despite this potential advantage there is little difference between the primary and secondary Brayton cycles operating with plant parameters associated with PPCS models B and AB, with the exception of the primary CBTDT Brayton cycle.

What the above examples highlight is the dependency of the Brayton cycle upon the top cycle temperature for cycle efficiency. This indicates that the Brayton cycles are best applied to situations where steam cycles cannot be used because of the temperature limitation of steam turbines.

3.1.3 Binary Cycle

A binary cycle consists of one power cycle operating at a higher temperature which provides heat for another power cycle operating at a lower temperature. The high-temperature cycle, the topping cycle, is usually a Brayton cycle because its cycle efficiency is more strongly dependent upon the top cycle temperature. The low-temperature cycle, the bottoming cycle, which receives heat from the high-temperature Brayton cycle, is usually a Rankine cycle because it has the advantage of rejecting all its heat at the lowest temperature. A binary cycle with Brayton topping and Rankine bottoming is commonly known as a combined cycle gas turbine, abbreviated to CGGT. A range of working fluids can be used for either power cycle in a binary setup, but in the context of a DEMO-type fusion reactor the Brayton cycle will most likely operate with helium; though the Rankine cycle need not operate using water since it would be external to the reactor.

The efficiency of a CGGT is defined as

$$\eta_{CGGT} = \frac{\dot{W}_{net\ Brayton} + \dot{W}_{net\ Rankine}}{\dot{Q}_{blanket} + \dot{Q}_{divertor}} = \frac{\dot{W}_{net\ overall}}{\dot{Q}_{blanket} + \dot{Q}_{divertor}} \tag{3.1}$$

Due to low helium temperatures in PPCS models B and AB a CGGT cycle wouldn't be suitable since there would be insufficient heat rejection in the Brayton cycle. The high-temperature liquid metal breeder and high-temperature divertor target zone in PPCS model C suggests that a CGGT could be implemented. However, the existing power cycle for this model consists of a secondary Brayton cycle only, with a CICBTX configuration. The application of a CGGT cycle with PPCS model C will be revisited later in chapter 5. The blanket and divertor parameters for PPCS model D make it particularly suitable for CGGT, but due to its advanced nature, both from a physics perspective and an engineering perspective, it will not be considered further.

3.2 Alternative Energy Sources

It is worth considering if any alternative energy sources, other than thermal energy, exist within a fusion power plant that could be utilised for large-scale electricity generation. It seems unlikely, but considering existing technologies that are used to generate electricity, and different forms of energy available for conversion, might highlight something that has been overlooked which could, at least, be used for low-level power applications.

Firstly, there does not seem to be any latent chemical energy that can be utilised to generate electricity. The hydrogen isotopes in the core are used for the fusion reaction. Helium in the blanket and divertor is inert and the lithium is used for breeding, neutron moderation and neutron multiplication. The structural materials, which under heavy neutron irradiation can undergo transmutation, are, in general, chemically stable. Therefore, there seems no way of utilising chemical energy to generate large amounts of electricity.

DEMO will be a large reactor, with a considerable height. This presents the possibility of utilising gravitational potential energy. A method to take advantage of this possible energy conversion process has not yet been identified.

Within a fluidic medium pressure waves can be used to drive a linear induction generator, or be used in conjunction with piezoelectric devices. Not only does it seem that there are no secondary energy sources of this kind produced by a tokamak, piezoelectric devices are unsuitable for large-scale electricity generation and would only find application for low-level power requirements, such as the conversion of mechanical strain between component junctions, perhaps caused by thermal expansion, or by converting mechanical vibrations. It is likely, however, that the cost of installing a large number of piezoelectric devices would outweigh any benefit derived from the generation of low-level electrical power.

A tokamak does not emit significant amounts of electromagnetic radiation in a range useful for photovoltaic cells. Thermal energy from a tokamak could be used to raise the temperature of an object to emit EM radiation in the required spectral range, but this would be an extremely inefficient use of thermal energy and is therefore not viable.

A free neutron will undergo β^- decay, converting itself into a proton by the emission of an electron and an electron antineutrino. Outside of a nucleus a neutron is unstable and will decay after approximately ten minutes [Stacey, 2010]. However, not only is it difficult to modify the path of a free neutron in order to utilise its decay products, the high-energy neutrons from the D-T reaction are needed for tritium breeding within the blanket. Any ‘stray’ neutrons are stopped by the shield at the rear of the blanket.

One final possibility of note is a process called ‘selective leaking’, whereby charged particles are deliberately bled from a plasma. This was suggested by Moir [1977] who described a device where the conversion to electricity could be performed, however, since there is considerable effort in maintaining plasma confinement, it seems unlikely this approach will be adopted for DEMO.

The ideas presented in this brief discussion range from the common to the exotic, however, they serve to highlight the very broad range of methods that have been examined for generating electrical power from a fusion reactor.

The conclusion that can be drawn from this section is that converting thermal energy is the only viable route for generating large amounts of electrical power. However, there is another way of converting thermal energy to electrical energy without using conventional turbo-machinery.

3.3 Direct Energy Conversion

Direct energy conversion, DEC, may be deemed unconventional, but there are various available methods which hold promise for power generation. Most conversion processes between different energy forms are not 100% efficient and any additional steps that are taken in the conversion process, between energy source and desired energy type, tend to increase losses.

One definition of direct energy conversion is given [Soo, 1968] as "the conversion of chemical, nuclear, solar, and thermal energies into electrical energy, without the necessary use of mechanical elements such as reciprocating or rotating machinery", where it most commonly refers to the process of converting a thermal energy source to electrical energy without any intermediate mechanical step. DEC offers reliability, long life, and the added simplicity of not using any moving parts. The four types of DEC generators that can be utilised to convert thermal energy directly to electrical energy are the thermoelectric, thermionic, electrohydrodynamic (EHD) and magnetohydrodynamic (MHD) generators. All graphs, unless specified, in the following subsections have been generated using the governing equations, which will be presented, and material data, which will be referenced.

3.3.1 Thermoelectric Energy Conversion

The method of converting thermal energy to electrical energy by using the 'bound' electrons in a solid is called thermoelectric power generation. The term 'bound'

refers to electrons that remain within the material, whilst ‘free’ electrons exist outside the material [Decher, 1997].

Semiconductors, in which electrons are free to move, can respond to electric fields and temperature gradients [Soo, 1968]. Thermoelectric generators consist of individual thermoelectric modules, which are themselves comprised of two types of semiconductor: n-type and p-type.

A p-type material is a semiconductor in which a doping agent, a group 3 element such as boron, aluminium or gallium, has been introduced to produce an excess of ‘holes’. The doping agents have three valence electrons and form a trivalent bond with a group 4 element such as silicon or germanium. However, there are insufficient valence electrons in the doping agent which cause a gap, or hole, to form in the covalent bonding.

N-type semiconductors use group 5 doping agents, such as phosphorus, antimony or arsenic, to produce excess electrons. P-type semiconductors therefore have the ability to accept electrons from n-type semiconductors when the two types of semiconductors are mated. The case for silicon as a doping agent is shown in figure 3.14.

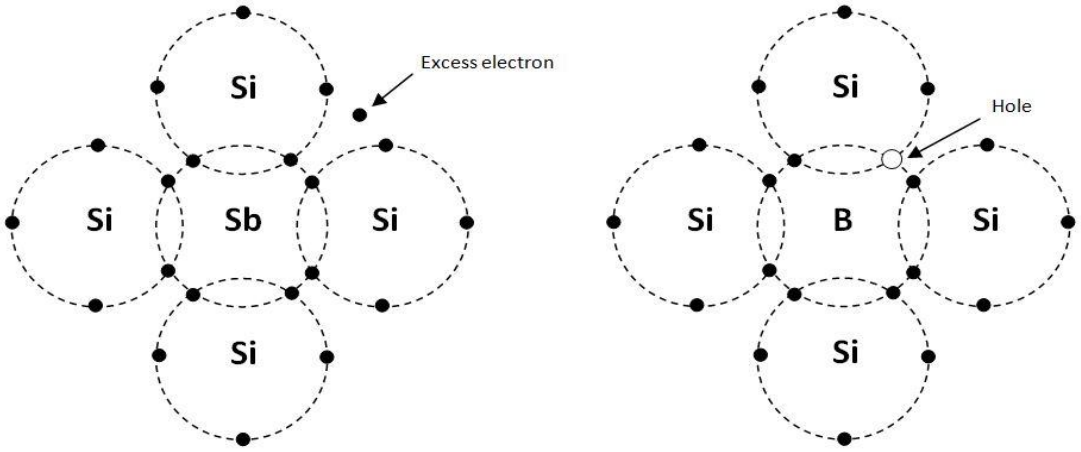

Figure 3.14 Diagram showing hole formation in p-type semiconductor (right) and excess electron in n-type semiconductor (left).

An important thermoelectric material property is the Seebeck coefficient, α. When a conducting p-based bar is connected to n-based wires, as shown in figure 3.15, and the two ends of the bar are maintained at differing temperatures, a voltage, V, arises.

Thermoelectric materials are then sandwiched between hot and cold junctions, as shown in figure 3.16, to form a thermoelectric module. Positive holes and negative electrons migrate from the heat source to the heat sink. This causes an electric current to flow. Existing thermoelectric generators (TEGs) consist of numerous individual modules.

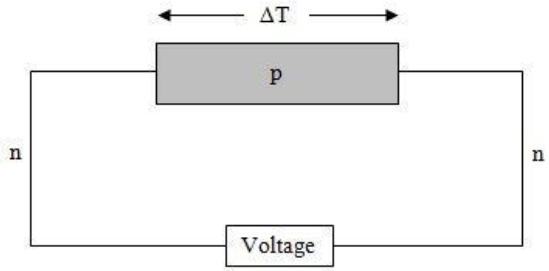

Figure 3.15 Representation of Seebeck effect, reproduced from Decher [1997]

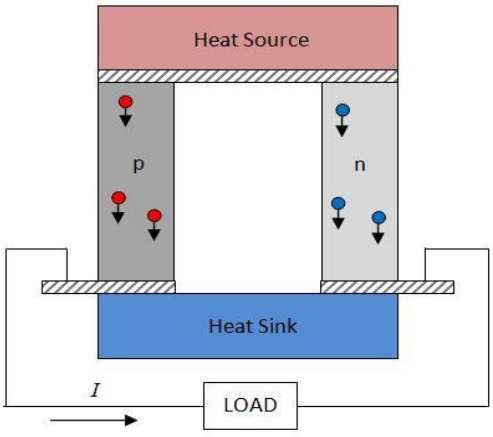

Figure 3.16 Thermoelectric module showing arrangement of p-based and n-based thermoelectric elements in conjunction with hot and cold reservoirs. Positive holes (red, left) and negative electrons (blue, right) migrate towards the cold reservoir and produce electric current. Redrawn and modified from Bos [2012]

The properties of p-based or n-based thermoelectric materials are often grouped into a figure of merit, Z, given by Angrist [1965] as

$$Z_{p,n} = \frac{\alpha_{p,n}^2}{\rho_{p,n}\kappa_{p,n}}$$

(3.2)

where ρ is the electrical conductivity and κ is the thermal conductivity. The subscripts p and n represent p-type and n-type materials, respectively.

Thermoelectric generators can be designed for maximum efficiency or maximum power output. The maximum efficiency of a thermoelectric module, where two thermoelectric materials are used, is given by Soo [1968] as

$$\eta_{max} = \frac{T_H - T_C}{T_H} \frac{\sqrt{1 + Z^*\overline{T}} - 1}{\sqrt{1 + Z^*\overline{T}} + \frac{T_C}{T_H}}$$

(3.3)

where $\overline{T}$ is the average temperature between the hot and cold junctions and Z* is the figure of merit for any combination of p-type and n-type materials

$$Z^* = \frac{\left(|\alpha_p| + |\alpha_n|\right)^2}{\left(\left(\sqrt{\rho_p\kappa_p}\right) + \left(\sqrt{\rho_n\kappa_n}\right)\right)^2}$$

(3.4)

Since the thermoelectric module is basically a heat engine, the Carnot efficiency, $(T_H\text{-}T_C)/T_H$, is seen in (3.3).

Figure 3.17 shows the maximum efficiency of a thermoelectric module for a range of $Z^*\overline{T}$ values using a hot junction temperature range of 400 - 1000 K whilst the cold junction is held constant at 300 K. The product $Z^*\overline{T}$ has been a limiting factor for some time. For high efficiency, the Seebeck coefficient needs to be high, whilst the electrical resistivity must be low. The thermal conductivity must also be low so that the temperature difference between the hot and cold junction can be maintained.

Bismuth telluride, Bi_2Te_3 and Lead telluride, PbTe, are commercially available thermoelectric materials. The former is useful as the cold junction, since it operates well at 300 K. However, the latter could potentially operate up to 900 K, possibly 1000 K, and therefore could be suitable for use as the hot junction [He et al., 2011].

Both of the aforementioned thermoelectric materials can be doped so that they are p-based or n-based, but as a bulk material their $Z^*\overline{T}$ is limited to just under 1. Taking the case where a thermoelectric module using these materials achieves a $Z^*\overline{T}$ of 1, with the cold junction at 300 K and the hot junction at 1000 K, then the efficiency of such a thermoelectric module, and generator as a whole, is only going to reach about 16%.

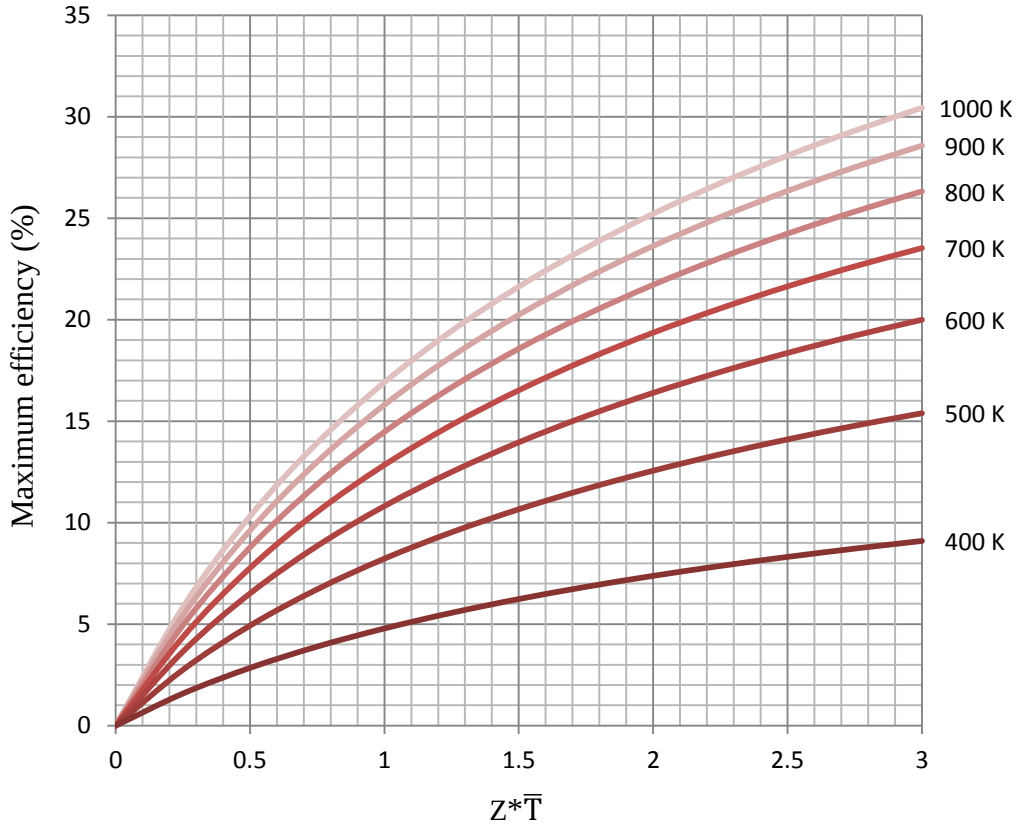

Figure 3.17 Maximum efficiency of a thermoelectric module using a cold junction temperature of 300 K for a range of $Z^*\overline{T}$ and hot junction temperatures

Focus has now shifted towards complex materials called skutterudites and clathrates, which possess qualities relating to both crystals and glass. Crystals tend to have high electrical conductivities, but also high thermal conductivities. Meanwhile, glass has a low thermal conductivity, but also poor electrical conductivity. Taking the high electrical conductivities of crystals and the low thermal conductivity of glass has led to figures of merit approaching 1.5. Efficiencies of thermoelectric modules could approach 20% if manufacturing methods for these relatively scarce materials are developed [J. Bos, 2012].

The power density of a thermoelectric generator is given by Angrist [1965] as

$$\frac{\dot{W}_{TEG}}{A_{total}} = \frac{\left(|\alpha_p| + |\alpha_n|\right)^2 (\Delta T)^2}{4L\left[\left(\rho_p/A_p\right) + \left(\rho_n/A_n\right)\right]\left[A_n + A_p\right]} \tag{3.4}$$

where A_{total} represents the sum of the cross-sectional area of the thermoelectric elements A_p and A_n. Equation (3.4) is maximised when the ratio A_n/A_p is equal to the ratio $\sqrt{\rho_n}/\sqrt{\rho_p}$, which is arrived at by taking the derivative of the denominator in (3.4) with respect to A_n/A_p [Angrist, 1965].

For a thermoelectric generator the choice of p-type and n-type elements is dependent upon the mean temperature, $\overline{T}_{TEG}$, of the hot and cold junctions, where the combined figure of metric Z* should be maximised [Angrist, 1965]. An n-type material consisting of bismuth telluride, $Bi_2(75\%)Te_3(25\%)$, is suitable for values of ΔT, the temperature difference between the hot and cold junctions, between 100 K and 700 K. This corresponds with existing blanket designs. However, the p-type material $Bi_2(25\%)Te_3(75\%)$ is only suitable for values of ΔT up to about 445 K. Beyond this value the p-type material silver antimony telluride, $AgSbTe_2$, yields a higher figure of merit, contributing to a higher Z* value and therefore leading to a higher power density. Figure 3.18 shows the power density for these arrangements.

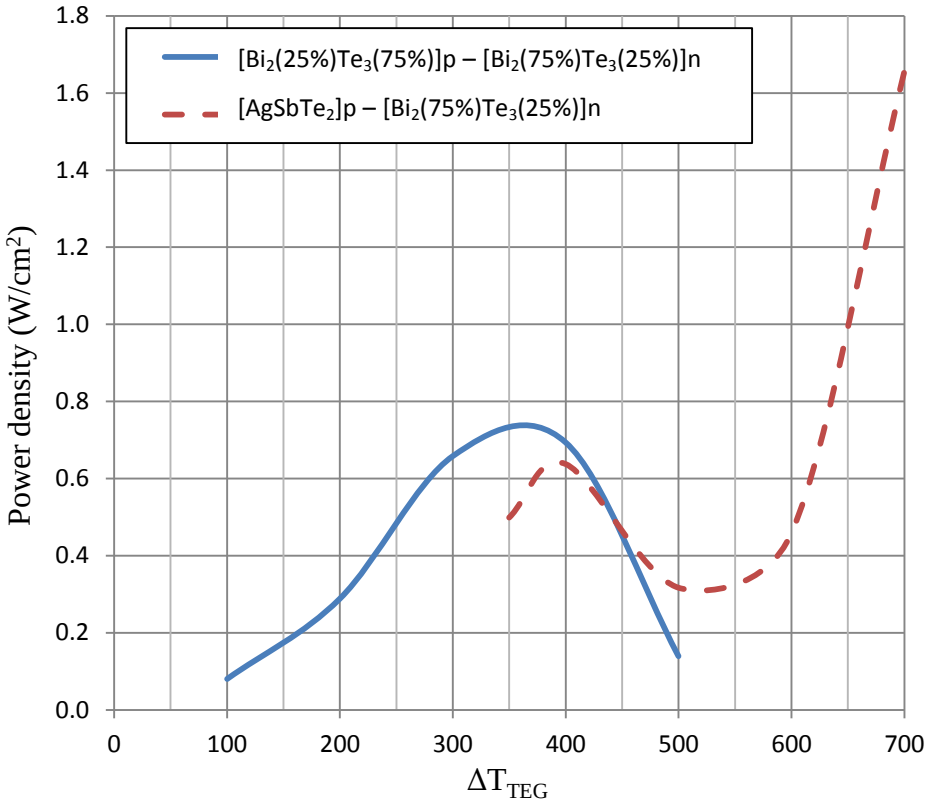

Figure 3.18 Power density of a TEG where the cold junction temperature is 300 K and the hot junction temperature varies from 400 K to 1000 K. Comparison using an n-type $Bi_2(75\%)Te_3(25\%)$ thermoelectric element with p-type thermoelectric elements consisting of $Bi_2(25\%)Te_3(75\%)$ and $AgSbTe_2$

The figure of merit, electrical resistivity and Seebeck coefficient for the thermoelectric materials in figure 3.18 all reach a maximum value at different temperatures. The variation in the electrical resistivity and Seebeck coefficient causes the variation in power density. For the n-type $Bi_2(75\%)Te_3(25\%)$ the figure of merit peaks at about 370 K, the electrical resistivity peaks at around 600 K and the Seebeck coefficient peaks at around 570 K [Rosi et al, 1961]. For the p-type $Bi_2(25\%)Te_3(75\%)$ these values peak at about 300 K, 550 K and 420 K, respectively, [Rosi et al., 1961] whilst for the p-type $AgSbTe_2$ these values are about 650 K, 300 K and 670 K, respectively [Rosi et al., 1961].

By taking a scenario where a hot junction temperature of 973 K is obtained by using the parameters of a DCLL blanket, then by referring to figure 3.18 a power density of 14 kW/m^2 is achieved. However, to generate a gross electric power output of almost 1700 MW_e, associated with PPCS-C model, a surface area of just over 121000 m^2 would be required. This is equivalent to an approximate area of eleven football pitches.

The $Z^*\overline{T}$ value for the aforementioned scenario is 1.07. Referring to figure 3.17, and using the same ΔT of 973 K, it can be seen that this would yield an efficiency of approximately 17%. This makes thermoelectric power generation an unattractive prospect as a stand-alone method for generating large-scale electricity.

Advancements in thermoelectric materials that can yield higher power densities would allow more compact generators to be designed, however, these materials must also possess higher $Z^*\overline{T}$ values for increased efficiency. This would permit thermoelectric generators to be considered a competitive technology for the generation of large-scale electricity. For now, however, it must be concluded that thermoelectric power generation is best suited to the small-scale and not suitable for use in conjunction with any proposal that is intended to generate large amounts of electrical power using PPCS model C plant parameters.

3.3.2 Thermionic Energy Conversion

A thermionic energy converter can be considered to be a heat engine that uses electrons as the working fluid [Webster, 1959]. A heated cathode emits electrons, which are then collected by a cooler anode. The electrons are transported back to the cathode via an external load, where useful work can be done. Thermionic systems, like all direct energy conversion systems, have the distinct advantage in that they operate in the solid state, i.e. no moving parts, and therefore present the possibility of a very reliable means of generating electricity [Decher, 1997].

Within a material there exists a conduction band, a valence band and also a band gap. This is shown in figure 3.19. Within the valence band electrons try to exist in

the lowest possible energy configuration, but due to the Pauli Exclusion Principle these electrons cannot occupy identical energy states. The top most energy state within the valence band is called the Fermi level. At absolute zero there is a clean distinction between the valence band and the higher-energy conduction band. No electrons can cross between the bands at absolute zero. Thus, there is an energy 'band' gap. As the temperature of a material increases, some electrons acquire sufficient energy to cross the band gap and enter the conduction band. Once in the conduction band, electrons can further acquire energy to be emitted from the surface of the material. The energy required to do this varies over a range of materials, but if electrons are emitted they are said to have overcome the work function, φ, a quantifiable energy level that the electrons must overcome. The flux of emitted electrons increases with temperature, particularly for materials with low work functions.

The energy level, or Fermi level, of the anode must be more negative than the Fermi level of the cathode for a thermionic device to be a converter [Houston, 1959], however, the space between the electrodes into which emitted electrons proceed may be occupied by a large number of other electrons. The charge of this electron 'cloud' in this inter-electrode gap constitutes a repulsive potential barrier that hinders the electron emission and thus limits the flow of current. Thus, the electrons must have sufficient energy to overcome both the work function and space-charge effects.

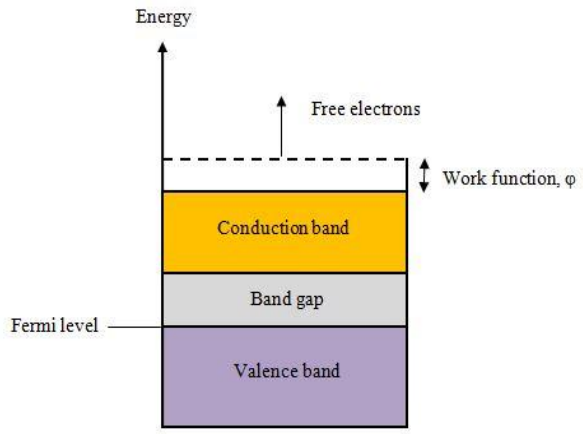

Figure 3.19 Energy bands within a material showing work function, adapted from Decher [1997]

Space-charge effects such as this have proved difficult to overcome and as a result limited the applications to which thermionic converters have been applied. One approach is to coat metals with materials that possess low ionisation energies, such as caesium. Tungsten has a work function of 4.52 eV [Smithells, 1967], but via chemisorption tungsten with a caesium coating can have a work function between 1.36 eV and 1.69 eV [Wolf, 1995]. This process of chemisorption can be applied to a range of materials, but once a critical temperature is reached the coating material can be 'boiled' off the surface, thus returning the material to its original work function.

The diagram in figure 3.20 is a reproduction [Webster, 1959] of the electron energy diagram for a thermionic energy converter, where φ_c and φ_a are the work functions of the cathode and anode, respectively. The potential barriers due to space charge for the cathode and anode are represented by φ_k and φ_p, respectively. V_0 is the voltage which appears across the external load, whilst d is the separation distance between cathode and anode. X_1 and X_2 are the distances from the peak of the potential barrier to the cathode and anode, respectively. J is the electron current density flowing to the cathode and anode.

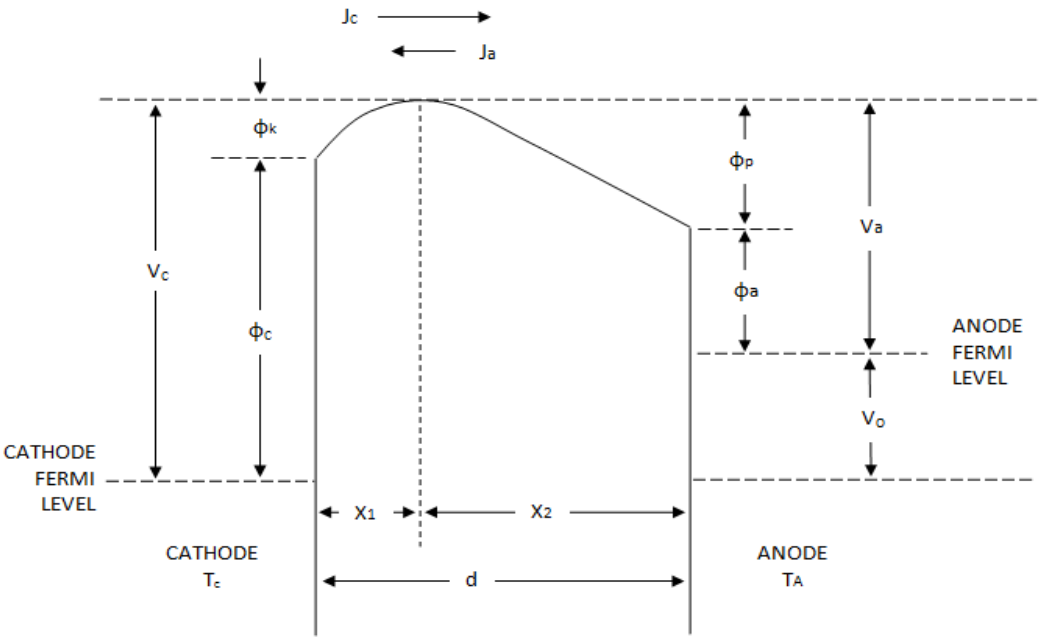

Figure 3.20 Electron energy diagram for a thermionic energy converter reproduced from Webster [1959]

The Richardson equation [1901], derived from Richardson's Law, relates current density to work function and temperature

$$J = A_0 T^2 exp\left(-\frac{e\phi}{kT}\right)$$

(3.5)

where T the material temperature, e the electron charge, φ the work function of the material, and k the Boltzmann constant.

The Richardson constant, A_0, was given by Crowell [1965] as

$$A_0 = \frac{4\pi m_e e k^2}{h^3} \sim 1.2\ x\ 10^6\ A\ m^{-2}\ K^{-2}$$

(3.6)

where m_e is the mass of the electron, and h is Planck's constant.

Due to the dependency upon both physical and thermal characteristics of materials the Richardson constant is often defined in terms of a material correction factor, λ_R, and given by

$$A_G = \lambda_R A_0$$

(3.7)

This modified Richardson constant can account for experimental results differing, or exceeding, the value of the theoretical limit by incorporating the reflection coefficient of the material [Kaye & Laby, 1973]. The RHS of equation (3.7) can be substituted into equation (3.5) to provide a more accurate calculation of current density. This form of the equation is often referred to as the Richardson-Dushman equation due to later research conducted by Dushman [1923] into electron emission from metals as a function of temperature.

For a pair of electrodes the Richardson-Dushman equations for cathode and anode respectively are given by

$$J_c = A_G T_c^2 exp\left(-\frac{e(\phi_c)}{kT_c}\right)$$

$$J_a = A_G T_a^2 exp\left(-\frac{e(\phi_a)}{kT_a}\right)$$

(3.8)

The exponents in equation (3.8) can be written as non-dimensional performance parameters for cathode and anode respectively.

$$\beta_c = -\frac{e\phi_c}{kT_c}$$

$$\beta_a = -\frac{e\phi_a}{kT_a}$$

(3.9)

Similarly, non-dimensional performance parameters for the space charge potential barriers for cathode and anode, respectively, can be given by

$$\beta_k = -\frac{e\phi_k}{kT_c}$$

$$\beta_p = -\frac{e\phi_p}{kT_a}$$

(3.10)

The net current density, including space charge effects, is therefore given by

$$J_{net} = J_{c+k} - J_{a+p} = J_c exp(\beta_c + \beta_k) - J_a exp\big(\beta_a + \beta_p\big)$$

(3.11)

The graphs in figures 3.21 and 3.22 have been generated using material data taken from literature [Smithells, 1967], [Wolf, 1995]. They compare the current density generated by a single electrode for a range of materials using a maximum temperature of 2000 K. Figure 3.21 compares electrodes consisting of pure elements, whilst figure 3.22 uses electrodes consisting of coated materials. It is clear that to get useable current densities at low temperatures, materials with low work functions must be used. For simplicity the current density due to space charge effects has been omitted. The output voltage of a thermionic energy converter is given by Webster [1959] as

$$V_0 = V_c - V_a = (\phi_c - \phi_k) - (\phi_a - \phi_p)$$

(3.12)

where ϕ_k and ϕ_p are the reduced work functions due to space charge effects. For simplicity these can also be omitted.

The power density, $\dot{W}_d$, the power per unit area, is given by Decher [1997] as

$$\dot{W}_d = J_{net} V_o$$

(3.13)

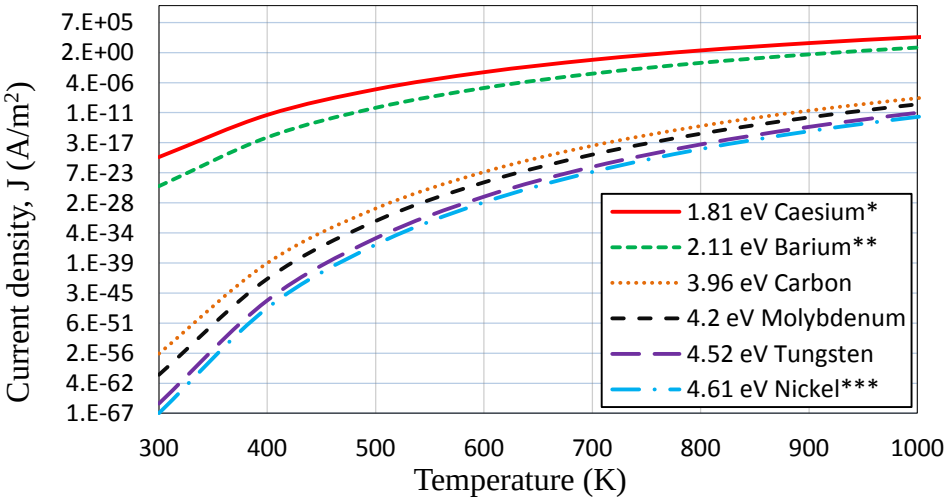

Figure 3.21 Current density (semi log) versus temperature for given elements and their work functions *Caesium melting point 301K **Barium melting point 1000K ***Nickel melting point 1728K

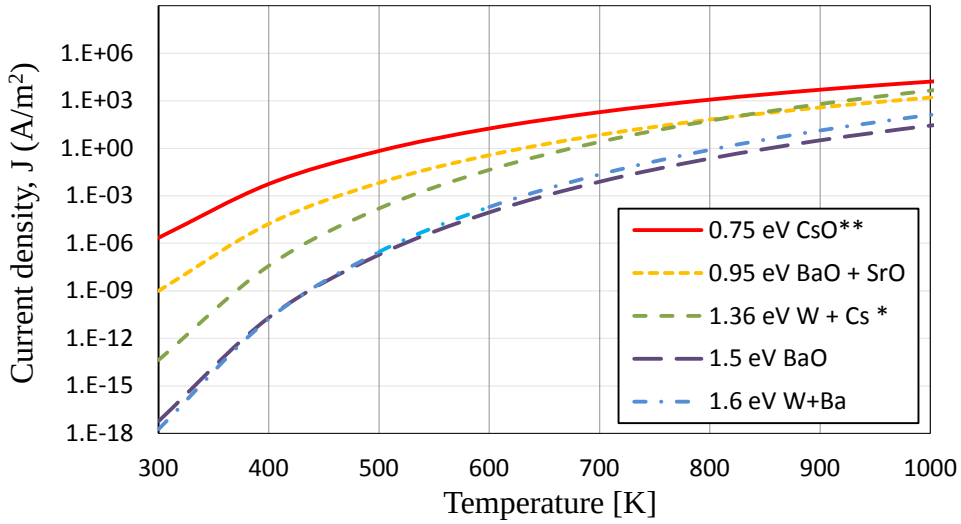

Figure 3.22 Current density (semi log) vs. temperature for oxides, ceramic compounds and coated surfaces *Boiling point of caesium 944K (Best figure used for W + Cs) **Melting point of CsO is 763K

Equation (3.12) highlights the importance of the difference between the work functions of the cathode and anode. Figure 3.23 shows the power density for two thermionic energy converters using two different sets of electrodes. The cathode temperature is fixed at 1000 K whilst the anode temperature is allowed to vary between 300 K and 900 K. Space charge effects have been neglected.

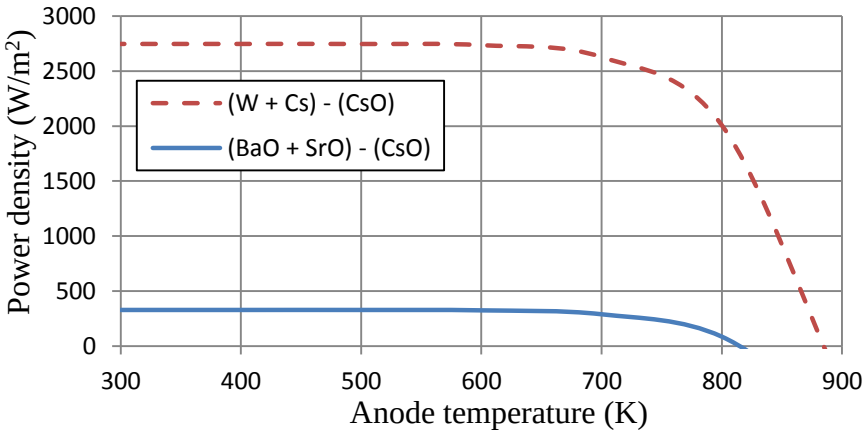

Figure 3.23 Power densities for two thermionic converters, neglecting space charge effects, using different electrode materials with a maximum cathode temperature of 1000 K

The efficiency of a thermionic energy converter is found by determining the net heat input to the thermionic energy converter as a system. The potential energy of the cathode electrons required to reach the potential maximum at X_1, and the thermal energy carried away from the surface, which equals particle flux multiplied by the energy carried per particle, are two energy inputs to the hot cathode.

There are also two energy gains that are realized from the anode side: the thermal energy brought by anode emitted electrons at temperature T_a, and the fall of the anode emitted electrons through the cathode potential, V_c. These energy gains are proportional to the current J_a and must be subtracted from the net input to the emitter.

Radiative heat transfer must also be considered. For small inter-electrode gaps the radiating area can be assumed to be equal to the emission area. Decher [1997] gives the net heat supplied per unit area as

$$\dot{Q}_H = \frac{\sigma(T_c^4 - T_a^4)}{\left(\frac{1}{\varepsilon_c} + \frac{1}{\varepsilon_a} - 1\right)} + J_{c+k}\left(V_c + \frac{2kT_c}{e}\right) - J_{a+p}\left(V_c + \frac{2kT_a}{e}\right) \tag{3.14}$$

where ε is the emissivity and σ the Stefan-Boltzmann constant.

Writing the Stefan-Boltzmann law simply as R, the efficiency of a thermionic energy converter can be represented by

$$\eta = \frac{\dot{W}_d}{\dot{Q}_H} = \frac{J_{net}V_o}{R + J_{c+k}\left(V_c + \frac{2kT_c}{e}\right) - J_{a+p}\left(V_c + \frac{2kT_a}{e}\right)} \tag{3.15}$$

where Ẇ is the power output and A_e the surface area of one electrode, where it is assumed both cathode and anode possess equal surface areas.

For simplicity, black-body conditions can be assumed for both electrodes. By substituting the values for a caesium coated tungsten cathode and a caesium oxide anode into equation (3.14) the heat input to the thermionic system is found.

Figure 3.23 shows that the power density for a thermionic converter, using a cathode of W + Cs and an anode of CsO, is similar between 300 K and 600 K. Choosing an anode temperature of 600 K, therefore, lowers the heat input, whilst maintaining the power density, and increases efficiency. Using a cathode temperature of 1000 K and an anode temperature of 600 K the heat input is found to be approximately 56 kW.

The efficiency is plotted in figure 3.24 for a range of electrode emissivities, where both emissivities of cathode and anode are assumed equal.

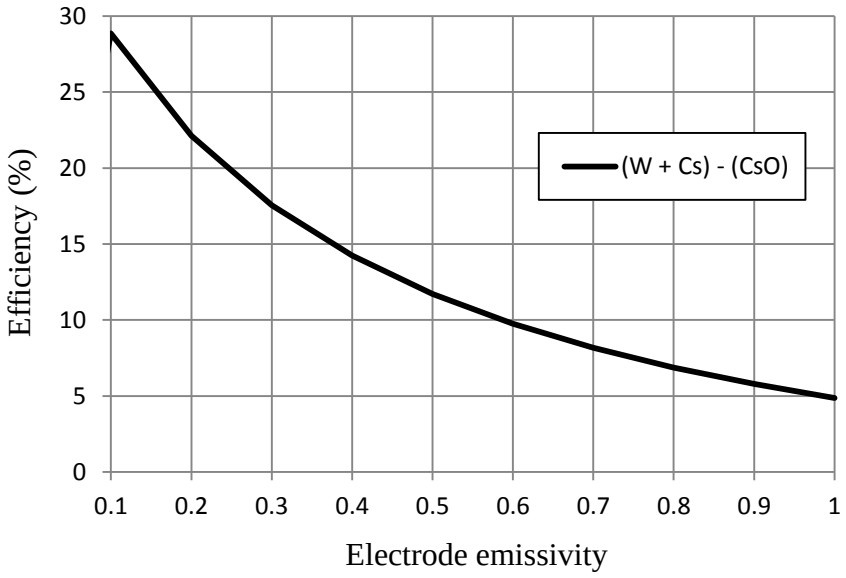

Figure 3.24 Efficiency of a thermionic converter with cathode fixed at 1000 K and anode fixed at 600 K for a range of electrode emissivities

The focus of this analysis has been to establish the feasibility of a thermionic energy converter as a topping device, or as a stand-alone energy converter, in the context of fusion constraints. The work function and temperature have been important parameters in determining the performance of a thermionic energy converter. The inter-electrode distance, which has been disregarded in this analysis, also plays an important role since space charge effects limit performance. Electrode emissivities also limit performance.

By considering the idealised scenario where a power density of 2.5 kW/m^2 is achieved, when the cathode is close to 1000 K and the anode is in the range 300 – 600 K, it would require a surface area of nearly 680000 m^2 in order to generate 1696 MW_e of gross electric power as required by PPCS model C. This is equivalent to the surface area of nearly 63 football pitches. If electrode emissivities are low, a reasonable efficiency in the approximate range 15-30% could be achieved, however, under such idealised conditions this is still lower than a Brayton cycle using a gas turbine inlet temperature of nearly 1000 K and rejecting heat at 300 K.

There also seems to be limited potential for a thermionic energy convertor, with a cathode temperature close to 1000 K and an anode temperature of 600 K, to act as a topping device to a low-temperature power cycle, such as a water-based Rankine cycle. Since steam turbines can operate with inlet temperatures above 600 K, up to nearly 900 K [General Electric], a Rankine cycle with thermionic topping would be less efficient than a stand-alone Rankine cycle.

With such large surface areas required to generate the large amounts of electricity specified by the PPCS models, particularly for PPCS model C, the materials and manufacturing costs would likely be prohibitive. Advancements in materials could yield higher power densities, but for now thermionic energy converters seem an unattractive prospect for use in fusion power plants for the purpose of large-scale electricity generation.

3.3.3 Electrohydrodynamic Energy Conversion

Fundamentally, in the following order, power generation using an EHD generator involves three processes: ionisation of the flowing medium, deceleration of ions formed, neutralisation (recombination) of ions to form a neutral flow. A discharge is produced between the corona electrode and the attractor electrode that constitutes an ion source [Soo, 1968]. The attractor electrode removes the electrons from the flow leaving just the ions, and neutrals, assuming partial ionisation only, to flow downstream towards the collector electrode.

The electrons flow through the external circuit to the collector electrode in order to neutralise the ions. The resistance of the circuit causes an electric field to build-up at the positive downstream collector electrode, establishing the EHD power generator as a cell. The gas must drive the ions downstream against the opposing field, and therefore the power output is the result of the mechanical work done by the moving gas [Soo, 1968]. The maximum power is a function of the ion slip Λ, ion mobility μ, and electric field strength at channel entry E_0 [Decher, 1997].

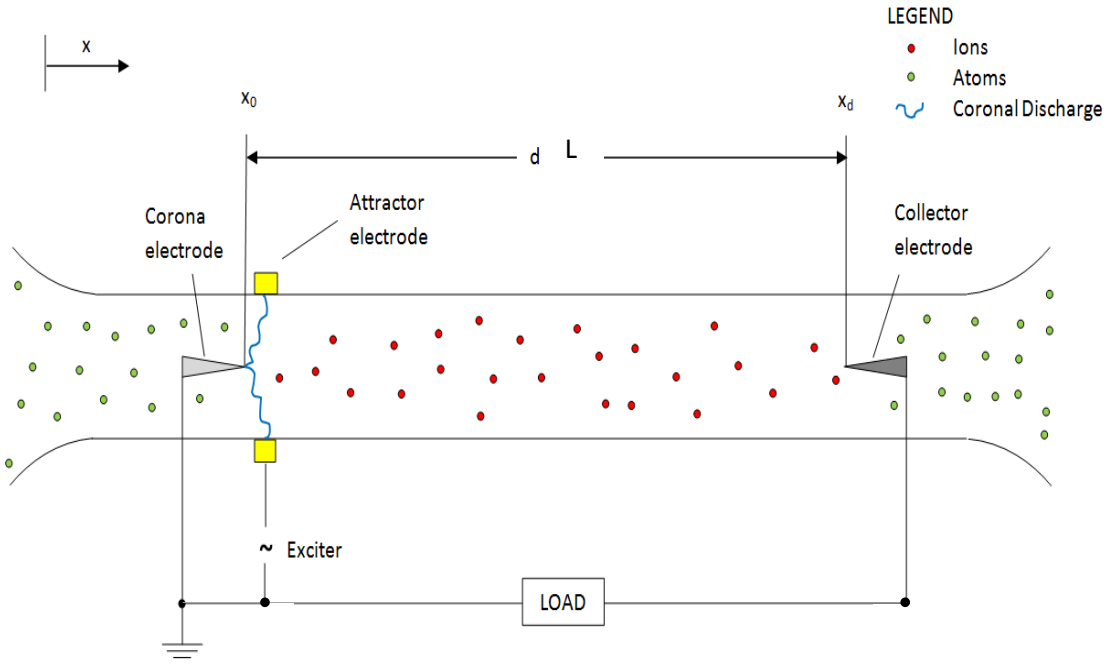

Figure 3.25 Schematic of EHD generator reproduced from Soo [1968]

The non-dimensional power density of an EHD generator is given by Decher [1997] as

$$\dot{w} = \left[\frac{4\Lambda}{3}(\gamma_L^3 - 1) - (\gamma_L^2 - 1)\right]\frac{2}{\Lambda} \tag{3.16}$$

where Λ is the ion slip and γ_L is the non-dimensional electric field at some point along the channel length, given by

$$\gamma_L = \frac{E_x(L)}{E_0}$$

(3.17)

where $E_x(L)$ is the electric field in the x-direction at channel length L. A plot of the variation of non-dimensional power density, reproduced from Decher [1997] using equations (3.16) and (3.17), is shown below in figure 3.26. As the channel length increases γ_L decreases, highlighting the case for short EHD channel lengths. Cases where ion slip is low produce higher non-dimensional power densities.

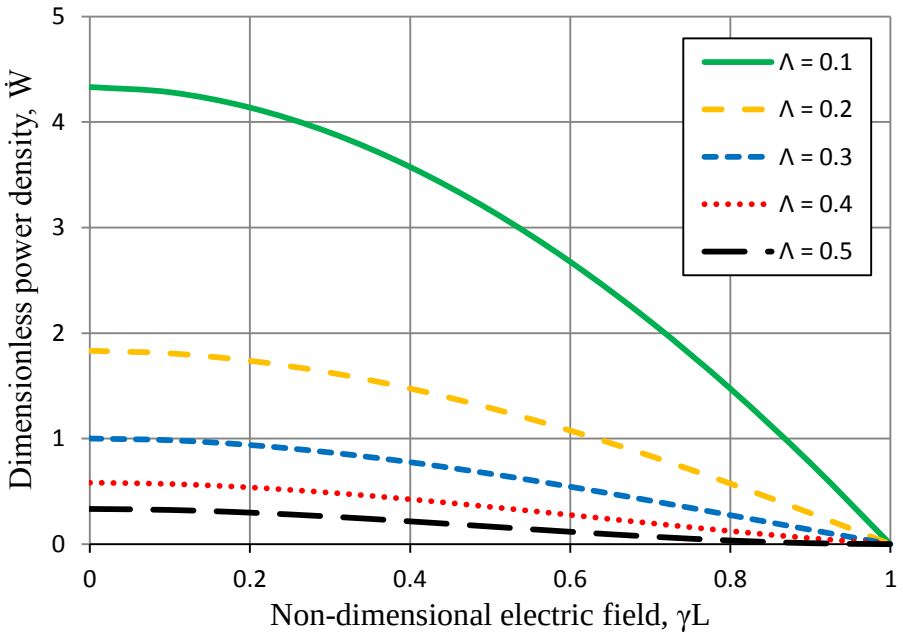

Figure 3.26 Variation of non-dimensional power density for various values of ion slip, Λ, reproduced from Decher [1997] using non-dimensional power density equation

Ion slip is given by Soo [1968] as

$$\Lambda \equiv \frac{v_{d0}}{2v_x} = \frac{\mu E_0}{2v_x}$$

(3.18)

where v_{d0} is the drift velocity at channel entry, v_x is the neutral gas velocity and μ the electrical mobility of the ions, a measure of how they move relative to the neutral gas particles in response to an electric field.

To minimise ion slip, therefore, EHD generators should use low mobility gases with high-speed neutrals in conjunction with low electric fields at channel entry. The maximum power per unit electrode area is given by Soo [1968] as

$$\dot{W}_{max} = \frac{1}{2}\varepsilon_0 v_x E_0^2 \left(\frac{3-4\Lambda}{6\Lambda}\right) = \frac{1}{2}\varepsilon_0 \mu E_0^3 \left(\frac{3-4\Lambda}{6\Lambda}\right)$$

(3.19)

where ε_0 is the permittivity of free space.

The electric field at channel entry, E_0, is limited by an instability known as electric breakdown, E_b, which means that v_x is then limited by

$$v_x = \frac{\mu E_b}{2\Lambda}$$

(3.20)

When an electric field reaches breakdown strength electrons are accelerated to energies that cause a cascade event, which leads to the production of more electrons.

The growing number of electrons will allow the conduction of current which then reduces the strength of the electric field. The maximum field achievable depends upon the electrical properties of the dielectric material. For gases E_b is largely dependent upon pressure p, and therefore equations (3.18) and (3.19) can be expressed as

$$\Lambda = \frac{(\mu P)\left(\frac{E}{P}\right)_b}{2v_x}$$

(3.21)

$$\dot{W}_{max} = \frac{1}{2}\varepsilon_0(\mu P)\left(\frac{E}{P}\right)_b^3\left(\frac{3-4\Lambda}{6\Lambda}\right)$$

(3.22)

By extrapolating the Paschen curve, derived from Paschen's Law [Paschen, 1889], for helium the breakdown voltage can be estimated for a given pressure, p, and electrode separation distance, L. Existing helium-based blanket module designs use a pressure of 8 MPa, and from Paschen's Law L should be small to maximise E_b. For values of L of the order 10^{-2} m E_b is of the order 10^6 V/m. Figure 3.27 below shows E_b for a range of EHD generator duct lengths. A trendline is included to reinforce the curve, which shows irregularities caused by the extrapolation and estimation process.

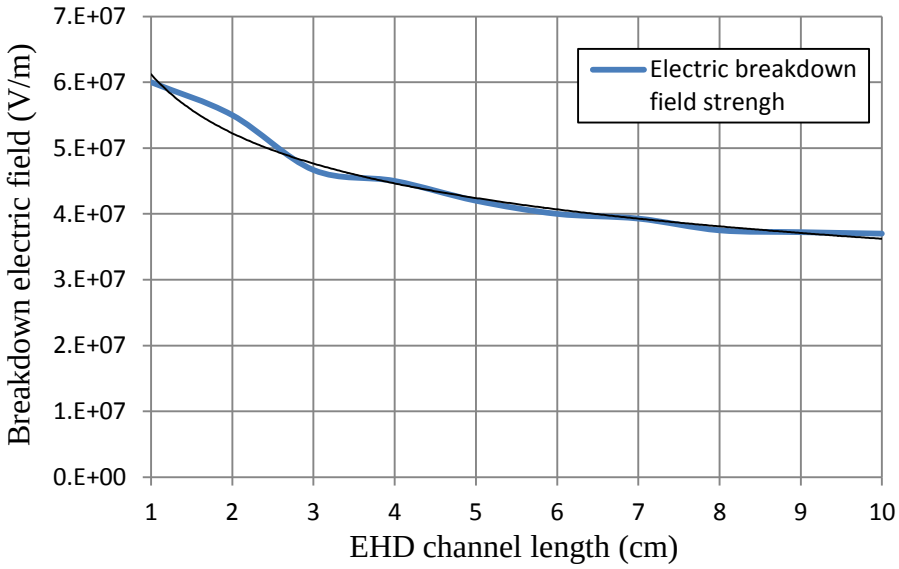

Figure 3.27 Electric breakdown field strength of helium for a range of electrode gap separations, also showing trend line

By substituting the value for the mobility of helium ions at 8 MPa and 773 K, which meets the specifications for PPCS models B and AB, with C being close at 753 K, into (3.19) the maximum power density, and gas velocity, v_x, found via equation (3.20), can be plotted for a range of ion slip values, using E_b as a limit for E_0.

The graph in figure 3.28 shows, for the aforementioned helium pressure and temperature, the power densities for a range of channel lengths and ion slip.

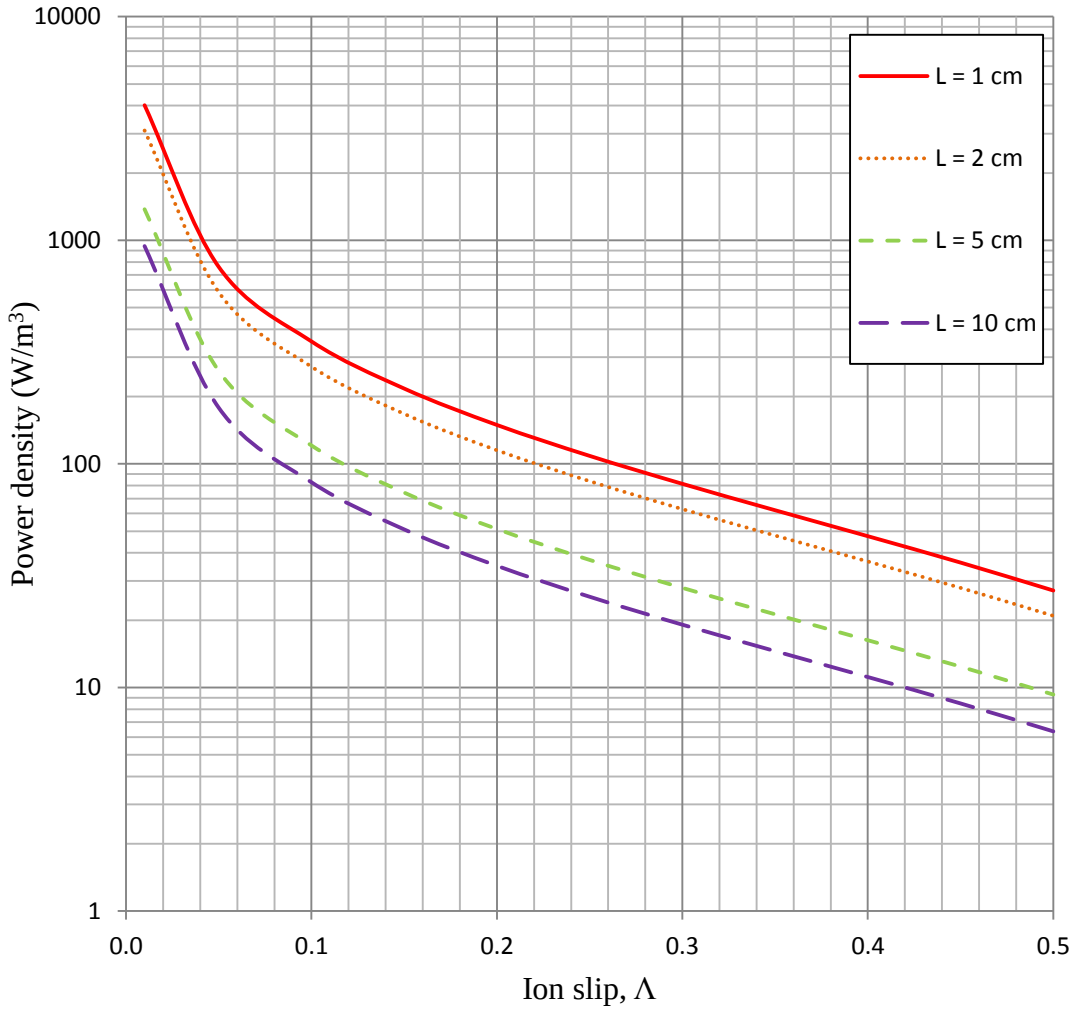

Figure 3.28 Semi-log plot showing power densities for a range of channel lengths and ion slip in an EHD generator operating with helium at 8 MPa and 773 K. E_b used as a limit for E_0

The conversion efficiency of an EHD generator is defined as the ratio of actual work output to flow work [Decher, 1997], where the power input is expressed as the sum of electric pressure drop and friction loss per unit electrode area [Soo, 1968].

Integrating the body force per unit volume over the volume of the duct gives the momentum lost by the fluid. At low Mach number, where $M^2 << 1$, the pressure drop is largely due to an electrostatic body force per unit volume [Decher, 1997]. This is given by [Soo, 1968] as

$$\Delta p = \int_{x=0}^{x=L} \rho_e E \, dx = \frac{1}{2}\varepsilon_0 E_0^2$$

(3.23)

where ρ_e is the space charge density. In terms of E_b the pressure drop limit can be written as

$$\Delta P_{lim} = \frac{1}{2}\varepsilon_0 E_b^2$$

(3.24)

Hence, the power input per electrode area can be expressed, as Soo [1968] does, as the sum of the electrostatic body force and friction loss multiplied by the neutral gas flow velocity

$$\dot{w}_{in} = (\Delta P) v_x = \left(\frac{1}{2}\varepsilon_0 E_0^2 + C_D \rho \frac{v_x^2}{2}\right) v_x$$

$$= \dot{w}\left(1 - \frac{4\Lambda}{3}\right)^{-1} + C_D \rho \frac{v_x^3}{2}$$

(3.25)

where C_D is the drag loss coefficient.

The conversion efficiency of an EHD generator is therefore

$$\eta = \frac{\dot{w}}{\dot{w}_{in}} = \frac{\left(1 - \frac{4\Lambda}{3}\right)}{\left(1 + \frac{k_1 C_D}{\Lambda^2}\right)}$$

(3.26)

where k_1 is a non-dimensional loss coefficient given by

$$k_1 \equiv \frac{\rho\mu^2}{4\varepsilon_0}$$

(3.27)

The variation in EHD efficiency against ion slip and drag is plotted in figure 3.29 below. This graph highlights the need for low loss and low drag coefficients. For the case of helium at 8 MPa and 773 K, the density ρ and mobility μ are determined. So too is the relative permittivity of free space. This leaves only the drag coefficient that must be reduced. For existing fusion blanket conditions k_1 is around 340.

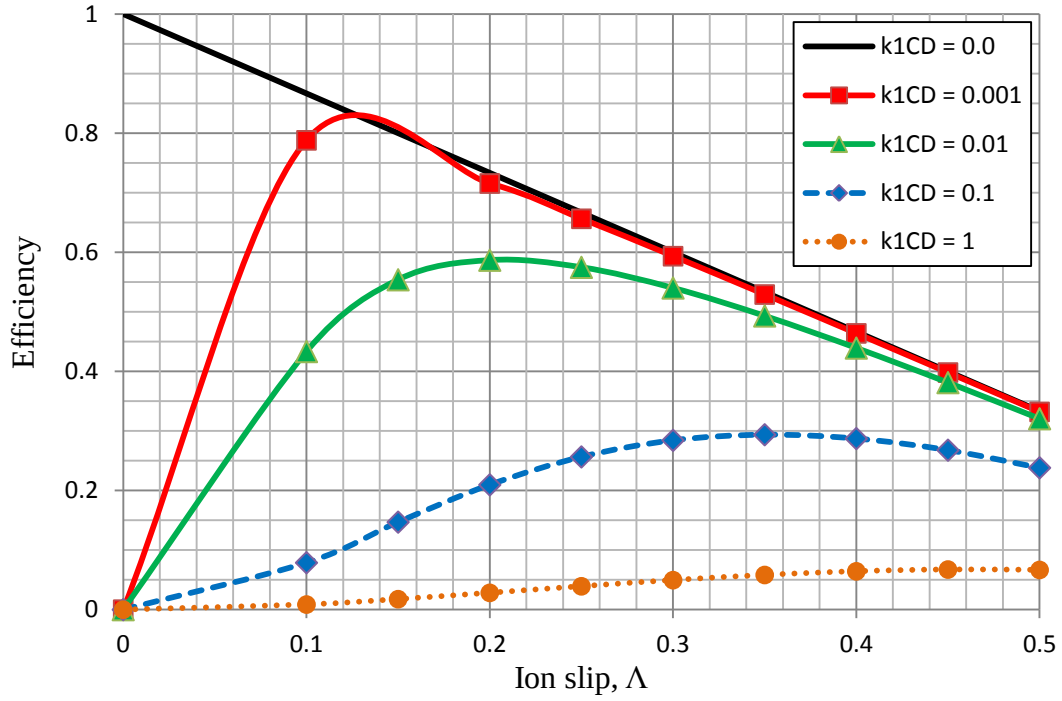

Figure 3.29 Variation of EHD efficiency with ion slip

The EHD generator requires the separation of electrons from a gas. Due to this requirement steam has not been included in this analysis since the first ionisation energy of steam is higher than that of helium. Thus, focus has been paid to PPCS models B, AB and C, where helium at 8 MPa exits the blanket around 500°C.

The EHD generator has the potential to provide high energy conversion efficiencies since it is not a heat engine and therefore not limited by the Carnot efficiency, as are thermoelectric and thermionic generators. However, gases with low mobility at low pressures are required, along with a very low drag coefficient, to produce k_1C_D values low enough for high conversion efficiencies.

Under highly idealised conditions figure 3.28 shows that an EHD generator with a channel length of 1 cm and an ion slip of about 0.01 has the potential to provide a power density of approximately 4 kW/m^3. To generate the required 1696 MW_e of gross electric power, as specified by PPCS model C, using a channel length of 1 cm, an electrode surface area of nearly 4240 m^2 would be required. Under these conditions, however, figure 3.29 shows that the efficiency, assuming a k_1C_d value of 0.001, would be less than 20%. Assuming an ion slip of 0.1, however, the efficiency could be raised to nearly 80%, but, the power density for 1 cm channel would be reduced to about 350 W/m^3, which would increase the required electrode surface area to generate 1696 MWe to over 4800000 m^2. In terms of volume, this would equate to over 1900 Olympic swimming pools.

The conclusion of this analysis, therefore, is that EHD generators, operating under current fusion constraints, cannot provide the necessary power densities, at suitably high conversion efficiencies, required for large-scale electricity generation. The materials and manufacturing costs would very likely be prohibitive.

3.3.4 Magnetohydrodynamic Energy Conversion

The MHD generator is based upon Faraday's law: when a conductor moves through a magnetic field an electric current is induced within the conductor. The MHD generator, however, produces electricity by moving an electrically conductive fluid, instead of a solid conductor, through transverse magnetic fields. The combined influence of a pressure gradient within the flow and the magnetic field causes the kinetic energy of the flow to be exchanged for the electrical power induced in a load circuit, via electrodes which connect to an external circuit [Soo, 1968]. This analysis will be looking at the simplest form of MHD generators, namely the linear types.

Figure 3.30 shows a diagram of one form of linear MHD generator, where the gas flows through a linear channel. The magnetic field is perpendicular to the flow, which induces an electric field at right angles to both the flow and the magnetic field.

By placing suitable electrodes on either side of the MHD channel, and connecting them to an electric load, electrical current will flow through the gas, electrodes and load. This geometry is called a continuous electrode linear MHD generator. The magnetic field causes a Hall current to flow in the direction of the conductive fluid, which effectively lowers the electrical conductivity and causes the power density to fall [Decher, 1997].

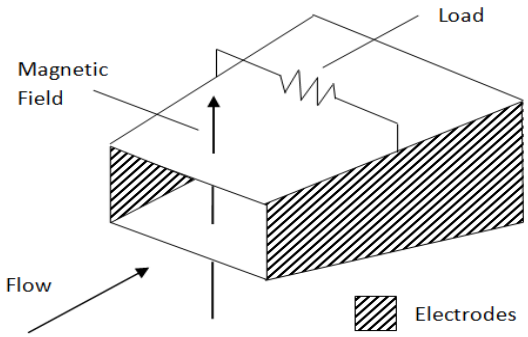

Figure 3.30 Continuous electrode MHD generator, redrawn from an example in Sutton & Sherman [2006]

The Hall current can be prevented by using segmented electrodes, another form of linear MHD generator. A diagram depicting the Hall effect is shown in figure 3.31, whilst the geometry of a segmented electrode MHD generator is shown in figure 3.32. The segmented electrodes allow for the development of a Hall electric field in the direction of fluid flow.

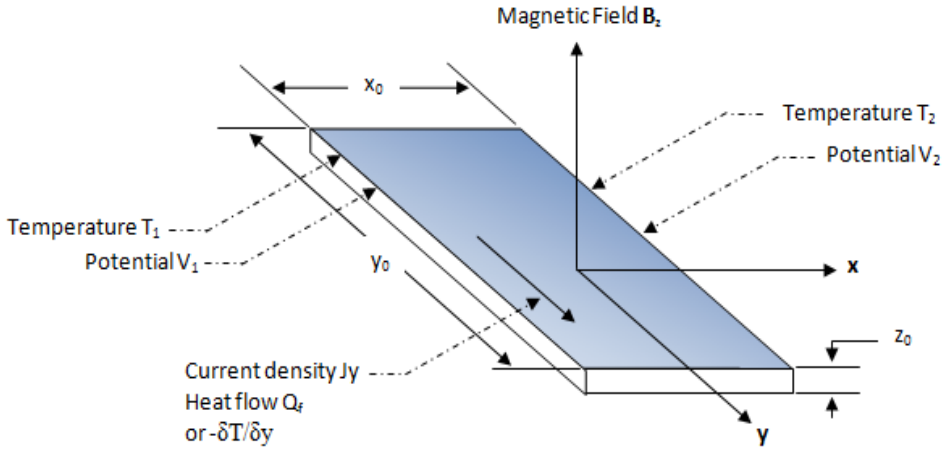

Figure 3.31 Hall effect, where J_y produces $V_1 < V_2$ at $T_1 = T_2$, redrawn from an example in Soo [1968]

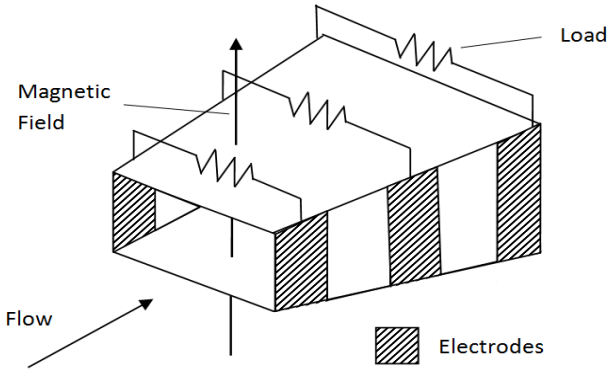

Figure 3.32 Segmented electrode MHD generator, redrawn from an example in Sutton & Sherman [2006]

A further type of linear MHD generator is the Hall MHD generator, shown in figure 3.33. By short-circuiting the Faraday current, the Hall current can be allowed to flow through the electric load [Sutton & Sherman, 2006].

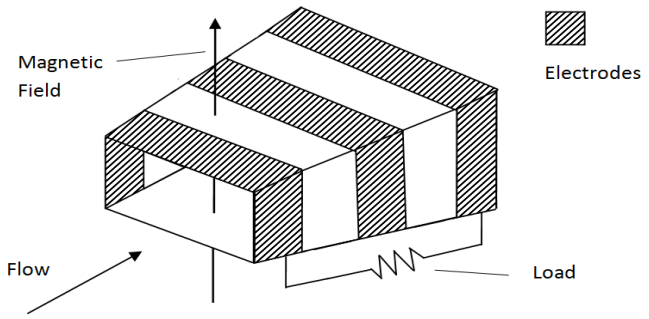

Figure 3.33 Hall linear MHD generator redrawn from an example in Sutton & Sherman [2006]

3.3.4.1 Continuous Electrode Governing Equations

A schematic and vector diagram, reproduced from Soo [1968], is shown in figure 3.34. The flow velocity is v and the channel width is b. The electron drift velocity is v_e, J_e the electron current density, σ the electrical conductivity, B the magnetic field strength, E the electric field and E' the electric field experienced by any charged particle moving with the fluid.

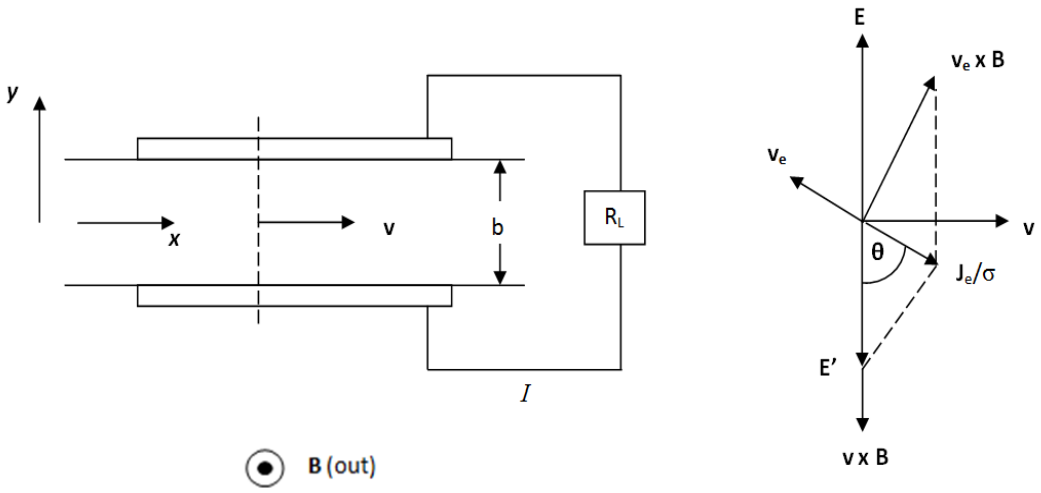

Figure 3.34 Continuous electrode MHD generator schematic and vector diagram redrawn from an example in Soo [1968]

The electron current densities, taking into account the Hall Effect, in the x-direction and y-direction are given by Soo [1968] as

$$J_{ex} = \frac{\sigma\left(E'_x - \beta_e E'_y\right)}{(1+\beta_e^2)} \tag{3.28}$$

$$J_{ey} = \frac{\sigma\left(E'_y - \beta_e E'_x\right)}{(1+\beta_e^2)} \tag{3.29}$$

where β_e is the Hall Effect coefficient, given as the product of the angular cyclotron frequency, ω, and the collision frequency, τ

$$\beta_e = \omega\tau \tag{3.30}$$

Both Soo [1968] and Decher [1997] define the ratio of the operating electric field to the open circuit electric field as

$$\delta = \frac{E_y}{vB} \tag{3.31}$$

where, for net power output, $0 < \delta < 1$ and

$$E_y^{'} = E_y - vB \tag{3.32}$$

In this system both E_x and E'_x are zero, as shown in the vector diagram. Hence, the product $J_{ex}E_x$ is zero. Considering the vector diagram, the electron current density in the y-direction, J_{ey}, is negative. Equation (3.29) reduces to

$$-J_{ey} = \frac{-\sigma vB(1-\delta)}{(1+\beta_e^2)}$$

Using equation (3.31) the power output per unit volume for a continuous electrode linear MHD generator can therefore be given as

$$\dot{w} = -J_{ey}E_y = \frac{\sigma v^2 B^2 \delta(1-\delta)}{(1+\beta_e^2)}$$

(3.33)

The power input per unit volume is given by Soo [1968] as

$$J_{ey}vB = \frac{\sigma v^2 B^2 (1-\delta)}{(1+\beta_e^2)}$$

(3.34)

This leads to the electrical efficiency, through (3.32), as

$$\eta_e = \frac{-J_{ey}E_y}{J_{ey}vB} = \delta$$

(3.35)

3.3.4.2 Segmented Electrode Governing Equations

The schematic for a segmented electrode MHD generator, and vector diagram, reproduced from Soo [1968], are given in figure 3.35. In this system the electron current density in the x-direction is zero. Hence, the product $J_{ex}E_x$ is zero.

Soo [1968] gives the following electric field

$$E_x' = \beta_e E_y'$$

(3.36)

From the vector diagram in figure 3.35 the electron current density is in the negative y-direction. Using equations (3.31) and (3.36), (3.29) reduces to

$$-J_{ey} = \sigma vB(1-\delta)$$

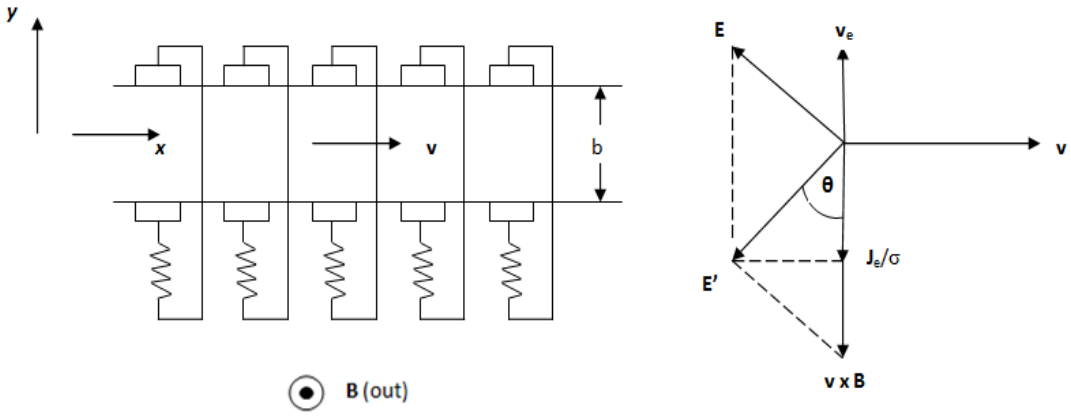

Figure 3.35 Segmented electrode MHD generator schematic and vector diagram redrawn from an example in Soo [1968]

This leads to the power per unit volume as

$$\dot{w} = -J_{ey}E_y = \sigma v^2 B^2 \delta(1-\delta)$$

(3.37)

The power input per unit volume is given by Soo [1968] as

$$J_{ey}vB = \sigma v^2 B^2 (1-\delta)$$

(3.38)

Hence, the electrical efficiency, via (3.31), is the same as for the continuous electrode MHD generator

$$\eta_e = \frac{-J_{ey}E_y}{J_{ey}vB} = \delta$$

3.3.4.3 Hall Generator Governing Equations

A schematic and vector diagram for this type of MHD generator is shown in figure 3.36. For the Hall MHD generator Soo [1968] defines δ as

$$\delta = \frac{E_x}{E_{x0}} = \frac{-E_x}{vB\beta_e} \tag{3.39}$$

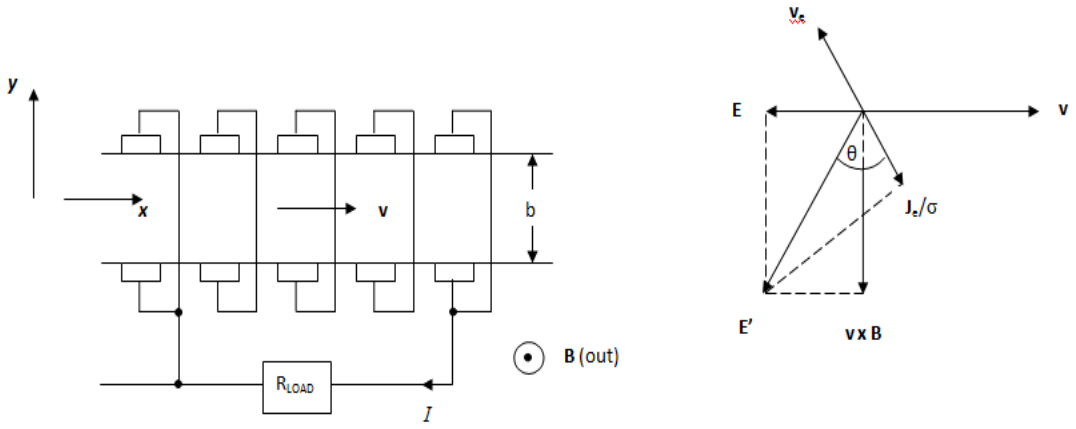

Figure 3.36 Hall MHD generator schematic and vector diagram redrawn from an example in Soo [1968]

The electric field in the y-direction, E_y, is zero. Hence, the product $J_{ey}E_y$ is zero and no contribution to power will be provided by the y-component of the electron current density. Soo [1968] gives the remaining electric fields as

$$E'_x = E_x \tag{3.40}$$

$$E'_y = -vB \tag{3.41}$$

Noting from the Hall generator vector diagram that J_{ex} is positive, using (3.39) equation (3.28) reduces to

$$J_{ex} = \frac{\sigma v B \beta (1 - \delta)}{(1 + \beta_e^2)}$$

Since the x-component of the electric field, E_x, is negative, and once again using (3.39), the power per unit volume for a Hall MHD generator can be defined as

$$\dot{w} = -J_{ex} E_x = \frac{\sigma v^2 B^2 \beta_e^2 \delta (1 - \delta)}{(1 + \beta_e^2)}$$

(3.42)

The power input per unit volume is given by Soo [1968] as

$$-J_{ey} v B = \frac{\sigma v^2 B^2 (1 + \delta \beta_e^2)}{(1 + \beta_e^2)}$$

(3.43)

This yields an electrical efficiency written as

$$\eta_e = \frac{\beta_e^2 \delta (1 - \delta)}{(1 + \beta_e^2 \delta)}$$

(3.44)

Way [1963] summarises the advantages and disadvantages, given in table 3.5, of the three types of linear MHD generators presented in this section, including comments relating to the external load circuitry, Hall coefficient and forces.

Type	Advantages	Disadvantages
Continuous electrode	- Simple - Easier insulation problems	- Low ẇ at large β_e - Transverse body force and stress
Segmented electrode	- Best ẇ - Axial force only - Suitable for reasonably high β_e	- Complicated load circuitry - More difficult control - Strong axial potential gradient
Hall	- Single load circuit - Take advantage of large β_e - High voltage-low current	- Low ẇ - Limited η_{max} (β_e not usually as high as is desired) - Strong axial potential - Transverse body force

Table 3.5 Comparison between linear MHD types reproduced from Way [1963]

3.3.4.4 MHD Power Considerations

It is worth discussing possible ionisation methods, since insufficient ionisation of the fluid flow would affect MHD power density. The temperature of the helium in PPCS models B, AB and C is too low for thermal ionisation. A modification of the Saha equation for a slightly ionised gas at a prescribed temperature and pressure was used by Lin et al. [1955] to take account of close encounters between neutrals and electrons, which dictate the electron mobility, to gain a more accurate calculation of the electrical conductivity for a slightly ionised gas.

$$\sigma_0 = 7.05\ x\ 10^{-13} \frac{T^{3/4}}{p^{1/2}\ exp\left(\frac{eV_i}{2kT}\right)} \frac{1}{Q_C} \tag{3.45}$$

where T is temperature, p is pressure, eV_i the ionisation potential in electron volts, k Boltzmann's constant, and Q_C the electron-atom collision cross-section.

The values of eV_i and Q_C for helium can be taken as 15.75 eV and 4 x 10^{-20} m^2, respectively [Kaye & Laby, 1973], and assuming a temperature of 1000K and a pressure of 8 MPa, equation (3.45) gives a negligible electrical conductivity for helium since the exponential term becomes infinitely large. For water the ionisation potential is 75 eV $\pm$ 3 eV [Deasey, 1994], hence despite the value of Q_C, for either water of dry steam, the exponential term becomes infinitely large and hence the conductivity is effectively zero. Thermal ionisation is therefore not adequate to partially ionise any of the coolants used in the PPCS models

Common techniques used with non-thermal ionisation include radio frequency discharge, coronal discharge, external radiation and electron injection. All produce a volume of electrons and ions, but none would be viable with an MHD generator since recombination, where electrons recombine with ions to form neutral atoms or molecules, will occur inside the MHD channel due to insufficiently high temperatures. Moreover, it would take electrical power to use these aforementioned non-thermal ionisation methods.

A further non-thermal ionisation option would be to seed the coolant with a small quantity of an easily ionisable vapour of low ionisation potential. Caesium is favoured for its low ionisation potential of 3.89 eV, but is expensive, and instead potassium with a value of 4.34 eV could be used. For a seeded gas [Frost, 1961] equation (3.45) becomes

$$\sigma_0 = 7.05\ x\ 10^{-13} \frac{T^{3/4}}{p^{1/2}\ exp\left(\frac{eV_i}{2kT}\right)} \frac{i^{1/2}}{\bar{Q}_C} \quad for\ i \ll 1$$

(3.46)

where i is the ratio of partial pressure of seed vapour to partial pressure of carrier gas, and $\overline{\bar{Q}_C}$ is given by

$$\bar{Q}_C = i\ Q_C\ seed + \ Q_C\ gas$$

(3.47)

For a helium coolant, if caesium is used to maximise the electrical conductivity, then Q_C for caesium can be taken at a best value of 400 x 10^{-20} m^2 [Kaye & Laby, 1973].

If a partial pressure value of 10% is assumed for the seed vapour, where the value for i would then be 0.1, equation (3.47) yields 44 x 10^{-20} m^2. After substitution into (3.46) the value for the electrical conductivity is still negligible due to the exponential term. A similar case arises again for a water coolant, even if it is seeded, due to the very large exponential term.

A final comment should be made about filtration. If a seeding agent is used, further complications will be added due to the requirement for the seeding agent to be removed from the coolant at some stage, probably before the blanket, which would likely require more electrical power. It would seem, therefore, that both thermal and non-thermal ionisation methods are unsuitable.

An alternative option is to use the liquid metal breeder Pb-17Li that is used in PPCS models AB and C. The electrical conductivity of Pb-17Li is in the approximate range 7 x 10^7 – 8 x 10^7 S/m for temperatures between 508 and 933 K [Schulz, 1991]. To achieve high power densities, high liquid metal flow velocities and high magnetic field strengths are required.

Soo [1968] believes the use of a conventional pump to be the most efficient way of achieving high liquid metal flow velocities, but liquid metals tend to be corrosive and a conventional pump may suffer. An approach used by the steel industry, however, is to use electromagnetic pumps, which are essentially MHD pumps, or thrusters, where $\delta > 1$. This is the approach currently envisaged for both PPCS models AB and C.

Another way of achieving a high liquid metal velocity is to use a nozzle to expand a liquid metal with uniformly distributed bubbles of its vapour [Elliot, 1961], but Soo [1968] notes that the chief difficulty lies with the ability to produce uniformly distributed vapour bubbles in the liquid metal. Soo [1968] instead suggests using a jet vapour from the liquid metal to accelerate the bulk liquid metal to a high velocity, but the ideal thermodynamic efficiency would be low, about 10% [Sowa, 1963].

A final idea presented by Soo [1968] is to use a vapour, produced by nozzle expansion, to give a high velocity vortex which yields a high velocity layer of the liquid metal via friction. However, Soo [1968] notes that this relies upon the friction between phases and would be an inherently low-efficiency device.

Commercially available Halbach arrays can provide magnetic field strengths of up to 1 Tesla, something that Soo [1968] was aware of and also notes. Whilst this is low, compared to magnetic field strengths available from copper-wound electromagnets, or even superconducting magnets, the benefit of permanent magnets is that no electrical power is required to produce the magnetic field. If an MHD generator is providing small amounts of electrical power, using a portion of this power to generate the magnetic field seems somewhat counterproductive. This, of course, depends upon the percentage of MHD power used for the magnets. Superconducting magnets do not require any electricity to generate their high magnetic fields, only an initial input power, however, they do require cryogenic cooling.

Some attention should also be given to determine the most suitable type of linear MHD generator for use with a liquid metal. Neglecting the complications associated with load circuitry, the magnitude of the Hall coefficient is an important factor.

The value for the electrical mobility μ_e can be found by using

$$\sigma = \mu_e n_e e \tag{3.48}$$

where e is the electron charge, and n_e is the electron number density, given by

$$n_e = \frac{n_v N \rho}{M_w} \tag{3.49}$$

where n_v is the number of valence electrons per atom, N is Avogadro's number, ρ the density and M_w the molecular weight.

The molecular weight of Pb-17Li is 0.173 kg/mol [Coen & Sample, 1990], whilst the density of Pb-17Li is given by [Schulz, 1991]

$$\rho_{Pb-17Li} = 10.45x10^{3}\left(1 - (161x10^{-6}T_{Pb-17Li})\right) \tag{3.50}$$

It can be assumed that Pb-17Li has only one valence electron per atom. Substitution of the required values into (3.49), noting that there is a difference in Pb-17Li blanket outlet temperature between PPCS models AB and C, yields an electron number density of approximately 3 x 10^{28} m^{-3}.

By rearranging equation (3.48) for electrical mobility, and substituting in the known values, an approximate electrical mobility for Pb-17 Li can be given as 1.4 x 10^{-2} As^2/kg.

Using equations for collision frequency and cyclotron frequency [Sutton & Sherman, 2006] the Hall coefficient can be determined from (3.31)

$$\tau = \frac{\sigma m_e}{n_e e^2} \tag{3.51}$$

$$\omega = \frac{eB}{m_e} \tag{3.52}$$

where m_e is the electron mass, e the electron charge and B the magnetic field strength. For a magnetic field strength of 1 Tesla the Hall coefficient is found to be 1.4 x 10^{-2}. Valence number is inversely proportional to the Hall coefficient, so assuming a valency of 1 gives the highest Hall coefficient.

Figure 3.37 shows the variation in power per unit volume for the three types of linear MHD generator presented in this analysis. There is little difference in using the Pb-17Li blanket outlet temperatures for PPCS models AB and C, but in this instance the latter has been used.

The graph highlights that the maximum power density occurs when δ is equal to 0.5 for all three types of linear MHD generator. Though difficult to interpret from the graph in figure 3.37, the power density of the segmented generator, using PPCS model C conditions, is 174 kW/m^3. This is slightly higher than the continuous generator because the Hall coefficient does not appear in the denominator of equation (3.37). Since the Hall generator is not suited for use with Pb-17Li a choice between the continuous MHD generator, with marginally lower power densities, and the segmented MHD generator, with its complicated load circuitry, must be made.

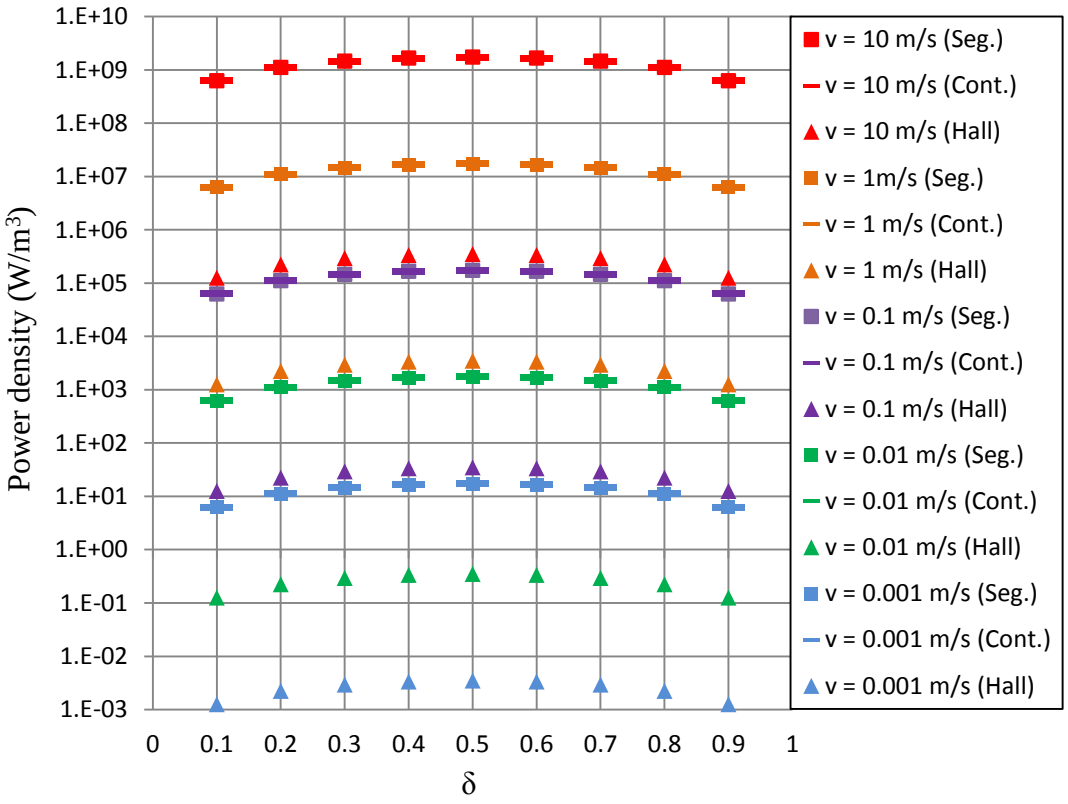

Figure 3.37 Variation of power density with Pb-17Li velocity and α for a magnetic field strength of 1 Tesla, Hall coefficient of approximately 0.014 and electrical conductivity of 7 x 10^7 S/m

A significant problem with liquid metal MHD power generation is that if an electric pump is used, the power input will always exceed the power output. This is easy to determine from inspection of the electrical efficiency definition for both continuous and segmented MHD generators. Since δ cannot exceed 1, the power input is always going to be higher than the power output. This is also true of the Hall MHD generator.

3.4 Summary

This chapter has looked at a variety of energy forms and energy conversion devices in an attempt to identify alternative methods of generating large amounts of electricity from a fusion reactor. Whilst some of the ideas explored could be used for low-level power systems, the conclusion is that heat is the only primary source of energy available within a fusion power plant from which large amounts of electricity can be generated.

Using plant parameters consistent with PPCS models B and AB, and receiving thermal power from HCPB and HCLL blankets, and divertors, respectively, several water-based Rankine cycles were explored. Despite these cycles being highly idealised, a water-based regenerative Rankine cycle utilising the divertor for reheat could offer attractive cycle efficiencies and net work outputs.

It was shown that a CICBTDTX cycle offers the best performance for primary Brayton cycles operating under both PPCS-B and PPCS-AB plant parameters, whilst for secondary Brayton cycles the best performance is achieved using a CICBTX configuration. Using PPCS model B constraints offered no advantage of a primary CICBTDTX Brayton cycle over a secondary CICBTX Brayton cycle in terms of cycle efficiency or net cycle power output. Using PPCS model AB parameters, however, a secondary CICBTX Brayton cycle can provide a marginal advantage in terms of cycle efficiency, but a primary CICBTDTX cycle yields a higher net power output.

An evaluation of DEC technologies showed that the power densities and efficiencies of modern thermoelectric generators are too low for generating large-scale electricity from a tokamak. TEGs, however, do have the potential for low-level power generation and electricity could be generated from waste heat sources.

The power density of a thermionic generator is low for blanket outlet temperatures associated with PPCS models B, AB and C. Furthermore, efficiencies are low and there is a strong requirement to reduce electrode emissivity. Furthermore, large surface areas would be needed to yield large electrical power outputs and the use of composite materials may be prohibitively costly.

An EHD generator is only suitable for PPCS models that utilise helium as a blanket coolant, since the first ionisation level of steam is higher than that of helium. An advantage of EHD power generation is the utilisation of non-thermal ionisation, which suits the low-temperature helium blankets. Large power densities could be possible from EHD generators, but this relies on short channel lengths and low values of ion slip. EHD generators are not limited by the Carnot efficiency, but electrode drag and gases at high-pressure are expected to significantly reduce efficiency.

The use of seeding has a negligible effect on the electrical conductivity of helium at temperatures associated with HCPB, HCLL and DCLL blankets. Due to these temperature constraints the MHD generator is only viable for those PPCS models that use a liquid metal breeder. Pb-17Li has a high electrical conductivity, but its low Hall coefficient value renders it useable only for the continuous and segmented MHD generators that have been surveyed. Permanent magnets seem preferable as no electrical power is required to generate the magnetic field, or for cryogenic cooling.

None of the DEC technologies that have been analysed in this chapter seem to have the potential to completely replace conventional turbo-machinery. However, in conjunction with conventional power cycles, such as a Rankine or Brayton cycle, their application seems very plausible. High power densities appear to be more easily achievable using liquid metal MHD power generation when compared to the other

DEC devices, providing higher flow velocities can be attained. MHD power generation, therefore, seems the most promising DEC technology to pursue, but to produce net electrical power output a method of reducing the liquid metal pumping power must be identified.

Chapter 4: Two-Phase Liquid Metal MHD

The previous chapter presented several direct energy conversion methods, which led to the conclusion that single-phase liquid metal MHD power generation is the most attractive, and most applicable in the current low-temperature context of fusion, due to the potentially high power density. However, the major drawback, which was highlighted, is the large pressure drop associated with single-phase liquid metal MHD that limits the net electrical power output.

This chapter will begin by introducing basic parameter definitions for two-phase systems, followed by the introduction of two different one-dimensional two-phase flow models that are commonly used for predicting the total two-phase pressure gradient. The various correlations that are used with these flow models will also be presented. The concept of two-phase liquid metal MHD power generation will then be introduced followed by the derivation of the equations that will be used to predict its performance.

4.1 Two-Phase Flow Models

Two-phase systems can be comprised of gas-liquid, liquid-liquid, gas-solid and solid-liquid flows. In this chapter only gas-liquid two-phase flows are considered, for which the subscripts g and l for gas and liquid, respectively, will be used.

The prediction of the two-phase flow pressure loss through the MHD generator will be important in determining its viability as a direct energy conversion device, which must not only maintain appreciable power densities to remain an attractive prospect, but crucially also be able to produce a net power output.

The total two-phase pressure gradient for a two-phase system is comprised of three pressure gradient terms: frictional, gravitational and momentum. Two-phase systems do not usually include the additional MHD pressure loss term associated with MHD ducts.

A further factor in relation to the performance of a two-phase MHD generator is the two-phase flow regime. It is unclear how a particular flow regime will affect charge separation in a liquid metal, but it is expected that bubbly flows will be preferable over annular flows because charge separation between the electrodes will not be hindered by large volumes of gas. Plug flows are also thought to offer interesting intermittent charge separation effects since there will be moments, between the plugs, where there will be an uninterrupted charge separation in the liquid metal.

Two commonly used flow models for predicting two-phase pressure gradients are the homogeneous and separated models. Both of these models assume adiabatic flow conditions. They can each work well for different flow regimes and therefore determine which flow model is more suitable. However, before the flow models are introduced some basic parameters of two-phase systems should be defined.

4.1.1 Basic Parameter Definitions

The slip ratio, S, is defined, in gas-liquid two-phase systems, as the ratio of the gas phase velocity to the liquid phase velocity

$$S \equiv \frac{u_g}{u_l} \tag{4.1}$$

The two-phase flow quality, x, is defined as

$$x \equiv \frac{\dot{m}_g}{\dot{m}_{total}} = \frac{\dot{m}_g}{\dot{m}_g + \dot{m}_l} \tag{4.2}$$

The cross-sectional void fraction, α, is an indicator of the area occupied by the gas phase. This is equal to unity when a duct is occupied solely by the gas phase and zero when occupied entirely by the liquid phase. The total mass flux, G, is the ratio of the total mass flow rate to the total cross-sectional area

$$G \equiv \frac{\dot{m}_{total}}{A_{total}} = \frac{\dot{m}_g + \dot{m}_l}{A_{total}} \tag{4.3}$$

Both the gas mass flux, G_g, and the liquid mass flux, G_l, can be defined in a similar way

$$G_g \equiv \frac{\dot{m}_g}{A_g} = \rho_g u_g \tag{4.4}$$

$$G_l \equiv \frac{\dot{m}_l}{A_l} = \rho_l u_l \tag{4.5}$$

It can be shown from the above equations that

$$\alpha \equiv \frac{A_g}{A_g + A_l} = \frac{1}{1 + \left(S \frac{1-x}{x} \frac{\rho_g}{\rho_l}\right)} \tag{4.6}$$

4.2 Homogeneous Flow Model

The homogeneous model assumes that complete mixing has occurred between the two phases, and their velocities are also assumed equal, so that the two phases can be treated as a single fluid. For the homogeneous flow model, therefore, S is unity.

The total two-phase pressure gradient is given in Whalley [1987] as

$$-\frac{dP}{dz} = \left(\frac{2C_{flo}G^2}{d_{tube}\rho_h}\right)_{fric} + (\rho_h g \sin\theta)_{grav} + \left(G^2 \frac{d}{dz}\left(\frac{1}{\rho_h}\right)\right)_{mom}$$

(4.7)

where C_{flo} is the liquid only friction factor

$$C_{flo} = \frac{0.079}{Re_h^{0.25}}$$

(4.8)

and Re_h is the Reynolds number of the homogeneous mixture

$$Re_h = \frac{G d_{tube}}{\mu_h}$$

(4.9)

There are several suggestions presented in Whalley [1987] for a definition of the homogeneous viscosity, μ_h, for which a simple definition was used by Isbin et al. [1958]

$$\mu_h = \left(\frac{x}{\mu_g} + \frac{1-x}{\mu_l}\right)^{-1}$$

(4.10)

The homogenous mixture density, ρ_h, is given by Whalley [1987] in a similar way to (4.10)

$$\rho_h = \left(\frac{x}{\rho_g} + \frac{1-x}{\rho_l}\right)^{-1}$$

(4.11)

Whalley [1987] writes that the homogeneous flow model gives reasonable predictions for the momentum component of the total two-phase pressure gradient, whilst for the frictional component good results are often achieved. However, if the ratio of the liquid density to the gas density is greater than 10, or if the total mass flux is less than 2000 kg/m^{2}s, then the homogeneous model can predict incorrect values by a factor of 5 or 10 when determining the mean density of the flow. The density ratio for Pb-17Li and helium, at the relevant temperatures for the DCLL concept is approximately 6000 and therefore the homogeneous flow model may be inadequate.

4.3 Separated Flow Model

The separated flow model assumes that the phases are separate, each with a different velocity. The gas phase moves faster than the liquid phase so that S is typically greater than unity. The total pressure gradient is given in Whalley [1987] as

$$-\frac{dp}{dz} = \left(\frac{4\tau}{d_{tube}}\right)_{fric} + \left(\left[\alpha\rho_g + (1-\alpha)\rho_l\right]g\sin\theta\right)_{grav} + \left(G^2\frac{d}{dz}\left[\frac{x^2}{\alpha\rho_g} + \frac{(1-x)^2}{(1-\alpha)\rho_l}\right]\right)_{mom} \tag{4.12}$$

where τ is the wall shear stress

The gravitational and momentum components of equation (4.12) use the cross-sectional void fraction, which is not present in the homogeneous flow model.

Equation (4.12) can be simplified, however, by neglecting the momentum term, which is deemed to be reasonable since one can assume that the flow quality at system inlet and outlet is unchanged, i.e. the mass flows of the two phases are constant. There are several void fraction correlations that have been developed to calculate α for gas-liquid two-phase systems, most of them for air and water, some are actually correlations for slip ratio.

4.3.1 Gravitational Component

Whalley [1987] gives a list of slip correlations that will now be presented in increasing order of accuracy, starting with the homogeneous model, which uses a slip ratio of unity to derive the value of α in equation (4.3). The Zivi [1964] slip correlation was developed for annular flow and is given by

$$S = \sqrt[3]{\frac{\rho_l}{\rho_g}}$$

(4.13)

The Smith [1969] correlation, also for annular flow, is given in terms of the void fraction and it assumes a separated flow where the liquid phase is entrained in the gas phase by an entrainment fraction e, which can vary between zero and unity, but empirically is set to 0.4 to agree with the experimental data. The slip is given by

$$S = e + (1 - e)\left(\sqrt{\frac{\frac{\rho_l}{\rho_g} + e\frac{1-x}{x}}{1 + e\frac{1-x}{x}}}\right)$$

(4.14)

thereby giving the void fraction as

$$\alpha = \frac{1}{1 + 0.79\left(\frac{1-x}{x}\right)^{0.78}\left(\frac{\rho_g}{\rho_l}\right)^{0.58}}$$

(4.15)

Another annular flow correlation is the Chisolm [1972] slip ratio correlation

$$S = \sqrt{(1-x)\left(1 - \frac{\rho_l}{\rho_g}\right)}$$

(4.16)

The final and most accurate correlation given by Whalley [1987] is the CISE slip correlation for annular flow. This was developed by Premoli et al. [1970] for determining the effects of two-phase coolant reactivity in nuclear reactors for upward flow in vertical channels

$$S = 1 + E_1 \sqrt{\frac{y}{1 + yE_2} - yE_2}$$

(4.17)

where the parameters E_1, E_2 and y are

$$E_1 = 1.578\, Re^{-0.19} \left(\frac{\rho_l}{\rho_g}\right)^{0.22}$$

(4.18)

$$E_2 = 0.0273\, We\, Re^{-0.51} \left(\frac{\rho_l}{\rho_g}\right)^{-0.08}$$

(4.19)

$$y = \frac{\beta}{1 - \beta}$$

(4.20)

and the volumetric flow quality, β, is

$$\beta = \frac{\rho_l x}{\rho_l x + \rho_g (1 - x)}$$

(4.21)

The Reynolds and Weber numbers in the CISE correlation [Premoli et al., 1970] are given in terms of the total mass flux, G

$$Re = \frac{G d_{tube}}{\mu_l} \tag{4.22}$$

$$We = \frac{G^2 d_{tube}}{\gamma_l \rho_l} \tag{4.23}$$

where γ is the surface tension.

A final mention is given to a void fraction correlation that was specifically designed for high-density liquid metal two-phase vertical flows. It was developed by El-Boher et al. [1988] and used by Satyamurthy et al. [1995] to predict the performance of a conceptual design to utilise waste heat from a nuclear reactor in order to drive a liquid metal around a vertical loop via buoyancy and generate electricity via a single-phase MHD generator.

The El-Boher et al. [1988] void fraction is given as

$$\alpha = (1 + 0.27 * Y_1^{-0.69} * Y_2^{-0.177} * Y_3^{0.378} * Y_4^{0.067})^{-1} \tag{4.24}$$

where the parameters Y_1, Y_2, Y_3, and Y_4 are

$$Y_1 = \left(\frac{x}{1-x}\right)\frac{\rho_l}{\rho_g} \tag{4.25}$$

$$Y_2 = \frac{u_l^2}{g d_{tube}} \tag{4.26}$$

$$Y_3 = \frac{\mu_l}{\mu_g} \tag{4.27}$$

$$Y_4 = \frac{\gamma_l}{\mu_l u_l} \tag{4.28}$$

4.3.2 Frictional Component

The frictional component can be found by using one of several correlations that have been developed, ranging from simple, such as the Lockhart and Martinelli [1949] correlation, which Whalley [1987] suggests is of low accuracy, to complex empirical formulae, as developed by Friedel [1979]. Some correlations are exclusively for use with steam-water two-phase systems, such as those developed by Martinelli and Nelson [1948], and Thom [1964], whilst the Barcozy [1966] correlation uses a graphical approach.

Chisolm [1967] also developed a frictional pressure gradient correlation that is applicable to any fluid, but Whalley [1987] also suggests its accuracy is questionable. The Friedel correlation is also applicable to any fluid and is considered by Whalley [1987] to be the best generally available and applicable correlation, but only if the viscosity ratio μ_l/μ_g is less than 1000 and the total mass flux G is less than 2000 kg/m^{2}s. The viscosity ratio for Pb-17Li and helium is well below this figure: approximately 20.

The Friedel correlation was also used by Satyamurthy et al. [1995] for their concept involving high-density liquid metal two-phase flows. Considering the further recommendation of its use by Whalley [1987] this can be deemed a reasonable basis from which to adopt the use of the Friedel correlation for determining the frictional pressure gradient component.

4.3.3 Friedel Correlation for Friction

A two-phase multiplier, ϕ_{lo}^2, where the subscript *lo* denotes liquid only phase, is given by

$$\phi_{lo}^2 = \frac{(-dp/dz)_{fric}}{(-dp/dz)_{lo}} = E + \frac{3.24 * F * H}{Fr^{0.045} We^{0.035}}$$

(4.29)

where the parameters E, F and H are given by

$$E = (1-x)^2 + x^2 \frac{\rho_l C_{fgo}}{\rho_g C_{flo}}$$

(4.30)

$$F = x^{0.78}(1-x)^{0.224}$$

(4.31)

$$H = \left(\frac{\rho_l}{\rho_g}\right)^{0.91} * \left(\frac{\mu_g}{\mu_l}\right)^{0.19} * \left(1 - \frac{\mu_g}{\mu_l}\right)^{0.7}$$

(4.32)

where C_{fgo} and C_{flo} are the gas-only and liquid-only friction factors, respectively, for flows occupied by a single-phase gas or single-phase liquid. Assuming flow in smooth pipes, the Blasius correlation [Blasius, 1913] could be used to give

$$C_{fgo} = \frac{0.079}{Re_{go}^{0.25}}$$

(4.33)

$$C_{flo} = \frac{0.079}{Re_{lo}^{0.25}}$$

(4.34)

where the subscript *go* represents gas-only. This approach is adopted by Whalley [1987] for vertical flows of steam and water, but is only valid for Reynolds numbers up to 1 x 10^5.

The dimensionless Froude and Weber numbers are given as

$$Fr = \frac{G^2}{g d_{tube} \rho_h^2} \tag{4.35}$$

$$We = \frac{G^2 d_{tube}}{\gamma_l \rho_h} \tag{4.36}$$

4.4 Two-Phase Liquid Metal MHD

The addition of a gaseous phase introduces an element of compressibility which serves to lower the pressure drop through the MHD duct and produce a net power output. The expansion of the gas phase in the MHD duct is almost isothermal, due to the much higher heat capacity of liquid metals, which continuously supplies heat to the gas phase and acts like an infinite re-heater [Blumenau et al. 1986].

In Branover et al. [1981] the two-phase liquid metal MHD generator is preceded by a mixer, where the gas and liquid phases are combined. The two-phase mixture, which has undergone direct contact heat exchange, then enters the MHD duct where the liquid metal is driven against the Lorentz force by the gas expansion. A nozzle follows the MHD generator where the mixture is accelerated before being separated in a hydrocyclonic separator. The separated gas phase returns to the associated power cycle whilst the liquid metal returns to an indirect heat exchanger to receive thermal energy from the heat source. After this the liquid metal re-enters the mixer.

Since the liquid metal operates on a closed cycle it must be pumped. This can be achieved mechanically or electrically through the use of an MHD pump, however, Branover et al. [1981] note that if this arrangement is orientated vertically, with the use of a high-density liquid metal, then the need to pump the liquid metal could be removed.

Satyamurthy et al. [1995] adopted this approach in their conceptual study by using buoyancy to drive high-density liquid metal two-phase flows in conjunction with nuclear waste heat. Water is injected into a mixer where it is converted into steam via direct contact heat exchange with the hot liquid metal. The two-phase mixture then proceeds via an upcomer, a vertical conduit of constant cross-section, to a separator utilising gravitational separation. The steam returns to a condenser before proceeding to a circulating pump, whilst the single-phase liquid metal enters a downcomer, which has the same cross-section as the upcomer, where it will return to the base of the loop via a single-phase liquid metal MHD generator.

Since the liquid metal is essentially being circulated by the gas phase, the single-phase MHD generator is capable of achieving a net power output, but even at modest magnetic field strengths around 0.5 – 1 T the pressure drop in the MHD generator due to the Lorentz force is likely to be of the order of a few MPa, thus necessitating a very tall downcomer which would also increase frictional pressure losses.

In a feasibility analysis by Wu et al [2007] a vertical setup is also adopted in conjunction with a lead-cooled fission reactor. A shorter downcomer is achieved by the placement of a two-phase MHD generator between the mixer and upcomer, which lowers the MHD pressure loss. However, they do not utilise buoyancy to drive the lead around the vertical loop and instead opt to include a liquid metal pump.

4.4.1 Two-Phase Mixture Electrical Conductivity

To determine the performance of a segmented-electrode constant-velocity (SECV) two-phase liquid metal MHD generator the electrical power output, which leads to the determination of the conversion efficiency, must be known.

However, this is dependent upon the electrical conductivity of the two-phase flow. The power output of a SECV MHD generator is given by multiplying the power density, given by equation (3.38), by the inlet area, A_{MHD_in} and the duct length, L_{MHD}, but must include the two-phase mixture conductivity, σ_m

$$\dot{W}_{MHD} = \sigma_m u_l^2 B^2 A_{MHD\_in} L_{MHD} \delta(1-\delta)$$

(4.37)

The theoretical value of the electrical conductivity of a compound was given in terms of the void fraction by Maxwell [1904], where it was assumed that small spheres of electrical conductivity, σ_1, are dispersed in a medium of electrical conductivity, σ_2

$$\sigma_m = \frac{2\sigma_2 + \sigma_1 - 2\alpha(\sigma_2 - \sigma_1)}{2\sigma_2 + \sigma_1 - \alpha(\sigma_2 - \sigma_1)}\sigma_2$$

(4.38)

However, if the small spheres of gas possess zero electrical conductivity, (4.38) reduces to

$$\sigma_m = \frac{2(1-\alpha)}{2+\alpha}\sigma_2$$

(4.39)

Tanatugu et al. [1972] used (4.38) to achieve good agreement with experimental results by using (4.38) for the mixture NaK-N_2, however, only at void fractions below 20%. Wu et al. [2007] used a formula for finding the mixture conductivity which was proposed and based upon the tests carried out by Petrick et al. [1978] involving NaK-N_2

$$\sigma_m = \frac{\sigma_l(1-\alpha)^2}{1+\alpha}$$

(4.40)

A complex route is taken by Saito et al. [1978] where the electrical conductivity is correlated with the void fraction. They assume that the two-phase electrical conductivity of a mixture is a linear function of the void fraction with two coefficients a_1 and a_2

$$\sigma_m \equiv f(\alpha) = (a_1 + a_2\alpha)\sigma_l \tag{4.41}$$

where a_1 and a_2 are taken from experimental results and equal to 1 and -1.1, respectively. Saito et al. [1978] found that for NaK-N_2 mixtures where void fractions were above 40% that the linear dependence of σ_m on α was not valid.

Yakhot and Branover [1982] also suggest that the electrical conductivity of a two-phase mixture is a function of the flow pattern and cite the results of Bouman et al. [1974] to show that the assumption of linear dependence of σ_m on α may be valid for bubble or slug flow, but can lose accuracy when annular flows are considered, where the dependence becomes almost exponential. The calculations of Yakhot and Branover [1982] were based upon those of Saito et al. [1978] and did not agree with experimental data produced by Petrick et al. [1978], which seems to suggest that (4.39) may be inaccurate at low void fractions.

Due to the lack of an explicit formula for the electrical conductivity of a two-phase mixture, which works well for a wide range of void fractions and different fluid sets, the accuracy of (4.39), (4.40) and (4.41) would need to be determined experimentally.

4.4.2 Thermodynamics of MHD Section

The total pressure drop experienced by the two-phase mixture in a SECV MHD duct is a combination of the pressure drop due to MHD forces and the pressure drop caused by frictional losses. The latter can be found through the Friedel correlation, or other frictional correlation, whilst the former is

given by Soo [1968] and is related to (4.37)

$$\Delta P_{MHD} = \sigma_m u_l B^2 L_{MHD}(1-\delta) = \frac{\dot{W}_{MHD}}{u_l A_{MHD\_in}\delta} = \frac{\dot{W}_{MHD}}{\dot{V}_{lMHD\_in}\delta}$$

(4.42)

Equation (4.42) is likely to be equally applicable to continuous-type MHD generators since the β-parameter for liquid metal is negligible. For gases the β-parameter can be relatively high and could affect the accuracy of (4.42) if applied to a continuous-type two-phase MHD generator operating with a high void fraction.

Soo [1968] uses the following isentropic identities to find the temperature drop through the MHD duct and the area expansion of the duct

$$T_{out} = T_{in}\left(\left(\frac{P_{out}}{P_{in}}\right)^{\frac{(\delta(\gamma-1))}{\gamma}}\right)$$

(4.43)

$$A_{out} = A_{in}\left(\left(\frac{P_{in}}{P_{out}}\right)^{\frac{\left(\delta+(\gamma(1-\delta))\right)}{\gamma}}\right)$$

(4.44)

However, these equations are for use with gaseous MHD generators. The introduction of a two-phase adiabatic index is proposed

$$\Gamma = \frac{c_{pm}}{c_{vm}} = \frac{\left(xc_{pg}\right) + \left((1-x)c_l\right)}{\left(xc_{vg}\right) + \left((1-x)c_l\right)}$$

(4.45)

which allows (4.42) and (4.43) to be rewritten as

$$T_{out} = T_{in}\left(\left(\frac{P_{out}}{P_{in}}\right)^{\frac{(\delta(\Gamma-1))}{\Gamma}}\right) \tag{4.46}$$

$$A_{out} = A_{in}\left(\left(\frac{P_{in}}{P_{out}}\right)^{\frac{\left(\delta+(\Gamma(1-\delta))\right)}{\Gamma}}\right) \tag{4.47}$$

4.5 Summary

The assumption of neglecting the momentum term for determining the total two-phase pressure loss in a vertical system is reasonable providing no significant leaking from the system occurs. Flooding, a process that can occur in annular flow regimes where the liquid phase is only partially lifted in an upcomer, can also make this assumption invalid.

For the gravitational component the homogeneous flow model is not suitable for use with high-density liquid metals since the liquid to gas density ratio must be less than 10. This, therefore, makes the use of the separated flow model the appropriate choice for determining the gravitational pressure loss.

Whalley [1987] performed a comprehensive survey of two-phase flow models, including published correlations for void fraction and frictional pressure drop. The use of the Friedel correlation [1979] for viscosity ratios below 1000 makes it applicable for two-phase mixtures using helium or steam as the gaseous phase and eutectic lead alloys as the liquid phase. Attention should be given to the total mass flux validity, which for the Friedel correlation must be below 2000 kg/m^{2}s.

A later study by Tribbe and Müller-Steinhagen [2000] compared various frictional pressure loss correlations and found the Müller-Steinhagen and Heck [1986], which

used flow qualities ranging from 0 to 1, to be reliable, giving results similar to the Friedel [1979] correlation, but only for mixtures involving low-density liquid phases.

The void fraction correlation must be chosen carefully since the literature seems to suggest that most correlations are only compatibility with certain two-phase flow regimes. Whalley [1987] suggests the use of the CISE correlation of Premoli et al. [1970], but the correlation of El-Boher et al. [1988], designed for vertical flows using high-density liquid metals, should also be considered.

Care must also be applied to the choice of correlation for mixture conductivity. Most of the correlations reviewed in the literature apply to earlier research involving NaK-N_2 mixtures. Since liquid metals all have electrical conductivities of the order 10^6-10^7 S/m these correlations could be applicable, but experimental determination is probably prudent for achieving the best results.

The MHD slip loss could be an extra factor to consider in two-phase liquid metal MHD systems. Its applicability is uncertain and may only produce negligible losses, however, experimental verification could show the effects of this loss upon electrical power output and efficiency, which may be significant.

Flow pattern maps for vertical flows involving liquid metals seem to be lacking in the literature and would almost certainly provide valuable insights into two-phase liquid metal MHD systems. Due to the introduction of a gaseous phase, thus reducing the detrimental effects associated with single-phase liquid metal MHD, some attention has been given to two-phase liquid metal MHD for many decades.

Despite an apparent decline in attention from the late 1980s onwards, applications still exist for two-phase liquid metal MHD within solar, nuclear waste heat and fission related areas. In the context of fusion, with the need to pump a high-density liquid metal breeder through a blanket, its application could be of significant interest.

Chapter 5: Proposed Power Cycle

A design for a two-phase loop builds upon work by Satyamurthy et al. [1995] who investigated buoyancy driven two-phase flows of liquid metals and steam, and Wu et al. [2007] who investigated two-phase MHD electrical power generation. A two-phase separated flow model, incorporating the CISE [Premoli et al., 1970] correlation for cross-sectional void fraction, is used to predict the behaviour of a buoyancy-driven two-phase flow, consisting of helium and Pb-17Li, around a vertical loop. The concurrent generation of electrical power via an MHD generator is possible due to the electrical conductivity of the mixture as a result of using a liquid metal breeder. Combining the aforementioned approaches provides a novel method for generating electrical power from a fusion reactor that uses plant parameters consistent with PPCS model C. The two-phase loop is accompanied by a proposed Brayton power cycle, to which the two-phase loop acts as a topping cycle, and uses the same PPCS-C plant parameters to help define its operation. Three bottoming Rankine cycles also feature as part of the proposed power cycle and receive heat from the Brayton cycle.

This chapter will begin with an introduction to the two-phase loop, where the reader will be made familiar with its constituent parts and their respective functions. The existing PPCS-C power cycle will then be described, before detailing a proposal for an alternative power cycle configurations for PPCS model C. The governing equations used to predict the performance of the proposed power cycle will then be given, before the performance of the proposed power cycle is presented, which will demonstrate its applicability to a fusion plant operating under PPCS-C plant parameters.

5.1 Introduction to Two-Phase Loop

In existing fusion plant designs that incorporate liquid metal breeders, electrical energy is used to circulate the breeder through the blanket and around the ancillary areas of the plant. In PPCS model C this accounts for 6.3 MW_e [Norajitra et al., 2003]. However, this expenditure can be removed by directly mixing a relatively small fraction of helium with Pb-17Li in a vertical loop to drive it through a DCLL blanket via buoyancy.

Referring to figure 5.1, a small percentage of helium is bled from a Brayton cycle, at a pressure just above that of the breeder in order to minimize the loss of energy in the nozzle, through which helium enters the loop. Helium flow through the nozzle is assumed to be isentropic. At nozzle exit helium mixes directly with the breeder, where it is assumed that the phases reach thermal equilibrium over the mixing length with negligible pressure loss. The two-phase flow rises vertically through the diverging MHD duct, where the mixture enthalpy is converted to electrical energy.

The mixture continues to rise isothermally in the constant cross-sectional upcomer to the separator, where the phases are physically separated under atmospheric pressure and the baffle acts to prevent any helium bubbles entering the downcomer. Helium is rejected from the loop and undergoes multi-stage compression with inter-cooling before reintegration into a Brayton cycle. The liquid metal breeder enters the downcomer and must return to the blanket at the pressure and temperature specified by the DCLL blanket design. The return temperature is controlled by three indirect heat exchange processes: IHX2, IHX4 and IHX6, in the downcomer, which reject heat to a Brayton cycle, whilst the correct pressure is accomplished through the combination of static head, through the height of the downcomer, and dynamic head, provided by the buoyancy due to the density differential between the two-phase upcomer and single-phase downcomer. Any MHD, frictional or inertial pressure losses in the blanket must be accounted for when choosing the combination of static and dynamic head, i.e., if the height of the downcomer is insufficient, the static head will be too low and must be compensated for by a larger dynamic head, brought about through a higher mass flow of helium.

Once the liquid metal returns to the DCLL blanket the loop is complete. All flow in the loop is assumed to be adiabatic, with exception of the downcomer IHX processes, the blanket, nozzle entry and helium exit.

The MHD generator can generate small amounts of electrical power to supplement the power output provided by the gas turbines and steam turbines, which increases the gross electrical power output of the fusion plant. Deducting from this the power requirement for the various plant systems gives the plant net electrical power. The requirement for the various plant systems is now reduced because the liquid metal breeder is circulated without the need for an electric pump. A small increase in overall plant efficiency, the ratio of the plant net electrical power to the fusion power, can therefore be achieved.

For ease of notation and calculation, numerical subscripts are used to denote the state points for each two-phase section of the loop. The subscripts that have been adopted are due to the numbering convention for the Brayton cycle, which can be observed in figures 5.2, 5.3 and 5.4. Since the liquid metal state points in the downcomer are not shown in the Brayton cycle figures, none will be adopted here. All physical properties of the gas and liquid phases in the two-phase sections are either calculated or taken from the literature.

5.2 PPCS-C Power Cycle

The existing power cycle configuration for PPCS model C comprises four external CICICBTX Brayton cycles [Norajitra et al., 2003]. The layout for a single Brayton cycle is shown in figure 5.2 and generates 424 MW_e. The combined power output of the four cycles equates to 1696 MW_e [Norajitra et al., 2003]. Heat is received from four tokamak zones, summarised below in table 5.1: blanket helium (IHX1), divertor bulk (IHX2), liquid metal breeder (IHX3) and divertor target (IHX4). Recuperation (IHX5) and inter-cooling is used, but no reheat is present. Heat is rejected via IHX6 to cooling water.

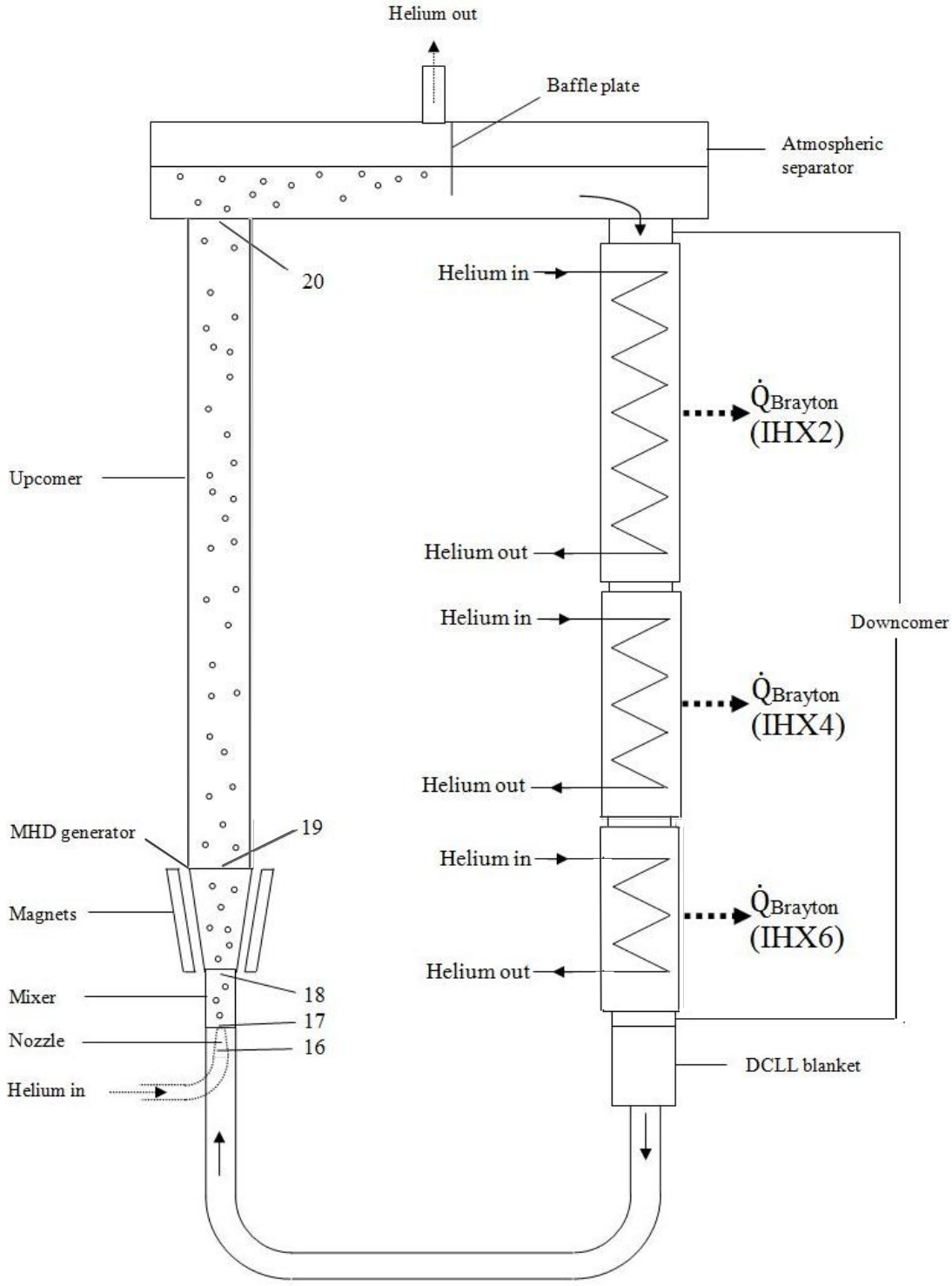

Figure 5.1 Schematic of vertical loop showing individual components, thermodynamic state points and indirect heat exchange (IHX) processes

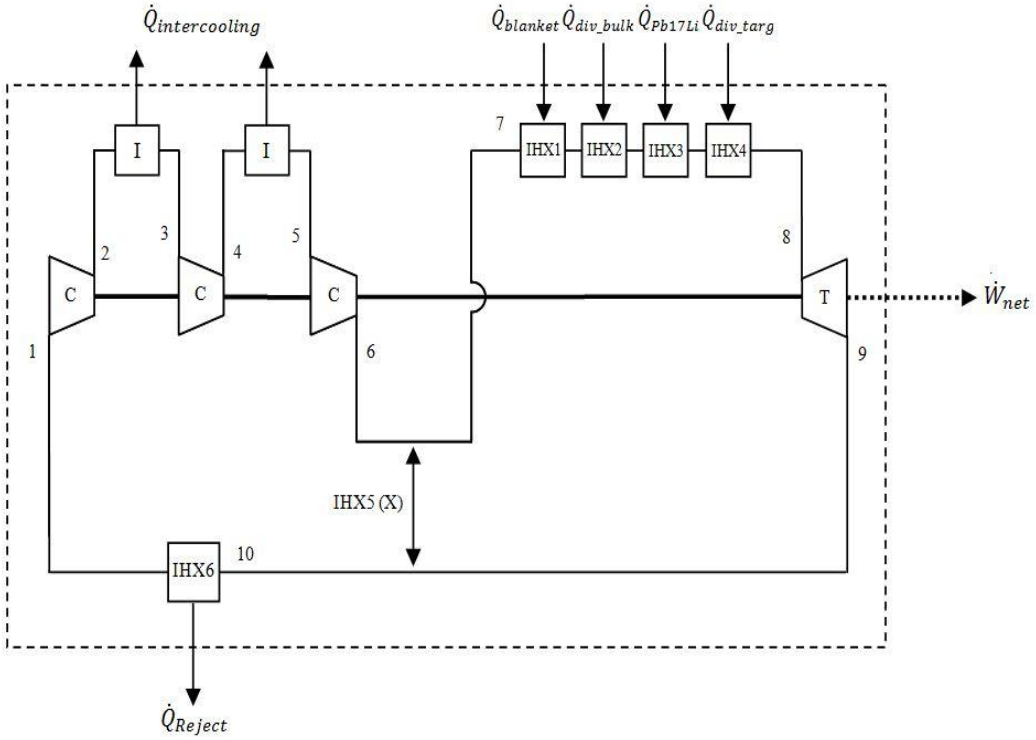

Figure 5.2 Brayton cycle layout of DCLL concept, reproduced from Norajitra et al. [2003]

Helium, with a mass flow rate of 466 kg/s, enters the first compressor at state point 1 at 307 K and 3.4 MPa and leaves at state point 2 at 381 K and 5.63 MPa. An inter-cooler is used to return the helium to 307 K at state point 3, but a pressure loss of 0.03 MPa within the inter-cooler reduces the helium pressure to 5.6 MPa. A second compression stage raises the helium pressure from 5.6 MPa to 9.25 MPa at state point 4, before a second inter-cooler returns the helium to 307 K at state point 5 with the same 0.03 MPa loss in pressure. The final compression stage raises the helium from 9.22 MPa to 15.24 MPa at state point 6. Regeneration at state point 7 raises the helium temperature to 560 K, but pressure losses in the regenerator reduce the pressure to 15.18 MPa. IHX processes 1 to 4 reject a total of 3991 MW_t into the four Brayton cycles. This raises the helium to a temperature of 973 K at state point 8. The total pressure loss through IHX1 to IHX4 is 0.18 MPa. At state point 9 the helium enters the gas turbine at 973 K and 15 MPa and exits at state point 10 where the

helium temperature and pressure is 570 K and 3.52 MPa, respectively. This delivers approximately 976 MW of shaft power, of which 541 MW is used to drive the compressors. At state point 11, after the regenerator, the helium is at 391 K and 3.45 MPa. Just over 203 MW_t is rejected by IHX6, thus returning the helium to state point 1. A bottoming cycle does not feature in this configuration because the temperature of the helium at state point 10 is too low.

Tokamak zone	**T in/out (°C)**	**Pressure (MPa)**	**ṁ (kg/s)**	**Power (MW_t)**
Blanket helium	300/480	8	1528	1432
Pb-17Li breeder	480/700	2	46053	1976
Divertor bulk	480/615	10	473	335
Divertor target	700/800	10	477	248

Table 5.1 Model-C coolant parameters [Norajitra et al., 2003]

The T-s diagram for the cycle is shown in figure 5.3. The cycle efficiency is found through the ratio of the net power output of the four cycles, 1696 MW_e, to the heat supplied, 3991 MW_t. This yields a cycle efficiency of 42.5%. The overall plant efficiency is given as 43.4% [Norajitra et al., 2003] and is found by subtracting the power requirements of the plant, 216 MW_e, from the net power output and dividing the result by the fusion power, 3410 MW_t. Due to the more advanced nature of PPCS-C, values for the isentropic efficiencies of the compressors and turbines were extrapolated beyond the state-of-the-art to 92% and 94%, respectively. An electromechanical generator conversion efficiency of 97.5% was also assumed [Norajitra et al., 2003].

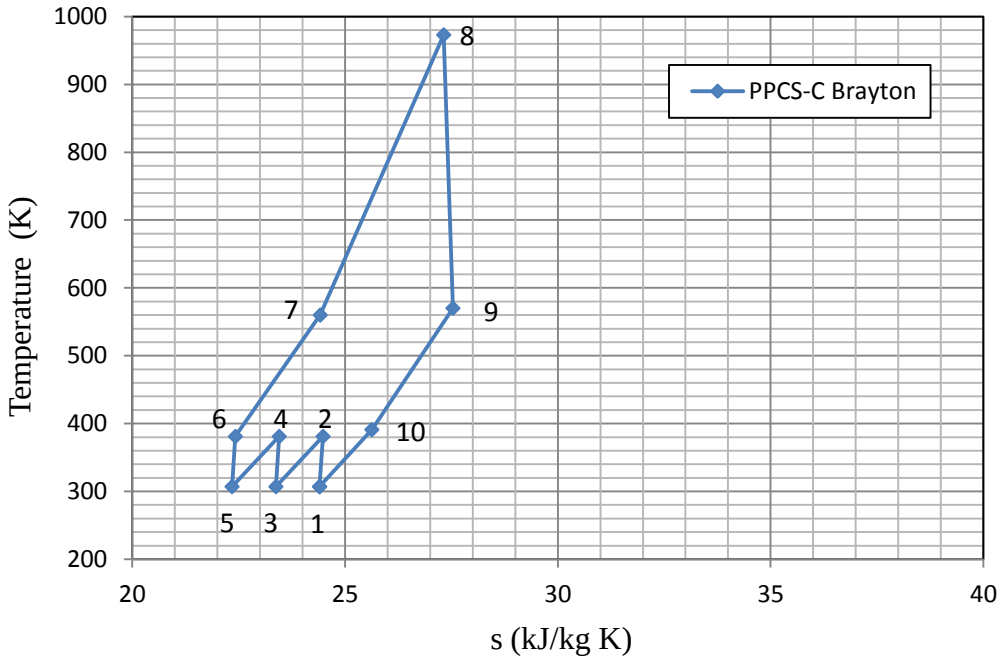

Figure 5.3 T-s diagram of PPCS-C Brayton cycle with state points

5.3 Outline of Proposed Power Cycle

A proposal for an alternative power cycle configuration for a fusion plant operating under PPCS-C parameters is shown in figure 5.4, where the helium state points are included. Similarly to the existing PPCS-C power cycle, the proposed power cycle uses multi-stage compression with inter-coolers, but there are three distinct differences.

The first distinction is that the proposed power cycle can be termed a ‘direct’ cycle because the working fluid passes through the blanket and is subsequently expanded in a gas turbine. This is in contrast to the PPCS-C power cycle where the working fluid is external to the blanket. The primary advantage of an external, or secondary, power cycle is that the top cycle pressure is not constrained by the blanket pressure, but a direct cycle associated with the DCLL design is limited by the specified helium pressure of 8 MPa.

An external cycle also removes the issue of tritium contamination on turbine blades, though this may be only a minor advantage as the effect upon turbo-machinery is not

clear. The aforementioned pressure restriction can be overcome, however, by compressing the helium above 8 MPa and subsequently using a gas turbine to expand down to the required helium pressure prior to blanket entry at state point 9.

The second distinction is that there is a two-phase MHD topping cycle. This is made possible by using a higher mass flow of helium than is required by the DCLL blanket. Consider some mass flow of helium greater than 1528 kg/s entering the first compressor at state point 1. At state point 9 the required 1528 kg/s helium mass flow is diverted to the blanket, but the remaining helium can be further expanded in the gas turbine to state point 16, and subsequently used in a two-phase topping cycle between state points 17 and 26. This excess helium, or 'bleed' helium, introduces buoyancy into the vertical loop, and, as already described, allows the liquid metal breeder to be circulated through the DCLL blanket, thus saving 6.3 MW_e. The bled helium then undergoes multi-stage compression with inter-cooling before reintegration via direct mixing at state point 13. The inclusion of the two-phase MHD topping cycle is justified by the amount of electrical power generated via the two-phase MHD generator. This should offset the extra compressor power necessary to compress a higher mass flow of helium and the compressor power required to recompress the bleed helium before reintegration at state point 13.

The third distinction is the inclusion of three bottoming Rankine cycles, which will use the heat rejected via IHX8 and the main inter-coolers in the Brayton cycle to generate more electrical power and further increase the overall plant efficiency.

The proposed power cycle uses sixteen separate IHX processes, eight more than the existing PPCS-C power cycle. This includes the four inter-coolers in the Brayton cycle and the three condensers in each of the bottoming Rankine cycles. The blanket is also included because whilst the total pressure drop is the same, 0.12 MPa [Norajitra et al., 2003], for both concepts, pressure losses for all IHX processes are neglected in the calculations for the proposed power cycle.

Similarly to the PPCS-C power cycle, the proposal uses both an exhaust gas heat exchanger, to simultaneously lower the mean temperature of heat rejection and reception, and inter-cooling, to further lower the mean temperature of heat reception.

However, the proposal also includes a reheat process between state points 9 and 12, which further raises the mean temperature of heat reception and increases cycle efficiency. Thermal power transferred from the divertor bulk zone (IHX1) and the divertor target zone (IHX3) is fixed by the PPCS-C plant parameters, but the thermal power transferred from the Pb-17Li breeder via IHX2, IHX4 and IHX6 is not as strictly bound. Referring back to figure 5.1, the reader can comprehend that the temperature of the liquid metal entering the downcomer determines the total amount of heat that must be rejected so that the liquid metal can return to the DCLL blanket at the correct temperature. Since the temperature of the liquid metal in the two-phase section drops very little, the liquid metal temperature at downcomer entry is high.

Several IHX processes can be used to transfer heat to three areas of the proposed power cycle: IHX2 and IHX4 are used to raise the inlet temperature of the main gas turbine and reheat turbine, respectively, whilst IHX6 raises the helium temperature prior to regeneration (IHX7) so that a greater amount of heat can be transferred to state point 7.

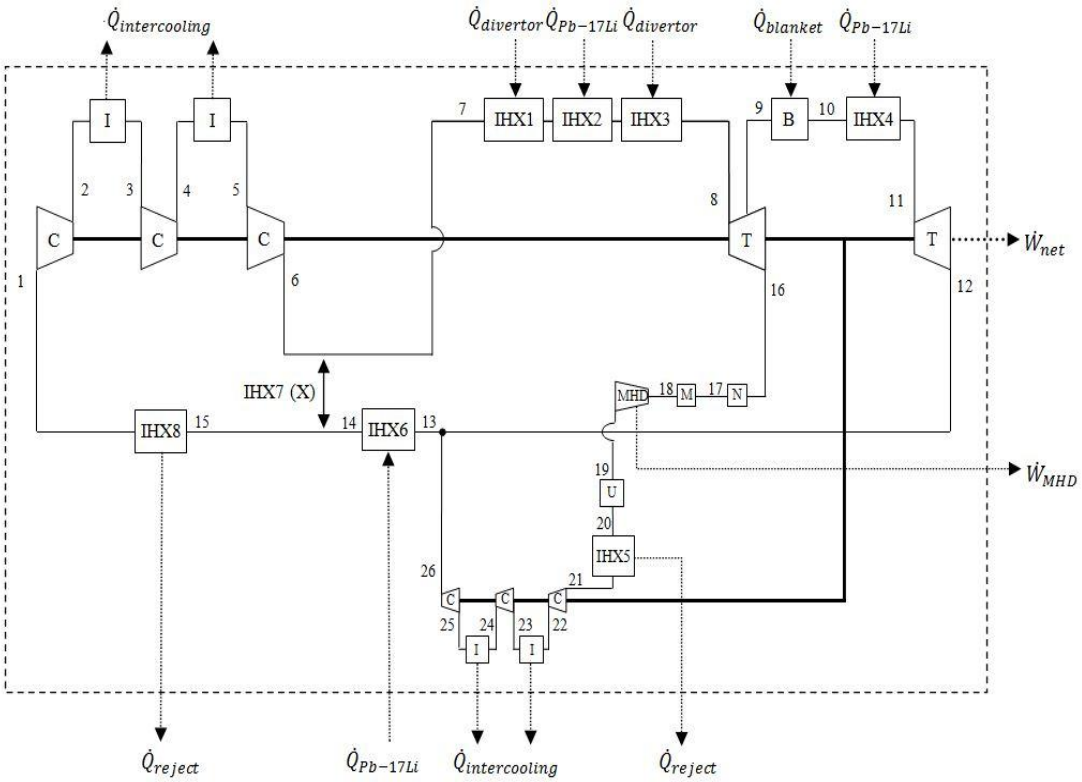

Figure 5.4 Schematic of proposed power cycle, without bottoming Rankine cycles

After regeneration heat must be rejected via IHX8 to return the helium to state point 1. The heat rejected via IHX8, and the main inter-coolers, is received by three bottoming Rankine cycles (see subsection 5.4.7) operating with water, which further improves cycle efficiency. The temperature of the helium leaving the separator, at state point 20, will be high and therefore must be cooled via IHX5 before undergoing multi-stage compression, with inter-cooling, between state points 21 and 26. In the current proposal the heat rejected from IHX5 and the bleed inter-coolers is not received by the bottoming Rankine cycles.

For the proposed power cycle to be viable there will be a regime in which the overall cycle pressure ratio must operate. The values of T_9 and P_9 must be matched precisely to the specifications of the DCLL blanket, whilst others must either be fixed or chosen so that some optimisation can be achieved. Furthermore, a range of helium bleed fractions must be determined so that the inclusion of the two-phase loop can be justified. To do this, however, the equations governing the entire power cycle must first be introduced.

5.4 Governing Equations

For each component comprising the vertical loop, where calculations are necessary in order to predict the performance in that area, the equations and iterative procedures will be outlined below. The numerical subscripts introduced in section 5.1 are further augmented with the subscripts g and l, which denote the gas and liquid phases, respectively. Despite knowing the composition of the gas and liquid phases for the proposed power, the subscripts g and l are used to serve as a reminder that the following equations are applicable to a range of fluids. The equations governing the Brayton cycle are then given, including those for all IHX processes and turbo-machinery, followed by empirical relations for determining some of the thermo-physical properties of Pb-17Li.

5.4.1 Nozzle

A contraction angle below ten degrees over the length of the converging nozzle is assumed so that the following isentropic relations hold. Given a nozzle inlet temperature T_{16}, inlet pressure P_{16} and inlet velocity u_{16} the stagnation temperature, T_0, is given by

$$T_0 = T_{16} + \frac{u_{16}^2}{2c_{pg}} \tag{5.1}$$

whilst the stagnation pressure, P_0, is

$$P_0 = P_{16}\left(\frac{T_0}{T_{16}}\right)^{\frac{\gamma}{\gamma-1}} \tag{5.2}$$

The nozzle outlet pressure, P_{17}, is equal to the liquid metal pressure at nozzle outlet and therefore design specific. The Mach number M_t at the throat of the nozzle is calculated by

$$M_t = \sqrt{\frac{\left(\frac{P_0}{P_{17}}\right)^{\frac{\gamma-1}{\gamma}} - 1}{\frac{\gamma-1}{2}}} \tag{5.3}$$

The nozzle outlet temperature T_{17g} is given by

$$T_{17g} = T_{16}\left(\frac{P_{17}}{P_{16}}\right)^{\frac{\gamma-1}{\gamma}} \tag{5.4}$$

and the nozzle exit velocity u_{17g} is given by

$$u_{17g} = M_t \sqrt{\gamma R_s T_{17g}}$$

(5.5)

where R_S is the specific gas constant. The mass flow of helium entering the loop is controlled through the choice of bleed fraction. The nozzle outlet area is given by

$$A_{17g} = \frac{\dot{m}_g}{P_0 M_t \left(\sqrt{\frac{\gamma}{RT_0}}\right)\left(\left(1 + \frac{\gamma - 1}{2} M_t^2\right)^{\frac{\gamma+1}{2(1-\gamma)}}\right)}$$

(5.6)

The outlet density is given by the ideal gas law

$$\rho_{17g} = \frac{P_{17g}}{R_S T_{17g}}$$

(5.7)

The total fluid thrust, F_T, is given by

$$F_T = \left(\left(P_{17g} + \rho_{17g} u_{17g}^2\right) A_{17g}\right) + \left(\left(P_{17} + \rho_{17l} u_{17l}^2\right) A_{17l}\right)$$

(5.8)

5.4.2 Mixer

The parameters of interest are those that impact the performance of the MHD generator, namely both the void fraction and liquid metal velocity at MHD inlet. The enthalpy drop over the MHD generator, for which both the mixture temperature and pressure at MHD inlet are required, is necessary to determine the conversion efficiency of the MHD generator. Furthermore, knowledge of the mixture temperature is important to the application of the proposed power cycle. The mixer length is only required to determine the two-phase pressure drop and is not included

in this section. Instead, a mixer length can be chosen and the pressure drop found using equation (4.7).

The temperature at mixer exit can be determined by assuming thermal equilibrium and constitutes a direct contact heat exchange, DHX, process

$$T_{18} = \frac{c_{pg}\dot{m}_g T_{17g} + c_l \dot{m}_l T_{17l}}{c_{pg}\dot{m}_g + c_l \dot{m}_l}$$

(5.9)

By assuming a fixed diameter, D_{17}, continuity can be used to determine the area of flow occupied by liquid metal, A_{17l}, through knowledge of the liquid metal mass flow rate. This can be added to (5.6) to give the total flow area, A_{18}. The area of flow occupied by helium, A_{18g}, can found through an iterative process. The first iteration step involves assuming ρ_{18g} is equal to ρ_{17g}. The thermo-physical properties of both phases, before entering the mixer, are used in the CISE [Premoli et al., 1970] model to give S_{17}. The slip ratio in the mixer, S_{18}, is assumed equal to S_{17}. Equation (5.10) is made to balance by altering A_{18g}. This provides a new value of ρ_{18g} which is substituted into the CISE model to give a revised S_{18}. This iterative process is repeated until there is no further change in (5.10). Once this occurs, convergence has been reached. The values obtained, including the cross-sectional void fraction α_{18}, and phase velocities, are taken to describe the two-phase flow conditions at mixer exit.

$$\frac{U_{18g}}{S_{18}} = \frac{\dot{m}_g}{\rho_{18g} A_{18g} S_{18}} = \frac{\dot{m}_l}{\rho_{18l}(A_{18} - A_{18l})} = u_{18l}$$

(5.10)

By rearranging (5.8) an estimate for P_{18} can be found

$$P_{18} = \left(\frac{F_T}{A_{18}}\right) - \left(\rho_{18g} u_{18g}^2 \left(\frac{A_{18g}}{A_{18}}\right)\right) - \left(\rho_{18l} u_{18l}^2 \left(1 - \left(\frac{A_{18g}}{A_{18}}\right)\right)\right)$$

(5.11)

5.4.3 MHD Generator

Liquid metals tend to have small β-values (see chapter 3) and lead to a reduced electrical power output for some types of linear MHD generator. This makes a constant-velocity segmented-electrode MHD generator a suitable choice for a two-phase topping cycle, despite the increased complexity associated with its load circuitry. The void fraction at MHD inlet, α_{18}, allows the mixture conductivity, σ_m, to be calculated by using the empirical relation of Petrick et al. [1978], suitable for larger void fractions, given by equation (4.40)

$$\sigma_m = \frac{\sigma_l(1-\alpha_{18})^2}{1+\alpha_{18}}$$

The power output of the two-phase MHD generator is given by equation (4.37) and the pressure drop through the MHD generator by (4.42)

$$\dot{W}_{MHD} = \sigma_m u_{18l}^2 B^2 A_{18} L_{MHD} \delta(1-\delta)$$

$$\Delta P_{MHD} = \sigma_m u_{18l} B^2 L_{MHD} 1-\delta$$

where the two-phase pressure gradient has been neglected since it is small in comparison with the MHD pressure gradient. To determine the enthalpy drop through the MHD duct the temperature at MHD outlet, T_{19}, must be determined via (4.46)

$$T_{19} = T_{18}\left(\left(\frac{P_{19}}{P_{18}}\right)^{\frac{(\delta(\Gamma-1))}{\Gamma}}\right)$$

The MHD duct is designed to expand from A_{18} to area A_{19} thus maintaining a constant liquid phase velocity. Assuming this expansion angle is below 10 degrees, the isentropic relation given in (4.47) can apply

$$A_{19} = A_{18}\left(\left(\frac{P_{18}}{P_{19}}\right)^{\frac{(\delta+(\Gamma(1-\delta)))}{\Gamma}}\right)$$

where the two-phase adiabatic index, Γ, is given by (4.45)

$$\Gamma = \frac{c_{pm}}{c_{vm}} = \frac{\left(xc_{pg}\right) + \left((1-x)c_l\right)}{\left(xc_{vg}\right) + \left((1-x)c_l\right)}$$

With knowledge of the pressure and temperature of the helium at MHD exit its density can be estimated. Substituting this into the CISE model gives both the cross-sectional void fraction, α_{19}, and slip ratio, S_{19}, at MHD exit.

5.4.4 Upcomer

This vertically aligned section has a constant cross-section along its height. The flow is still assumed adiabatic. The helium expands and cools as it reaches the upcomer exit, but due to the relatively high thermal capacity of the breeder it is assumed no temperature drop occurs in this section.

Since the separator is atmospheric the pressure at upcomer exit, P_{20}, is known. This means that the helium density can be calculated. By substituting the helium density into the CISE model both the slip ratio, S_{20}, and cross-sectional void fraction, α_{20}, can be found at upcomer exit.

5.4.5 Downcomer

The height of the downcomer provides hydrostatic head, which is combined with the dynamic head, caused by the density differential between the two-phase sections and downcomer, to allow the liquid metal to circulate and return to the DCLL blanket.

MHD and frictional pressure drops in the blanket vary from module to module: there is a higher MHD pressure loss for inboard modules, those that are located closer to the central solenoid. There are also MHD and frictional losses in the loop to consider. All pressure losses must be overcome if liquid metal is to be circulated via buoyancy.

Equation (5.12) gives the resulting dynamic pressure after all other pressure losses are taken into consideration

$$0 = \left(\bar{\rho}_l - \bar{\rho}_{tp}\right) g h_{tp} - \Delta P_{blanket} - \Delta P_{MHD} - \Delta P_{tp} - \Delta P_{flo}$$

(5.12)

where $\bar{\rho}_{tp}$ denotes the mixture density averaged over the total height of the two-phase sections, which is equal to the downcomer height. The required downcomer height can be found via

$$h_{downcomer} = \frac{\left(P_{blanket\_in} - P_{separator}\right)}{\bar{\rho}_l g} - h_{dynamic}$$

(5.13)

If $h_{dynamic}$ is negligible, the height of the downcomer will provide almost the entire head to overcome the blanket pressure losses. An argument for allowing the downcomer height to provide the total head can be made on the basis of safety: should some failure cause any loss of dynamic head, the instantaneous volume of liquid metal residing in the downcomer would keep the breeder flowing through the blanket for a short time. This could prevent overheating in the blanket and allow time for the reactor to be shut down.

5.4.6 Brayton Cycle

The isentropic compressor outlet temperatures, T_{2s}, T_{4s} and T_{6s} can be found from a chosen inlet temperature T_1, where it is assumed that inter-cooling returns the helium to the compressor inlet temperature so that T_3 and T_5 are equal to T_1

$$T_{2s,4s,6s} = T_{1,3,5}\left(r_{pi}^{\frac{\gamma-1}{\gamma}}\right)$$

(5.14)

The optimum pressure ratio, r_{pi}, per stage between inter-coolers is given in terms of the root, n, of the number of compressors used in the multi-stage compression process and the overall cycle pressure ratio, r_p

$$\sqrt[n]{r_p}$$

(5.15)

Taking into account the isentropic efficiency of the compressors the actual outlet temperatures T_2, T_4 and T_6 can be obtained through

$$T_{2,4,6} = \left(\frac{T_{2s,4s,6s} - T_{1,3,5}}{\eta_{C\_isen}}\right) + T_{1,3,5}$$

(5.16)

The power input to the compressors is given by

$$\dot{Q}_C = \left(C_{main}\left(T_{2,4,6} - T_{1,3,5}\right)\right) n$$

(5.17)

where n is the number of compressors and C_{main} is the heat capacity rate, given by

$$C_{main} = \dot{m}_{main\_helium} * c_{p\_main\_helium}$$

(5.18)

The heat rejected by the inter-coolers is given by

$$\dot{Q}_{inter-cooler} = C_{main}\left(T_{1,3,5} - T_{2,4,6}\right)$$

(5.19)

Helium entering the first gas turbine receives thermal power from the divertor bulk zone (IHX1), the Pb-17Li breeder (IHX2) and the divertor target zone (IHX3). If T_7 is chosen, the temperature of the helium leaving IHX1 is found by

$$T_{IHX1out} = \left(\frac{\dot{Q}_{div\_bulk}}{C_{main}}\right) + T_7 \tag{5.20}$$

The helium temperature leaving IHX2 is found through

$$T_{IHX2out} = \left(\frac{\dot{Q}_{LM\_IHX2}}{C_{main}}\right) + T_{IHX1out} \tag{5.21}$$

The third indirect heat exchange process, IHX3, which transfers thermal power from the divertor target to the helium, can then be defined

$$T_8 = T_{IHX3out} = \left(\frac{\dot{Q}_{div\_target}}{C_{main\_helium}}\right) + T_{IHX2out} \tag{5.22}$$

Though the blanket inlet temperature and pressure is fixed by the DCLL design, to determine the correct value of T_9 the isentropic temperature, T_{9s}, must be found through the following equations

$$T_{9s} = \frac{T_8}{\left(\left(\frac{P_8}{P_9}\right)^{\frac{\gamma-1}{\gamma}}\right)} \tag{5.23}$$

$$T_9 = T_8 - \left(\eta_{T\_isen}(T_8 - T_{9s})\right) \tag{5.24}$$

The mechanical power output generated by the first expansion process is given by

$$\dot{W}_1 = C_{reduced}(T_9 - T_8)$$

(5.25)

where $C_{reduced}$ is due to the lower helium mass flow flowing through this part of the circuit and described by rewriting equation (5.18) as

$$C_{reduced} = \dot{m}_{blanket\ helium} c_{p\_blanket\ helium}$$

(5.26)

For the continued expansion in the first gas turbine the outlet temperature, T_{16}, is found via

$$T_{16s} = \frac{T_9}{\left(\left(\frac{P_9}{P_{16}}\right)^{\frac{\gamma-1}{\gamma}}\right)}$$

(5.27)

$$T_{16} = T_9 - \left(\eta_{T\_isen}(T_9 - T_{16s})\right)$$

(5.28)

P_9 is prescribed by the DCLL design specifications [Norajitra et al. 2003] and P_{16} is chosen with consideration to the breeder pressure in the two-phase loop. The mechanical power output generated by this second expansion process is given by

$$\dot{W}_2 = C_{bleed}(T_{16} - T_9)$$

(5.29)

where

$$C_{bleed} = \dot{m}_{bleed\_helium} c_{p\_bleed\_helium}$$

(5.30)

The blanket outlet temperature, T_{10}, is also provided by the DCLL design specification. More thermal power from the liquid metal in the downcomer can then be transferred to the helium leaving the blanket to give T_{11}

$$T_{11} = T_{IHX4out} = \left(\frac{\dot{Q}_{LM\_IHX4}}{C_{reduced}}\right) + T_{10}$$

(5.31)

The outlet temperature, T_{12}, of the reheat turbine is found in the same way as for the first gas turbine

$$T_{12s} = \frac{T_{11}}{\left(\left(\frac{P_9}{P_{12}}\right)^{\frac{\gamma-1}{\gamma}}\right)}$$

(5.32)

$$T_{12} = T_{11} - \left(\eta_{T\_isen}(T_{11} - T_{12s})\right)$$

(5.33)

The mechanical power generated by the third, reheat, expansion process is given by

$$\dot{W}_3 = C_{reduced}(T_{12} - T_{11})$$

(5.34)

At state point 13 the bleed helium is reintegrated with the main helium. To find the mixing temperature due to this direct contact heat exchange process, IHX5 and the bleed multi-stage compression must be defined. The outlet temperature, T_{21}, after IHX5 is given by

$$T_{21} = \left(\frac{\dot{Q}_{IHX5}}{C_{bleed}}\right) + T_{20}$$

(5.35)

The isentropic outlet temperature of the bleed compressors T_{22}, T_{24} and T_{26} can be found via

$$T_{22s,24s,26s} = T_{21,23,25}\left(r_{pi\_bleed}^{\frac{\gamma-1}{\gamma}}\right)$$

(5.36)

where r_{pi_bleed} is the optimum bleed pressure ratio, per stage, between bleed inter-coolers.

Care must be taken in defining the correct pressure ratio, r_p, in (5.15). In this instance, it involves the ratio of the low cycle pressure to the separator pressure, not the ratio of the high cycle pressure to the low cycle pressure. Taking into account the isentropic efficiency of the compressors the actual outlet temperatures T_{22}, T_{24} and T_{26} are obtained through

$$T_{22,24,26} = \left(\frac{T_{22s,24s,26s} - T_{21,23,25}}{\eta_{C\_isen}}\right) + T_{21,23,25}$$

(5.37)

The heat rejected by the bleed inter-coolers is given by

$$\dot{Q}_{bleed\_inter-cooler} = C_{bleed}\left(T_{21,23,25} - T_{22,24,26}\right)$$

(5.38)

The mixing temperature at state point 13 can then be given by

$$T_{13} = \frac{c_{pg}\dot{m}_{g\_bleed}T_{26g} + c_{pg}\dot{m}_{g\_main}T_{12}}{c_{pg}\dot{m}_{g\_bleed} + c_{pg}\dot{m}_{g\_main}}$$

(5.39)

The recuperation in the Brayton cycle is an indirect heat exchange process and is denoted IHX7. The bleed helium has been re-integrated with the main cycle helium and so the temperature leaving the recuperator is given by

$$T_{14} = \left(\frac{\dot{Q}_{recuperation}}{C_{main}}\right) + T_{13}$$

(5.40)

Finally, IHX8, which rejects heat from the Brayton cycle into two of the three bottoming Rankine cycles, is given by

$$\dot{Q}_{reject} = C_{main}(T_{14} - T_1)$$

(5.41)

The net mechanical power output of the power cycle is given by

$$\dot{W}_{net} = \dot{W}_T + \dot{W}_{MHD} - \dot{W}_C$$

(5.42)

and the cycle efficiency is

$$\eta_{cycle} = \frac{\dot{W}_{net}}{\dot{Q}_{supplied}} = \frac{\dot{W}_{net}}{\dot{Q}_{blanket} + \dot{Q}_{div\_bulk} + \dot{Q}_{Pb-17Li} + \dot{Q}_{div\_target}}$$

(5.43)

5.4.7 Rankine Cycle

Three simple water-based Rankine cycles will receive heat from IHX8 and the main inter-coolers. Considering the first of the three bottoming Rankine cycles, and continuing with the subscript notation from figure 5.4, the enthalpy at turbine inlet, h_{27}, is obtained from data tables [Rogers & Mayhew, 1995] by choosing a boiler pressure, p_{boiler}, and turbine inlet temperature, T_{27}. The entropy at this point can also be denoted as s_{27} and is shown in the temperature-entropy diagram of figure 5.5. The isentropic value at turbine outlet s_{28s} is equal to s_{27}.

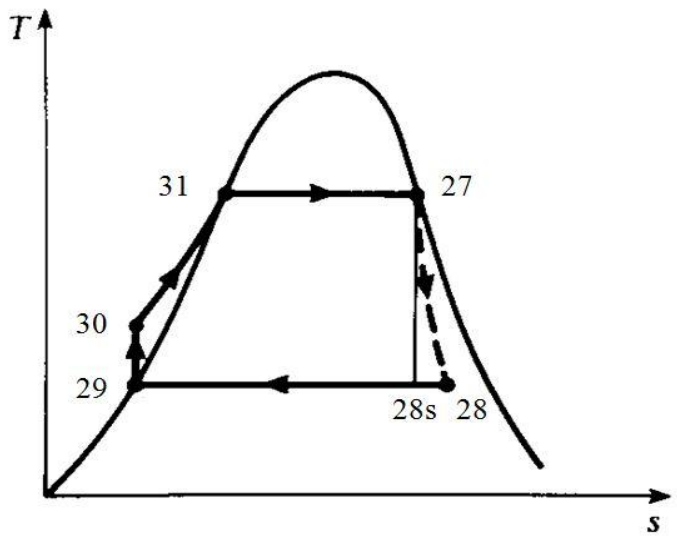

Figure 5.5 Temperature entropy diagram showing state points for the first simple Rankine cycle, reproduced from Eastop and McConkey [1993]

The dryness fraction for this state point is given by

$$x_{28s} = \frac{s_{28s} - s_{l28}}{s_{lg28}}$$

(5.44)

whilst the enthalpy is

$$h_{28s} = h_{l28} + \left(x_{28s} h_{lg28}\right)$$

(5.45)

This allows the isentropic work output of the steam turbine to be found

$$W_{Ts} = (h_{27} - h_{28s})$$

(5.46)

The actual turbine work output is given by

$$W_T = W_{Ts}\eta_{T\_isen} \tag{5.47}$$

yielding values for the actual enthalpy and dryness fraction at state point 28

$$h_{28} = h_{27} - W_T \tag{5.48}$$

$$x_{28} = \frac{h_{28} - h_{l28}}{h_{lg28}} \tag{5.49}$$

The enthalpy at state point 29, h_{29}, is found from the data tables using the saturation temperature listed for the choice of condenser pressure, $p_{condenser}$. The feed pump work, neglecting any entropy generation, can then be found

$$W_P = (h_{30} - h_{29}) \tag{5.50}$$

where h_{30} is found by using the specific density, v_f

$$h_{30} = \left(v_{f\_water}(p_{boiler} - p_{condenser})\right) + h_{29} \tag{5.51}$$

The steam mass flow can be found through an energy balance, once the values of h_{27} and h_{30} have been established. The enthalpy at state point 31, h_{31}, is found from steam tables using the wet saturated value for the given boiler pressure.

$$\dot{m}_{steam} = \frac{\dot{Q}_{supplied}}{(h_{27} - h_{30})} \tag{5.52}$$

The net power output can be calculated via

$$\dot{W}_{net\_steam} = \dot{m}_{steam}(W_T - W_P)$$

(5.53)

The Rankine cycle efficiency and CCGT efficiency can then be described, respectively

$$\eta_R = \frac{\dot{W}_{net\_steam}}{\dot{Q}_{supplied}}$$

(5.54)

$$\eta_{CCGT} = \frac{\dot{W}_{net\_total}}{\dot{Q}_{supplied}} = \frac{\dot{W}_{net\_gas} + \dot{W}_{net\_steam}}{\dot{Q}_{blanket} + \dot{Q}_{div\_bulk} + \dot{Q}_{Pb-17Li} + \dot{Q}_{div\_target}}$$

(5.55)

The state points for the remaining two bottoming Rankine cycles can be found by following the above procedure. With reference to figure 5.5 it can be seen that by continuing the subscript notation used in figure 5.4, the enthalpy at turbine inlet for the remaining two Rankine cycles will be h_{32} and h_{37}, respectively, whilst the enthalpy at turbine outlet will be h_{33} and h_{38}, respectively. The condenser pressure and boiler pressure must be chosen for the remaining Rankine cycles so that all state points can be fully defined. The heat supplied to each of the remaining Rankine cycles can be used to give the steam mass flow rate via equation (5.52). Finally, the net power outputs and cycle efficiencies can then be determined.

5.4.8 Pb-17Li Physical Properties

The following empirical relations for the density, specific heat, electrical conductivity and dynamic viscosity of Pb-17Li are given by Schulz [1991]

$$\rho_{Pb-17Li} = 10.45x10^{3}(1 - (161x10^{-6}T_{Pb-17Li})) \quad [508 - 625\ K] \tag{3.50}$$

$$c_{Pb-17Li} = 195 - 9.116x10^{-3}T_{Pb-17Li} \quad [508 - 800\ K] \tag{5.56}$$

$$\sigma_{Pb-17Li} = \frac{1x10^{9}}{10.23 + (0.00426T_{Pb-17Li})} \quad [508 - 933\ K] \tag{5.57}$$

$$\mu_{Pb-17Li} = 0.187x10^{-3}e^{(1400/T_{Pb-17Li})} \quad [521 - 900\ K] \tag{5.58}$$

whilst the surface tension for Pb-17Li is given by Feuerstein et al. [1991]

$$\gamma_{Pb-17Li} = 0.52 - 0.11x10^{-3}T_{Pb-17Li} \quad [520 - 1000\ K] \tag{5.59}$$

The above empirical relations are given with their range of validity. Since the temperature of the Pb-17Li in the two-phase MHD topping cycle falls within the range 573.15 – 973.15 K there is some uncertainty in using equations (3.50), (5.56), (5.57) and (5.58). Norajitra et al. [2003] do not use (5.56) to calculate the thermal power available in the liquid metal. Therefore, for consistency, (5.56) will not be used to calculate the specific heat of Pb-17Li when determining the performance of the proposed power cycle. Instead, a value of 195 J/kg K, consistent with Norajitra et al. [2003] will be used. The inclusion of (5.56) serves to highlight this aberration.

5.5 Proposed Power Cycle Performance

To achieve some optimisation of the proposed power cycle certain parameters must first be fixed. For all IHX processes pressure losses are neglected and the isentropic efficiencies of the compressors and turbines are assumed equal to the values give in the PPCS-C report [Norajitra et al., 2003], which are extrapolated beyond the state-of-the-art to 92% and 94%, respectively.

A value of 307 K has been chosen for T_1, which is the same as the value for T_1 in the existing PPCS-C power cycle. Assuming adequate inter-cooling T_3 and T_5 are equal to T_1. However, heat must be rejected via IHX8 to return the helium to T_1. A pinch-point of at least fifteen degrees, a value used by Norajitra et al. [2003] for their helium-water IHX processes, requires that the temperature of the cooling water entering IHX8 is 292 K. A condenser pressure of 0.0215 bar in the bottoming Rankine cycles, to which IHX8 rejects heat, is suitably low to achieve this. Any increase in water temperature after pumping can be considered negligible.

A value of 743 K for T_7 has been chosen because it is the highest temperature permissible, taking into account a ten degree pinch-point, as used by Norajitra et al. [2003] for their helium-helium IHX processes, between T_7 and the divertor bulk outlet temperature of 753 K. This also allows the highest turbine inlet temperature at T_8 to be attained using the thermal power received from IHX1, IHX2 and IHX3. A high level of regeneration also improves Brayton cycle efficiency.

The helium outlet temperature from IHX1 is easily found since both the thermal power transferred by IHX1 and the helium mass flow between state points 7 and 8 are known. Assuming a minimum pinch value of approximately ten degrees for IHX2, a value also used by Norajitra et al. [2003] for their liquid metal-helium IHX process, and the thermal power transferred from IHX2 via the downcomer, the outlet temperature from IHX2 can be found. Using the same approach as was used for IHX1, the outlet temperature from IHX3, T_8, can then be determined.

The DCLL design fixes the values at blanket entry, T_9 and P_9, and blanket outlet, T_{10} and P_{10}, but varying the overall cycle pressure ratio varies the top cycle pressure. In

this case P_{10} is equal to P_9, since helium pressure losses in the blanket have been neglected. The top cycle pressure, denoted by P_6, must therefore be chosen to ensure that the correct value for T_9 is achieved. Once the correct top cycle pressure, P_6, is chosen, then T_6 can be determined from (5.16) via (5.14). Similarly, since the cycle pressure ratio is now defined, T_2 and T_4 can also be found using the same equations. Since pressure losses in IHX processes are neglected, P_7 and P_8 are equal to P_6.

The thermal characteristics of IHX4 and IHX6 can be defined using a similar approach used for IHX2. The DCLL blanket specifications provide a value for T_{10} and a helium mass flow, thus aiding in defining IHX4 and subsequently $T_{11,}$ providing that the thermal power delivered by IHX4 is known. Before the outlet temperature of IHX6, T_{14}, can be defined, however, T_{13} must be determined. For this, the characteristics of the topping cycle must be examined.

A breeder pressure in the blanket of 2 MPa is given by Wong et al., [2008]. To minimise losses in the nozzle the helium nozzle inlet pressure, P_{16}, is chosen to be 2.1 MPa, which allows the nozzle inlet temperature, T_{16}, to be determined. The temperatures T_{17} and T_{18} follow from equations (5.4) and (5.9), respectively.

In previous topping cycle optimisations a lower upcomer exit temperature, T_{19}, was used, where all the heat in the downcomer could be rejected using only two IHX processes. It was realised, however, that if T_{19} was higher a third IHX process could be added which would supply heat to the helium before the regenerator, thus enabling more expansion to take place in the reheat turbine. A value of 961 K was chosen for $T_{19,}$ based upon trial-and-error optimisations, which allowed a suitable MHD power output to be achieved whilst allowing more output from the reheat turbine. This meant a lower T_{12} value and thus necessitated IHX6 to aid the regeneration process.

Assuming a value of 300 K for T_{21}, based upon trial-and-error optimisation, the heat rejected via IHX5 can be determined, since T_{20} is assumed equal to T_{19}. By using the governing equations for multi-stage compression, T_{13} can be determined. T_{14} is then found through knowledge of the helium mass flow, the heat delivered by IHX6 and an assumed pinch-point value for IHX6, taking a minimum pinch of ten degrees.

Since T_6, T_7, T_{13} and T_{14} can be found, the viability of the regeneration via IHX7 can be determined. Once all the state points are found, using the above procedure, the expansion processes can be defined.

To determine the bleed fraction that produces the largest MHD power output, some topping cycle parameters must be constrained. The working pressure of the two-phase sections of the topping cycle ranges between 2 MPa and atmospheric, whilst the temperature range for the two-phase sections lie between 973 K and 961 K. Once the conditions at mixer exit/MHD entry have been determined, state point 18, the maximum permissible pressure and temperature losses in the MHD duct are defined since T_{19} and P_{19} are fixed. The magnetic field strength is chosen to be 1 T since this is a field strength that can be achieved using a Halbach array available from commercial suppliers. The length of the Halbach array has been chosen to be 5 m, which may be beyond the state-of-the-art since it may not be possible to manufacture a continuous array of this length, however, it is deemed reasonable due to the relatively advanced nature of the PPCS-C model. Since state points 16 and 19 are constrained, the start and end of the two-phase sections, the MHD power output for a given bleed fraction can be calculated in isolation to the main cycle. The two-phase mixture conductivity, liquid metal velocity, magnetic field strength and MHD duct length can be found from the governing equations, leaving only the MHD generator coefficient, δ, to be determined from an iterative procedure to yield the MHD power output.

Figure 5.6 shows the performance of the MHD topping cycle for a range of bleed fractions. Bleed fractions below 14 kg/s are deemed unviable, marked in red, since they require MHD duct expansions that are prohibitively large and require upcomer diameters in excess of 20 m, whilst beyond 35 kg/s the MHD duct begins to converge and the power output is zero.

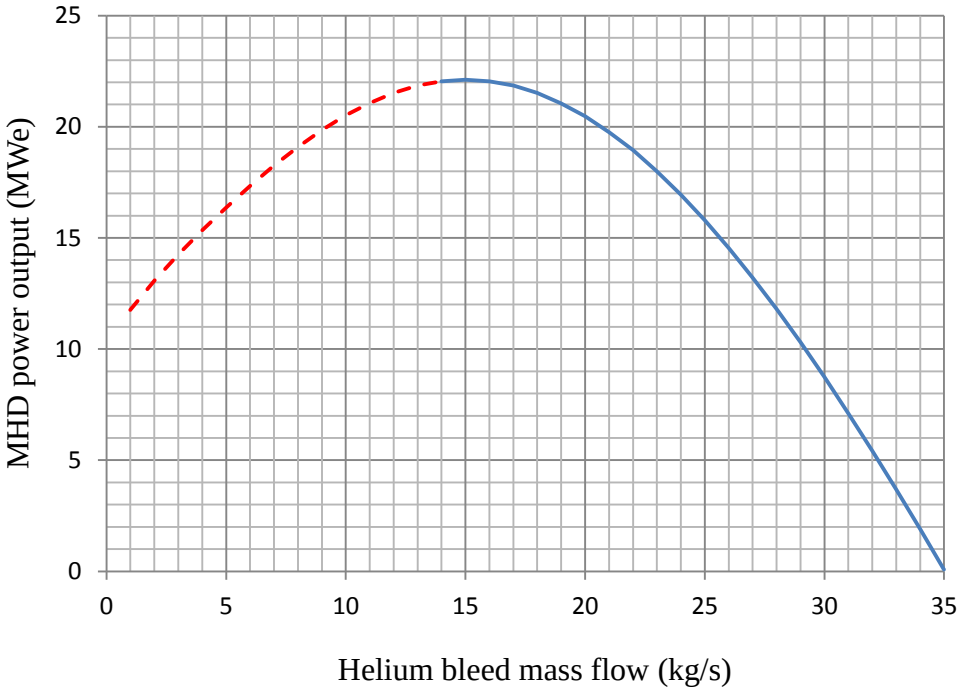

Figure 5.6 Optimum bleed fraction for maximum MHD power output using certain topping cycle parameters, where the unviable bleed fractions are shown in red (dashed).

Figure 5.7 shows the performance of the proposed power cycle without Rankine bottoming. Both the cycle efficiency and the electrical power output are inversely proportional to the bleed fraction, as perhaps is expected. However, by noting the limit imposed on the Brayton cycle by the MHD topping cycle, as shown in figure 5.6, the bleed fraction that yields the best possible performance for the Brayton cycle with MHD topping is 14 kg/s. The mass flow of helium between state points 1 and 8, and between 13 and 1, is therefore 1542 kg/s. The efficiency is then just under 42.9% and the cycle net electrical power output approximately 1710 MW_e.

The thermal characteristics of IHX8 can now be determined. With a helium inlet and outlet temperature of 403 K and 307 K, respectively, approximately 771 MW_t can be transferred via IHX8 to the bottoming Rankine cycles. Both of the main inter-coolers transfer approximately 1349 MW of thermal power, with a driving temperature of just over 391 K. Using a fifteen degree pinch point for all helium-water heat

exchangers, the steam conditions at turbine inlet can be established. A condenser pressure of 0.0215 bar and a steam turbine isentropic efficiency of 90% have been adopted for all Rankine cycles. Using an electromechanical conversion efficiency of 97.5% the electrical power output of the Rankine cycle can be determined.

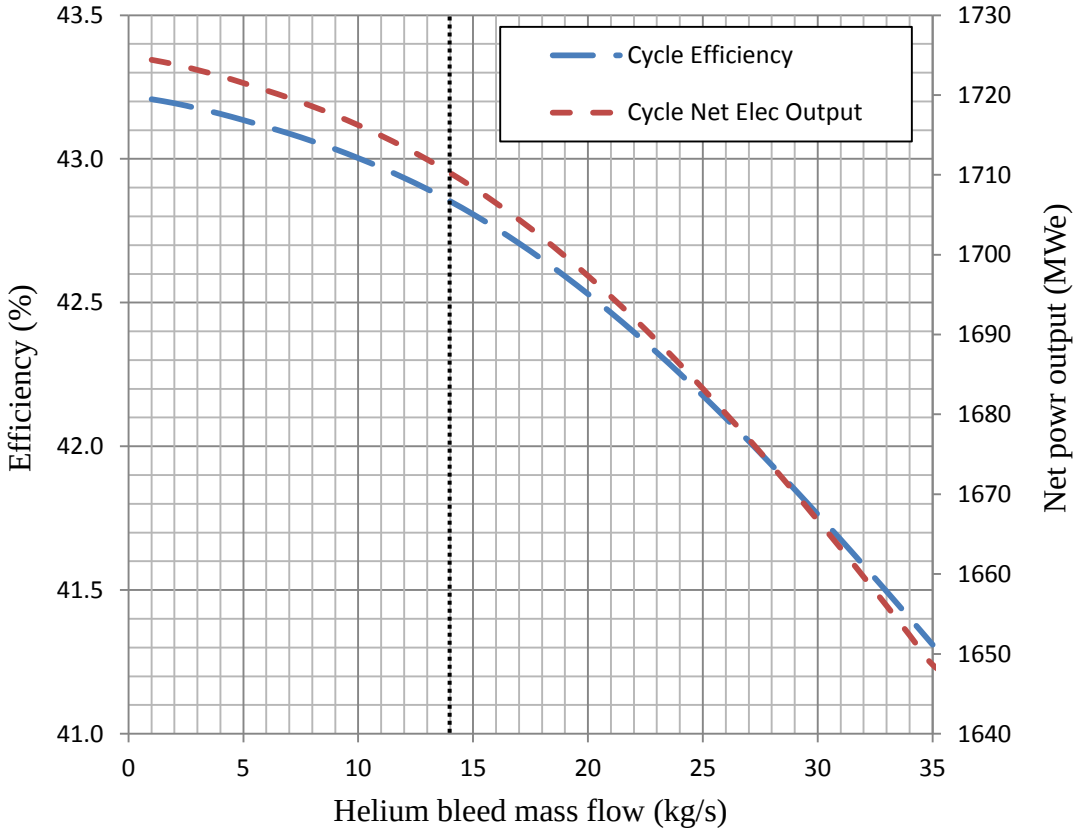

Figure 5.7 Variation of proposed power cycle performance, without Rankine cycle contribution, with increasing helium bleed fraction using a cycle pressure ratio of 5.4.

Figure 5.8 shows the arrangement of the three once-through boilers associated with the three separate low-temperature, low-pressure bottoming Rankine cycles. The inlet and outlet temperatures of the boilers are matched to the thermal characteristics of both main inter-coolers and IHX8. Figure 5.9 shows the arrangement of the three bottoming Rankine cycles.

The first cooling circuit consists of water with a mass flow rate of 1915 kg/s, which enters the first boiler at 292 K. Helium from main inter-cooler 1, MIC1, enters at 391 K and is cooled to 307 K. This raises the water temperature to 376 K, whilst helium from IHX8, at 403 K, is used to raise 273 kg/s of steam at 388 K and 1.6 bar.

Helium from IHX8 leaving the first boiler at 398 K then enters the second boiler where it is subsequently cooled to 307 K by water which enters the second boiler at 292 K with a mass flow rate of 1915 kg/s. Steam is raised at 383 K and 1.4 bar with a mass flow of 280 kg/s. The third cooling circuit uses helium from MIC2, which enters the third boiler at 391 K and exits at 307 K. The water entering the third boiler is also at 292 K and the mass flow rate is also 1915 kg/s. The helium supply from MIC2 raises 259 kg/s of steam at 376 K and 1.1 bar. A fourth cooling circuit uses water to cool IHX5 and then subsequently both bleed inter-coolers in parallel. These cooling circuits are summarised in Table 5.2, whilst table 5.3 summarises the Rankine cycle parameters.

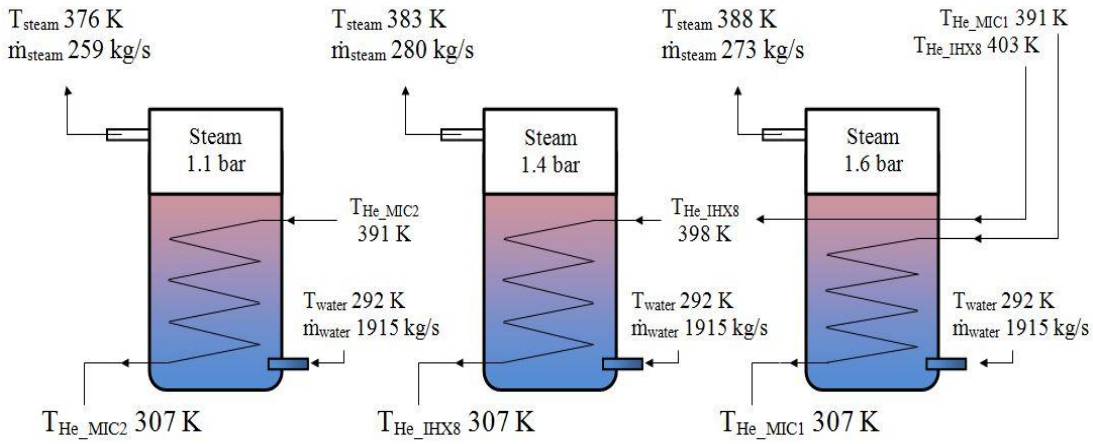

Figure 5.8 Arrangement of once-through boilers for utilising heat rejected from main inter-coolers and IHX8

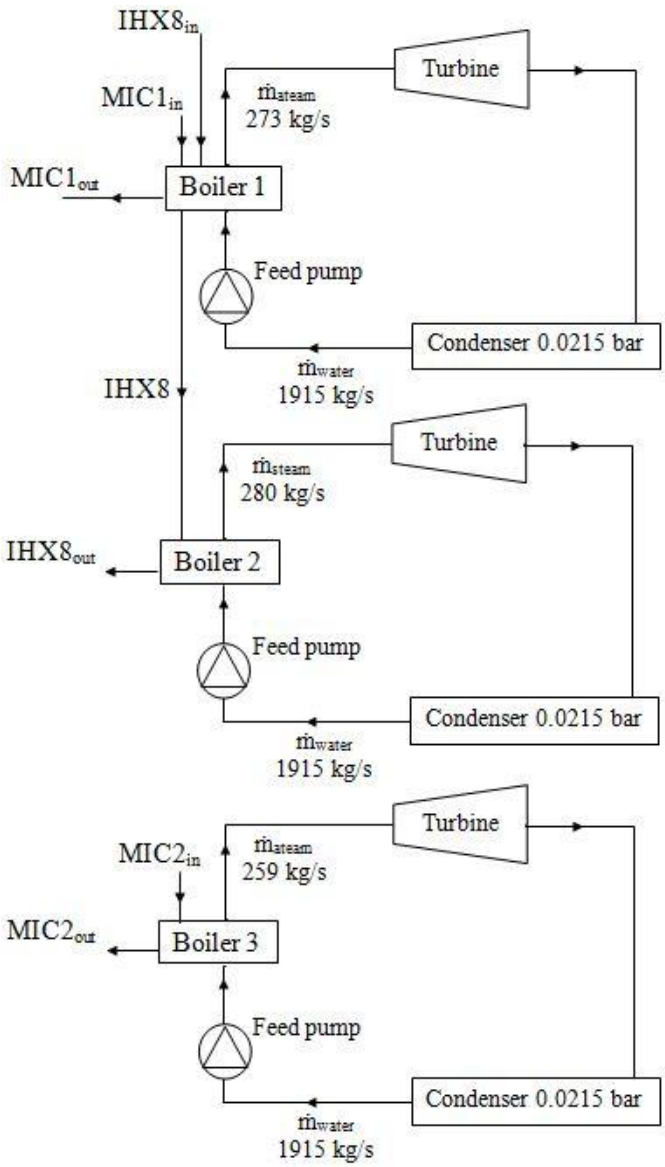

Figure 5.9 Configuration of the three low-temperature, low-pressure bottoming Rankine cycles

The circuit diagram of figure 5.9 shows the arrangement of the three Rankine cycles, which generate a total of approximately 409 MW_e, assuming an electromechanical conversion efficiency of 97.5%, with cycle efficiencies of 20%, 19.4% and 18.5%, using steam pressures of 1.6 bar, 1.4 bar and 1.1 bar, respectively. These bottoming Rankine cycles increase the gross electrical power output of the proposed cycle to just over 2119 MW_e, giving a combined cycle efficiency of 53.1%.

To determine the overall plant efficiency the net plant power electrical output must be determined. The same power requirements for the PPCS-C model, 216 MW_e, given by Norajitra et al. [2003], can be used, but the 6.3 MW_e pumping for the liquid metal breeder must be subtracted, which gives a PPCS-C plant power requirement of just under 210 MW_e. Subtracting this from the gross plant electrical power output, which is equal to 2119 MW_e, gives the net plant power output of just under 1910 MW_e. Dividing this by the fusion power, 3410 MW, yields an overall plant efficiency of 56%. This is, however, idealised since pressure losses in the IHX processes are neglected.

Cooling Circuit	**Cooling Zones**		**$\dot{m}_{water}$ (kg/s)**	**T_{water} in/out (K)**	**Power Received (MW_t)**	
1	IHX8		1915	403/398	40	
	MIC1			292/376	674	
2	IHX8			398/307	731	
3	MIC2			391/307	674	
4	IHX5		7000	283/285	48.1	
	BIC1	BIC2	3500	285/286	17.5	17.5

Table 5.2 Summary of cooling circuits

Rankine cycle	**Boiler pressure (bar)**	**T_{steam} (K)**	**Net Electrical Power (MW_e)**	**Cycle Efficiency (%)**
1	1.6	388	147	20.0
2	1.4	383	146	19.4
3	1.1	376	127	18.4

Table 5.3 Summary of Rankine cycle parameters

A T-s diagram of the proposed cycle, with a cycle pressure ratio of 5.4 and a 14 kg/s helium bleed, is given in figure 5.10. Some state points are difficult to interpret in the T-s diagram since they are close in temperature, however, referring to table 5.4, which summarises the state points for the proposed power cycle, should help to clarify figure 5.10. For greater clarity the T-s diagram for the three bottoming Rankine cycles, and parts of the Brayton cycle from which the Rankine cycles receive heat, is shown in figure 5.11. It should be noted that the Rankine cycles have been plotted so that the graph better shows from which part of the Brayton cycle they are receiving heat.

Figure 5.12 shows a T-Q diagram for IHX processes where helium is the working fluid receiving thermal power, i.e., IHX1-IHX4, IHX6 and IHX7. All IHX processes are counter-flow processes. A minimum pinch-point of ten degrees occurs during both IHX2 and IHX4, which matches the ten degree pinch-point value used by Norajitra et al. [2003] to define their liquid metal-helium IHX2 process. IHX6 has been shifted to the right in figure 5.12 to avoid it being obscured by IHX1.

Figure 5.13 provides a T-Q diagram showing how the thermal power from IHX8 and both of the main inter-coolers is deposited into the three bottoming Rankine cycles, whilst figure 5.14 shows a T-Q diagram that deals with IHX5 and the bleed inter-coolers. A minimum pinch-point of fifteen degrees has been adopted for helium-water IHX processes, which is consistent with Norajitra et al. [2003].

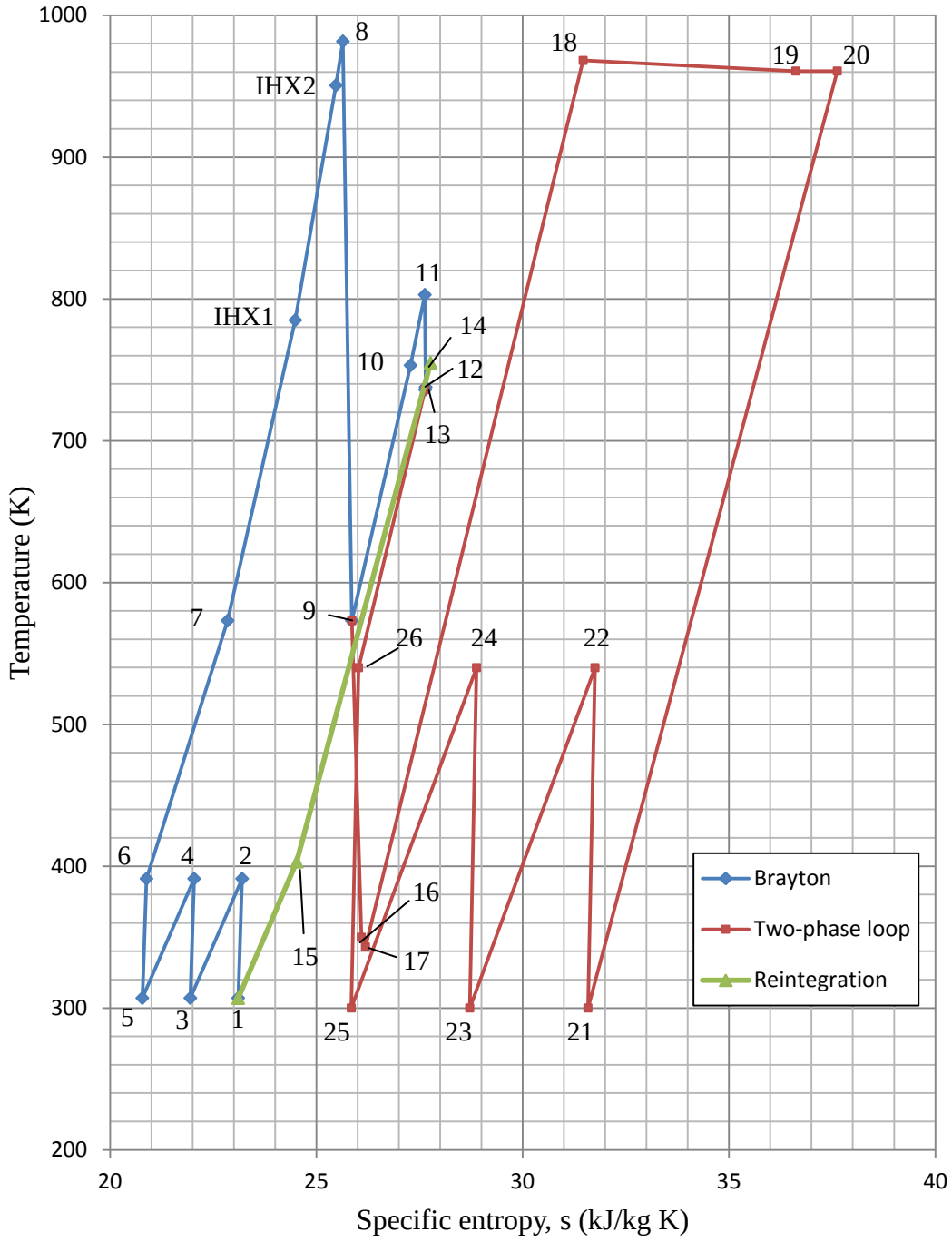

Figure 5.10 T-s diagram of proposed power cycle, including state points, not showing bottoming Rankine cycles

State point	T K	P MPa	ṁ kg/s	S kJ/kg K	State point	T K	P MPa	ṁ kg/s	s kJ/kg K
1	307	6.4	1542	23.10	21	300	0.101	14	31.58
2	391	11.2	1542	23.20	22	540	0.4	14	31.75
3	307	11.2	1542	21.94	23	300	0.4	14	28.72
4	391	19.7	1542	22.04	24	540	1.6	14	28.88
5	307	19.7	1542	20.78	25	300	1.6	14	25.84
6	391	34.5	1542	20.88	26	540	6.4	14	26.02
7	743	34.5	1542	22.84	27	388	0.16	273	7.21
IHX1	785	34.5	1542	24.49	28	292	2E-3	273	8.70
IHX2	951	34.5	1542	25.47	29	292	2E-3	273	0.28
8	982	34.5	1542	25.64	30	292	0.16	273	0.28
9	573	8	1528	25.86	31	386	0.16	273	7.20
10	753	8	1528	27.28	32	383	0.14	280	7.25
11	803	8	1528	27.63	33	292	2E-3	280	8.70
12	738	6.4	1528	27.65	34	292	2E-3	280	0.28
13	736	6.4	1542	27.64	35	292	0.14	280	0.28
14	755	6.4	1542	27.77	36	382	0.14	280	7.25
15	403	6.4	1542	24.52	37	376	0.11	259	7.33
16	350	2	14	26.09	38	292	2E-3	259	8.70
17	343	2	14	26.19	39	292	2E-3	259	0.28
18	968	2	14	31.46	40	292	0.11	259	0.28
19	961	0.16	14	36.62	41	375	0.11	259	7.33
20	961	0.101	14	37.62					

Table 5.4 Summary of state points for proposed cycle denoting temperature, pressure, mass flow and specific entropy

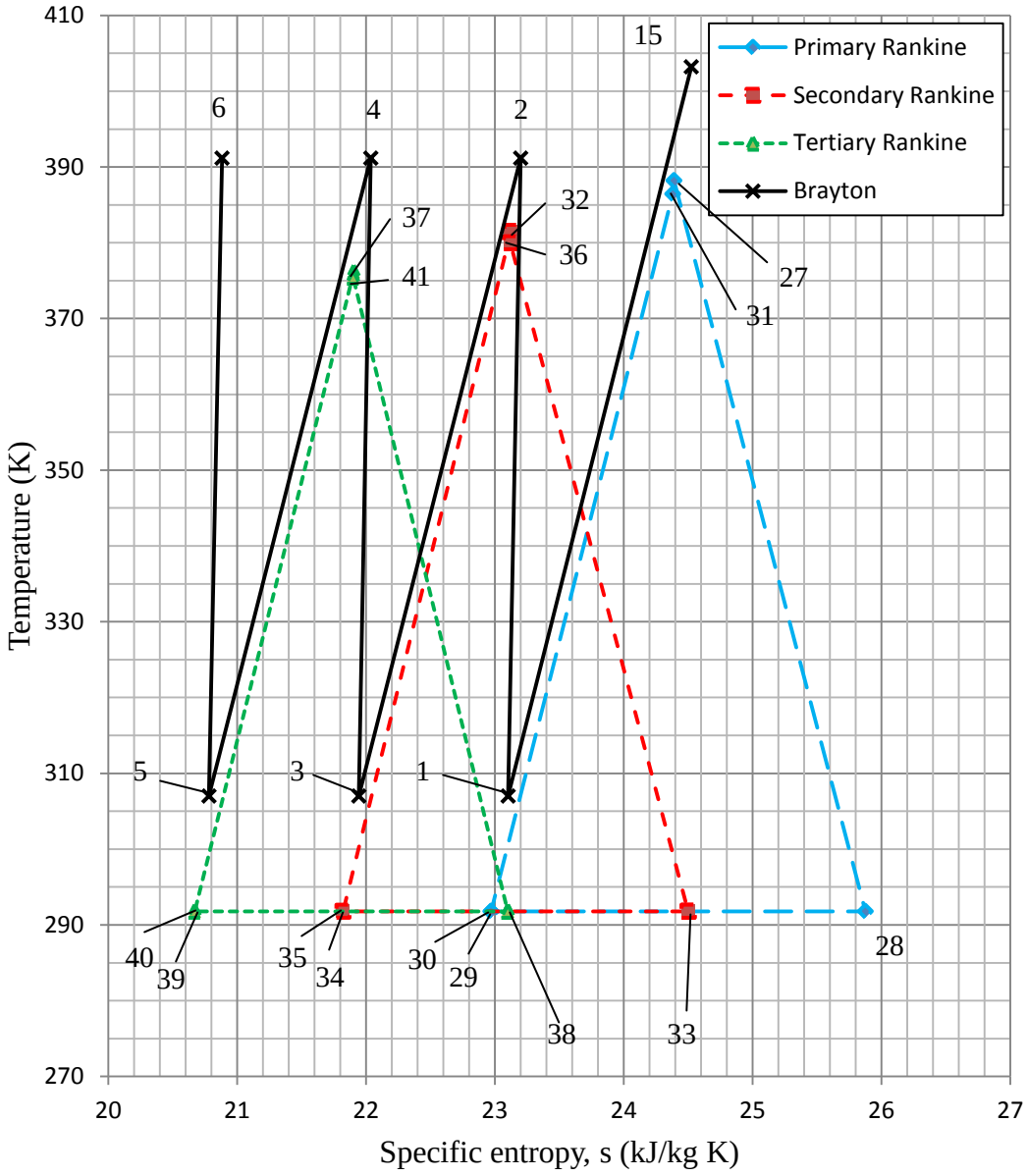

Figure 5.11 T-s diagram showing the three bottoming Rankine cycles

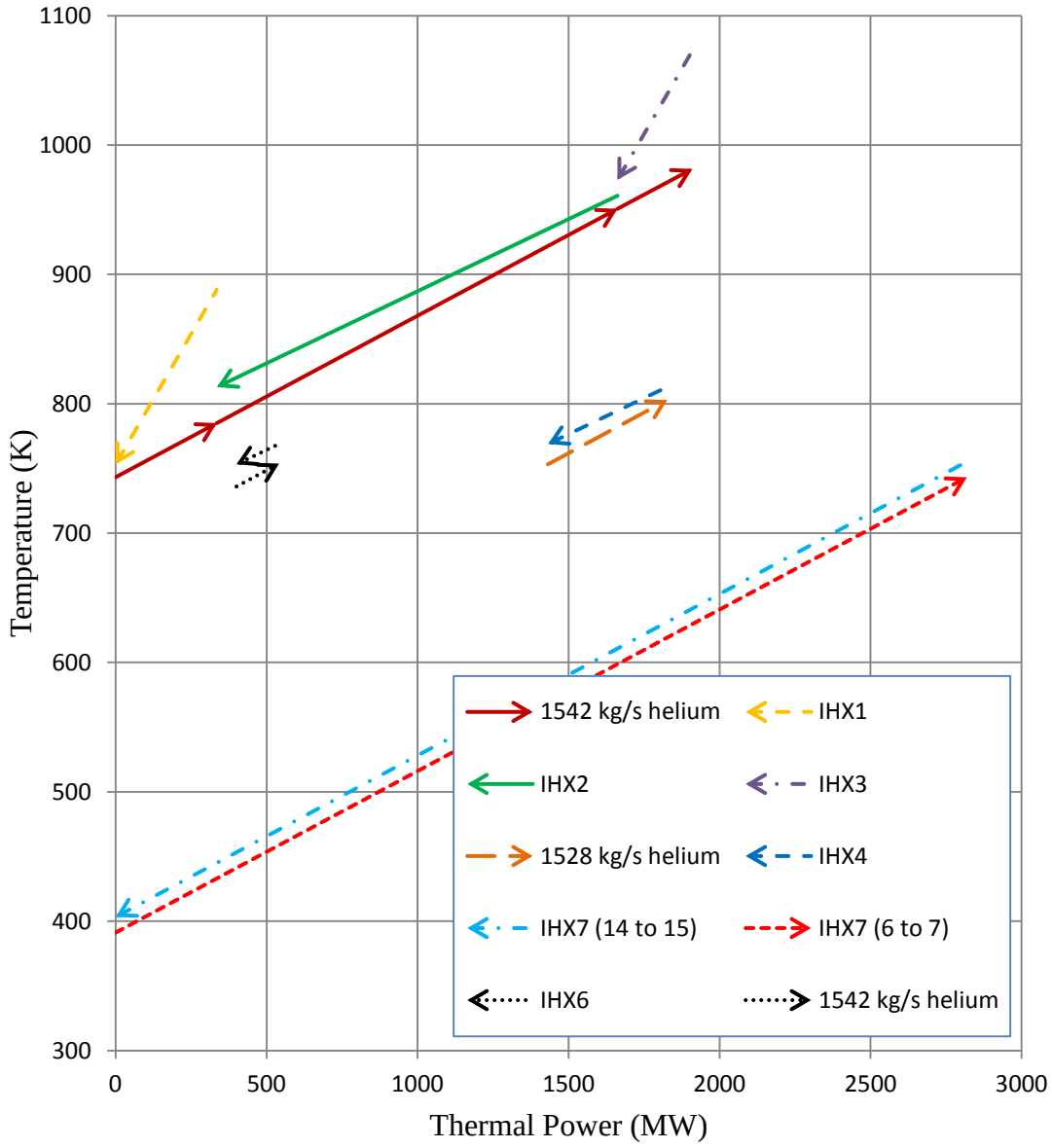

Figure 5.12 T-Q diagram showing IHX1, IHX2, IHX3, IHX4, IHX6 and IHX7 counter-flow processes

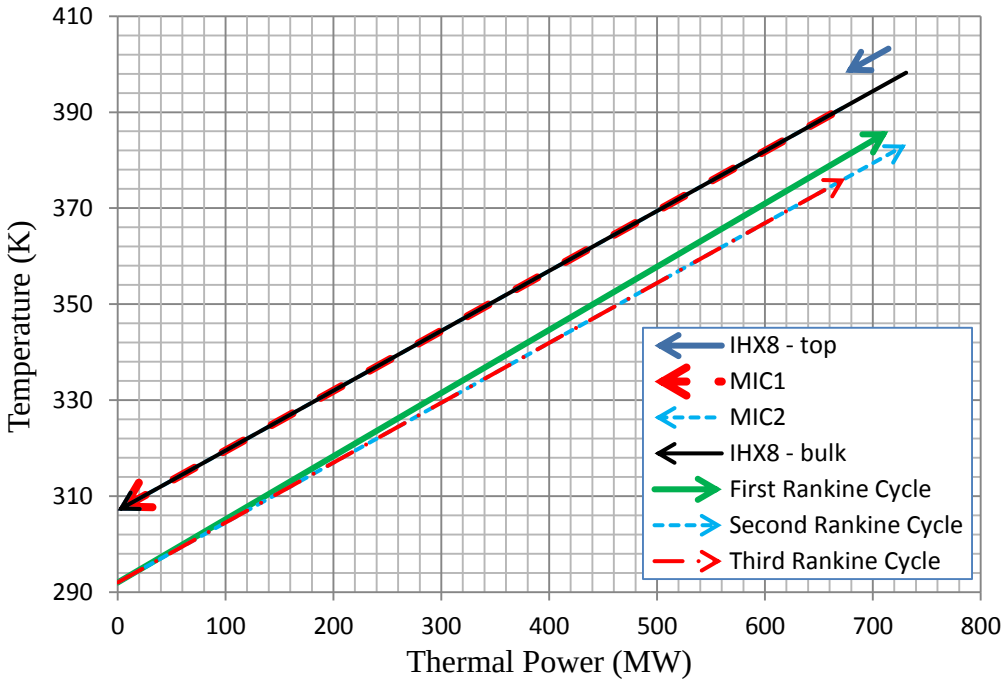

Figure 5.13 T-Q diagram showing power transferred from IHX8 and both main inter-coolers to the three bottoming Rankine cycles

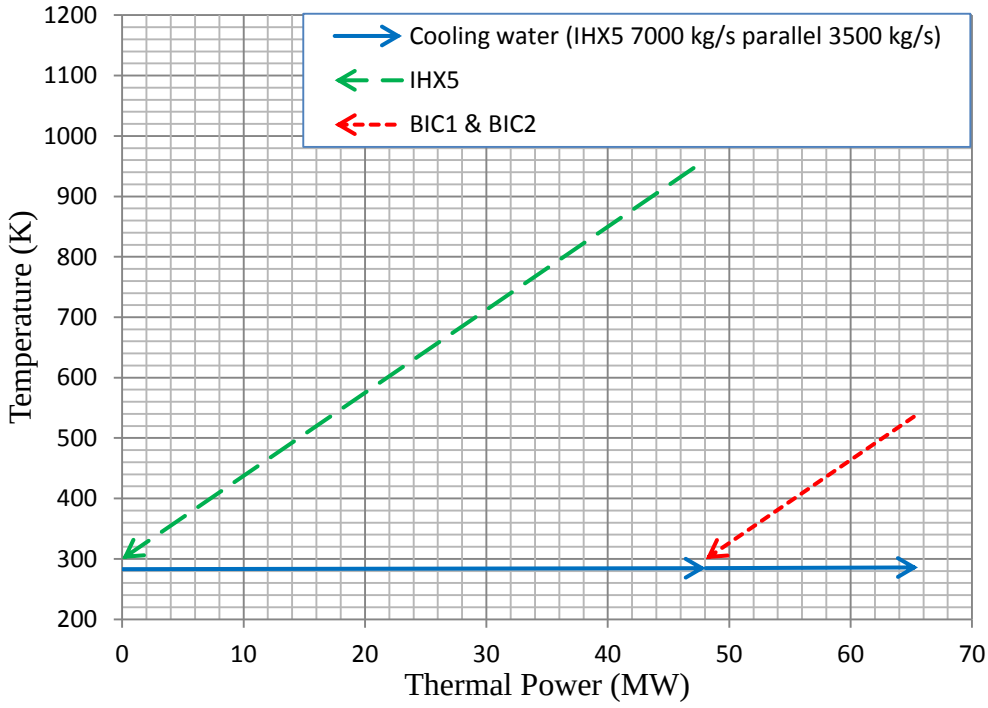

Figure 5.14 T-Q diagram showing cooling water used for IHX5 and both bleed inter-coolers

Table 5.5 summarises all IHX processes where heat is received by the proposed power cycle, i.e., IHX1, IHX2, IHX3, IHX4 and IHX6, including the internal process IHX7. All IHX processes where heat is rejected from the proposed Brayton cycle, i.e., both main inter-coolers, both bled inter-coolers, IHX5, and IHX8 are given in table 5.2. The key parameters for the two-phase sections of the topping cycle are given in table 5.6, whilst table 5.7 summarises the performance of the power cycle.

IHX	He ṁ (kg/s)	T in/out (K)	ṁ coolant (kg/s)	T in/out (K)	Thermal power (MW)	Min. Pinch (°)	IHX type
1	1542	743/785	473	753/888	335	10	Counter
2	1542	785/951	46053	813/961	1327	10	Counter
3	1542	951/982	477	973/1073	248	21	Counter
4	1528	753/803	46053	769/813	395	10	Counter
6	1542	736/754	46053	753/769	141	15	Counter
7	1542	391/743	1542	403/755	2819	12	Counter

Table 5.5 Summary of IHX processes for heat reception in proposed power cycle

Two-phase section	P (MPa)	T (K)	x	α	S	σ (S/m)	D (m)
$Mixer_{out}/MHD_{in}$	2	968	3E-04	0.60	1.80	7.0E6	5
$MHD_{out}/Upcomer_{in}$	0.164	961	3E-04	0.82	7.27	1.3E6	17
$Upcomer_{out}/Separator_{in}$	0.101	961	3E-04	0.84	9.82	6.7E-2	17

Table 5.6 Summary of key two-phase parameters of topping cycle

Cycle pressure ratio	5.4
Compressor/Turbine isentropic efficiency (%)	92/94
Total main/bleed compressor power input (MW)	2023/51
1st Turbine power output – main expansion/bleed expansion (MW)	3272/16
Reheat turbine power output (MW)	517
Brayton net power output (MW)	1731
Brayton net electrical power output (MW_e)	**1688**
Brayton cycle efficiency (%)	**43.4**
MHD power output (MW_e)	**22**
Brayton cycle efficiency, including MHD (%)	**42.9**
Rankine boiler pressures (bar)	1.6/1.4/1.1
Rankine condenser pressure (bar)	0.0215
Total Rankine net power output (MW)	420
Total Rankine net electrical power output (MW_e)	**409**
Rankine cycle efficiencies (%)	**20/19.4/18.4**
Electrical conversion efficiency (%)	97.5
Gross electrical power output (MW_e)	**2119**
Heat supplied (MW_t)	**3991**
PPCS-C fusion power (MW)	3410
PPCS-C plant power requirement (MW_e)	210
Combined Cycle Efficiency/ Overall plant efficiency (%)	**53.1/56**

Table 5.7 Summary of proposed power cycle performance

An energy balance is given in tables 5.8 through to 5.11, where the sign convention is used: negative for power leaving a system, or process, and positive for power entering a system or process.

To determine any first law discrepancy the electrical power generated by the proposed power cycle must be subtracted from the heat supplied to give the expected heat rejection. The gross electrical power generated by the proposed cycle is 2119 MW_e.

Subtracting this value from the heat supplied, 3991 MW_t, gives an expected heat rejection of 1872 MW_t. Adding the rounded heat rejection values from the bleed compressors (~35 MW_t), IHX5 (~48 MW_t) and the three condensers (~1700 MW_t) gives a total of 1783 MW_t.

The difference between the total heat rejected by the MHD generator and the electrical power output yields a net heat rejection of approximately 45 MW_t for the MHD generator. Including the losses between the electromechanical conversion stages, approximately 43 MW_t for the Brayton cycle and almost 11 MW_t for the Rankine cycle, the total heat rejection is just under 1882 MW_t. This represents a first law discrepancy of almost 9 MW, which is approximately 0.23% of the supplied heat: 3991MW_t.

State point (process)	**$\dot{W}$ (MW_e)**	**$\dot{Q}$ (MW)**
Blanket reception		1976
Mixer out		-46
MHD out	**-22**	**-67**
Upcomer out		0
IHX2		-1327
IHX4		-395
IHX6		-141

Table 5.8 Pb-17Li energy balance of proposed power cycle

State point (process)	**$\dot{W}_e$ (MW)**	**$\dot{Q}$ (MW)**
2 (compression)	674	
3 (MIC1)		**-674**
4 (compression)	674	
5 (MIC2)		**-674**
6 (compression)	674	
7 (IHX7)		2819
(IHX1 - Div bulk)		335
(IHX2 - Pb17Li)		1327
8 (IHX3 - Div target)		248
9 (main expansion)	-3272	
10 (blanket)		1432
11 (IHX4 – Pb17Li)		395
12 (reheat expansion)	-517	
13 (reintegration) Main/bleed		-14/14 (net 0)
14 (IHX6 – Pb17Li)		141
15 (IHX7)		-2819
1 (IHX8)		**-771**
16 (bleed expansion)	-16	
17 (nozzle out)		-0.5
18 (mixer out)		46
19 (MHD out)		-0.5
20 (upcomer out)		0
21 (IHX5)		**-48**
22 (bleed compression)	17.5	
23 (BIC1)		**-17.5**
24 (bleed compression)	17.5	
25 (BIC2)		**-17.5**
26 (bleed compression)	17.5	

Table 5.9 Helium energy balance of proposed power cycle

State point (process)	**$\dot{W}$ (MW)**	**$\dot{Q}$ (MW_t)**
31-27 (boiler)		714
28 (turbine out)	-143	
29 (condenser out)		**-568**
30 (feed pump out)	0.04	
36-32 (boiler)		731
33 (turbine out)	142	
34 (condenser out)		**-585**
35 (feed pump out)	0.04	
41-37 (boiler)		674
38 (turbine out)	-124	
39 (condenser out)		**-547**
40 (feed pump out)	0.03	

Table 5.10 Water energy balance of proposed power cycle

Total Combined Cycle Power (MW_e)	2119
Heat supplied to cycle (MW_t)	3991
Expected heat rejection (MW_t)	1872
Actual heat rejection from combined cycle (MW_t)	1783
Heat rejected via electromechanical conversion in Brayton cycle (MW_t)	43
Heat rejected via electromechanical conversion in Rankine cycle (MW_t)	11
Total heat rejection (MW_t)	1882
1^{st} Law discrepancy (MW)	9
1^{st} Law discrepancy (%)	0.23

Table 5.11 Summary energy balance of proposed power cycle

5.6 Summary

A major advantage of the proposed power cycle is due to the use of a significantly higher gas cycle pressure of 34.5 MPa. This is very high for any turbo-machinery casing, especially since the molecular diameter of helium is very small, thus making it prone to leaking. However, pressures between 30 MPa and 35 MPa are possible for supercritical steam cycles [Hordeski, 2011]. The proposed power cycle has the potential to outperform the existing PPCS model C power cycle, but there are some assumptions that underpin this prediction which should be mentioned.

For this initial design of the proposed power cycle, large diameter ducts have been used in the topping cycle to circulate the liquid metal. Further improvements would likely see these replaced with several smaller diameter ducts, especially as the magnetic field in the MHD section becomes less uniform due to the reduction in field strength with the cube of the duct radius. Following a similar course of reasoning, the Brayton cycle would need to consist of several loops, as in the existing PPCS-C design, as a single gas turbine could not deliver such high mechanical power outputs. Other improvements to the topping cycle could involve the use of higher liquid metal breeder pressures, where there is a benefit in extracting more energy from the MHD generator by allowing the mixture to expand further.

Pressure drops have also been neglected in all IHX processes for the proposed power cycle and it is therefore likely that greater pumping requirements will reduce 2119 MW_e further. A figure for the gross electrical power output of the PPCS-C plant is given, 1780 MW_e [Norajitra et al., 2003], in which pressure losses in heat exchangers are neglected. Whilst this figure is still lower than the 2119 MW_e given for the proposed power cycle, where pressure losses are also neglected, there are fewer IHX processes in the PPCS-C power cycle: eight compared to sixteen in the proposed power cycle, also including the blanket and the three condensers in the bottoming Rankine cycles. On this basis, the PPCS-C cycle without IHX pressure drops has a cycle efficiency of 44.6% and yields an overall plant efficiency of 45.9%.

The equations governing the performance of the Brayton and Rankine cycles are well established, so too is the buoyancy effect. The uncertainty associated with these aspects of the proposed power cycle is therefore low. However, the effects of tritium on the turbo-machinery, and MHD generator, cannot be predicted or experimentally verified. The mixer length, which is required in the CISE correlation to predict the two-phase pressure drop, may be too short to allow full mixing of the two phases; whether full mixing is required to generate the predicted electrical output from the MHD generator is unknown. There is further uncertainty regarding the effect of the two-phase flow regime upon the performance of the MHD duct, and the accuracy of the empirical relation used to determine the electrical conductivity of a two-phase mixture. The inclusion of a two-phase adiabatic index may also prove to be incorrect.

The electrical power generated by the proposed power cycle has been calculated to be 2119 MW_e. The cycle efficiency of the Brayton cycle with MHD topping is 42.9%, whilst the addition of the bottoming Rankine cycles gives a combined cycle efficiency of 53.1%. The power requirement of a model-C plant is 216 MW_e, but to pump Pb-17Li through a DCLL blanket requires 6.3 MW_e [Norajitra et al., 2003]. In the proposed power cycle this is not required since Pb-17Li is circulated through the blanket via buoyancy, thus the power requirement falls to just under 210 MW_e. Due to the increase in the electrical power output of the plant, the overall plant efficiency is 56%. The proposal, therefore, provides an improvement in cycle efficiency of over 8.5% and an increase in overall plant efficiency of nearly 10.1%. These figures, however, carry the uncertainty involved with the MHD topping cycle. A bench-top scale experiment will allow the accuracy of the two-phase MHD equations to be verified and help to determine whether the prototype design can perform as predicted in this chapter.

Chapter 6: Experimental Design Process

The conclusions of the previous chapter strongly support the need for experimental verification. This chapter will begin by discussing the experimental objectives and then proceed to outline the design process. At the end of this chapter the equations for similitude will be presented, before discussing the method used for determining an energy balance on the experimental setup.

6.1 Identifying the Objectives

There are many uncertainties associated with the two-phase MHD topping cycle that require experimental verification, particularly the electrical conductivity of a two-phase mixture and the two-phase flow regime in the MHD duct, but also the equations associated with the performance of the two-phase MHD generator.

Crucially, the buoyancy principle with the concurrent generation of electricity via a two-phase MHD generator must be demonstrated. It is therefore necessary to outline the objectives for an experiment which will verify the performance of the two-phase MHD topping cycle.

6.1.1 First Tier Objectives

The first tier objectives can be summarised as:

- 1a - Demonstrate the buoyancy principle with the concurrent generation of electrical power via a two-phase MHD generator
- 1b - Verify the accuracy of the mathematical model by comparing the output values of the model with experimental values

The experimental apparatus must be designed to meet these primary objectives. The success of the experiment can be measured against whether these criteria are met.

6.1.2 Second Tier Objectives

The experimental setup requires a heater to simulate the thermal reception in the blanket module. A component to help simulate heat rejection in the downcomer is also required. To determine the heat reception and rejection, and also any heat lost through the MHD duct and through the walls of the flow channels, temperature measurements must be made at certain locations on the experimental apparatus. This is most easily achieved by using thermocouples.

There are two locations where pressure losses should be measured. The first should measure the pressure loss through the MHD duct, whilst the second should measure the pressure loss caused by a component that simulates the pressure loss in the blanket. For these pressure measurements, manometers offer a simple solution.

The MHD duct must have electrodes to collect electrical charge. An external load would also be useful to help vary the value of the generator coefficient, δ, associated with the MHD generator. A suitable device must also be used to measure the electrical output of the two-phase MHD generator.

It will also be desirable to observe two-phase fluid interactions, to determine for a given void fraction whether certain flow regimes occur. This will have ramifications for the available types of materials used for constructing an experiment. The flow regime is important for visually determining the void fraction, which allows the slip ratio to be calculated. By taking all these considerations into account, the second tier objectives can be summarised as:

- 2a - observe the two-phase flow regime in the mixer, MHD and upcomer sections
- 2b - show that the two-phase liquid metal MHD generator behaves as expected
- 2c - perform an energy balance on the loop

6.1.3 Third Tier Objectives

After choosing a suitable metal to use in the experiment, where density values are commonly given in literature, other properties such as dynamic viscosity and surface tension are not and may introduce further uncertainties. Both the dynamic viscosity and surface tension are required inputs for the CISE correlation and therefore two further tests are likely to be needed. These tests should allow measurement for a chosen temperature range. The third tier objectives could be summarised as:

- 3a - measure the dynamic viscosity of the liquid phase
- 3b - measure the surface tension of the liquid phase

6.2 Liquid Metal

Finding a suitable liquid metal substitute for experimental work was based upon three factors: cost, melting temperature and toxicity. Galinstan is a low-melt eutectic alloy that is liquid at room temperature, non-toxic and possesses the lowest melting point of all the liquid metals that were surveyed. However, its high price rendered it cost-ineffective at the bench-top scale. The cost of low-melt alloys seemed to be inversely proportional to their melting temperatures and after eliminating the low-melt alloys containing cadmium, a substitute was settled upon: low-melt 136. A comparison of melting temperature, density, cost and composition for the main liquid metals surveyed is presented in table 6.1.

Alloy	T_{Melt} (°C)	ρ (kg/m^3)	£/kg	£/cm^3	Composition (%wt)
Galinstan	-19	6440	1795 - 2262	12 - 1450	Ga 68 In 22 Sn 10
Low-melt 136	58	8581	129 - 195	1 – 1.7	Bi 49 In 21 Pb 18 Sn 12
Field's Metal	62	7800	364	2.8	In 51 Bi 32.5 Sn 16.5
Low-melt 203	95	9716	18 - 25	0.2 - 0.24	Bi 52.5 Pb 32 Sn 15.5

Table 6.1 Comparison of low-toxicity, low-melting alloys: cost per kg, melting temperature, composition. *not including quantity discounts or shipping considerations [Bolton Metal Products, RotoMetals, Lowden Ltd]

6.3 Experimental Apparatus

This subsection will briefly discuss the design issues that were encountered, and which subsequently shaped the design of the apparatus, shown in figure 6.1, and the individual components. The governing equations used in the design process are also included.

6.3.1 Materials

The primary concern for choosing the structural material of the apparatus was transparency, so that the second-tier objective concerning the observation of the two-phase flow regime in the mixer, MHD and upcomer could be met. Several plastics were considered for these components, but their structural stability at elevated temperatures, above the melting point of LM136, were uncertain and caused concern. This led to the conclusion that glass was more suitable for all two-phase

sections of the experimental apparatus. It was also concluded that the use of glass for the heating section of the apparatus was prudent since the temperature of the heating wire would very likely exceed the melting temperature of most, if not all, plastics.

Metals were considered for the single-phase sections of the loop, however, a concern existed regarding the mating of glass and metal components. Therefore, a decision was made to manufacture the entire experimental apparatus using glass, which provided complete transparency throughout. Glass is also an electrical insulator and this eliminated a concern over whether any magnetohydrodynamic pressure losses would occur due to Lenz's Law.

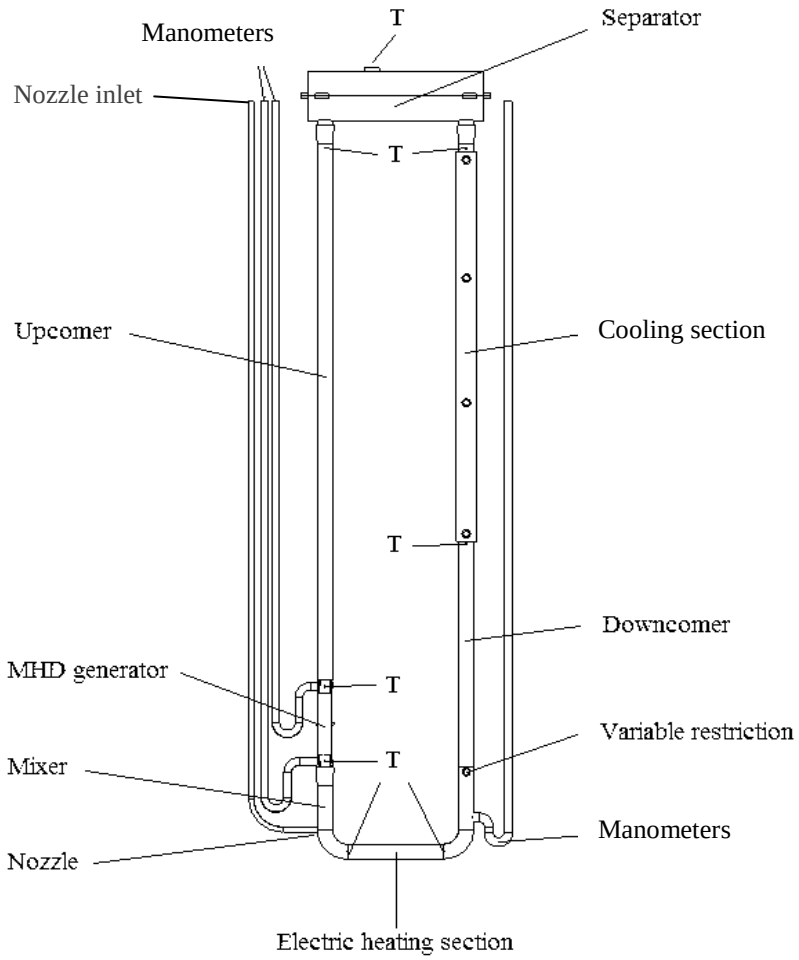

Figure 6.1 Experimental apparatus, created using 3D modelling software Pro Engineer, showing temperature measurement, denoted by T

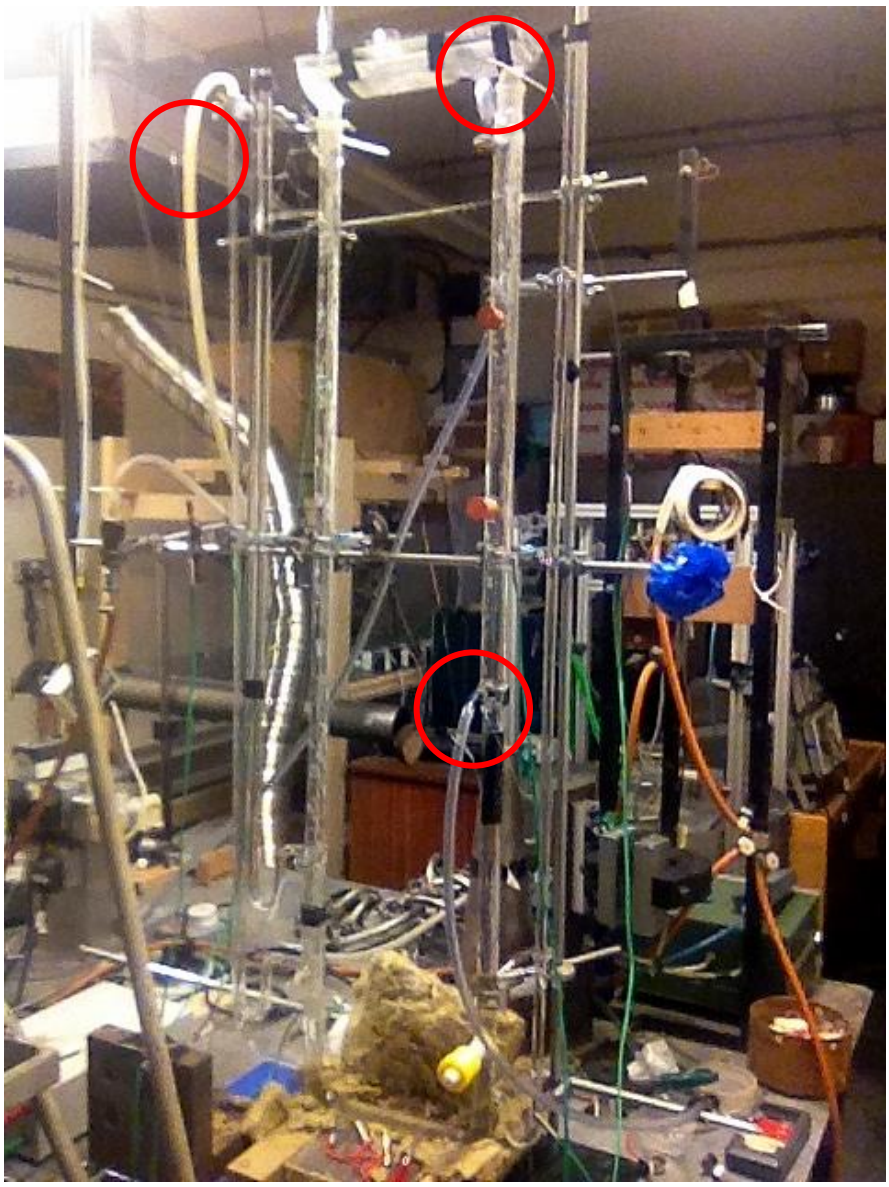

Figure 6.2 Picture of experimental apparatus showing additional thermocouple locations (circled red) for cooling water (top and bottom right) and air entry (top left)

6.3.2 Safety

Several safety measures were embedded into the experimental apparatus during the design process, to ensure the safety of any person in close vicinity to the apparatus. Due to the use of molten metal, care needed to be taken by adopting the appropriate safety equipment to mitigate the risk of accidental exposure to eyes and

skin: safety goggles, thermal gloves and long sleeves. The lead content in LM136 raised the risk of exposure to the inhalation of fumes during the heating process and this required adequate ventilation. This was achieved by using the laboratory air extraction system and the adoption of face masks with filters graded to FFP3.

Since water was easily available from a supply present in the lab, it was used as the cooling fluid to simulate heat rejection in the downcomer. This, however, carried with it the risk of exposing molten LM136 to water, which, due to the high thermal capacity of LM136, would result in the rapid vaporisation of the water and the risk of explosion. This risk was deemed acceptable by the author and the primary supervisor.

At the start of an experimental run an amount of LM136 was melted in a separate vessel before being poured into the separator and 'loading' the apparatus. This presented a risk due to the necessity of handling molten metal at height, where splash-back or spillage could occur. A lid was designed for the separator to reduce the risk of exposure to molten LM136 that might be caused by the bubbling of the two-phase flow in the separator.

Completion of an experimental run required the LM136 to be drained before solidification occurred within the glass apparatus. Melting LM136 from its solid state within the glass would cause the glass to fracture. In a previous attempt at heating LM136 in a glass beaker it was allowed to solidify and subsequent heating caused the glass to crack, leading to the conclusion that a difference in thermal expansion coefficients was to blame. The expansion of solidified LM136 against an unmelted blockage would also likely cause the glass in the apparatus to crack.

Draining of the loop was therefore deemed vital and was expected to be achieved by using a flexible hose to initiate a siphon effect that would allow molten LM136 to be collected in an external vessel, where it would subsequently be allowed to cool.

6.3.3 Electric (Joule) Heating

This part of the experimental apparatus replicated the thermal reception process in the blanket. Nichrome wire, possessing a high resistance, carrying an electric current was wound around a length of glass section and lagged to prevent heat loss. The electrical power supplied to the nichrome wire was used to raise the temperature of LM136. This method was chosen as it provided a reasonably uniform, steady heat input over the length of the glass heating section.

A value of ten degrees was deemed to be a sufficiently measurable temperature difference for the heating section, where a top LM136 temperature of 80°C, deemed sufficiently above the melting point of LM136, and a low temperature of 70°C, brought about by the water jacket, was used.

Using these values for the inlet and outlet temperature of the heating section, a range of LM136 mass flows could be established, given the specific heat of LM136 supplied by the manufacturer and the available power of the electrical supply.

The equation which describes Joule heating is given by

$$\dot{Q}_{Joule} = I_{supply}^2 R_{nichrome} = V_{supply}^2 / R_{nichrome} \tag{6.1}$$

The gauge of nichrome determined the maximum safe current limit before burnout occurred. The correct resistance was subsequently found from equation (6.1).

Using the wire resistivity, $\rho_{nichrome}$, and diameter, d_{wire}, the resistance per unit length, L, is determined

$$\frac{R_{nichrome}}{L} = \frac{4\rho_{nichrome}}{\pi d_{wire}^2} \tag{6.2}$$

Providing that the value for resistivity is accurate for a certain wire temperature, the required wire length for correct resistance can be found and the number of coils determined

$$N_{coil} = \sqrt{\frac{L_{wire}}{\pi d_{tube} p}} \tag{6.3}$$

where p represents the pitch of the coil. If the coiled nichrome wire does not span the length of the heating section, for a given pitch, then several parallel windings are necessary.

6.3.4 Nozzle

The nozzle has been designed to be removable from the experimental apparatus to mitigate the problem of having a fixed component that may not perform adequately, but being constructed from glass means that this small-diameter component carries with it a high risk of breakability. The contraction angle has been designed to be less than ten degrees, to ensure that the isentropic equations given in the previous chapter are applicable. The pressure at nozzle inlet and the pressure loss through the nozzle can be calculated to yield the nozzle outlet pressure. An image of the glass nozzle is given in figure 6.3 below.

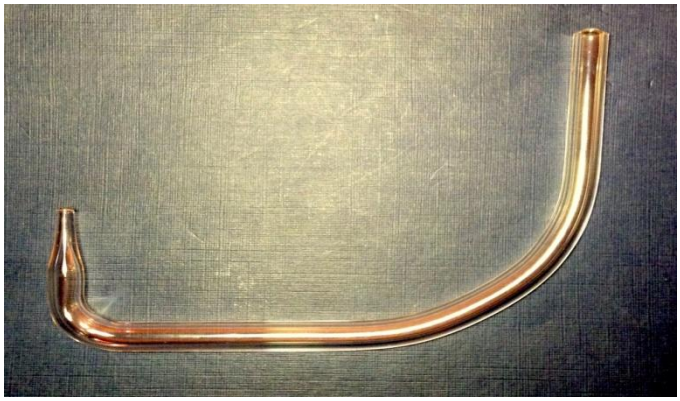

Figure 6.3 Glass nozzle used in experiment

6.3.5 Mixer

The length of the mixer in the topping cycle was chosen to be small because the two-phase pressure loss was predicted to be greatest in this section, due to the higher mixture density. For the experimental apparatus a mixer length of 10 cm was chosen for convenience, but by virtue of using glass in this section it was hoped that the effects of mixing might be observed. Conversely, the impact of ineffective mixing upon the performance of the MHD generator might also be observed.

6.3.6 MHD Generator

An MHD duct length of 10 cm was also chosen for convenience. A square glass section is required for the MHD duct and was manufactured using a graphite former, against which the glass of a round section tube was slumped to form the square MHD duct.

A further consideration for the MHD section was the type of generator that should be used in the experiment. A segmented-electrode constant-velocity (SECV) MHD generator was used in the topping cycle calculations. However, due to the added complexity of the external load circuitry associated with SECV MHD generators it was decided that a continuous-electrode constant-velocity (CECV) MHD generator should be used because the load circuitry would be relatively simple. The MHD equations outlined in the previous chapter are equally applicable to this type of device since the β-value (see chapter 3) is negligibly small for LM136: 2.2×10^{-5}.

Constant-velocity MHD generators require a duct expansion, but at the bench-top scale this expansion was calculated to be negligible. It was therefore decided to keep the MHD duct as a constant-area section to simplify an already difficult manufacturing process.

The electrodes were designed to be manufactured from thin copper sheet, each with a centralised stud that protruded through the walls of the square glass section and attached to an external circuit. Due to the slight rounding of the glass corners inside

the square MHD duct, however, the width of the electrodes were marginally smaller than the internal width of the MHD duct. The electrodes were positioned by placing the two-phase section of the apparatus horizontally and then using gravity to slide them into the MHD duct, where the locating pins, which protruded through the glass wall of the MHD duct, were subsequently used to fix the electrodes into position. By using Araldite the electrodes could be further secured. Any remaining gaps between the electrodes and the glass could also be sealed.

A permanent magnet provided the magnetic field strength, B, and a gauss meter procured to measure its value. The magnet's poles should slightly over-span the length of the MHD duct so that the magnetic field lines intersecting the liquid metal duct are uniform over the duct length and end losses are minimised.

The value of the generator coefficient, δ, can be fixed by the choice of load resistance, R_L, in the external circuit

$$\delta = \frac{R_L J_{CECV} A_e}{b v_{LM136} B} \tag{6.4}$$

where A_e is the cross-sectional area of the electrodes, b is the distance between the electrodes and J is the current density for a continuous-type MHD generator.

6.3.7 Separator

An atmospheric separator included a moveable glass plate that acted as a baffle to prevent any air entering the downcomer and to aid in the phase separation process.

Different baffle positions helped to determine how the phase separation process was affected by baffle position. A secondary effect of the baffle was to promote air flow through the gas exit located in the separator lid. A smaller second hole above the downcomer allowed any air not stopped by the baffle to escape from the system

Pre-heating the glass of the apparatus with hot air prevented fractures caused by thermal shock when LM136, having been melted in an external vessel to 80°C, was emptied into the separator. However, perhaps the greater concern was due to the relatively high-density LM136 impacting the base of the apparatus during the loading process and causing impact fractures to the glass. Measuring the temperature of the air leaving the separator contributed to the energy balance of the loop.

6.3.8 Upcomer, Downcomer and Cooling Section

Choosing the height of the downcomer was based upon convenience, but also upon economics as the inventory of LM136 was proportional to downcomer height. The upcomer height was defined by the height of the downcomer minus the combined length of the mixer and MHD sections.

The cooling section of the apparatus was designed to simulate, in a single counter-flow process, IHX2, IHX4 and IHX6, which collectively allowed the Pb-17Li to return to the DCLL blanket at the specified temperature. A glass jacket surrounded a portion of the downcomer in order to cool the LM136 to 70°C. Three water jacket inlets provided sufficient flexibility to cope with a range of LM136 mass flow rates.

The volumetric flow rate and temperature of the water leaving the jacket was measured to help with the energy balance of the loop

The following equation gives the heat rejected in the downcomer of the apparatus

$$\dot{Q}_{downcomer} = UA\Delta\bar{t}_{ln} \tag{6.5}$$

where the overall heat transfer coefficient U is given by

$$U = \frac{1}{r_{out}}\left[\frac{1}{r_{out}h_{out}} + \frac{\ln r_{out}/r_{in}}{\kappa} + \frac{1}{r_{in}h_{in}}\right]^{-1} \tag{6.6}$$

and the subscripts *in* and *out* refer to the inside and outside of the downcomer wall, respectively, κ is the thermal conductivity and h is the convective heat transfer coefficient.

$\overline{A}$ is the mean surface area of the cooling section and is given in terms of a unit length, L, as

$$\bar{A} = \pi 2 r_0 L \tag{6.7}$$

and $\overline{\Delta T}_{ln}$ the log-mean temperature difference

$$\Delta \bar{T}_{ln} = \frac{\left(T_{LM136\_in} - T_{water\_out}\right) - \left(T_{LM136\_out} - T_{water\_in}\right)}{\ln\left(\left(T_{LM136\_in} - T_{water\_out}\right)/\left(T_{LM136\_out} - T_{water\_in}\right)\right)} \tag{6.8}$$

where the subscript w represents water. If the overall heat transfer coefficient is multiplied by the ratio of the mean surface area to unit length, equation (6.6) can be given as the sum of three thermal resistances, R: internal film R_{if}, wall conduction R_{wc} and external film R_{ef}

$$U\frac{\bar{A}}{L} = \left[\frac{1}{h_{out}(A_{out}/L)} + \frac{\ln r_{out}/r_{in}}{2\pi\kappa_{glass}} + \frac{1}{h_{in}(A_{in}/L)}\right]^{-1} = \left(R_{if} + R_{wc} + R_{ef}\right)^{-1} \tag{6.9}$$

The heating rate per unit length is given by

$$\frac{\dot{Q}_{downcomer}}{L} = \frac{U\bar{A}\Delta T_{ln}}{L} = \bar{T}_{ln}(\Sigma R)^{-1} \tag{6.10}$$

The LM136 in the downcomer was predicted to be turbulent. By using the Dittus-Boelter [Çengal, 2003] equation, which gives the Nusselt number for turbulent flows that are being cooled, the internal film resistance can be found

$$Nu = \frac{h_{in} D_{in}}{\kappa_{LM136}} = 0.023 * Re^{0.8} * Pr^{0.33}$$

(6.11)

The internal film resistance is

$$R_{if} = \left(\frac{h_{in} A_{in}}{L}\right)^{-1}$$

(6.12)

The flow in the annulus of the cooling section is expected to be laminar and so the following correlation for Nusselt number can be used [Incropera & DeWitt, 2006]

$$Nu = 1.86 * (Re * Pr)^{\frac{1}{3}} * (D_{out}/L)^{\frac{1}{3}} * (\mu_{bulk}/\mu_{wall})^{0.14} = \frac{h_{out} D_{out}}{\kappa_{water}}$$

(6.13)

where the viscosities of the water at the bulk mean temperature and wall temperature were assumed equal. Using equations (6.11) and (6.12) with the appropriate subscripts the external film resistance can be found. Knowing the mass flow for LM136 in the experimental apparatus the heat rejected in the downcomer can be found

$$\dot{Q}_{downcomer} = \dot{m}_{LM136} c_{LM136} (\Delta T_{LM136})$$

(6.14)

Providing that the value of κ_{glass} is known, finding the wall conduction resistance is simple (see equation 6.9). By rearranging equation (6.10) the required length of the water jacket can be found

$$L = \frac{\dot{Q}_{downcomer}}{\bar{T}_{ln} (\Sigma R)^{-1}}$$

(6.15)

6.3.9 Variable Flow Restriction/Drain

This component was designed to simulate the MHD pressure drop experienced by the liquid metal breeder in the blanket, but also to act as a drain to remove the LM136 from the apparatus. A glass stopcock valve adjoined to the base of the downcomer could be opened or closed to provide a variable restriction and give a desired pressure loss by monitoring the reading of a manometer, see section 6.3.11, and comparing it to the level in the separator. Since the flow restriction consisted of an internal flow over a cylinder, it was deemed that the loss coefficient was most easily determined from experiment.

6.3.10 Thermocouples

Eleven locations around the experimental apparatus provided knowledge of the temperature of the flow. Two thermocouples located at heating entry and heating exit allowed the LM136 mass flow to be determined. Two further thermocouples located at MHD entry and exit helped to determine the temperature drop across the MHD duct and measure the accuracy of both equations (4.45) and (4.46).

Measuring the temperature of the two-phase flow at the top of the upcomer determined the heat lost through the glass walls. The location of the thermocouple before the cooling section entry determined the extent of any temperature drop through the separator, whilst the thermocouple at the exit of the cooling section helped to determine if sufficient cooling water was being supplied.

Air entered the nozzle through a flexible hose, into which one thermocouple was inserted to measure the gas inlet temperature to the apparatus. A further thermocouple measured the temperature of the gas leaving the apparatus via the separator. A similar arrangement was made for the water used in the cooling section, where flexible hosing supplying the water had thermocouples inserted to measure the water inlet and outlet temperature. All eleven thermocouples helped to provide a complete energy balance for the experimental setup.

6.3.11 Manometers

Manometers at MHD entry and exit were chosen because they provided a simple and inexpensive method of determining the pressure drop across the MHD generator, where they also measured the accuracy of equation (4.42). The diameters of these manometers were chosen to allow sufficient structural strength, but they were also small enough to reduce the LM136 inventory.

A manometer was designed to be located near the base of the loop, just after the variable restriction, but also at the same height as the nozzle outlet. This manometer helped to determine the pressure drop caused by the variable restriction and the pressure of LM136 at nozzle outlet.

6.4 Viscosity Test

The purpose of this test was to measure the viscosity of LM136, which was not supplied by the manufacturers, or available in other literature, in the temperature range used in the experiment: 70 - 80°C. A glass dip cup viscometer, shown in figure 6.4, was subsequently designed and manufactured to perform this task. The reservoir of the dip cup was approximately 20 mm in diameter and 55 mm deep. Due to the manufacturing process the base of the reservoir was not perfectly flat and instead resembled a cone measuring approximately 12 mm in depth. The capillary was 25 mm in length with an ID of 0.696 mm. By heating an amount of LM136 in a glass beaker via electrical heating, using nichrome wire wrapped around the beaker, the metal was heated to a prescribed temperature. The glass viscometer was then submerged in the molten LM136 bath and the reservoir was allowed to fill to the uppermost reservoir mark.

The dip cup was subsequently raised above the free surface where a stopwatch was started. When the second reservoir mark was reached the stopwatch was stopped and the time recorded. Assuming the flow in the capillary was laminar, and neglecting pressure and velocity heads, the energy equation reduced to the head loss form of the Hagen-Poiseuille equation [Douglas et al., 2005]

$$h = \frac{128\mu_{LM136}L_{capillary}\dot{V}_{LM136}}{\pi\rho_{LM136}gd^4_{capillary}}$$

(6.16)

If the volumetric flow rate, Q, is rewritten as the ratio of the volume change between two fixed points in the viscometer reservoir to the elapsed time, the above equation can be rearranged to give the efflux time

$$t_{efflux} = \frac{128\mu_{LM136}L_{capillary}\Delta V_{reservoir}}{\pi\rho_{LM136}g\bar{h}_{res}d^4_{capillary}}$$

(6.17)

where $\bar{h}_{res}$ can be approximated by the average height of LM136 in the reservoir.

Before testing LM136 the performance of the dip cup was tested using water, for which the above equations are equally applicable. A risk assessment document was also written for this test.

Figure 6.4 Glass dip cup viscometer

6.5 Surface Tension Test

To measure the surface tension of LM136, another physical property not available from the manufacturer or any other literature, the Wilhelmy plate method [Wilhelmy, 1850] was utilised. The design of the apparatus, shown in figure 6.5, allowed the total force, F_{Total}, on the glass plate to be transmitted to a Sartorius 1712 balance via the fulcrum.

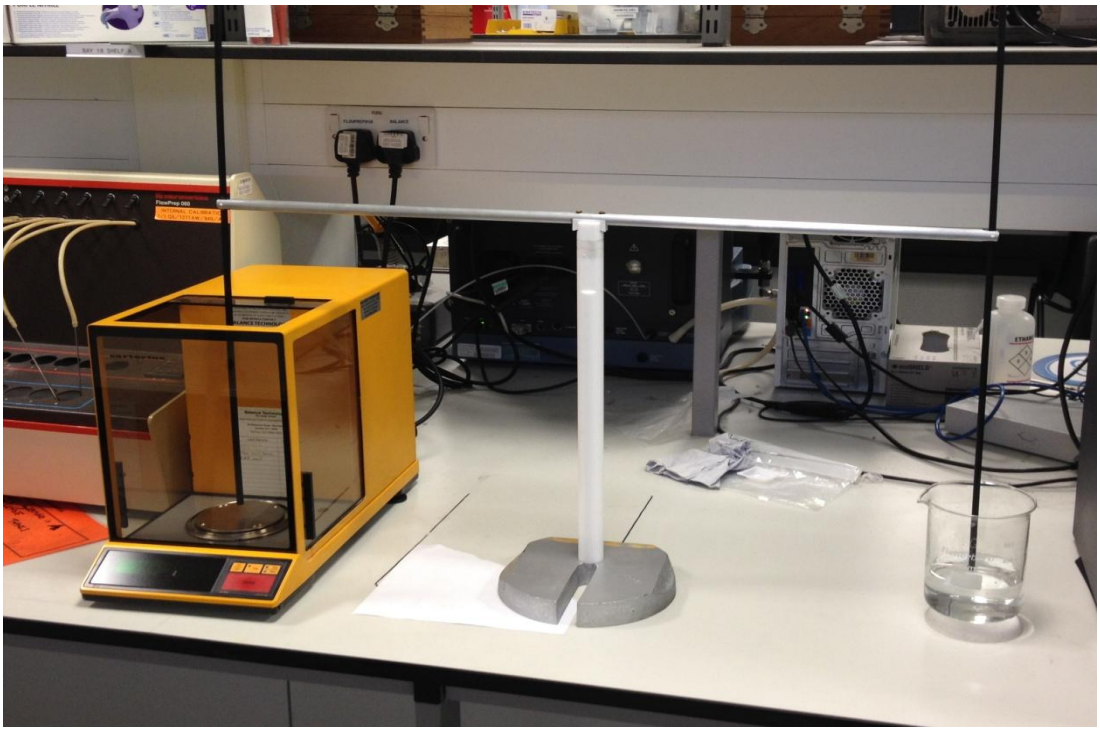

Figure 6.5 Wilhelmy plate apparatus (test showing water)

The total force on the glass plate is the sum of the buoyancy force, which acts in the positive y-direction and the force due to surface tension, which acts in the opposite direction. This is shown in figure 6.6. The buoyancy force on the glass plate was calculated via knowledge of the wetted perimeter, L_{wetted}, draught, D, and liquid density

$$F_{Buoyancy} = L_{wetted} D \rho_l \tag{6.18}$$

The force due to surface tension, F_γ, was found by multiplying the balance reading by the acceleration due to gravity and subtracting the buoyancy force. The surface tension of the fluid being tested was then found by

$$\gamma_l = \frac{F_\gamma}{L_{wetted}\cos(\theta)} \tag{6.19}$$

where cos(θ) is a correction term called the contact angle and appears when incomplete wetting occurs. For complete wetting the contact angle is zero.

Measuring the surface tension of a fluid with known properties, such as water, allowed the correction term to be calculated and the accuracy of the apparatus determined.

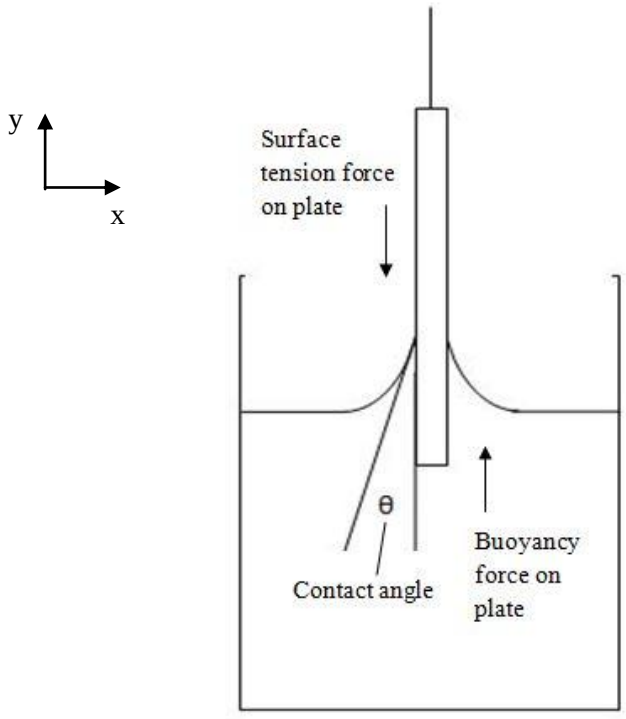

Figure 6.6 Forces on Wilhelmy plate

6.6 Similitude

Due to the difference in scale between the prototype and experiment an attempt to attain geometric similitude was impractical. The internal diameter of the glass tubing was chosen to be 20 mm, which was sufficiently large to avoid significant frictional pressure drops, but also small enough to reduce the liquid metal inventory. To achieve geometric similitude with the aforementioned diameter the height of individual sections in the loop would be prohibitively small, ranging from a few millimetres for the mixing section to a few centimetres for the MHD and upcomer sections. Conversely, for a mixer length of 10 cm the diameter would be prohibitively large, whilst for MHD and upcomer sections in the range 10 – 100 cm the diameters become prohibitively small.

The different fluids in the experiment also made matching the Reynolds, Weber and Froude numbers impractical for each two-phase section. Although this was primarily due to scale, there were sufficient physical differences between both sets of gas and liquid phases between prototype and experiment that contributed to this impracticality. There are, however, two other non-dimensional parameters that could be used to attain some dynamic similitude. The flow quality, defined as

$$x = \frac{mass\ flow\ of\ air}{mass\ flow\ of\ air + mass\ flow\ of\ liquid} \tag{6.20}$$

and the cross-sectional void fraction, defined by

$$\alpha = 1 + \frac{1 - x}{x} * \frac{\rho_g}{\rho_l} * S \tag{6.21}$$

These parameters cannot be matched simultaneously because of the differing physical properties of the phases in the prototype and experiment. However, by

varying the mass flow of air entering the apparatus the flow quality could be adjusted and matched with the prototype. To make an adjustment to the void fraction required knowledge of a third dimensionless parameter, the slip ratio, which is difficult to measure.

The dimensionless numbers associated with the MHD section include the use of the MHD duct length, the magnetic field strength, the MHD inlet area, the electrical conductivity of the medium and the liquid metal velocity. A magnetic interaction number, *I*, can be defined as

$$I = \frac{magnetic\ body\ force}{inertia\ force} = \frac{\sigma_m B^2 L_{MHD}}{\rho_{LM} u_{LM}} \tag{6.22}$$

The Reynolds number is defined as

$$Re = \frac{inertia\ force}{viscous\ force} = \frac{\rho_{LM} u_{LM} L_{MHD}}{\mu_{LM}} \tag{6.23}$$

which leads to the definition of the Hartmann number

$$Ha = \sqrt{\frac{magnetic\ body\ force}{viscous\ force}} = \sqrt{IRe} = \sqrt{\frac{\sigma_m}{\mu_{LM}}} B L_{MHD} \tag{6.24}$$

Since the dynamic viscosity values of Pb-17Li and LM136 were expected to be of a similar order of magnitude, and the length of the MHD duct was fixed at 10 cm, only the magnetic field strength and mixture conductivity could be altered in an attempt to match the Hartmann number in the prototype. Altering the magnetic field strength using permanent magnets would be more difficult than altering the mixture conductivity, which could be achieved by changing the mass flow of air entering the loop and thus changing the cross-sectional void fraction. However, this would affect

the flow quality. Therefore, the model would need to be verified for low Hartmann numbers and subsequently extrapolated from the bench-top scale to higher Hartmann numbers that are applicable to the prototype.

6.7 System Energy Balance

There is no work input to the system. Heat is supplied by the nichrome wire heating section and is balanced by the work output of the MHD generator, the heat exiting the system via the gas phase and the heat rejected to the cooling water. The energy balance is given in equation (6.25), assuming negligible heat loss in the heating section through the lagging. Only the heating section is lagged, therefore some heat is liable to escape and contribute to any discrepancy in the energy balance.

$$\begin{aligned}\dot{Q}_{heating} &= \dot{Q}_{air} + \dot{Q}_{water} + \dot{Q}_{MHD} + \dot{W}_{MHD} \\ &= \dot{m}_{air} c_{p\_air}\left(T_{air\_out} - T_{air\_in}\right) \\ &+ \dot{m}_{water} c_{water}\left(T_{water\_out} - T_{water\_in}\right) \\ &+ \dot{m}_{l} c_{l}\left(T_{l\_out} - T_{l\_in}\right) + \dot{W}_{MHD}\end{aligned} \tag{6.25}$$

The voltage and current settings on the bench-top power supply provided the thermal input to the system, assuming negligible heat loss through the lagging. The thermocouples located in the heating section, and the specific heat of the liquid phase, determined the mass flow of the liquid phase.

Determining the mass flow of air entering the system, as well as the air inlet temperature and air outlet temperature, provided a check on the heat exiting the system via the gas phase. Measuring both the temperature of the water at inlet and outlet to the jacket, and the water volumetric flow rate, provided a check on the heat rejection via the IHX process in the downcomer. Temperature measurements via thermocouples located in the MHD section determined the heat output from the system. Temperature measurements around the apparatus helped to determine the heat loss from sections where no lagging was present.

6.8 Summary

This chapter has laid out the experimental objectives in three tiers. The design process that has been described revolves around meeting these objectives, but also takes into account safety and cost.

The experimental apparatus; with heating section, permanent magnets, electrodes and external circuit that comprise the two-phase MHD generator; allows one of the first-tier objectives to be met through the visible demonstration of a buoyancy-driven liquid metal with the concurrent generation of electricity via a two-phase MHD generator. Due to the use of glass as the structural material the observation of the two-phase flow is permitted, thus meeting the first of the second-tier objectives.

The remaining first-tier objective is met through the use of the manometers and thermocouples to provide a quantifiable check on the mathematical model, where they also help by meeting the remaining second-tier objectives and third tier objectives.

It is essential to determine how accurately the mathematical model predicts the power output and performance of the MHD generator under certain two-phase flow regimes for the flow quality, void fraction and Hartmann number calculated in the prototype. Determining the behaviour of the system for a range of these parameters also provides a further insight into the behaviour of the system.

Chapter 7: Experimental Results

This chapter will outline the results obtained for the viscosity and surface tension measurements, before presenting the results obtained from the main experiment, where a limited run of testing was performed for an air/water mixture and a single test run, due to technical difficulties, for an air/LM136 mixture. Changes made to either the design or theoretical approach will also be mentioned.

7.1 Dynamic Viscosity

Three tests using water at approximately 20°C were performed to determine the accuracy of the glass viscometer dip cup. These are given in table 7.1. Initially, a water level change of 55 mm within the reservoir of the dip cup was used to give the average efflux time. This water level change represented a change between full and empty, but it was realised that this might not give accurate measurements due to the reduction in efflux velocity as the level of the water in the reservoir reduced. A second test was performed using a 40 mm water level change, from full to a level 15 mm above the base of the reservoir. Finally, a third test used a 13 mm water level change from full to 37 mm above the base of the reservoir.

The results in table 7.1 show that there is a small error between the measured dynamic viscosity of water and the accepted value [Kaye & Laby, 1973]. The systematic errors are marginally reduced when a smaller value of level change in the reservoir, Δh_{res}, of the dip cup is used. For the case where Δh_{res} is 13 mm the total error was reduced to 17%, whilst the slightly higher error when Δh_{res} is 40 mm is likely due to experimental error.

Test No.	T (°C)	ρ_{water} (kg/m^3)	Δh_{res} (mm)	ΔV (m^3)	$\bar{t}_{efflux}$ (s)	$\mu_{measured}$ (Pa s)	$\mu_{accepted}$ (Pa s)	Error (%)
1	20	998	55	1.3E-5	144	1.23E-3	1.00E-3	22.9
2	20	998	40	1.2E-5	123	1.26E-3	1.00E-3	25.4
3	20	998	13	4.1E-6	31	1.17E-3	1.00E-3	17.1

Table 7.1 Averaged dynamic viscosity results using water as a test fluid

Initial viscosity tests with LM136 presented an immediate problem. The transparency of the glass, which had been relied upon to view the level in the reservoir of the dip cup when using water, had been compromised by a coating of LM136 that formed on the glass. The solution was to use a small aluminium measuring stick that was bent over the rim of the reservoir and pressed against the contours of the dip cup. The measuring stick extended down into the reservoir of the dip cup approximately 10 mm. The stick was small so that its volume would have a negligible effect upon any measurements that were taken. Two deep grooves were cut into the measuring stick, measuring 10 mm apart, to prevent any LM136 coating rendering these marks unreadable. This enabled the efflux time to be measured between two marks. However, after two tests it was noticed that the distance between the marks was actually 13 mm. A new measuring stick was made and the distance between the level marks were checked and determined to actually be 10 mm. There was a further problem with using electric heating. Winding nichrome wire and fixing the position of the coils using Araldite was a time-consuming and delicate task. After the glass beaker was broken twice, due to solidified LM136 that had expanded, and due to time constraints, the electric heating was substituted for a Bunsen burner.

The temperature of LM136 was measured using a type-K thermocouple, with a class 1 tolerance and an associated accuracy of ± 0.004T in the temperature, T, range -40 to 1000°C [BSI, 2013], which was connected to a handheld Digitron thermocouple reader. Approximately 500 ml of LM136 was heated above 80°C and allowed to

cool. Measurements were made when the temperature of the molten LM136 reached 80 ± 0.3°C and ceased once the volume of LM136 reached 70 ± 0.3°C.

Eleven test runs involving LM136 were undertaken. The first used a level change within the reservoir of 55 mm. The results of this test are presented in table A.1 of appendix A. The second two tests used a measuring stick and a level change of 13 mm. The results of these tests are given in tables A.2 and A.3. The remaining tests used a revised measuring stick and a level change of 10 mm within the reservoir. The results of these tests are presented in tables A.4 through to A.11 and are the basis for the results summary given in table 7.2. Within a single test run several efflux times were measured whilst the molten LM136 cooled from 80°C to 70°C. The geometric mean of the efflux times was taken to give the dynamic viscosity for a single test.

The standard deviation of efflux times within a single test was calculated and the arithmetic mean dynamic viscosity was taken for the last eight tests (tables A.4 to A.11). The final value for the dynamic viscosity of LM136 was determined to be 8.8 +/- 0.4 x 10^{-3} Pa s. This takes into account the systematic error in measuring between the level marks due to the meniscus, which lead to uncertainties in determining the volumetric flow rate in the reservoir.

Test Run	**μ (Pa·s)**
4	8.90E-3
5	9.19E-3
6	9.53E-3
7	8.60E-3
8	8.28E-3
9	8.89E-3
10	8.50E-3
11	8.38E-3
Arithmetic mean	**8.78E-3**
Standard deviation of μ	**4.26E-4**

Table 7.2 Summary of dynamic viscosity test results, using a Δh of 10 mm and data given in tables A.4 through to A.11 for LM136 between 70°C and 80°C

7.2 Surface Tension

The accuracy of the surface tension test apparatus was determined by first using a substance with a known surface tension: water at 20°C, where the surface tension is 7.3×10^{-2} N/m [Kaye & Laby, 1973]. Liquid temperatures were determined using a Digitron handheld thermocouple reader. The buoyancy force registers as a positive reading on the balance, whilst a negative reading is registered for the force relating to surface tension, providing that the balance is zeroed when the glass slide is out of the water. The level of water in the glass beaker was varied by using a syringe to gently draw or express the water from a small-diameter plastic tube. A second test was conducted where the draught intervals were increased from 2 mm to 5 mm to reduce the error in visually determining the draught on the glass plate. A balance reading was also taken when the glass slide was just removed from the water, i.e., at zero draught. If the balance did not read zero then this would indicate some cause of error or hysteresis. The results in table 7.3 represent readings taken whilst operating between two fixed volumes, dictated by two states: full syringe and empty syringe, giving two levels in the beaker and on the slide. This cyclical emptying and filling process was performed to investigate the effects of water retention of the glass slide.

Syringe State	Reading (g)
Empty 1	0.0000
Full 1	+0.7200
Empty 2	-0.0060
Full 2	+0.7560
Empty 3	-0.0203
Full 3	+0.7542
Empty 4	-0.0280
Full 4	+0.7598
Empty 5	-0.0241
Full 5	+0.7620

Table 7.3 Investigation into hysteresis by alternating two known volume states

These results perhaps show the effects of water retention on the glass plate when in the 'empty' state. However, this could also indicate water retention in the syringe, or perhaps some error associated with determining the draught on the glass plate. A combination of water retention on the glass plate, water retention in the syringe and draught angle measurement may account for some discrepancies in earlier tests, such as those presented in tables B.1 and B.2 of appendix B.

The glass beaker and glass plate were cleaned using acetone. Fresh de-ionised water was then added to the glass beaker before three further tests were performed. These are presented in appendix B as tables B.3, B.4 and B.5, respectively. They show an increasing level of deviation between the measured values and the known surface tension of water at 20°C.

The deviations are larger for higher draught values, but the results also show that a contact angle hysteresis exists, where a higher deviation is recorded when the glass is approaching the water. It was concluded that in addition to the discrepancies caused by the potential build-up of impurities on the glass plate, on the glass beaker and in the water, these discrepancies could be due to incomplete wetting of the glass plate, i.e., the contact angle $\theta \neq 0$. Thus, the procedure for carrying out a single test run was altered. The glass beaker was cleaned using acetone before each test and a clean glass plate was also used for each new test.

Furthermore, upon deeper examination of surface tension theory, it was found that Young's equation (7.1) describes the contact angle of a liquid drop on an ideal surface as the mechanical equilibrium of a drop under the action of three interfacial tensions [Yuan & Lee, 2013]

$$\gamma_{lv} \cos \theta_{\gamma} = \gamma_{sv} - \gamma_{sl} \tag{7.1}$$

where the subscripts lv, sv and sl refer to the liquid-vapour, solid-vapour and solid-liquid interfacial tensions, respectively. θ_{γ} is Young's contact angle.

The force diagram for the Wilhelmy plate method in figure 7.1 shows how the three thermodynamic parameters, γ_{lv}, γ_{sv} and γ_{sl}, are distributed. The contact angle formed whilst increasing the liquid volume, i.e., when the glass plate is approaching the liquid, gives rise to what is called the approaching contact angle. When the liquid volume is decreasing and the glass plate is receding from the liquid, the receding contact angle is achieved.

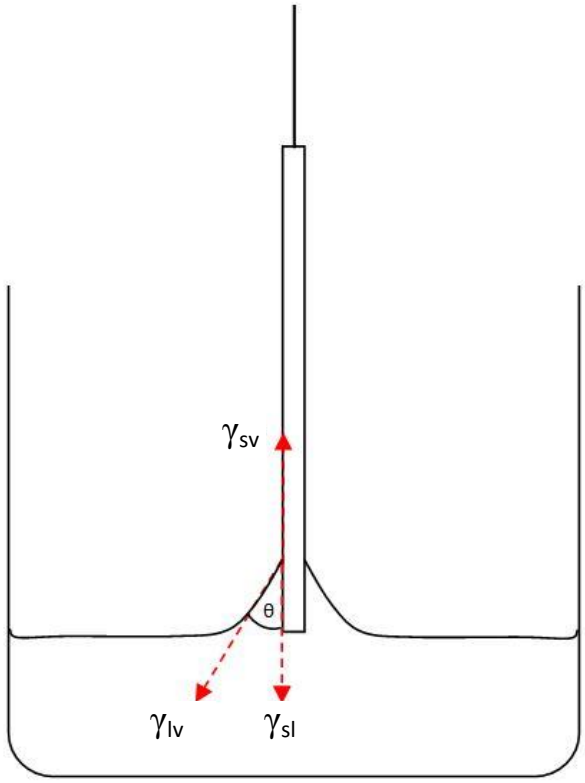

Figure 7.1 Wilhelmy plate method showing interfacial tensions

These 'dynamic' contact angles fall within a range: a maximum for the approaching contact angle, θ_a, and a minimum for the receding contact angle, θ_r. At low speed the dynamic contact angles approach the static contact angle. The hysteresis is given by

$$H = \theta_a - \theta_r \tag{7.2}$$

The general conclusion is that either heterogeneity or surface roughness causes contact angle hysteresis, or some combination of both. On ideal surfaces there is no contact angle hysteresis, but where it is present the experimentally observed θ_a is expected to be a better approximation than θ_r because of lower reproducibility due to liquid sorption or solid swelling [Yuan & Lee, 2013].

A further three tests (tables B.6, B.7 and B.8, respectively, presented in appendix B) were conducted and the averaged results are shown in table 7.4. The results indicate, however, that the receding contact angle offers the lowest deviation, suggesting that surface tension values for LM136 should be determined using the receding contact angles, where the deviations are found to be lowest. Furthermore, the corrected contact angle indicates incomplete wetting.

The surface tension apparatus was setup for liquid metal. Nichrome windings were added to the glass beaker and the LM136 was subsequently heated to 80°C and successfully held at this temperature. Using the same syringe method, used previously for altering the level of water in glass beaker, resulted in the LM136 solidifying within the syringe tube, prompting an alternative method to be sought. A further problem was also caused by the LM136 coating the glass slide and thus preventing the reading of any draught marks. However, now that the surface tension apparatus had been calibrated using water, it was realised that only one draught need be measured, providing that the same draught, using a receding contact angle, was used.

Approximately 150 ml of LM136 was heated to 80°C and held at this temperature using electric heating. The balance reading was taken and then the power supply to the nichrome wire was switched off, allowing the LM136 to cool to 70°C where a second balance reading was then taken. This was repeated three times. Due to LM136 coating the inside of the beaker the draught needed to be measured after the test. Due to the need for a receding contact angle, which produced lower deviations than approaching contact angles, the glass plate needed to be submerged past the desired draught and allowed to return to the desired draught. This created the

required receding contact angle. At the end of the first test, however, it was noticed that the glass slide was not entering the LM136 perpendicularly, which likely gave inaccurate readings. For the second and third tests fresh, clean slides were used and care was taken to insert the slides perpendicularly. The results are presented in table 7.5 below and show that within the specified temperature range there is negligible variance in the surface tension of LM136.

D (mm)	**5**	**10**	**15**	**20**	**15**	**10**	**5**	**0**
Balance (g)	-1.44 E-01	5.71 E-02	2.53 E-01	4.75 E-01	1.05 E-01	-1.26 E-01	-3.02 E-01	-2.27 E-03
F_{Total} (N)	-1.41 E-03	5.61 E-04	2.48 E-03	4.65 E-03	1.03 E-03	-1.23 E-03	-2.96 E-03	-2.20 E-05
$F_{Buoyancy}$ (N)	1.91 E-03	3.83 E-03	5.74 E-03	7.65 E-03	5.74 E-03	3.83 E-03	1.91 E-03	0
F_{γ} (N)	-3.32 E-03	-3.26 E-03	-3.26 E-03	-3.00 E-03	-4.71 E-03	-5.06 E-03	-4.87 E-03	-2.20 E-05
γ (N/m)	4.16 E-02	4.08 E-02	4.07 E-02	3.74 E-02	5.89 E-02	6.32 E-02	6.10 E-02	2.77 E-04
γ_{water} (N/m)	7.30 E-02	7.30 E-02	7.30 E-02	7.30 E-02	7.30 E-02	7.30 E-02	7.30 E-02	0
Deviation (%)	43	44	44	49	19	13	17	~0
Revised θ (°)	55.3	56	56.1	59.1	36	30	33.4	90

Table 7.4 Averaged results of water surface tension tests using a wetted perimeter of 80 mm, given in tables B.6, B.7 and B.8, for a range of draught values, D

However, for the results given in table 7.5, the draught was not equal between tests, likely due to the glass slide not being fully inserted into its holding slot. Once this was recognised the tests were repeated. A final balance reading was taken to determine any hysteresis experienced by the apparatus.

Test no.	**1**		**2**		**3**	
D (m)	0.022	0.022	0.019	0.019	0.017	0.017
L_{Wetted} (m)	0.08	0.08	0.08	0.08	0.08	0.08
T_{LM136} (°C)	80	70	80	70	80	70
ρ_{LM136} (kg/m^3)	8581		8581		8581	
Balance (g)	1.37E+01	1.36E+01	1.30E+01	1.30E+01	1.38E+01	1.37E+01
F_{Total} (N)	1.34E-01	1.33E-01	1.28E-01	1.27E-01	1.36E-01	1.35E-01
$F_{Buoyancy}$ (N)	7.22E-02	7.22E-02	6.24E-02	6.24E-02	5.58E-02	5.58E-02
F_γ (N)	6.17E-02	6.07E-02	6.54E-02	6.49E-02	7.98E-02	7.90E-02
γ (N/m)	7.71E-01	7.59E-01	8.18E-01	8.11E-01	9.97E-01	9.87E-01
Balance final (g)	9.00E-04		0		3.00E-04	

Table 7.5 Summary of first results for LM136 surface tension tests

Given in table 7.6 are the averaged results of the repeated tests, the full results themselves are given in table B.9 of appendix B. The results of table 7.6 indicate that at 80°C the surface tension of LM136 is approximately 0.814 N/m, whilst at 70°C the surface tension is found to be 0.807 N/m.

Surface tension tends to be inversely proportional to temperature, so these results must have some error associated with them. Since there appears to be very little dependence upon temperature, however, a value of 0.8 N/m for LM136 in the temperature range 70°C to 80°C can be used. Visual inspection of the contact angle had been made for water by looking through the side of the beaker at the level of the free surface. Due to LM136 coating the sides of the beaker, however, a visual estimation of the contact angle could not made in this manner. A visual inspection of contact angle for LM136 could be made from observing the free surface above the rim of the beaker, but estimation on this basis would be questionable due to parallax error. However, it was observed that when the glass slide approached the molten LM136 a visible non-zero approaching contact angle was formed, but when the glass plate was receding, the receding contact angle appeared to be zero, or very close to zero. Noting the lower deviation values for receding contact angles in the water surface tension tests, and estimating systematic errors due to the determination of the contact angle and draught interval, a maximum deviation of approximately 16% was calculated for the surface tension of LM136 in the aforementioned temperature range. Table 7.6 below summarises the final surface tension results for LM136.

Draught (m)	**0.018**	**0.018**
Wetted perimeter (m)	0.08	0.08
T_{LM136} (°C)	80	70
ρ_{LM136} (kg/m^3)	8581	
Balance (g)	0.127	0.127
Total F (N)	0.124	0.124
F_B (N)	5.91E-02	
F_γ (N)	6.51E-02	6.50E-02
γ (N/m)	**0.814 +/- 0.16**	**0.813 +/- 0.16**
Final Balance (g)	1.00E-04	

Table 7.6 Averaged results of final LM136 surface tension tests, given in table B.9 of appendix B

7.3 Two-Phase Air/Water Mixture

This initial investigation into buoyancy-driven air/water mixtures allowed both the two-phase flow regime and the buoyancy principle to be observed, albeit without any electrical power generation via the MHD generator. The accuracy of the mathematical model was tested and compared against predicted values. An energy balance was carried out using experimental values.

A Plaxton NGX rotameter capable of measuring air flow rates between 10 cm^3/min and 100 cm^3/min, with a resolution of 5 cm^3/min, was used to investigate air/water mixtures in the main experimental apparatus for a range of volumetric air flow rates.

Since this was an initial exploration into buoyancy-driven two-phase flows, the choice of air flow rate was less important. Hence, the Plaxton NGX rotameter already installed was used.

Air flow rates below 70 cm^3/min produced a pulsating effect from the nozzle. It was decided, therefore, that data should be recorded for air flow rates between 70 cm^3/min and 100 cm^3/min, as it was deemed desirable to comprehend the buoyancy-driven two-phase circuit under a steady-state condition. However, data was also recorded for flow rates of 50 cm^3/min and 60 cm^3/min because they offered a potential insight into pulsed MHD power generation: if there are sections of liquid metal passing through an MHD generator without bubbles, which are thought to limit charge separation, then potentially higher power densities could be achieved.

With lagging around the glass of the heating section, the heat supplied to the apparatus was assumed equal to the electrical input registered on the EA-PS 2042-20B power supply, which had output voltage and output current tolerances of $\leq 0.2\%$ and $\leq 0.05\%$, respectively.

Equation (7.3) was used to convert the volumetric flow of air in the rotameter to the actual mass flow rate of air entering the apparatus. Using the temperatures recorded by the thermocouples, and the averaged specific heat of water in the heating section, the mass flow of water in the heating section was determined. These values are given

in table 7.7, along with the flow quality, x, calculated by using the ratio of the air mass flow to the total mass flow (see equation 4.2). The maximum and minimum thermocouple temperatures for the heating section (see table 7.7) enable the maximum and minimum water mass flow rates to be calculated. The error in flow quality is found by using these calculated maximum and minimum water mass flow rates.

$$\dot{m}_{actual} = \dot{V}_{actual}\rho_{actual} = \left[\dot{V}_{rot\_air}\left(\frac{T_{NTP}P_{actual}}{T_{actual}P_{NTP}}\right)^{-1/2}\right]\left[\rho_{rot\_air}\left(\frac{T_{NTP}P_{actual}}{T_{actual}P_{NTP}}\right)\right] \tag{7.3}$$

where T_{NTP} and P_{NTP} are temperature and pressure under NTP conditions, respectively.

There were two locations where it was deemed, when designing the experimental apparatus, desirable to measure the pressure drop: over the length of the MHD duct and across the flow restriction. Since no MHD pressure losses were present, any pressure loss over the length of the MHD duct was due to gravity and friction. The penetration of the flow restriction could vary in the range 0 - 20 mm and could control the water mass flow depending upon the penetration. For the purpose of a limited air/water test run the penetration was set to 10 mm. This was sufficient to allow a measurable pressure drop and suitably low impedance to the flow.

At the start of the test the apparatus was filled with water. The water level in the manometers was equal to the water level in the separator. Once the air flow was started the level in the manometers for the two-phase sections fell to indicate the loss of head, whilst the single-phase manometer indicated the loss of head in the downcomer. These values were determined visually using a ruler.

Using the water density at the restriction, assumed equal to the water density at downcomer exit, and the water velocity upstream from the restriction, determined from continuity, the loss coefficient, K, was calculated. Table 7.8 provides the manometer readings and loss coefficients for all volumetric air flow rates used in the experiment.

$\dot{V}_{air\_rot}$ (cm^3/min)	**50**	**60**	**70**	**80**	**90**	**100**
P_{rot_air} (kPa)	111.4	111.4	111.4	111.4	111.4	111.3
$\dot{V}_{air\_actual}$ (m^3/s)	8.3E-7	9.9E-7	1.2E-6	1.3E-6	1.5E-6	1.7E-6
$\dot{m}_{air\_actual}$ (kg/s)	1.0E-6	1.2E-6	1.5E-6	1.7E-6	1.9E-6	2.1E-6
Voltage (V)	41.9	41.2	41.4	41.3	41.9	41.9
Current (A)	7.60	7.51	7.56	7.57	7.63	7.64
Power (W)	318.4	309.4	313.0	312.6	319.7	320.1
Heating entry (°C)	41.3 ± 0.2	41.6 ± 0.2	41.1 ± 0.2	40.3 ± 0.2	41.9 ± 0.2	41.4 ± 0.2
Heating exit (°C)	42.2 ± 0.2	42.0 ± 0.2	41.7 ± 0.2	41.1 ± 0.2	42.7 ± 0.2	42.4 ± 0.2
Water mass flow (kg/s)	**0.085 ± 0.03**	**0.185 ± 0.07**	**0.115 ± 0.05**	**0.094 ± 0.04**	**0.096 ± 0.04**	**0.077 ± 0.03**
Flow quality	1.2E-05 ± 3E-6	6.7E-06 ± 2E-6	1.3E-05 ± 4E-6	1.8E-05 ± 6E-6	1.9E-05 ± 6E-6	2.7E-05 ± 7E-6
MHD entry (°C)	43.2 ± 0.2	43.1 ± 0.2	42.7 ± 0.2	41.9 ± 0.2	43.4 ± 0.2	42.9 ± 0.2
MHD exit (°C)	43.2 ± 0.2	43.1 ± 0.2	42.7 ± 0.2	41.9 ± 0.2	43.4 ± 0.2	42.9 ± 0.2
Upcomer exit (°C)	43.4 ± 0.2	42.5 ± 0.2	43.1 ± 0.2	42.3 ± 0.2	43.7 ± 0.2	43.2 ± 0.2
Downcomer IHX entry (°C)	43.2 ± 0.2	43.3 ± 0.2	42.8 ± 0.2	42.1 ± 0.2	43.5 ± 0.2	43.0 ± 0.2
Downcomer IHX exit (°C)	42.3 ± 0.2	42.4 ± 0.2	41.9 ± 0.2	41.2 ± 0.2	42.8 ± 0.2	42.2 ± 0.2
Gas entry (°C)	20.7 ± 0.1	20.4 ± 0.1	19.9 ± 0.1	19.9 ± 0.1	19.9 ± 0.1	19.9 ± 0.1
Gas exit (°C)	29.6 ± 0.1	29.4 ± 0.1	26.9 ± 0.1	26.4 ± 0.1	28.4 ± 0.1	30.9 ± 0.1
IHX water entry (°C)	18.1 ± 0.1	19.3 ± 0.1	19.7 ± 0.1	19.4 ± 0.1	20.4 ± 0.1	20.1 ± 0.1
IHX water exit (°C)	24.8 ± 0.1	24.7 ± 0.1	25.1 ± 0.1	24.7 ± 0.1	26.7 ± 0.1	26.3 ± 0.1

Table 7.7 Recorded temperatures for a range of air flow rates, including deduced water mass flow rates and electrical power settings assuming negligible leakage

$\dot{V}_{air\_rot}$ (cm^3/min)	50	60	70	80	90	100
ρ_{tp} (kg/m^3)	982	985	982	979	977	972
Δh mixer outlet (mm)	6	7.5	7.5	7.5	9.5	10
Δh MHD outlet (mm)	4.5	6	5	5	7	8
Δh manometers (mm)	1.5	1.5	2.5	2.5	2.5	2
Δh downcomer (mm)	2.5	3	3	5	7.5	8
$\rho_{water\_restriction}$ (kg/m^3)	991	991	992	992	991	991
u_{water} upstream from restriction (m/s)	0.27	0.59	0.37	0.30	0.31	0.25
Restriction loss coefficient, K	0.67	0.17	0.43	1.10	1.53	2.51

Table 7.8 Summary of pressure losses, relative to reservoir, in MHD duct and from flow restriction with a penetration of 10 mm

Using the temperature data and water mass flows, presented in table 7.7, and averaged specific heats, an energy balance for the air/water two-phase system can be performed. This is shown in table 7.9. The volumetric flow rate of water leaving the cooling jacket on the apparatus was measured using an external reservoir, with a fixed volume, and a handheld stopwatch. There is a human error associated with this method, and this could be the reason why the values for the downcomer and external cooling circuit do not closely match in table 7.9.

The heat received in the heating section is also not matched by the heat rejected in the downcomer, however, taking into consideration the heat loss around the apparatus and no significant variation in the specific heat of water, with some unusual instances of heat reception likely due to an imperfect balance between thermocouples, the energy balances. An exception to this was when the volumetric flow rate of air in the rotameter was 70 cm^3/min. The minor discrepancy shown for 50 cm^3/min is due to rounding error. Heat reception should only occur in the heating section, but the proximity of the heating wire to the vertical two-phase section could have caused anomalous thermocouple readings.

$\dot{V}_{rot\_air}$ (cm^3/min)	**50**	**60**	**70**	**80**	**90**	**100**
$\dot{Q}_{heating\_section}$ (W)	**318**	**309**	**313**	**313**	**320**	**320**
$\dot{Q}_{downcomer}$ (W)	**-319**	**-696**	**-433**	**-352**	**-280**	**-256**
$\dot{Q}_{air}$ (W)	9.2E-6	1.1E-5	1.0E-5	1.1E-5	1.6E-5	2.3E-5
$\dot{Q}_{heating\_section-MHD\_section}$ (W)	354	851	482	313	280	160
$\dot{Q}_{MHD}$ (W)	0	0	0	0	0	0
$\dot{Q}_{upcomer}$ (W)	71	-464	193	156	120	96
$\dot{Q}_{separator}$ (W)	-71	619	-145	-78	-80	-64
$\dot{Q}_{downcomer\_exit-heating\_entry}$ (W)	-354	-619	-385	-352	-360	-256
$\dot{Q}_{net\_loop}$ (W)	**-1**	**0**	**25**	**0**	**0**	**0**
$\dot{Q}_{external\_cooling}$ (W)	**248**	**207**	**203**	**201**	**212**	**208**

Table 7.9 Energy balance for air/water two-phase system, showing heat reception (green) and expected heat rejection (orange) using thermodynamic sign convention

The temperature of air at nozzle inlet and outlet, the mass flow of air and the temperature of water at nozzle exit, given in table 7.7, formed the initial conditions for the model. This enabled a comparison between the model and the experimental results to be made, which is presented below in table 7.10.

Nominal $\dot{V}_{air}$ (cm^3/min)	**50**	**60**	**70**	**80**	**90**	**100**
Nozzle gas entry (specified/test)	20.7	20.7	19.9	19.9	19.9	19.9
Nozzle gas exit (specified/test)	19.5	19.5	18.7	18.7	18.7	18.7
Water at nozzle exit (specified/test)	42.2	42.0	41.7	41.1	42.7	42.4
Mixer exit (model/test)	42.2/ 43.2	42.0/ 43.1	41.7/ 42.7	41.1/ 41.9	42.7/ 43.4	42.4/ 42.9
MHD exit (model/test)	42.2/ 43.2	42.0/ 43.1	41.7/ 42.7	41.1/ 41.9	42.7/ 43.4	42.4/ 42.9
Upcomer exit (model/test)	42.2/ 43.4	42.0/ 42.3	41.7/ 43.1	41.1/ 42.3	42.7/ 43.7	42.4/ 43.2
Downcomer entry (model/test)	42.2/ 43.2	42.0/ 43.3	41.7/ 42.8	41.1/ 42.1	42.7/ 43.5	42.4/ 43.0
Downcomer exit (model/test)	41.3/ 42.3	41.6/ 42.4	41.1/ 41.9	40.3/ 41.2	41.9/ 42.8	41.4/ 42.2
Water mass flow (model/test)	**0.079/ 0.085**	**0.084/ 0.185**	**0.089/ 0.115**	**0.093/ 0.094**	**0.095/ 0.096**	**0.098/ 0.077**
Flow quality, x (model/test)	1.3E-5/ 1.2E-5	1.5E-5/ 6.7E-6	1.6E-5 1.3E-5	1.8E-5 1.8E-5	2.0E-5/ 1.9E-5	2.1E-5/ 2.7E-5

Table 7.10 Comparison of temperatures (°C), water mass flow rates (kg/s) and flow quality between the predicted and experimental results for a range of air volumetric flow rates using an air/water mixture

The difference between the predicted and measured water mass flow rates is shown below in figure 7.2. Increased air mass flow rates should decrease the two-phase mixture density in the two-phase sections, leading to an increase in dynamic head and higher water mass flow rates. An upward trend in the positive x-direction should be seen in figure 7.2, however, this is not present.

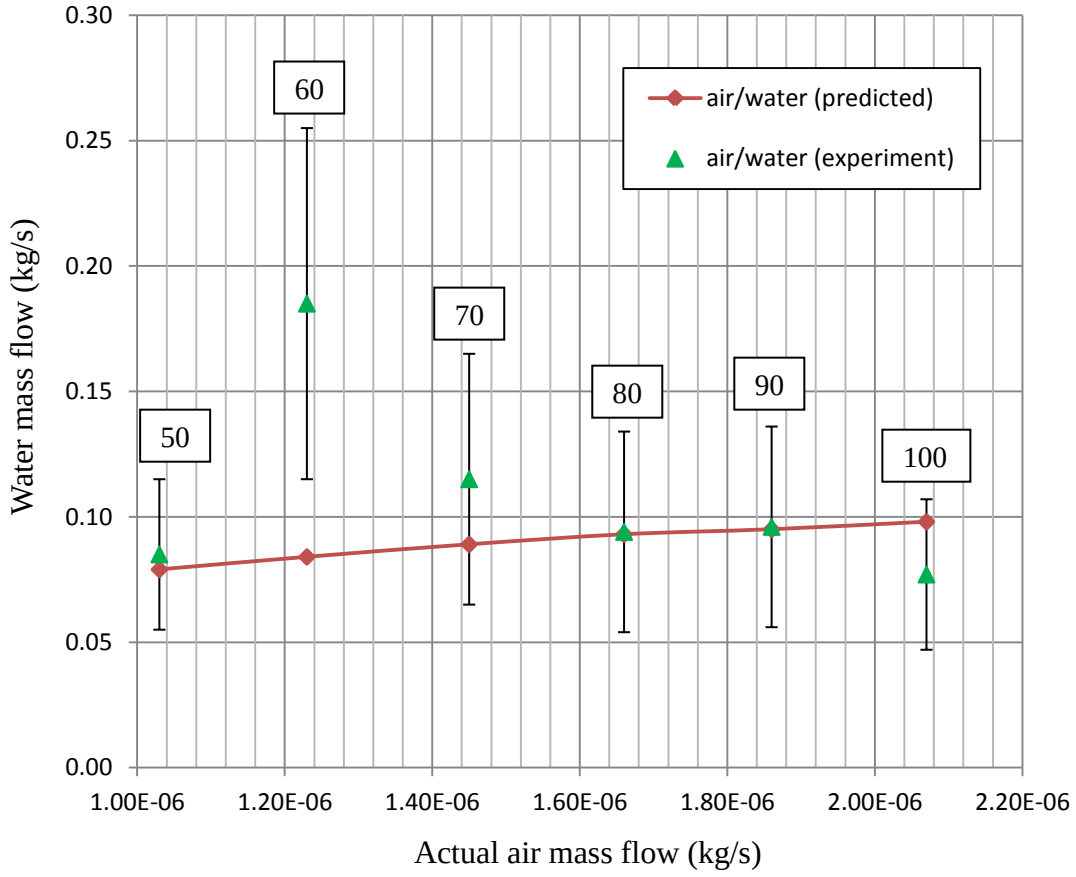

Figure 7.2 Comparison between predicted and experimental values (with error) of water mass flow rates for a range of air mass flow rates using an air/water mixture, also showing uncorrected rotameter air volumetric flow rates to which the data points refer

The loss coefficient, K, deduced from the experimentally determined water mass flow rates, and given in table 7.10, could not be relied upon for accuracy. Instead, using the ratio of the large pipe diameter to the smaller pipe diameter, and using

continuity to determine the water velocity at the restriction, values for K relating to a sudden contraction were taken from Brater et al. [1996]. These are given in table 7.11 below.

$\dot{V}_{air}$ (m^3/s)	50	60	70	80	90	100
Δh mixer outlet (model/test)	2.8/ 6.0	3.1/ 7.5	3.4/ 7.5	3.5/ 7.5	3.6/ 9.5	3.9/ 10.0
Δh MHD outlet (model/test)	1.7/ 4.5	1.9/ 6.0	2.1/ 5.0	2.3/ 5.0	2.3/ 7.0	2.4/ 8.0
Δh downcomer (model/test)	6.6/ 2.5	7.3/ 3.0	8.0/ 3.0	8.7/ 5.0	9.1/ 7.5	9.7/ 8.0
u_{water} restriction (model/test)	0.25/ 0.27	0.27/ 0.59	0.29/ 0.37	0.30/ 0.30	0.31/ 0.31	0.32/ 0.25
$K_{restriction}$ (model/test)	0.38/ 0.67	0.38/ 0.17	0.38/ 0.43	0.38/ 1.10	0.38/ 1.53	0.38/ 2.51

Table 7.11 Comparison of head loss (mm) and loss coefficient, K, between predicted and experimental results for a range of air volumetric flow rates using an air/water mixture

Photos of the two-phase flow were taken for the range of air flow rates used and are presented in figures 7.4, 7.5 and 7.6. It was hoped that these photos could be used to estimate the cross-sectional void fraction and, via the flow quality, subsequently deduce the slip ratio. The two-phase mixture density, for the mixer, MHD and upcomer, respectively, could then be estimated and compared with table 7.8.

These photos are included to show that for the volumetric air flow rates that were used, the two-phase flow remained in the bubbly flow regime. Figures 7.3, 7.4 and 7.5 show the two-phase flow regime.

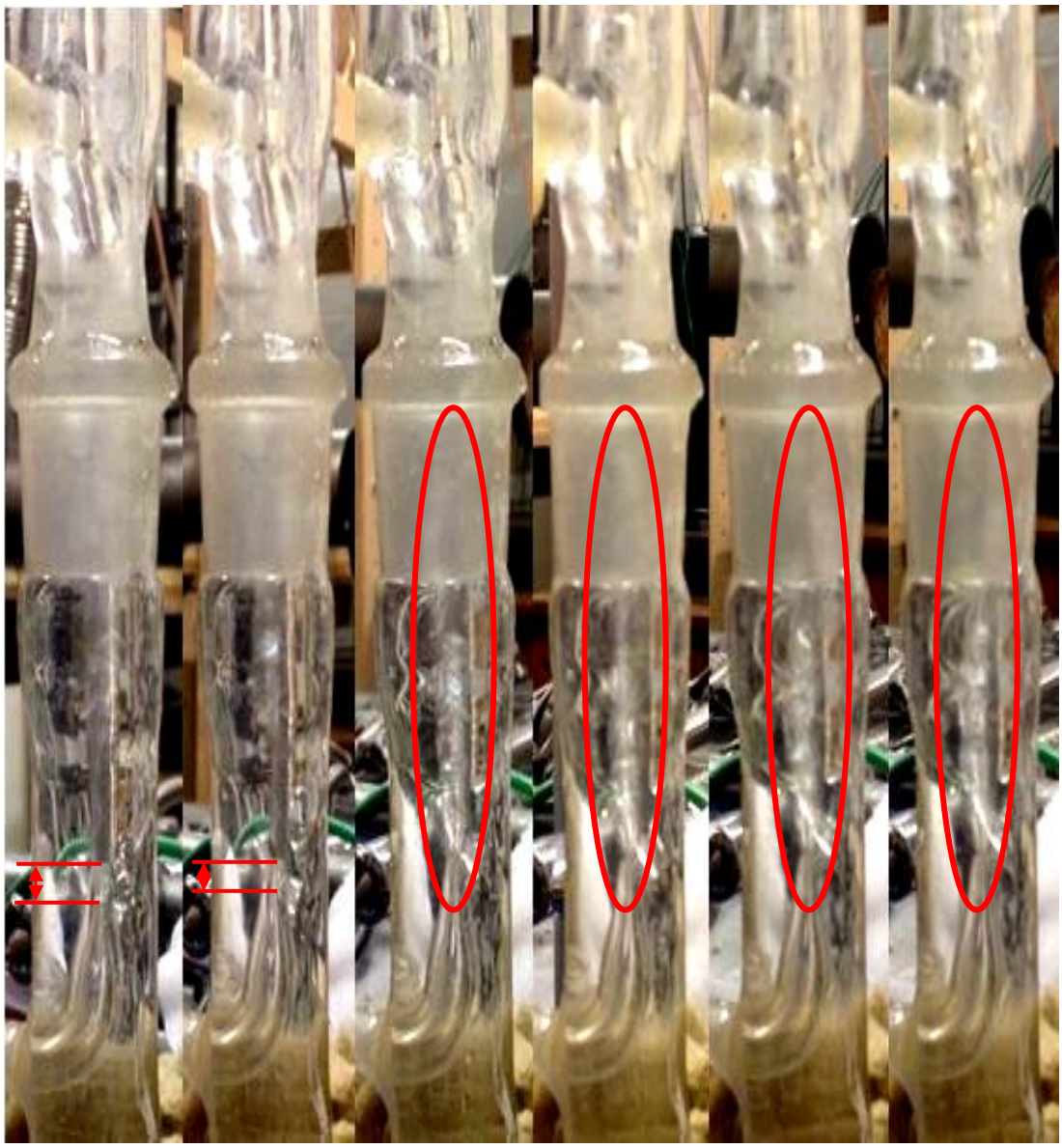

Figure 7.3 Pictures of two-phase flow regime at mixer inlet for air flow rates (left to right) between 50 and 100 cm^3/min. Parallel lines (red) highlight the nozzle back pressure that causes the pulsing effect. Ellipses (red) highlight the path of the air bubbles from the nozzle entering the mixer

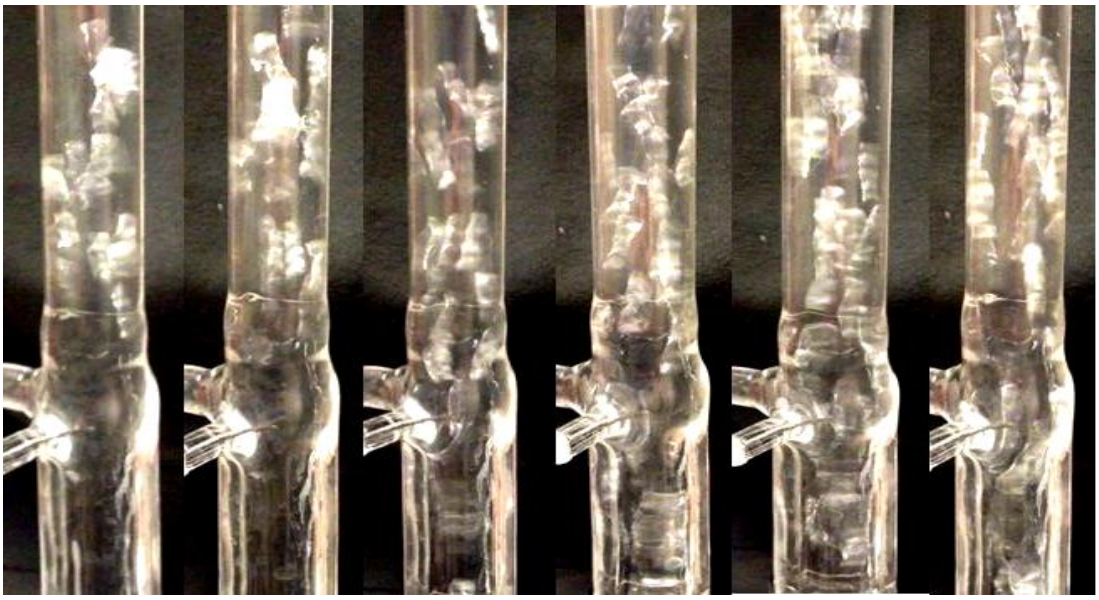

Figure 7.4 Pictures of two-phase flow regime at MHD outlet for nominal air flow rates (left to right) between 50 and 100 cm^3/min

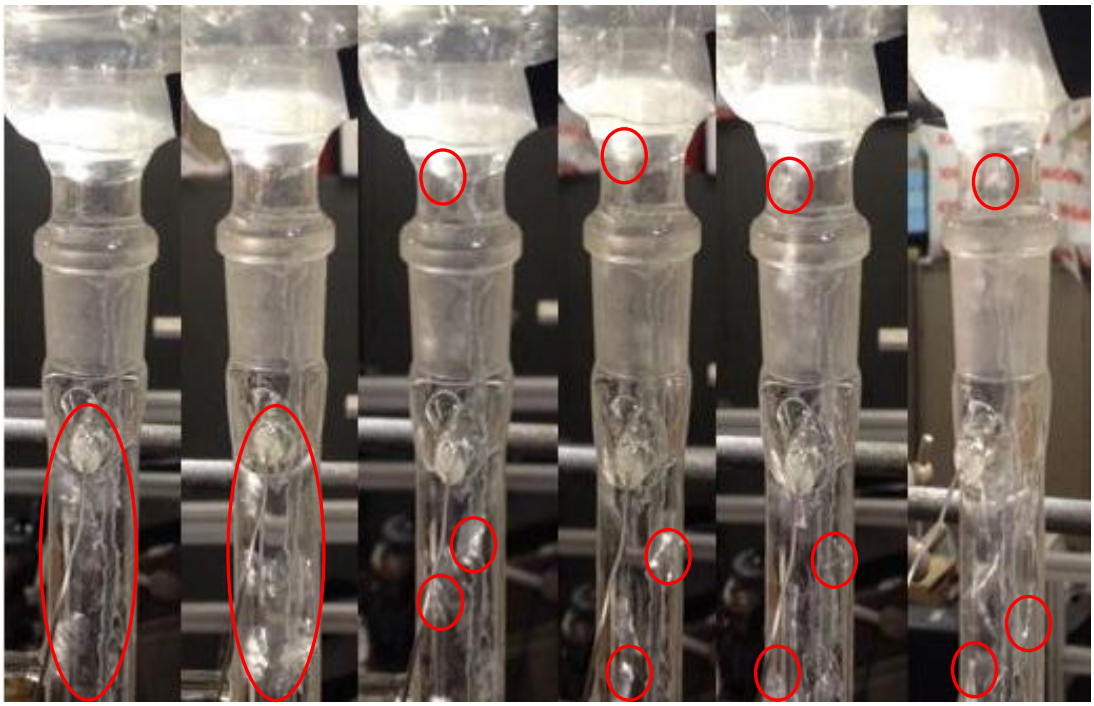

Figure 7.5 Pictures of two-phase flow regime at upcomer outlet for air flow rates (left to right) between 50 and 100 cm^3/min. Individual and grouped bubbles highlighted in red

The combined images in figure 7.3 show that for nominal air flow rates between 70 and 100 cm^3/min the bubbles exiting the nozzle, which are difficult to see without highlighting, follow a similar vertical path and appear to be the same diameter. This was also observed for nominal air flow rates of 50 and 60 cm^3/min, however, the back pressure on the nozzle, highlighted between the parallel lines, was instead shown because this produced the observed pulsing effect. In the case of nozzle pulsing, the pressure of the air reaching the nozzle exit was insufficient to overcome the water pressure. Air pressure within the nozzle built until it overcame the water pressure and released a stream of bubbles. The release of air pressure allowed water to flow back into the nozzle. Once the air pressure had again built-up within the nozzle the process repeated.

The combined images in figure 7.4 show no discernible difference in bubble size, only the increase in the frequency of bubbles, as expected. For nominal air flow rates of 50 and 60 cm^3/min the bubbles travel to the separator in 'packets'. Though difficult to discern from figure 7.5 the total height of these grouped air bubbles, highlighted in red, was observed to slightly increase with increasing air flow rate. A further observation was the deviation of air bubbles from a straight vertical path. As the air bubbles traversed the upcomer they began to follow a helical path. These individual bubbles, for nominal air flow rates between 70 and 100 cm^3/min, are highlighted in figure 7.5.

7.4 Air/LM136 Mixture

Similarly to the air/water tests, an investigation into a buoyancy-driven air/LM136 mixture allowed both the two-phase flow regime, albeit in a more limited sense, and the buoyancy principle to be observed. There wasn't any electrical power generation via the MHD generator due to experimental difficulties, which will be made clear in this subsection. The accuracy of the mathematical model was tested, however, and compared against predicted values. A limited energy balance was also carried out using experimental values.

A Bunsen burner was used to melt approximately 10 kg of LM136 in a large aluminium pan before attempts were made to gradually load the apparatus with molten LM136. The electric heating was activated to keep the LM136 in the liquid state within the apparatus. The first attempt involved bringing the level of molten LM136 to just below the drain hole. This was done so that the syringe technique, adopted for draining water from the apparatus via the drain hole, could be tested for use with LM136. This proved, however, to be problematic because molten LM136 solidified within the small diameter hose that was connected to the syringe. After solidification, a section of the hose containing the solid LM136 was cut and the fresh section of hose used to draw more molten LM136, which was a long and tedious process that highlighted the need for a new draining method to be identified.

Despite the tedious process of the current draining method, a second attempt at loading the apparatus was made, with the intention of bringing the level of molten LM136 above the MHD entry point. This was done to determine if a drip-draining method could be used to empty the apparatus down to the level of the drain, achieved by allowing a small opening in the drain to allow drips of molten LM136 to exit, in combination with the syringe method to drain the remaining molten LM136 below the drain. However, when molten LM136 began to fill the manometer at MHD inlet, it soon began solidifying. This had not occurred with the downcomer manometer, located near the base of the apparatus, due to its proximity to the heat source. Trace heating was needed and was subsequently applied to the manometers, where it was suspected that solidification would occur due to the increasing distance from the heat source with increasing manometer height.

Before a third attempt to completely fill the apparatus could be made, the blockage in the MHD entry manometer had to be cleared. Gentle warming with a heat gun re-liquefied the LM136 without any fracture occurring to the glass. After commencing with the third attempt it was noticed that due to marginal losses of LM136 inventory, mostly caused by adopting the syringe technique for draining, the existing LM136 inventory was insufficient to fill the entire apparatus and the level fell approximately two centimetres short of the separator. It was also noticed during this third attempt

that solidification had started to occur in the upcomer and downcomer. A heat gun had to be applied to keep the LM136 in the liquid state. Another problem was encountered due to the increased pressure head of LM136, which caused LM136 to flow back into the nozzle because the air flow rate was insufficient. An attempt to drip-drain was subsequently made, before a significant leak occurred from the MHD duct that short-circuited the electric heating. The molten LM136 could not be drained fast enough and solidification occurred in the heating section, causing the volume of the base of the apparatus to be completely occupied by LM136. Once cooled, an attempt was made to free this blockage with a heat gun, but trapped air inside the blocked section caused the glass to fracture, rendering the apparatus unviable for further use. A further blockage was noticed in the downcomer, but due to the extra layer of glass, comprising the external wall of the cooling jacket, the fracture caused by this blockage was not immediately noticed.

The subsequent course of action was to have two new nozzles, a new heating section and a new downcomer manufactured, which took approximately four weeks to complete. This experience prompted a review of the existing apparatus design and during the rebuild process a new drain was added to the base of the apparatus, consisting of a glass stopcock that was positioned at the very base of the apparatus that would allow the molten LM136 to be drained fully.

A new seal of Araldite was used around the MHD duct to protect against leaks and a different Plaxton NGX rotameter fitted, capable of supplying nominal volumetric flow rates of air up to 200 cm^3/min with a resolution of 10 cm^3/min. Once the entire apparatus was rebuilt, and more LM136 inventory delivered, a fresh attempt was made to circulate LM136 via buoyancy without a magnet.

The graphs in figure 7.6 show the limited data gathered during the only full test run using an air/LM136 mixture, where conditions within the apparatus were in their least transient state. It took approximately one hour to reach this reasonably steady-state condition, which lasted for just over six minutes, before leakage from the separator, caused by the bubbly two-phase flow seeping through the join between the

separator and its lid, pooled at the base of the apparatus and, despite the extra lagging, short-circuited the electric heating. An attempt to drain was made, but the weight of the entire LM136 inventory, now present in the apparatus, caused the drain to become lodged against the catching tray in such a manner that prevented any LM136 to escape. The remedying action, to lift the entire apparatus, caused the nozzle to break away from the apparatus since it was still clamped, which resulted in a major leak. The majority of the leaked LM136 was contained on the work surface, but a solidified volume remained at the base of the apparatus, unable to be drained.

After cooling, an inspection of the apparatus was performed, where a fracture was observed, once more, on the internal wall of the downcomer, between the downcomer and IHX section. Perhaps the most disappointing result occurred within a few moments of LM136 circulation, when one of the electrode plates was sheared away from its central locating stud, rendering any MHD measurements impossible. It was envisaged that once a steady-state was reached, photographic evidence of the two-phase flow regime in the mixer, MHD duct and upcomer would be gathered, but unfortunately there was insufficient time for this. Direct observation showed that the two-phase flow regime was mostly obscured by the LM136. However, coating of the internal glass tubing had not occurred, as was expected.

The same iterative procedure used for an air/water mixture enabled a comparison to be made between the predicted and experimental results for the limited air/LM136 testing. This is given in table 7.12, where the predicted head loss in the downcomer manometer was determined by using the same approach for the air/water tests. Since the penetration depth of the flow restriction was unchanged, and the liquid metal flow velocity similar to that of water, the same loss coefficient of 0.38 was assumed.

In the limited time that was available a pressure reading on the RDP E308 transducer, which measured the pressure in the rotameter to an accuracy of ± 0.1%, was noted as 0.84 bar. A head loss reading from the downcomer manometer, where the penetration depth of the flow restriction was 10 mm, of 160 mm was noted. Head loss readings from the manometers in the two-phase section were not taken, but the

electrical power input from the bench-top power supply was noted: 6.5 amps at approximately 30 volts. The volumetric flow rate of air was set at 200 cm^3/min.

By using a temperature of 80.2 (±0.3) °C for heating entry and 81.6 (±0.33) °C for heating exit outlet, using the values for when t is 14600 seconds in figure 7.6, and using the specific heat of 134 J/kg K [Bolton Metal Products], the mass flow rate of LM136 is found to be 1.04 kg/s. From this, a partial energy balance for the air/LM136 two- phase system can be performed. This is shown in table 7.13. Due to the lack of data for the mass flow of external cooling water, the energy balance between the downcomer and external cooling could not be performed.

Nominal $\dot{V}_{air}$ (cm^3/min)	**200**
Actual air mass flow	4.01E-6
Nozzle gas entry (specified/test)	27.0 (±0.11)
Nozzle gas exit (specified/test)	26.9 (±0.11)
LM136 at nozzle exit (specified/test)	81.6 (±0.33)
Mixer exit (model/test)	81.6/82.1 (±0.33)
MHD exit (model/test)	81.6/81.9 (±0.33)
Upcomer exit (model/test)	81.6/81.9 (±0.33)
Downcomer entry (model/test)	81.6/81.7 (±0.33)
Downcomer exit (model/test)	80.2/80.8 (±0.32)
LM136 mass flow (model/test)	**1.05/1.04 (±0.002)**
Flow quality, x (model/test)	3.82E-6/3.86 (±0.01) E-6
Δh downcomer (model/test)	10.5/160
U_{LM136} restriction (model/test)	0.4/0.39
$K_{restriction}$ (model/test)	0.38/0.41

Table 7.12 Comparison of temperatures (°C), LM136 mass flow rate (kg/s), LM136 velocity (m/s) and downcomer head loss (mm) between the predicted and experimental result for an air volumetric flow rate (rotameter) of 200 cm^3/min using a mixture of air and LM136

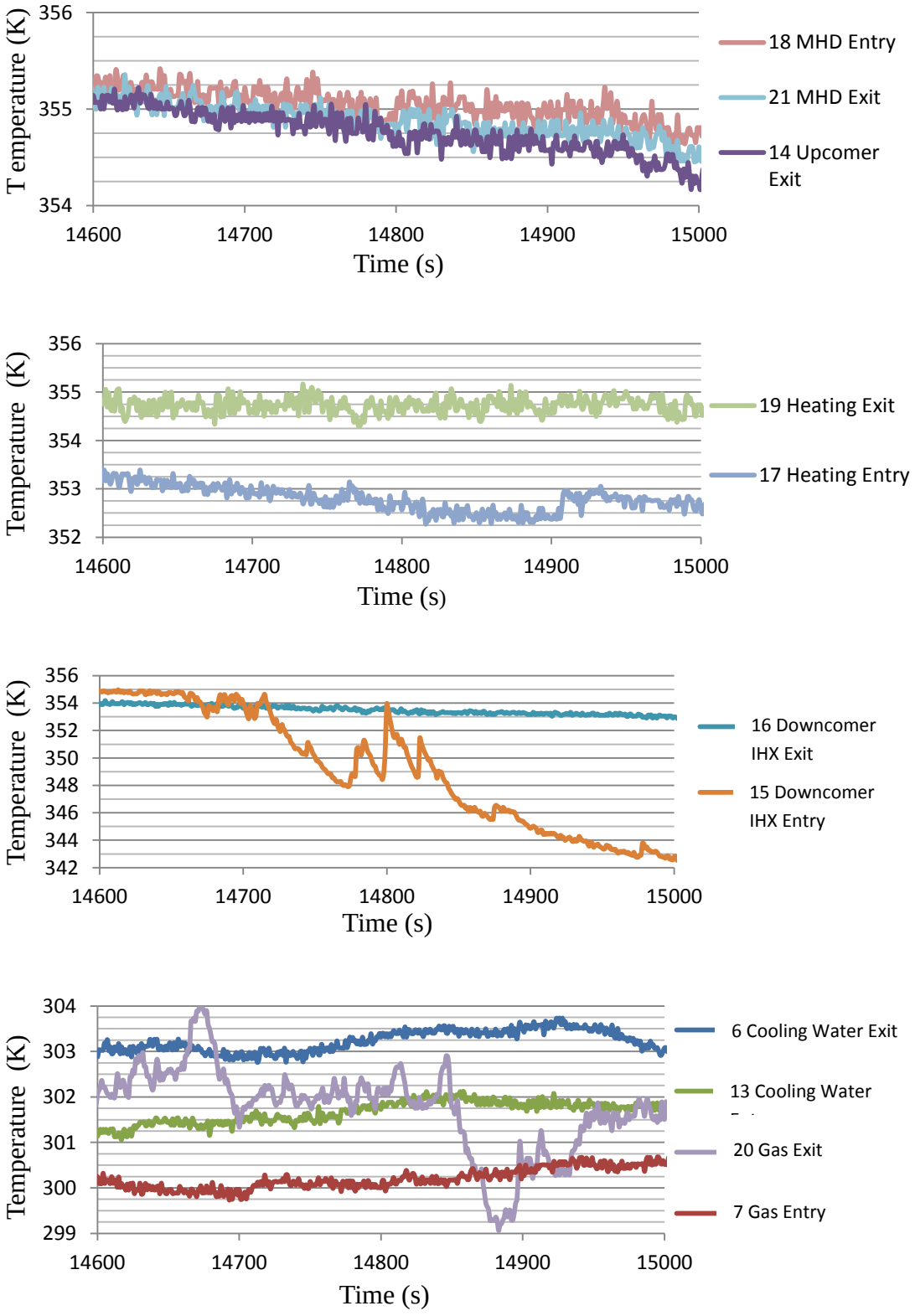

Figure 7.6 LM136, cooling water and air temperatures during quasi-steady conditions for an air/LM136 mixture

$\dot{V}_{rot\_air}$ **(cm^3/min)**	**200**
$\dot{Q}_{heating\_section}$ **(W)**	**195**
$\dot{Q}_{downcomer}$ (W)	-122
$\dot{Q}_{air}$ (W)	8.2E-3
$\dot{Q}_{heating\_section\text{-}MHD\_section}$ (W)	61
$\dot{Q}_{MHD}$ (W)	-27
$\dot{Q}_{upcomer}$ (W)	9
$\dot{Q}_{separator}$ (W)	-34
$\dot{Q}_{downcomer\_exit\text{-}heating\_entry}$ (W)	-82
$\dot{Q}_{net\_loop}$ **(W)**	**0**

Table 7.13 Energy balance for the air/water two-phase system, showing heat reception (green) and expected heat rejection (orange) using thermodynamic sign convention

7.5 Summary

Performing the initial tests using an air/water mixture was not only convenient, since the water was continuously in the liquid state and hence could remain in the apparatus without the need for draining, but the data also provided some insight into the workings of a buoyancy-driven apparatus. This was crucial due to the complexities and uncertainty of performing the same test with a previously untested air/LM136 mixture.

Despite the failure to measure any electrical power from the MHD duct, the circulation of a dense, electrically conductive liquid metal, using buoyancy via the addition of a gas phase, was achieved, thus partly meeting objective 1a.

Values for the viscosity and surface tension of LM136 were determined within the temperature range 70 – 80 °C, thus meeting objectives 3a, the measurement of the dynamic viscosity of the liquid phase, and 3b, the measurement of the surface tension of the liquid phase.

Data gathered from the thermocouples and manometers, with a penetration depth of 10 mm, for both air/water and air/LM136, allowed an energy balance to be performed, thus meeting objective 2c. Values predicted by the mathematical model can be compared with the experimental data, which will be done in chapter 8, and allow objective 1b to be met.

Objective 2a, the observation of the two-phase flow regime in the mixer, MHD and upcomer sections, could only be met for the air/water mixtures, whilst objective 2b, show that the two-phase liquid metal MHD generator behaves as expected, could not be met at all, due to the difficulties encountered when testing the air/LM136 mixture.

Unfortunately, time constraints did not allow for another rebuild of the experimental apparatus, which is felt could be made to work given the insights gained into some of the operational complexities. However, it is also apparent that a more robust design of the experimental apparatus, particularly of the MHD duct, would likely increase the chance of successfully meeting all the experimental objectives.

Chapter 8: Discussion

This chapter will begin with an examination of the elements that comprise the proposed power cycle configuration, namely the Brayton cycle, topping cycle and Rankine cycle, and the assumptions that have been made which have dictated its performance. This will be followed by a discussion of the experimental objectives and will conclude with a discussion of the experimental design process, where design flaws will be identified and remedial solutions offered.

8.1 Proposed Power Cycle

Many of the parameter values that dictated the performance of the proposed power cycle, such as the isentropic efficiencies of the turbo-machinery, the minimum pinch values for IHX processes, compressor inlet temperature and available thermal powers, were taken from a detailed report of PPCS model C by Norajitra et al. [2003]. These alone, however, do not comprise a power cycle and therefore further discussion of the other power cycle parameters is warranted.

8.1.1 Brayton Cycle

From an exploratory analysis of Brayton cycles in chapter 3, using the known plant parameters of PPCS model B and AB, it was clear that even under ideal circumstances a Brayton cycle operating with a turbine inlet temperature of 500°C would yield low cycle efficiencies. PPCS model C, therefore, with its high-enthalpy liquid metal breeder, offered a more attractive prospect.

A large difference between the PPCS-C power cycle configuration and the proposal is that the latter is a high-pressure primary Brayton cycle, compressing helium to 34.5 MPa and also using helium directly from the blanket for expansion in a gas turbine. This would inevitably incur tritium permeation effects and an understanding of this would be necessary to fully determine the viability of the Brayton part of the proposed power cycle. Filtration systems for the purpose of removing tritium from the blanket have already been designed, so it is reasonable to assume that these systems could be applied to the proposed power cycle. Furthermore, since tritium is more likely to permeate into the power cycle whilst helium is passing through the blanket, only the reheat section of the proposed power cycle will require filtration. If, however, tritium does permeate other parts of the cycle then existing filtration designs could be used throughout the entire power cycle.

Leakage of high-pressure helium through turbo-machinery casing could be problematic, but not insurmountable. As Hordeski [2011] notes, steam conditions between 30 MPa and 31.5 MPa are already achievable using chromium steels and austenitic steels, respectively. The extrapolation to 35 MPa steam conditions using nickel-based alloys is therefore reasonable. However, since helium has an atomic diameter of approximately 60 picometres [Cordero, 2008], and steam has a molecular diameter of approximately 275 picometres, interpolated from ionic radii data [Zhang and Xu, 1995], this presents a further challenge to confinement.

Pressure drops for all sixteen IHX processes have been neglected for the proposed power cycle. There are only eight IHX processes in the existing PPCS model C power cycle, for which Norajitra et al. [2003] provide an estimate of 1780 MW_e for the gross electrical power generated if pressure losses are neglected. This reduces to 1696 MW_e when pressure losses are included. The Brayton part of the proposed power cycle generates 1688 MW_e, but the MHD topping cycle and Rankine bottoming cycles add a further 431 MW_e to eclipse the existing value by 339 MW_e.

The proposal also removes the need to electrically pump the liquid metal breeder, saving 6.3 MW_e [Norajitra et al., 2003], thus reducing the power requirements of the plant to 210 MW_e. The additional pumping power required to overcome the pressure

losses for the IHX processes in the proposed power cycle might reach the point where the net electrical power output of the plant is lower than in the existing design, however, taking the same average pressure loss per IHX suggests that the extra losses will not negate the advantage.

A final remark should be made about the power output capability of gas turbines. At present the GE 9HA.02 gas turbine is listed as being capable of delivering a maximum output of 510 MW [General Electric]. The Brayton cycle in the proposal generates a net power output of nearly 1732 MW and would require at least four GE 9HA.02 gas turbines. The proposed power cycle, therefore, must consist of separate loops, much like Norajitra et al. [2003] have done with their configuration.

8.1.2 Two-Phase MHD Topping Cycle

This section of the proposed power cycle carries the greatest level of uncertainty due to its novelty. There are, therefore, several assumptions that require further discussion. The parameters associated with the topping cycle that required experimental verification, namely those in the two-phase sections, will be discussed first. This will be followed by a discussion concerning other parameters of the topping cycle where no attempt was made at experimental verification.

8.1.2.1 Experimentally Verifiable Assumptions

The nozzle outlet temperature is determined from the inlet conditions, as shown by (5.1). This is a well-established relationship and its accuracy holds providing that the contraction angle of the nozzle is less than ten degrees. The nozzle used in the experimental apparatus was designed and manufactured to possess such a contraction angle.

Initially, the nozzle outlet pressure must be higher than the static pressure of the liquid metal column present in the two-phase sections: mixer, MHD generator and upcomer. The mass flow of helium leaving the nozzle will lower the static pressure

in the two-phase sections due to a lower mixture density, as given by equations (4.11) and (4.2). Thus, for the proposed power cycle, the bleed pressure will start higher and subsequently be reduced once a steady-state condition is reached.

Using the outlet temperature of the nozzle and the liquid metal outlet temperature from the blanket, the mixing temperature can be determined through another well-established equation, given by (5.9). However, this equation assumes complete mixing has taken place over an indeterminate length. The pressure loss in the mixer has been assumed negligible, but this is only true if the mixer is short.

The mixing section of the experimental apparatus is approximately 10 cm, but observations showed, for both air/water and air/LM136, albeit for the latter with reduced visibility, that in the bubbly regime mixing did not occur. Air leaving the nozzle formed discrete bubbles which appeared to stay the same size as they traversed the full height of the two-phase sections and entered the separator. Bubble size seemed to be unaffected by the volumetric flow rates that were used. However, what is shown from the CISE correlation [Premoli et al., 1970] is that as the cross-sectional void fraction evolves with height, due to decreasing gas-phase density, two-phase pressure loss is reduced. This suggests, perhaps, that long mixing sections preceding the MHD generator might be beneficial for reducing two-phase pressure loss within the MHD duct by increasing compressibility. This is supported by equation (4.37), which describes the MHD power output. However, equation (4.37) is also dependent upon the electrical conductivity of the two-phase mixture, which is required for determining the MHD power output. It seems, therefore, there is an optimum mixer length whereby two-phase pressure loss is reduced and MHD power output maximised.

An attempt to experimentally verify equation (4.37), and the MHD pressure drop given by (4.42), was made by determining the cross-sectional void fraction. Since no other reasonable method for determining this had been identified, visual observation was relied upon. Cross-sectional void fraction is required to gain knowledge of the electrical conductivity of the two-phase mixture, given by equation (4.40) and used by Petrick et al. [1978] for determining the electrical conductivity of two-phase

flows involving Na-K. However, knowledge of the liquid-phase velocity; ascertained through the use of thermocouples, LM136 specific heat and thermal power input; and MHD generator coefficient, δ, is also required. The failure to verify equations (4.37) and (4.42) experimentally means that there is still uncertainty over their validity.

Determining the temperature drop through the MHD generator is also important for ascertaining the enthalpy drop and conversion efficiency. An attempt was made to measure this for an air/LM136 two-phase mixture, but unfortunately due to experimental difficulties this was not achieved. Equation (4.46), which gives the temperature drop through the MHD generator, is a standard isentropic relation modified by the MHD generator coefficient, δ, as suggested by Soo [1968], and by a two-phase adiabatic index. No reference in the literature has been found for a two-phase adiabatic index, but if one considers the approach to define the homogeneous mixture density in equation (4.11) [Whalley, 1987], and the homogeneous viscosity [Isben et al., 1958], then it is deemed reasonable that weighting the specific heat of each phase by flow quality, given in equation (4.45), is a valid approach. The MHD duct expansion, given by equation (4.47), is also a standard isentropic relation, modified by Soo [1968] with the inclusion of the MHD generator coefficient, and further modified with the inclusion of a two-phase adiabatic index.

Due to the technical difficulties involved in manufacturing a diverging square glass section, required due to the constant-velocity constraint within the linear MHD generator, no attempt was made to verify equation (4.47) using the existing experimental apparatus design. Its validity, therefore, remains uncertain, as equation (4.45), the two-phase adiabatic index, also does. Future experimentation should attempt to directly verify both of these equations.

8.1.2.2 Non-Experimentally Verified Assumptions

Halbach arrays, more specifically type-2 arrays in which the magnetic field within the internal space is uniformly straight, shown in figure 8.1, consisting of neodymium can achieve magnetic field strengths of 1 T by using a rotating magnetic field and specially shaped trapezoidal permanent magnets. Since neodymium is a rare-earth element the cost of producing a Halbach array large enough to encompass the MHD generator used in the proposed power cycle, with a 5 m diameter at MHD inlet, 17 m diameter at MHD outlet and a 5 m length, might be considerable. The length of the MHD duct was chosen to provide a balance between high power density, pressure loss and MHD duct expansion. The magnet could be shortened to reduce manufacturing cost, but the MHD interaction length would also be smaller which would lead to lower MHD electrical power outputs.

Furthermore, Halbach arrays usually have a cylindrical bore, but for application in the MHD topping cycle the Halbach array must possess a conical bore to follow the expansion of the MHD duct. Should the cost of manufacturing such a large Halbach array be prohibitive, several smaller MHD generators, with smaller duct diameters, should instead be used. This would reduce the effects of the reciprocal cube distance law, which states that magnetic field strength is reduced as the cube distance from a magnetic pole is increased. The manufacturing complexity of producing a Halbach array with a conical bore has not been estimated.

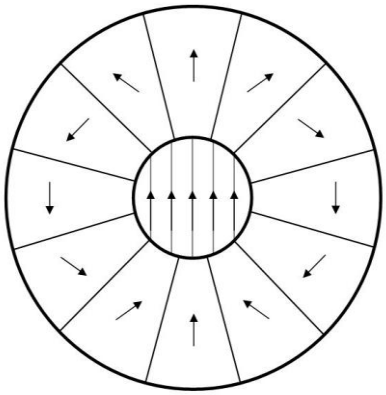

Figure 8.1 Diagram showing cylindrical type-2 Halbach array with rotating magnetic field direction and uniform internal magnetic field lines

Another manufacturing constraint could be the diameter of the pipes used in the topping cycle. A diameter of 5 m, before the MHD duct expansion, was chosen to accommodate the large mass flow of liquid metal and a liquid metal velocity in the range 0.1 - 1 m/s. The mixer and MHD inlet are therefore also 5 m in diameter. For a helium bleed fraction of 14 kg/s, however, from equation (4.47) the MHD duct is found to expand to 17 m in diameter. This yields an expansion angle of approximately 67° and is far in excess of the 10° criterion for the isentropic relation to be applicable. If the MHD duct expanded from a diameter of 5 m to approximately 7 m, the expansion angle would be 10° and the isentropic relation as described by equation (4.47) would hold. To achieve this, the bleed fraction of helium would need to be increased to 25 kg/s. By referring to the graphs in figures 5.6 and 5.7, however, it can be seen that this would lower both the MHD electrical output, since the electrical conductivity of the two-phase mixture would be lower, and the net power output of the Brayton cycle, since more helium would be bled away from the gas turbine.

8.1.2.3 Void Fraction Correlation

In subsection 4.3.1 of chapter 4 a list of correlations for calculating the gravitational two-phase pressure gradient and the cross-sectional void fraction were given. The CISE correlation [Premoli et al., 1970] is suggested by Whalley [1987] to be the most accurate, whilst the El-Boher correlation [1988] was designed for vertical two-phase flows of liquid metal. Some discussion therefore, should be given to the reason for adopting the CISE correlation [Premoli et al., 1970] to predict the performance of the topping cycle. The graphs in figures 8.2, 8.3 and 8.4 show and compare the gravitational two-phase pressure gradient, $(dp/dz)_{grav}$, and cross-sectional void fraction, α, for the mixer, MHD generator and upcomer, respectively. The above graphs show that the CISE correlation [Premoli et al., 1970] predicts larger cross-sectional void fractions, but lower gravitational two-phase pressure gradients. The El-Boher [1988] correlation predicts the opposite.

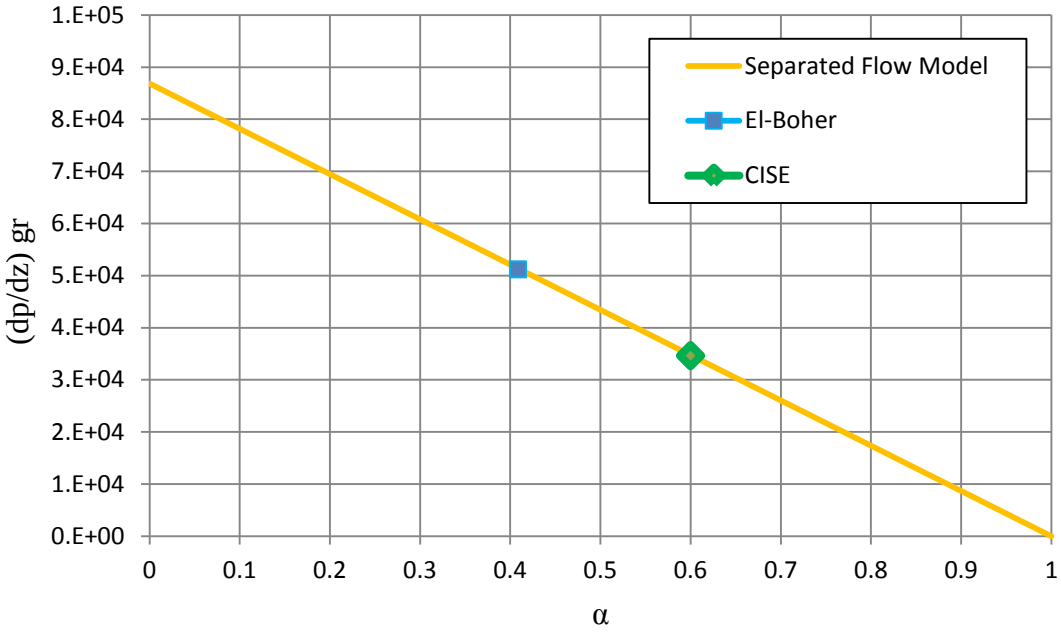

Figure 8.2 Comparison of CISE and El-Boher correlations used to determine $(dp/dz)_{grav}$ and α at mixer outlet for the proposed topping cycle

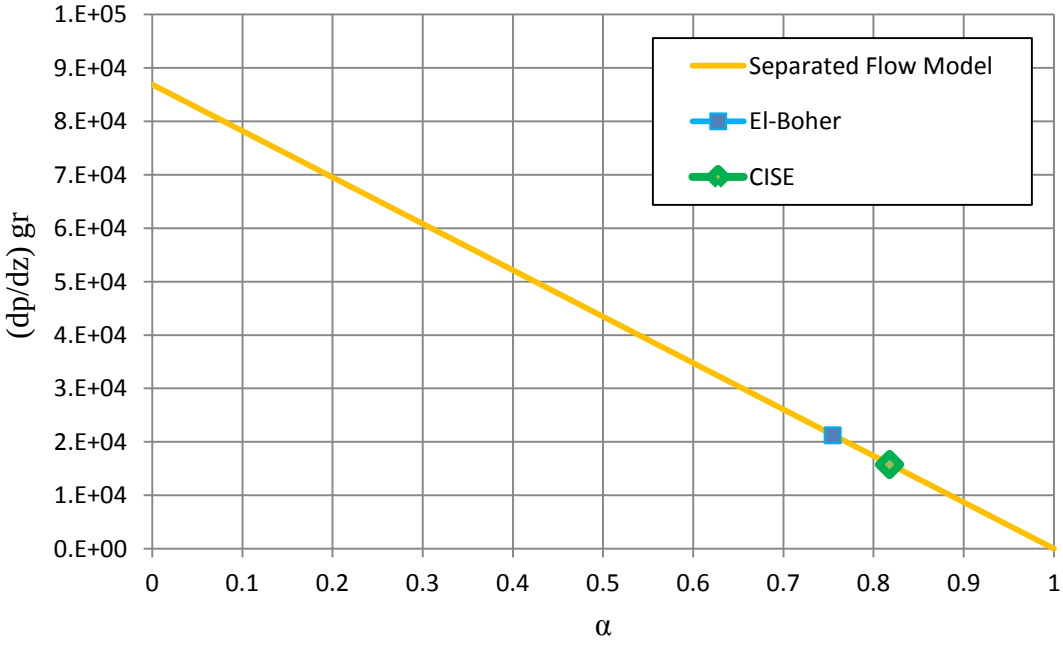

Figure 8.3 Comparison of CISE and El-Boher correlations used to determine $(dp/dz)_{grav}$ and α at MHD outlet for the proposed topping cycle

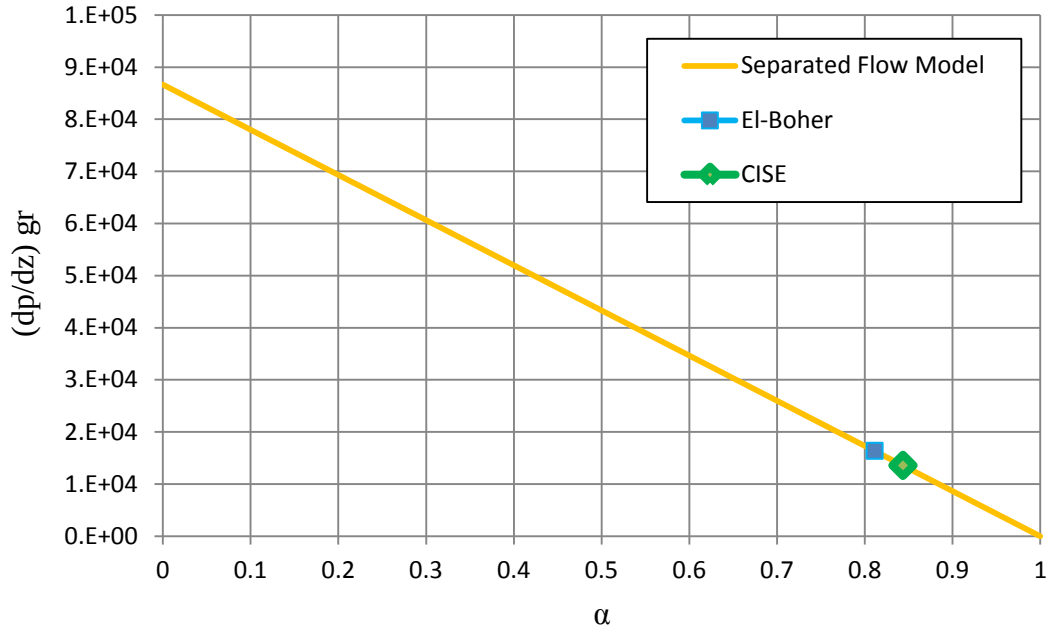

Figure 8.4 Comparison of CISE and El-Boher correlations used to determine $(dp/dz)_{grav}$ and α at upcomer outlet for the proposed topping cycle

The graphs show that the El-Boher correlation [1988] predicts a larger evolution of cross-sectional void fraction, developing from 41% at mixer outlet to 81% at upcomer outlet, whilst the CISE correlation [Premoli et al., 1970], predicts a cross-sectional void fraction range of 60% to 84% between mixer outlet and upcomer outlet.

Determining the electrical power output of the MHD generator, which is dependent upon α for the electrical conductivity of the two-phase mixture, the CISE correlation [Premoli et al., 1970] is favoured since a conservative prediction of MHD electrical power output is preferable due to the novelty of the topping cycle. Since the two-phase pressure gradients are small in comparison to the MHD pressure gradients, the difference between the two aforementioned correlations, with respect to the two-phase gravitational pressure gradient, is somewhat unimportant. However, the difference between the predicted MHD pressure gradient within the generator is significant and would likely affect the performance of the topping cycle.

This is illustrated by considering the component lengths of the two-phase sections, as shown in table 8.1, where the two-phase frictional pressure gradient is included for completeness. Also shown is a comparison of the predicted MHD power output and MHD pressure loss for both correlations.

Correlation	**CISE**	**El-Boher**
$[dp/dz]_{grav}$ mixer (kPa/m)	34.6	51.2
$[dp/dz]_{fric}$ mixer (kPa/m)	3.0×10^{-3}	2.9×10^{-2}
Mixer length (m)	1	
ΔP_{grav} Mixer (kPa)	34.6	51.2
α mixer outlet	**0.60**	**0.41**
MHD power output (MW_e)	**22**	**54**
MHD pressure loss (MPa)	**1.83**	**4.53**
$[dp/dz]_{grav}$ MHD (kPa/m)	15.8	21.3
$[dp/dz]_{fric}$ MHD (kPa/m)	8.2×10^{-5}	7.8×10^{-3}
MHD length (m)	5	
ΔP_{grav} MHD (kPa)	79	107
α MHD outlet	**0.82**	**0.75**
$[dp/dz]_{grav}$ upcomer (kPa/m)	13.6	16.4
$[dp/dz]_{fric}$ upcomer (kPa/m)	1.2×10^{-4}	1.7×10^{-2}
Upcomer Length (m)	37	
ΔP_{grav} Upcomer (kPa)	503	607
α upcomer outlet	0.84	0.81
Total ΔP_{fric} (kPa)	7.9×10^{-3}	7.0×10^{-1}
Total ΔP_{grav} (kPa)	**617**	**765**

Table 8.1 Comparison of CISE [Premoli et al. 1970] and El-Boher [1988] correlations for two-phase gravitational pressure gradient and cross-sectional void fraction. Including two-phase frictional pressure gradient

The MHD pressure gradients in the topping cycle are 3.6 MPa, where 1.83 MPa is due to the MHD generator and 1.8 MPa for the case where inboard blanket modules are used. This is reduced to 2.7 MPa for the case where outboard blanket modules are used [Norajitra et al,. 2003]. Comparing these values, however, with those in table 8.1 shows that the inclusion of the total two-phase gravitational pressure gradient only increases the total pressure losses in the loop using inboard blanket modules by 17% for the CISE correlation [Premoli et al., 1970] and 21% for the El-Boher correlation [1988].

The Friedel correlation [1979] for two-phase frictional pressure gradients can also be used to determine the liquid-only pressure loss in the downcomer, dp/dz_{lo}, which is found to be of the order 10^{-4} kPa/m. For the section of the loop between the blanket exit and nozzle entry, which is of indeterminate length, it is reasonable to assume that the frictional losses are negligible. A friction factor of 0.079 was taken from the Blasius correlation [1913], which is used for smooth pipes, and is valid for Reynolds numbers up to 1×10^5. This was later determined to be unsuitable, however, when the Reynolds numbers in the topping cycle were found to be of the order 1×10^6 - 1×10^7. Since the frictional pressure losses were ignored in the calculation of topping cycle performance, due to their value being much less than the MHD pressure losses, the unsuitability of the Blasius correlation [1913] is unimportant. However, further calculations that include frictional pressure losses should use a correlation that is valid under the operating conditions of the topping cycle.

8.1.2.4 Liquid Metal Dynamic Pressure

The vertical loop, shown in figure 5.1, which comprises the topping cycle, relies upon the buoyancy created by the density differential between the two-phase sections and the single-phase downcomer. However, there are four pressure losses that must be overcome for liquid metal to be circulated: MHD pressure loss in the blanket, MHD pressure loss in the generator, two-phase pressure loss and liquid-only frictional pressure loss.

A downcomer height of 43 m provides 3.8 MPa of static head required to overcome an inboard MHD blanket pressure gradient of 1.8 MPa [Norajitra et al., 2003] and return the Pb-17Li to the blanket at 2 MPa. If no other pressure gradients were present, a small mass flow of helium would cause liquid metal to circulate. Since the two-phase sections are the same height as the downcomer, a nozzle outlet pressure greater than 3.8 MPa, caused by the 43 m static column of liquid metal, would be required to initiate circulation.

Once helium is injected into the two-phase section, however, the density of the column in this section is reduced and the dynamic pressure head increases. This increases the pressure gradient in the MHD generator, since the liquid metal velocity is increasing, resulting in an MHD generator pressure drop of just over 1.8 MPa once the nozzle outlet pressure is reduced to 2 MPa. The two-phase pressure drop in the topping cycle is below 0.1 MPa and largely due to the gravitational component. The momentum term is neglected due to the assumption that the flow quality remains constant, whilst the frictional component is negligible. The liquid-only frictional pressure losses are also small and are neglected.

Writing equation (5.12) as

$$\left(\bar{\rho}_l - \bar{\rho}_{tp}\right) g h_{tp} = \Delta P_{blanket} + \Delta P_{MHD}$$

where the LHS is the buoyancy head, and by using

$$\dot{m}_l = \bar{A}_l \sqrt{2 P_{dynamic} \bar{\rho}_l} \tag{8.1}$$

it can be determined that the dynamic pressure in the topping cycle, where the bleed fraction of helium is 14 kg/s, produces a liquid metal mass flow that far exceeds the specified value of the DCLL blanket.

This can be remedied, however, by reducing the downcomer height, which would introduce a further pressure gradient to arrest the mass flow of Pb-17Li since there would be an insufficient static head of Pb-17Li to overcome the MHD blanket

pressure gradient. Decreasing the downcomer height would reduce the overall size of the topping cycle and therefore reduce the inventory of Pb-17Li.

A further method to arrest the mass flow of Pb-17Li in the topping cycle could involve increasing the pressure gradient within the MHD generator. This could be achieved by increasing the MHD interaction length or by increasing the magnetic field strength.

8.1.3 Summary

Uncertainties associated with the proposed power cycle chiefly lie with the two-phase MHD topping cycle. Experimental testing using air and LM136 showed that LM136 could indeed be circulated, but an attempt to measure the electrical power output of the two-phase MHD generator failed due to flaws in the experimental apparatus design. The validity of the MHD power output, given by equation (4.37), the MHD pressure drop, given by equation (4.42), the temperature drop through the two-phase MHD generator, given by (4.46), the MHD duct expansion, given by (4.47) and the two-phase adiabatic index, given by (4.45), should be verified by future experiments in order to determine the viability of the proposed two-phase MHD topping cycle. Furthermore, an investigation into the effects of mixer length should be included in future experimental work.

Since the equations governing the Brayton cycle, and Rankine cycles, are well-established, the electrical power output of the proposed power cycle falls within the range 2097 MW_e, without MHD power, and 2119 MW_e, with predicted MHD power.

Despite pressure losses from IHX processes being neglected, this is still markedly higher than the existing PPCS model C proposal. However, the proposed power cycle is idealised in places, such as the omission of pressure losses in the IHX processes, and its performance is likely to be lower in reality.

8.2 Experimental Results

This subsection will provide a general discussion of the experimental results relating to the main tests: air/water and air/LM136. The assumptions made during experimental testing, and the methods used to quantify parameter values that may have affected experimental error, will also be discussed.

8.2.1 Air/Water

There are no MHD pressure gradients and therefore the total pressure losses in the experimental loop will be due to the flow restriction, liquid-only frictional pressure loss and two-phase pressure loss. Equation (5.12) can be rewritten as

$$0 = \left(\bar{\rho}_l - \bar{\rho}_{tp}\right) g h_{tp} - \Delta P_{restriction} - \Delta P_{flo}$$

where the two-phase pressure loss is omitted since it has been taken into account by using the CISE correlation [Premoli et al., 1970] when determining $\bar{\rho}_{tp}$.

The internal diameter of the apparatus is much smaller than the diameter of the topping cycle and therefore the frictional losses will be larger and therefore cannot be neglected. Through iteration the Reynolds number for the single-phase downcomer can be determined and subsequently used to find the friction factor from the Moody chart [Moody, 1944] to give ΔP_{flo}, the liquid-only frictional pressure loss.

Since the water mass flow is not specified, it must be determined by adjusting the model. Firstly, a water mass flow rate is chosen. By rearranging equation (8.1) a value for the dynamic pressure can be determined

$$P_{dynamic} = \frac{\left(\frac{\dot{m}_l}{A_{loop}}\right)^2}{2\bar{\rho}_l}$$

Using the loss coefficient, the pressure loss due to the restriction can be determined

$$\Delta P_{restriction} = K P_{dynamic} \tag{8.2}$$

The liquid only frictional pressure loss can be found through

$$\Delta P_{flo} = f\left(\frac{L_{sp}}{D_{tube}}\right) P_{dynamic} \tag{8.3}$$

The CISE correlation [Premoli et al., 1970] can be used to determine the averaged two-phase mixture density to give a new value for $P_{dynamic}$ through equation (5.12) via

$$0 = \left(\bar{\rho}_{l\_downcomer} - \bar{p}_{tp}\right) g h_{tp} - \Delta P_{restriction} - \Delta P_{flo}$$

This value for the dynamic pressure is substituted into (8.1) to give a new value for the mass flow rate of water. The iterative procedure is repeated until the values for the water mass flow converge.

The state points of the two-phase sections are determined using the governing equations of chapter 5. Since no MHD effects are present, and the model assumes adiabatic flow conditions, the temperature of the mixture remains constant from the mixer outlet to the downcomer inlet, where heat is rejected via the cooling section.

The downcomer exit temperature was taken from the temperature measured in the experiment at heating section entry, whilst the water temperature at the nozzle was taken from the temperature measured in the experiment at heating section exit. The nozzle gas entry temperature was taken from the experimental measurements, whilst the nozzle gas exit temperature was taken from equation (5.4). Since the model assumes adiabatic flow conditions, no heat is lost in the upcomer, in the separator, or between the downcomer exit and heating section entry.

The contribution from the manometer trace heating to the thermocouple measurements is not factored into the model. However, the thermocouple readings, showing heat reception where there is none, could be due to the proximity of the heating coils to the vertical sections of the apparatus instead of manometer trace heating.

The predicted water mass flow rate values increase, as expected, as the mass flow of air is increased. Experimental results using rotameter air flow rates of 80 and 90 cm^3/min show excellent agreement with the model, whilst a reasonable agreement is achieved using an air flow rate of 50 cm^3/min. There is a larger departure between the model and experiment for the air flow rates 60 and 100 cm^3/min, which could be due to the combination of thermal leakage from the lagging, thermal leakage from the heating section into the two-phase section or thermocouple error. Since the same lagging in the heating section was used for all measurements, and there is good agreement between predicted and measured water mass flow, any discrepancy in water mass flow is unlikely to be due to thermal leakage from the lagging. The erroneous thermocouple measurements outside of the heating sections, where no heat reception occurs, is likely due to the combination of thermal leakage from the heating section, via the proximity of the heating coils to the vertical sections, and thermocouple error. A smaller ΔT in the heating section would allow those water mass flow values that do not follow the predicted trend to be increased and fit with expected values.

A mention should also be given to the placement of the thermocouple measuring the gas exit temperature. This could have been too high to provide accurate readings. On the apparatus, the thermocouple is located in the centre of the gas escape tube (see figure 6.1) which is approximately 20 mm away from the surface of the two-phase mixture in the separator, and only approximately 15 mm away from the atmosphere of the lab. It is reasonable, therefore, to believe that the gas exit thermocouple reading could be lower due to its proximity to the relatively cooler air in the lab.

The model was also used to predict the head loss in all three manometers. The head loss recorded by the manometer in the downcomer section was determined via

$$\Delta h_{downcomer} = \frac{\Delta P_{restriction} + \Delta P_{flo}}{g\rho_{water\_manometer}} \tag{8.4}$$

The head loss in the mixer and MHD duct were determined via

$$\Delta h_{mixer} = \frac{\Delta P_{tp\_mixer}}{g\rho_{water\_manometer}}$$

$$\Delta h_{MHD} = \frac{\Delta P_{tp\_MHD}}{g\rho_{water\_manometer}} \quad (8.5)$$

There is a discrepancy between the values predicted by the model and the experimental values for head loss in the mixer, MHD duct and downcomer. The gas-only friction factor has a negligible effect upon two-phase frictional pressure loss at low cross-sectional void fractions and the liquid-only friction factor is therefore dominant. However, this had already been determined from the Moody chart [1944] and therefore unlikely to be the cause of the discrepancy. During the experimental testing the levels in the manometers tended to fluctuate about a mean position. The error between the model and experimental values could therefore have been due to observational error whilst manometer readings were taken. Equation (8.5) also does not take into account the change in flow area encountered by the two-phase flow as it transitioned from a round tube in the mixer, into a square MHD duct and then back to a round tube in the upcomer.

8.2.2 Air/LM136

Since no MHD pressure losses were present during the test, due to experimental difficulties, and adiabatic conditions are also assumed in the model, the temperature of LM136 leaving the heating section should remain constant until it rejects heat in the downcomer. This assumes that there is no cooling effect due to the introduction of a cool gas-phase, which is reasonable under the circumstances because the air mass flow is small and its inlet temperature is not far below that of LM136.

The temperatures predicted are close to the experimental values, but as with the air/water test there are erroneous thermocouple readings showing heat reception outside of the heating section. The thermal conductivity of liquid metal is relatively high, and heat reception near the base of the manometers from trace heating could have contributed to elevated temperature readings at MHD inlet, MHD outlet and downcomer outlet. The contribution from the manometer trace heating to the thermocouple measurements in the MHD and upcomer sections was not factored into the model, but it is not thought that this would be a contributing factor since the trace heating was implemented to maintain the temperature of LM136, not increase it by any appreciable amount. Without any direct measurement of the LM136 temperature in the manometer tubes it remains inconclusive whether the trace heating contributed a heat input into the bulk flow of LM136 in the apparatus. However, trace heating was not used in the air/water tests and elevated thermocouple readings were present there too. Therefore, thermal leakage from the heating wires, which are located close to the vertical two-phase section, is suspected to be the cause.

A mention should be given to the insufficient heat rejection in the water jacket, which meant that local temperatures exceeded 80°C (see table 7.12). However, since the surface tension and dynamic viscosity did not change much over the temperature range 70 - 80°C, it is reasonable to use the experimentally measured values.

There is a large discrepancy between the predicted and experimentally measured value of head loss in the downcomer, which could be attributable to solidification within the manometer. However, there is excellent agreement between the predicted and experimentally determined value of LM136 mass flow rate.

8.2.3 Summary

The model, which incorporates the CISE correlation [Premoli et al., 1970] for determining the gravitational component of the two-phase pressure gradient and the cross-sectional void fraction, and the Friedel correlation [1979] for determining the frictional component of the two-phase pressure gradient, is still required for a comparison of temperatures, despite the absence of any MHD pressure gradients.

The assumption of adiabatic flow could be more closely approximated by using lagging to cover the entire experimental apparatus, whilst still allowing some visibility for observing the two-phase flow regime, and locating any heating source, such as the nichrome coils and manometer trace heating, further away from areas that might allow leakage between sections.

In the absence of MHD pressure gradients, the model can instead be used to determine the sum of the gravitational and frictional two-phase pressure gradients and provide a comparison with the experimental results. Inspection of figures 7.3, 7.4 and 7.5 gives an impression that the time-averaged cross-sectional void fraction could be close to 1% for all two-phase sections, across the range of air flow rates used. The model, meanwhile, predicts a value of approximately 1% for all two-phase sections when the volumetric air flow rate is 50 cm^3/min (rotameter), rising to 1.5% for 100 cm^3/min (rotameter) across the two-phase sections. The predicted cross-sectional void fraction varied from 1.3% at mixer exit to 2.5% at upcomer exit for air/LM136.

The model achieved excellent agreement with the predicted LM136 mass flow rate, and also for water mass flow rates where the volumetric air flow rate in the rotameter was 80 and 90 cm^3/min. Predicted temperatures were close to experimental values, but some discrepancy in head loss values between model and experiment were found. Despite this, however, the accuracy of the model, which incorporated the CISE correlation [Premoli et al., 1970], has been sufficiently validated at low cross-sectional void fractions.

8.3 Experimental Design Process

After the difficulties experienced whilst testing LM136, some flaws in the experimental apparatus design were highlighted. There were, however, aspects of the apparatus design that did function as expected and would be included in any redesign of the experimental apparatus. This subsection will discuss the key areas of the experimental apparatus.

8.3.1 Liquid Metal

The choice of low-temperature metal was dictated by safety, cost and melting temperature. Though mercury is liquid at room temperature, it was eliminated for its toxicity and handling difficulty. On this basis other low-melt alloys were dismissed for their cadmium content. Sodium-potassium (Na-K) alloys are also liquid at room-temperature, but due to their reactivity with water they were discounted for use in the experiment. Furthermore, Na-K alloys can ignite when exposed to air.

Galinstan, which is liquid at room temperature, and non-toxic, was an ideal candidate, but the cost per kg was prohibitive for the quantities required in the experiment. Moreover, suppliers offered insufficient quantities making it difficult to obtain in large amounts. Both indium and gallium are expensive elements and comprise approximately 90% of the alloy, the remainder consisting of relatively cheap tin.

LM136 is comprised of the much cheaper bismuth, lead and tin, comprising approximately 79% of its total weight; indium accounting for only 21%. Combined with a low melting point it made LM136 the second best candidate. Despite this it was still difficult to use because it needed to be melted, poured into the apparatus, constantly heated to prevent solidification and safely drained from the apparatus. It is believed that despite the cost any repeat experiment should attempt to use Galinstan to reduce operational difficulties. Furthermore, the dynamic viscosity and surface tension of Galinstan is known, making any further tests on these physical properties unnecessary.

8.3.2 Measurement Devices

Thermocouples are an inexpensive and effective tool for measuring temperature and their inclusion in further experimentation is justified. The experimental apparatus was designed to allow the tip of the thermocouples to be inserted perpendicular to the flow. However, it was later suspected that this orientation might have caused temperature gradients on the tip which could lead to marginal fluctuations in temperature measurement. For any repeat experimentation it would therefore be advised that some configuration be identified that would allow the thermocouples to be inserted so that they measure the temperature parallel to the flow.

Manometers are an inexpensive and simple way of measuring dynamic pressure losses in fluidic systems to respectable accuracies. Their inclusion in the experimental apparatus is justified on this basis, but their use with liquid metals that must continually be heated to prevent solidification proved to be problematic.

Since the top of the manometers were far away from the primary heat source, trace heating needed to be applied. This had not been considered when designing the experimental apparatus. Though time-consuming to apply, electric heating wires were used to prevent LM136 from solidifying. Heat guns were applied to the base of the manometers because it was difficult to wind heating wire around the u-bend sections. Lagging was considered as an alternative, but due to the small diameter of the manometers, approximately 8 mm ID and 12 mm OD, it was difficult to apply lagging to the u-bend sections. Any repeat experiment should include manometers, but consideration should be given to their dimensions to improve robustness. A length scale on the glass of the manometers would greatly improve visual accuracy when determining dynamic head loss.

8.3.3 Electric Heating

Despite the difficulty in winding nichrome wire around the heating section (four parallel loops were required) electric heating provided a stable and controllable method of supplying a uniform heat input to the apparatus. The application of

lagging to the heating section, covering the nichrome windings, presented no problems. However, on two occasions, leaks from the apparatus short-circuited the nichrome windings: one of the electrode studs in the MHD section was not adequately sealed and the separator lid was not adequate to prevent spillage caused by the bubbly two-phase flow in the separator. Under the action of gravity, leaks found their way under the lagging and made contact with the heating loops. It is believed that electric heating should be used in future experiments, but a suitable method of preventing any short-circuit from occurring should be identified.

8.3.4 Structural Materials and Experiment Scale

Glass provided excellent transparency for observing two-phase flow patterns, and good heat resistance, but the requirement for specialised skilled labour to replace damaged sections was limiting. Despite this, the use of glass is still recommended for future experimentation since the structural integrity of plastics at elevated temperatures may be insufficient. Using metals could introduce additional pressure losses due to Lenz's law.

The original apparatus design used four major sections: heating, MHD with upcomer, separator and downcomer with IHX. This was done in an attempt to reduce the number of disturbances to the flow which the glass sockets, used to mate these sections, introduced by virtue of their design. The estimation of these flow disturbances, however, may have been exaggerated and the benefit of having a greater number of sections, to isolate faults, may outweigh any losses caused by additional glass sockets.

If the metal used for future experimentation is Galinstan, however, then glass could be substituted with a plastic, such as PVC or polycarbonate, which would make it easier to replace any faulty section of the apparatus. A method for isolating spills and leaks, such as a catch tray surrounding the apparatus, would be essential to avoid the loss of such a costly metal.

The scale of the experimental apparatus seemed adequate for meeting the experimental objectives. The internal diameter of the main glass sections was large enough to avoid significant frictional pressure losses, but small enough to limit the LM136 inventory; an important consideration if Galinstan is used. However, there are sections of the apparatus where benefits could be realised if component dimensions were greater.

Despite any significant mixing effects being observed for air/water and air/LM136 at low volumetric gas flows, where the two-phase flow remained in the bubbly regime, a longer mixer might be useful for investigating higher volumetric gas flows where churn or annular two-phase regimes occur.

A greater distance between the heating section and vertical sections might limit the effects of thermal leakage. The heating wires were very close to the vertical sections and this appeared to have an effect upon thermocouple readings, which showed temperature increases within the MHD duct. This could have been partly due to the marginally larger cross-sectional area of the MHD duct, but a greater distance between the vertical sections and each end of the heating section would allow the effect of thermal leakage to be mitigated.

The wall height of the separator could be increased to prevent overspill when the two-phase mixture exits the upcomer. Combining this with a better lid design should mitigate the problems experienced with leakage from the separator. A greater distance between the upcomer exit and downcomer entry might also allow any phase separation effects to be better observed.

A longer MHD duct would allow the effects of magnetic field interaction and charge separation to be better observed. A larger square cross-sectional area at inlet would necessitate larger electrodes, which could be better secured since the surface area at the side of the MHD duct would be larger. Manufacturing square sections from glass, which also diverge, is difficult. Using plastics, however, would permit the use of four individual plates that could be glued or otherwise fixed together to make the MHD duct.

This would allow easier installation of the electrodes, but this is dependent upon which liquid metal is used for future tests.

It is believed, therefore, that if LM136 is used for future designs of the experimental apparatus, then glass should be used. Despite the manufacturing difficulties, and the reliance upon specialised skilled labour to replace faulty sections, no other material appears to offer both structural integrity at high temperature and transparency. If, however, Galinstan is used then plastic components offer a more attractive prospect since they can be manufactured with greater ease and allow more complex geometries to be produced.

8.3.5 Other Considerations

More attention could have been given to the stand on which the apparatus needed to be supported. During the construction of the main experimental apparatus it was supported in the clamps of several retort stands. This approach was subsequently adopted for the experiment, but had to be modified since the mass of LM136 required more support. Two blocks of wood, aligned perpendicular to the apparatus, were used to rest the glass upon, which allowed a gap for the nichrome wires to be added. This proved to be sufficient, even when the new drain was added, which required additional clearance from the worktop. Future apparatus designs could use this same approach with concern only for the clearance of any drain placed near the base of the apparatus, which should posses a larger diameter to avoid blockages.

Chapter 9: Conclusion

As the global demand for electricity increases, the structure of energy policy will determine the types of primary energy sources that will be relied upon to generate the required supply. It is expected that there will be a reduction in fossil-fuelled power plants, leading ultimately to their departure from the global electricity generating mix. This will leave renewable power plants to provide the peak or load-following capacity and fission plants to provide the base-load capacity. However, with the benefits afforded by fusion power plants, which could provide the world's base-load capacity using large, secure fuel reserves, without greenhouse gas (GHG) emissions and at a low risk to the environment and public health, fusion's place in the future electricity generating mix is extremely important.

The importance of this work, therefore, has been to explore a range of systems for generating electricity from a fusion reactor employing blankets, with the goal of identifying a method for improving the efficiency of a fusion plant in order to reduce the unit cost of electricity to the end consumer.

Conventional electricity power generating methods were examined which led to an investigation of various Rankine and Brayton cycle configurations, ranging from the simple to the complex, and including considerations of binary cycles. This subsequently led to a study of non-conventional electrical power generating methods through the analysis of direct energy conversion (DEC) technologies, which evaluated thermoelectric, thermionic, electrohydrodynamic (EHD) and magnetohydrodynamic (MHD) generators. The conclusion is that DEC technologies are best suited to a support role, where they can be used to supplement the electrical output achieved via conventional turbo-machinery because their power densities and efficiencies are low.

Model C of the power plant conceptual study (PPCS), with its high-enthalpy liquid metal breeder, offers the potential for a liquid metal MHD generator to be used to generate small amounts of electrical power in addition to the currently-assumed Brayton cycle. However, a method for reducing the high liquid metal pumping power, associated with single-phase MHD power generation, still needed to be identified.

A study of two-phase flows highlighted how a gas phase could introduce compressibility and reduce liquid metal pumping power. This was further supported by Wu et al. [2007] in their feasibility analysis of a two-phase MHD generator. The use of a vertically-aligned two-phase liquid metal MHD (TPLMMHD) generator was suggested by Branover et al. [1981] to remove the need for an electrical pump to circulate a liquid metal, whilst Satyamurthy et al. [1995] investigated vertical two-phase flows of steam and liquid metal in conjunction with a vertical loop and a single-phase MHD generator.

These ideas were incorporated into a novel method for utilising the high-enthalpy liquid metal breeder in conjunction with a fusion power plant operating under PPCS model C constraints, which provided a benchmark against which a comparison could be made and defined the boundary conditions for any power cycle.

The result is a proposed power cycle consisting of a novel two-phase MHD topping cycle, high-pressure Brayton cycle and three low-temperature, low-pressure bottoming Rankine cycles.

9.1 Specific Conclusions of this Research

- By using 3991 MW_t of available thermal power from four tokamak zones (divertor bulk, blanket, liquid metal Pb-17Li breeder and divertor target) a primary Brayton cycle, operating with a high cycle pressure of 34.5 MPa and an overall cycle pressure ratio of 5.4, can deliver 1688 MW_e assuming an electromechanical efficiency of 97.5% .

This performance is based upon the assumption that no pressure losses occur in any of the sixteen indirect heat exchange (IHX) processes. Furthermore, the minimum pinch-points for the IHX processes have been taken from Norajitra et al. [2003], where a minimum pinch of 10 K is used for all helium-liquid metal, and all helium-helium, IHX processes, and a minimum pinch of 15 K is used for all helium-water IHX processes.

A further assumption is the compression of helium to 34.5 MPa. This is supported, however, by the existing use of turbo-machinery where steam pressures in the range 30 - 31.5 MPa are achievable, and pressures up to 35 MPa believed possible if nickel-based alloys are used [Hordeski, 2011]. Since PPCS model C is a more advanced design, values for some of the plant components are extrapolated beyond the state-of-the-art and therefore the compression of helium to 34.5 MPa is reasonable. Perhaps the greater challenge will be to prevent helium leakage at this high pressure.

Another assumption is that tritium will not reduce the performance of any turbo-machinery used in a primary Brayton cycle. Tritium filtration has been included in plant designs and therefore it is reasonable to assume these same techniques can be applied to the Brayton part of the proposed power cycle to limit any impact that tritium may have on performance.

- By using a vertically-aligned loop and the injection of a small percentage of helium near the base, the liquid metal breeder can be circulated via buoyancy without the need for a pump. This reduces the plant electrical power requirement by 6.3 MW_e. Due to the high electrical conductivity of Pb-17Li, and the relatively small amount of helium, the concurrent generation of 22 MW_e can be achieved by using a two-phase MHD generator.

The calculated performance of the two-phase MHD topping cycle rests upon several assumptions. Determining the amount of electrical power generated from the two-phase MHD generator, and the state points of the phases around the loop, permits the characteristics of the topping cycle to be defined. An attempt was made to test the assumptions that dictated its performance, but some still remain unverified.

The ability to circulate a dense liquid metal around a vertically-aligned loop by using a small amount of gas to initiate a buoyancy effect was demonstrated. The amount of electrical power generated via TPLMMHD energy conversion, and the effects of the two-phase flow regime upon charge separation within a liquid metal, require further investigation.

The equations governing the temperature and pressure loss through the TPLMMHD generator must also be examined further. Determining the total pressure loss and buoyancy, both of which depend on the volumetric void fraction, in the topping cycle, where MHD effects in the generator and in the blanket cause the major losses, is important for achieving the mass flow of liquid metal that is specified by the blanket design. The temperature losses in the loop must be known since the design of the Brayton cycle, which delivers the majority of the electrical power, relies upon the thermal characteristics of several helium-liquid metal IHX processes.

Other assumptions underpinning the performance of the two-phase MHD topping cycle relate to manufacturing constraints, such as large diameter ducts, capable of withstanding large mass flows of high-temperature liquid metal, and suitable permanent magnets, capable of providing a magnetic field strength of 1 T, that can span the length and width of the MHD generator. Extrapolating beyond the state-of-the-art, however, is acceptable due to the advanced nature of PPCS model C, upon which many of the constraints of the topping cycle were based.

- By using just under 2120 MW_t rejected from the Brayton cycle, three low-pressure, low-temperature Rankine cycles can deliver 409 MW_e assuming an electromechanical conversion efficiency of 97.5%.

The performance of the bottoming Rankine cycles rests upon few unverified assumptions. Due to its low-pressure, low-temperature operation, there are no components that could be considered beyond the state-of-the-art. The only point of note is the use of a minimum pinch-point of 15 K, but this is supported by Norajitra et al. [2003] where it is used for their helium-water IHX processes.

- The power cycle associated with PPCS model C, without pressure losses in any IHX processes, delivers 1780 MW_e with a cycle efficiency of 44.6%, using a thermal input of 3991 MW_t After deducting plant power requirements, totalling 216 MW_e an overall plant efficiency, defined as the ratio of the net plant electrical power to the fusion power, of 45.9% is achieved. The proposed power cycle, however, consisting of a Brayton cycle, with a two-phase MHD topping cycle and three bottoming Rankine cycles, and without pressure losses in any IHX processes, delivers a total of 2119 MW_e with a combined cycle efficiency of 53.1%. After deducting plant power requirements an overall plant efficiency of 56% is achieved by using the same definition given above. This provides an improvement in overall plant efficiency of 10.1%.

9.2 Recommendations for Further Work

There are two areas where recommendation for further study can be made. The first is to further investigate the effects of tritium on high-pressure primary Brayton cycles. This would help to determine the viability of the Brayton part of the proposed power cycle.

The second, and perhaps more comprehensive, would be to further investigate the two-phase MHD topping cycle. It has been demonstrated that the buoyancy principle can be used to circulate a dense liquid metal around a vertically-aligned loop without the need for a pump, but the electrical power output and the accurate determination of the state points for each phase requires further experimental verification.

On the subject of experimental work, the following specific recommendations are made:

- If considerations of budget allow, Galinstan, which is liquid at room-temperature, should be used to make experimental verification easier. Its physical characteristics are available in the literature, which removes the need to experimentally verify any unknown parameters. Should Galinstan not be an option, the metal alloy low-melt 136 (LM136) used here is recommended due to its low melting temperature of 58°C and low toxicity.

- Measurements of the dynamic viscosity and surface tension of LM136, for a range of temperatures, including the range 70 - 80°C, should be undertaken to verify the results obtained in this work.

- Electric heating remains an excellent choice for providing a uniform heat input, but caution should be given to its use with certain materials because the wire can become locally red hot without melting.

- The robustness of the experimental apparatus should be improved, especially if LM136 is used. A suitable draining method should be identified, unless Galinstan is used, which could remain in the experimental apparatus. Steps should be taken to limit leakage from component junctions and, in the case of LM136, solidification from occurring. Glass still remains a suitable choice for testing, providing excellent transparency, however, due to the skilled labour required to manufacture glass components, they could be substituted by plastics

if Galinstan were used. Consideration should be given to the material used in the heating section, where the hot wires could pose structural integrity issues for plastics. Construction of the MHD generator from glass was difficult, but it could be repeated. Plastic sections, which can be joined and mated using a variety of methods, potentially offer an easier construction solution.

- A method of reliably determining the cross-sectional and volumetric void fraction, and the slip ratio, in liquid metals should be identified.

Appendix A: LM136 Dynamic Viscosity Results

Due to difficulties with the electric heating at the time of testing a Bunsen burner was used to heat approximately 500 ml of LM136 in a glass beaker to 80°C. The LM136 was allowed to cool to 70°C. The temperature of the LM136 was determined using a Digitron handheld thermocouple reader. Between these two temperatures several measurements of dynamic viscosity were taken.

The first test was limited. Only seven submersions of the viscometer were made, resulting in seven measurements of efflux. There was difficulty in determining when the second marker had been reached.

Measurement No.	Time (s)
1	28.70
2	27.94
3	28.99
4	28.35
5	27.40
6	29.56
7	28.86
Geometric mean t_{efflux} (s)	28.54
Standard deviation t_{efflux} (s)	0.66
μ (Pa s)	2.10E-03

Table A.1 Summary of first LM136 dynamic viscosity test results using a Δh of 55 mm in the reservoir

A measuring strip had been devised that carried two marks 10 mm apart. This reduced the error associated with timing the efflux as the reservoir level changed between two fixed marks. The measuring strip, made of soft aluminium sheet metal, was bent over the rim of the reservoir and further pressed to the contours of the dip cup. Residual LM136 that had solidified on the rim of the dip cup helped to hold the measuring stick in place. The width of the measuring stick was kept small, to avoid the volume of the measuring stick from interfering with the volume of molten LM136 within the reservoir.

Measurement No.	Efflux time (s)	Measurement No.	Efflux time (s)
1	32.96	8	31.30
2	30.52	9	26.75
3	30.36	10	26.67
4	30.82	11	30.83
5	28.49	12	29.34
6	30.27	13	27.74
7	25.59	14	25.81
Geometric mean t_{efflux} (s)	29.02	Standard deviation t_{efflux} (s)	2.28
μ (Pa s)	9.44E-3		

Table A.2 Summary of second LM136 dynamic viscosity test results using a Δh of 13 mm in the reservoir

Measurement No.	Efflux Time (s)	Measurement No.	Efflux Time (s)
1	29.37	11	20.53
2	29.13	12	33.17
3	27.43	13	33.17
4	22.64	14	31.29
5	21.93	15	28.81
6	23.99	16	28.84
7	21.81	17	29.42
8	24.43	18	27.02
9	26.66	19	29.17
10	25.12	20	27.97
Geometric mean t_{efflux} (s)	26.85	Standard deviation t_{efflux} (s)	3.67
μ (Pa s)	8.73E-3		

Table A.3 Summary of third LM136 dynamic viscosity test results using a Δh of 13 mm in the reservoir

To improve the readability of the markers a new measuring stick was devised. It was found that the old measuring stick was actually greater than 10 mm, approximately 13 mm. The new measuring stick was easier to read and reduced the standard deviation.

Measurement No.	Efflux time (s)	Measurement No.	Efflux time (s)
1	22.05	7	20.5
2	19.27	8	21.39
3	20.19	9	19.45
4	20.62	10	21.25
5	20.66	11	20.21
6	21.16	12	20.63
Geometric mean t_{efflux} (s)	20.60	Standard deviation t_{efflux} (s)	0.79
μ (Pa s)	8.90E-3		

Table A.4 Summary of fourth LM136 dynamic viscosity test results using a Δh of 10 mm in the reservoir

Measurement No.	Efflux time (s)	Measurement No.	Efflux time (s)
1	19.08	7	21.94
2	21.15	8	21.52
3	21.21	9	22.00
4	23.11	10	19.34
5	21.93	11	20.41
6	22.67		
Geometric mean t_{efflux} (s)	21.27	Standard deviation t_{efflux} (s)	1.27
μ (Pa s)	9.19E-3		

Table A.5 Summary of fifth LM136 dynamic viscosity test results using a Δh of 10 mm in the reservoir

Measurement No.	Efflux time (s)	Measurement No.	Efflux time (s)
1	22.13	7	20.61
2	22.76	8	22.77
3	22.68	9	22.80
4	21.73	10	21.68
5	21.35	11	22.46
6	21.64		
Geometric mean t_{efflux} (s)	22.04	Standard deviation t_{efflux} (s)	0.72
μ (Pa s)	9.53E-3		

Table A.6 Summary of sixth LM136 dynamic viscosity test results using a Δh of 10 mm in the reservoir

Measurement No.	Efflux time (s)	Measurement No.	Efflux time (s)
1	20.97	7	20.38
2	20.11	8	19.99
3	20.04	9	19.69
4	19.10	10	22.22
5	19.66	11	20.79
6	19.90	12	16.56
Geometric mean t_{efflux} (s)	19.91	Standard deviation t_{efflux} (s)	1.33
μ (Pa s)	8.60E-3		

Table A.7 Summary of seventh LM136 dynamic viscosity test results using a Δh of 10 mm in the reservoir

Measurement No.	Efflux time (s)	Measurement No.	Efflux time (s)
1	19.55	8	19.76
2	19.14	9	18.85
3	18.56	10	19.85
4	17.79	11	20.04
5	19.66	12	18.80
6	18.05	13	19.37
7	19.81		
Geometric mean t_{efflux} (s)	19.16	Standard deviation t_{efflux} (s)	0.72
μ (Pa s)	8.28E-3		

Table A.8 Summary of eighth LM136 dynamic viscosity test results using a Δh of 10 mm in the reservoir

Measurement No.	Efflux time (s)	Measurement No.	Efflux time (s)
1	20.40	8	20.62
2	20.44	9	21.27
3	19.98	10	20.66
4	20.92	11	21.64
5	19.82	12	20.71
6	20.19	13	20.39
7	20.53		
Geometric mean t_{efflux} (s)	20.58	Standard deviation t_{efflux} (s)	0.49
μ (Pa s)	8.89E-3		

Table A.9 Summary of ninth LM136 dynamic viscosity test results using a Δh of 10 mm in the reservoir

Measurement No.	Efflux time (s)	Measurement No.	Efflux time (s)
1	19.45	8	19.26
2	21.09	9	18.99
3	20.99	10	19.61
4	19.83	11	19.56
5	19.07	12	19.73
6	17.33	13	20.31
7	20.74		
Geometric mean t_{efflux} (s)	19.67	Standard deviation t_{efflux} (s)	0.99
μ (Pa s)	8.50E-3		

Table A.10 Summary of tenth LM136 dynamic viscosity test results using a Δh of 10 mm in the reservoir

Measurement No.	Efflux time (s)	Measurement No.	Efflux time (s)
1	19.02	8	19.07
2	20.38	9	19.48
3	19.50	10	19.82
4	19.15	11	17.12
5	21.04	12	18.85
6	19.75	13	19.77
7	19.76	14	19.19
Geometric mean t_{efflux} (s)	19.40	Standard deviation t_{efflux} (s)	0.88
μ (Pa s)	8.38E-3		

Table A.11 Summary of eleventh LM136 dynamic viscosity test results using a Δh of 10 mm in the reservoir

Appendix B: LM136 Surface Tension Results

A glass slide was marked at 2, 4, 6, 8 and 10 mm to provide a measurement of draught. The balance was zeroed and an advancing angle was measured, up to a draught of 10 mm, before the glass slide was retracted from the water and the receding contact angle measured. The contact angle was assumed to be zero, so that cos(θ) was unity. At the end of the run there was a slight discrepancy of 5.5 x 10^{-4} g, which could have been caused by residual water on the glass slide.

D (mm)	2	4	6	8	10	8	6	4	2
Balance (g)	-3.92 E-01	-2.67 E-01	-1.83 E-01	-1.13 E-01	7.90 E-03	-7.80 E-02	-1.50 E-01	-3.02 E-01	-3.95 E-01
F_{Total} (N)	-3.85 E-03	-2.61 E-03	-1.80 E-03	-1.11 E-03	7.75 E-05	-7.65 E-04	-1.47 E-03	-2.97 E-03	-3.88 E-03
$F_{Buoyancy}$ (N)	7.65 E-04	1.53 E-03	2.30 E-03	3.06 E-03	3.83 E-03	3.06 E-03	2.30 E-03	1.53 E-03	7.65 E-04
F_{γ} (N)	-4.61 E-03	-4.14 E-03	-4.09 E-03	-4.17 E-03	-3.75 E-03	-3.83 E-03	-3.77 E-03	-4.50 E-03	-4.64 E-03
γ (N)	5.76 E-02	5.18 E-02	5.11 E-02	5.21 E-02	4.69 E-02	4.78 E-02	4.71 E-02	5.62 E-02	5.80 E-02
Deviation (%)	21.0	29.1	30.0	28.6	35.8	34.5	35.5	23.0	20.5
Revised θ (°)	37.8	44.9	45.5	44.5	50.1	49.1	49.8	39.7	37.4

Table B.1 Summary of first test for surface tension measurements using water at 20°C for a range of draught values, D, and assuming an initial contact angle of zero.

The first test was conducted before contact angle hysteresis was fully appreciated and the beaker, slide and water were therefore cleaned before a new test was performed. The draught intervals were increased to minimise the error in visually determining their value. Four further tests were performed and the results are given in tables B.2, B.3, B.4 and B.5.

D (mm)	5	10	15	20	15	10	5	0
Balance (g)	-1.42 E-01	2.80 E-02	2.40 E-01	4.70 E-01	1.50 E-01	-7.20 E-02	-3.10 E-01	-2.00 E-03
F_{Total} (N)	-1.40 E-03	2.70 E-04	2.40 E-03	4.60 E-03	1.50 E-03	-7.10 E-04	3.00 E-03	-2.00 E-05
$F_{Buoyancy}$ (N)	1.90 E-03	3.80 E-03	5.70 E-03	7.70 E-03	5.70 E-03	3.80 E-03	1.90 E-03	0
F_{γ} (N)	-3.30 E-03	-3.60 E-03	-3.30 E-03	-3.10 E-03	-4.20 E-03	-4.50 E-03	-4.90 E-03	-2.00 E-05
γ (N/m)	4.10 E-02	4.40 E-02	4.20 E-02	3.80 E-02	5.30 E-02	5.70 E-02	6.10 E-02	2.50 E-04
Deviation (%)	43.4	39.1	42.8	47.6	27.4	22.4	16.0	~0
Revised θ (°)	55.6	52.5	55.1	58.4	43.5	39.1	32.9	0

Table B.2 Summary of second test results for surface tension measurements of water, using larger draught intervals to minimise visual error and new decontamination protocols for components. An initial contact angle of zero was assumed.

D (mm)	5	10	15	20	15	10	5	0*
Balance reading (g)	-1.74 E-01	8.12 E-02	3.18 E-01	5.22 E-01	2.69 E-01	0	-2.19 E-01	1.70 E-03
F_{Total} (N)	-1.70 E-03	7.97 E-04	3.12 E-03	5.12 E-03	2.64 E-03	0	-2.15 E-03	1.67 E-05
$F_{Buoyancy}$ (N)	1.91 E-03	3.83 E-03	5.74 E-03	7.65 E-03	5.74 E-03	3.83 E-03	1.91 E-03	0
F_{γ} (N)	-3.61 E-03	-3.03 E-03	-2.62 E-03	-2.53 E-03	-3.10 E-03	-3.83 E-03	-4.06 E-03	1.67 E-05
Expected F_{γ} (N)	-5.84 E-03	-5.84 E-03	-5.84 E-03	-5.84 E-03	-5.84 E-03	-5.84 E-03	-5.84 E-03	0
γ (N/m)	4.52 E-02	3.79 E-02	3.28 E-02	3.16 E-02	3.88 E-02	4.78 E-02	5.08 E-02	2.10 E-04
Deviation (%)	38.1	48.1	55.1	56.7	46.9	34.5	30.4	~0
Revised θ (°)	55.6	52.5	55.1	58.4	43.5	39.1	32.9	0

Table B.3 Summary of third test results for surface tension measurements of water using larger draught intervals to minimise visual error and new decontamination protocols. An initial contact angle of zero was assumed. *Slide knocked during draining

D (mm)	5	10	15	20	15	10	5	0
Balance reading (g)	-7.50 E-02	2.18 E-01	4.65 E-01	4.98 E-01	1.82 E-01	4.91 E-02	-2.85 E-01	0
F_{Total} (N)	-7.36 E-04	2.14 E-03	4.56 E-03	4.89 E-03	1.79 E-03	4.82 E-04	-2.80 E-03	0
$F_{Buoyancy}$ (N)	1.91 E-03	3.83 E-03	5.74 E-03	7.65 E-03	5.74 E-03	3.83 E-03	1.91 E-03	0
F_{γ} (N)	-2.65 E-03	-1.69 E-03	-1.18 E-03	-2.77 E-03	-3.95 E-03	-3.34 E-03	-4.71 E-03	0
Expected F_{γ} (N)	-5.84 E-03	-5.84 E-03	-5.84 E-03	-5.84 E-03	-5.84 E-03	-5.84 E-03	-5.84 E-03	0
γ (N/m)	3.31 E-02	2.11 E-02	1.47 E-02	3.46 E-02	4.94 E-02	4.18 E-02	5.89 E-02	0
Deviation (%)	54.6	71.1	79.8	52.6	32.3	42.7	19.3	0
Revised θ (°)	63.0	73.2	78.4	61.7	47.4	55.1	36.2	0

Table B.4 Summary of fourth test results for surface tension measurements of water using larger draught intervals to minimise visual error and new decontamination protocols, assuming an initial contact angle of zero

D (mm)	5	10	15	20	15	10	5	0
Balance reading (g)	-3.70 E-02	1.75 E-01	4.72 E-01	5.56 E-01	2.10 E-01	-9.50 E-03	-2.55 E-01	0
F_{Total} (N)	-3.63 E-04	1.72 E-03	4.63 E-03	5.45 E-03	2.06 E-03	-9.32 E-05	-2.50 E-03	0
$F_{Buoyancy}$ (N)	1.91 E-03	3.83 E-03	5.74 E-03	7.65 E-03	5.74 E-03	3.83 E-03	1.91 E-03	0
F_{γ} (N)	-2.28 E-03	-2.11 E-03	-1.11 E-03	-2.20 E-03	-3.68 E-03	-3.92 E-03	-4.41 E-03	0
Expected F_{γ} (N)	-5.84 E-03	-5.84 E-03	-5.84 E-03	-5.84 E-03	-5.84 E-03	-5.84 E-03	-5.84 E-03	0
γ (N/m)	2.85 E-02	2.63 E-02	1.38 E-02	2.75 E-02	4.60 E-02	4.90 E-02	5.52 E-02	0
Deviation (%)	61	63.9	81.1	62.4	37.1	32.9	24.4	0
Revised θ (°)	67.1	69.0	79.1	68.0	51.0	47.9	40.9	0

Table B.5 Summary of fifth test results for surface tension measurements of water using larger draught intervals to minimise visual error and new decontamination protocols**,** assuming an initial contact angle of zero

For the next set of tests the glass slide and beaker were cleaned before each test commenced. Fresh de-ionised water was used in each test. The results are presented in tables B.6, B.7 and B.8.

D (mm)	5	10	15	20	15	10	5	0
Balance reading (g)	-1.18 E-01	5.72 E-02	2.53 E-01	4.75 E-01	7.15 E-02	-1.30 E-01	-3.08 E-01	0
F_{Total} (N)	-1.16 E-03	5.61 E-04	2.48 E-03	4.66 E-03	7.01 E-04	-1.28 E-03	-3.02 E-03	0
$F_{Buoyancy}$ (N)	1.91 E-03	3.83 E-03	5.74 E-03	7.65 E-03	5.74 E-03	3.83 E-03	1.91 E-03	0
F_{γ} (N)	-3.07 E-03	-3.26 E-03	-3.26 E-03	-2.99 E-03	-5.04 E-03	-5.10 E-03	-4.93 E-03	0
Expected F_{γ} (N)	-5.84 E-03	-5.84 E-03	-5.84 E-03	-5.84 E-03	-5.84 E-03	-5.84 E-03	-5.84 E-03	0
γ (N/m)	3.84 E-02	4.08 E-02	4.08 E-02	3.74 E-02	6.30 E-02	6.38 E-02	6.17 E-02	0
Deviation (%)	47.4	44.1	44.1	48.8	13.7	12.6	15.5	0
Revised θ (°)	58.3	56.0	56.1	59.2	30.4	29.1	32.3	0

Table B.6 Summary of sixth test results for surface tension measurements of water using revised decontamination protocols. An initial contact angle of zero was assumed.

At the end of the test six it was noticed that the glass slide was not entering the LM136 perpendicularly. This could have given inaccurate results. For the seventh and eighth tests fresh, clean slides were used, which were inserted into the apparatus perpendicularly. The results are presented in tables B.7 and B.8 below.

D (mm)	5	10	15	20	15	10	5	0
Balance reading (g)	-1.48 E-01	6.04 E-02	2.77 E-01	4.76 E-01	1.21 E-01	-1.28 E-01	-3.06 E-01	-3.20 E-03
F_{Total} (N)	-1.46 E-03	5.93 E-04	2.71 E-03	4.66 E-03	1.19 E-03	-1.25 E-03	-3.00 E-03	-3.14 E-05
$F_{Buoyancy}$ (N)	1.91 E-03	3.83 E-03	5.74 E-03	7.65 E-03	5.74 E-03	3.83 E-03	1.91 E-03	0
F_{γ} (N)	-3.37 E-03	-3.23 E-03	-3.03 E-03	-2.99 E-03	-4.55 E-03	-5.08 E-03	-4.91 E-03	-3.14 E-05
Expected F_{γ} (N)	-5.84 E-03	-5.84 E-03	-5.84 E-03	-5.84 E-03	-5.84 E-03	-5.84 E-03	-5.84 E-03	0
γ (N/m)	4.21 E-02	4.04 E-02	3.78 E-02	3.73 E-02	5.69 E-02	6.35 E-02	6.14 E-02	3.90 E-04
Deviation (%)	42.3	44.6	48.2	48.8	22.1	13	15.8	~0
Revised θ (°)	54.8	56.4	58.8	59.2	38.9	29.6	32.7	0

Table B.7 Summary of seventh test results for surface tension measurements of water using revised decontamination protocols for components. An initial contact angle of zero was assumed.

D (mm)	5	10	15	20	15	10	5	0
Balance reading (g)	-1.65 E-01	5.38 E-02	2.29 E-01	4.73 E-01	1.22 E-01	-1.19 E-01	-2.92 E-01	-3.60 E-03
F_{Total} (N)	-1.62 E-03	5.28 E-04	2.25 E-03	4.64 E-03	1.19 E-03	-1.17 E-03	-2.87 E-03	-3.53 E-05
$F_{Buoyancy}$ (N)	1.91 E-03	3.83 E-03	5.74 E-03	7.65 E-03	5.74 E-03	3.83 E-03	1.91 E-03	0
F_{γ} (N)	-3.53 E-03	-3.30 E-03	-3.49 E-03	-3.01 E-03	-4.55 E-03	-5.00 E-03	-4.78 E-03	-3.53 E-05
Expected F_{γ} (N)	-5.84 E-03	-5.84 E-03	-5.84 E-03	-5.84 E-03	-5.84 E-03	-5.84 E-03	-5.84 E-03	0
γ (N/m)	4.42 E-02	4.12 E-02	4.36 E-02	3.76 E-02	5.6 E-02	6.24 E-02	5.97 E-02	4.40 E-04
Deviation (%)	39.5	43.5	40.2	48.5	22.1	14.4	18.1	~0
Revised θ (°)	52.8	55.6	53.3	59.0	38.9	31.2	35.1	0

Table B.8 Summary of eighth test results for surface tension measurements of water using revised decontamination protocols for components. An initial contact angle of zero was assumed.

The results of tests six, seven and eight gave similar results. It was therefore decided to now test the surface tension of LM136 since the hysteresis within the apparatus system had been minimised to give reasonably repeatable results. The final surface tension test results are presented in table B.9 below.

D (mm)	P_{Wetted} (mm)	T_{LM136} (K)	ρ_{LM136} (kg/m^3)	Balance reading (g)	F_{Total} (N)	$F_{Buoyancy}$ (N)	F_{γ} (N)	γ (N/m)	Final Balance (g)
18	80	353	8581	12.46	1.22 E-01	5.91 E-02	6.31 E-02	7.89 E-01	0
18	80	343		12.42	1.22 E-01	5.91 E-02	6.27 E-02	7.84 E-01	0
18	80	353	8581	12.93	1.27 E-01	5.91 E-02	6.78 E-02	8.47 E-01	3.00 E-04
18	80	343		12.85	1.26 E-01	5.91 E-02	6.70 E-02	8.37 E-01	3.00 E-04
18	80	353	8581	12.73	1.25 E-01	5.91 E-02	6.58 E-02	8.22 E-01	0
18	80	343		12.66	1.24 E-01	5.91 E-02	6.51 E-02	8.14 E-01	0
18	80	353	8581	12.74	1.25 E-01	5.91 E-02	6.59 E-02	8.24 E-01	3.00 E-04
18	80	343		12.68	1.24 E-01	5.91 E-02	6.53 E-02	8.16 E-01	3.00 E-04
18	80	353	8581	12.71	1.25 E-01	5.91 E-02	6.56 E-02	8.20 E-01	0
18	80	343		12.66	1.24 E-01	5.91 E-02	6.51 E-02	8.14 E-01	0
18	80	353	8581	12.41	1.22 E-01	5.91 E-02	6.26 E-02	7.83 E-01	0
18	80	343		12.36	1.21 E-01	5.91 E-02	6.22 E-02	7.77 E-01	0

Table B.9 Summary of final test results for surface tension measurements of LM136. An initial contact angle of zero was assumed.

References

Angrist, S. T. (1965). *Direct Energy Conversion.* Boston: Allyn and Bacon Inc.

Barcozy, C. J. (1966). *A systematic correlation for two-phase pressure drop.* Chemical Engineering Progress Symposium Series, 63, 64, pp. 232-249.

Biomass Energy Centre. *Typical Calorific Values of Fuels.* Available: URL http://www.biomassenergycentre.org.uk/portal/page?_pageid=75,20041&_dad=portal. [Accessed: May 2015].

Blasius, P. R. H. (1913). *The law of similarity in friction processes in liquids.* Communications on research in the areas of engineering, 131, 1-41.

Blumenau, L. (1986). *Liquid Metal MHD Energy Conversion in Fusion Reactors.* Fusion Science and Technology, 10, 3P2A, pp. 914-921.

Bolton Metal Products. *Specifications, Shop.* Available: URL http://www.boltonmetalproducts.com/Specifications.html. and URL http://shop.boltonmetalproducts.com/. [Accessed: November 2013].

Bos, J. W. (2012). *Thermoelectric materials: efficiencies found in nanocomposites.* Available: URL http://www.rsc.org/education/eic/issues/2012March/thermoelectric-materials-nanoparticles.asp. [Accessed: August 2015]

Bouman, K., Van Koppen, C. W. J., Raas, L. Y. (1974). *Some Investigations on the Influence of the heat flux on flow pattern in vertical boiler tubes.* European Two-Phase Flow Group Meeting, England.

Branover, H., El-Boher, A., Yakhot, A. (1981). *An Operating Model of Two-Phase Heavy-Metal MHD Power Systems.* 3rd International Seminar on MHD Flows and Turbulence, Israel.

Brater, E. F. et al. (1996), *Handbook of hydraulics for the solution of hydraulic engineering problems.* New York: McGraw-Hill.

BSI (2013), *BS EN 60584-1:2013 Thermocouples – Part 1: EMF Specifications and Tolerances*, Available: URL http://shop.bsigroup.com/ProductDetail/?pid=000000000030252011 [Accessed: May 2015]

CCFE. *The tokamak.* Available: URL http://www.ccfe.ac.uk/Tokamak.aspx. [Accessed: May 2015]

CCFE. *JET.* Available: URL http://www.ccfe.ac.uk/JET.aspx. [Accessed: May 2015]

CCFE. *How Fusion Works.* Available: URL http://www.ccfe.ac.uk/How_fusion_works.aspx. [Accessed: May 2015]

CEA. *Tritium breeding blankets.* Available: URL http://www-fusion-magnetique.cea.fr/gb/cea/next/couvertures/blk.htm. [Accessed: May 2015]

Çengal, Y. A. (2003). *Heat Transfer: A Practical Approach.* 2nd Ed. New York: McGraw-Hill.

Chisholm, D. (1972). *An equation for the velocity ratio in two-phase flow.* National Engineering Laboratory Report 535.

Chisholm, D. (1967). *A theoretical basis for the Lockhart-Martinelli correlation for two-phase flow.* International Journal of Heat and Mass Transfer, 10, 12, pp. 1767-1778.

Coen, V., Sample, T. (1990). *Pb17Li: A fully characterized liquid breeder*. Proceedings of the 16th Symposium on Fusion Technology, London, 3-7 September, pp. 248-252.

Cordero, B. et al. (2008). *Covalent Radii Revisited.* Dalton Transactions, 21, pp. 2832-2838.

Crowell, C. R. (1965). *The Richardson constant for thermionic emission in Schottky barrier diodes.* Solid-State Electronics, 8, 4, pp. 395-399.

Deasey, J. O. (1994). *ICRU Report 49, Stopping Powers and Ranges for Protons and Alpha Particles.* Medical Physics, 21, 5, pp. 709-710.

Decher, R. (1997). *Direct Energy Conversion.* New York: Oxford University Press.

Department of Energy and Climate Change. (2013) *Historical Electricity Data: 1920 to 2014.* Available: URL https://www.gov.uk/government/statistical-data-sets/historical-electricity-data-1920-to-2011 [Accessed: May 2015].

Department of Energy and Climate Change. (2014) *Digest of United Kingdom Energy Statistics.* Available: URL https://www.gov.uk/government/uploads/system/uploads/attachment_data/file/338750/DUKES_2014_printed.pdf. [Accessed: May 2015]

Douglas, J.F. et al. (2005). *Fluid Mechanics.* 5th Ed. Harlow: Pearson Education Ltd.

Drax Power Limited. (2007) *Environmental Performance Review.* Available: URL http://www.drax.com/media/31611/EPR_2007_FINAL.pdf. [Accessed: May 2015].

Dushman, S. (1923). *Electron Emission from Metals as a Function of Temperature.* Physics Review, 21, pp. 623-636.

Eastop, T. D & McConkey, A. (1993). *Applied Thermodynamics for Engineering Technologists.* 5th Ed. Harlow: Longman Group UK Ltd.

El-Boher, A., Lesin, S., Branover, H. (1988). *Liquid metal MHD generators in two-phase systems.* International Union of Theoretical and Applied Mechanics Symposium on Liquid MHD, Riga.

Elliot, D. G. (1961). *A Two-Fluid Magnetohydrodynamic Cycle for Nuclear-Electric Power Conversion.* Technical Report 32-116, Jet Propulsion Laboratory, California Institute of Technology.

Energy UK. *Electricity Generation in the UK from Fossil Fuels.* Available: URL http://www.energy-uk.org.uk/energy-industry/electricity-generation.html. [Accessed: May 2015].

EUROfusion. *JET financed until 2018.* Available: URL https://www.euro-fusion.org/newsletter/jet-financed-until-2018/. [Accessed: May 2015]

EUROfusion. *New JET results tick all the boxes for ITER.* Available: URL https://www.euro-fusion.org/2012/10/new-jet-results-tick-all-the-boxes-for-iter/. [Accessed: May 2015]

Feuerstein, H. et al. (1991). *Evaporation of lead and lithium from molten Pb17Li — Transport of aerosols.* Fusion Engineering and Design, 17, pp. 203-207.

Freidberg, J. P. (2010) *Plasma Physics and Fusion Energy.* Cambridge: Cambridge University Press.

Friedel, L. (1979). *Improved friction pressure drop correlations for horizontal and vertical two-phase flow.* European Two-Phase Flow Group Meeting, Ispra.

Frost, S. L. (1961). *Conductivity of Seeded Atmospheric Pressure Plasmas.* Journal of Applied Physics, 32, 10, pp. 2029-2035.

Fusion for Energy. (2012). *F4E signs contracts for TBM EUROFER subcomponent manufacturing procedures.* Available: URL http://fusionforenergy.europa.eu/mediacorner/newsview.aspx?content=595. [Accessed: September 2015]

General Electric. *GE Supercritical and Ultra-Supercritical Steam Turbines.* Available: URL https://www.ge.com/in/thermal-power/steam-turbine-manufacturers. [Accessed: July 2015]

General Electric. *9HA.01 / 9HA.02 Gas Turbine Product Specifications.* Available: URL https://powergen.gepower.com/plan-build/products/gas-turbines/9ha-gas-turbine/product-spec.html. [Accessed: August 2015].

Goldsmid, H. J. (2001). *Introduction.* In Tritt, T. M. *Recent Trends in Thermoelectric Materials Research 1: Semiconductors and Semimetals, Volume 69.* San Diego, California: Academic Press.

Haywood, R. W. (1980). *Analysis of Engineering Cycles.* 3rd Ed. Oxford: Pergamon Press Ltd.

He, J., Liu, Y., Funahashi, R. (2011). *Oxide Thermoelectrics: The challenges, progress and outlook.* Journal of Materials Research, 26, 15, pp. 1763-1772.

Hordeski, M. F. (2011). *Megatrends for Energy Efficiency and Renewable Energy*. Lilburn, Georgia: Fairmont Press.

Houston, J.M., (1959). *Theoretical Efficiency of the Thermionic Energy Converter*. J. App. Phys. 30, 4, pp. 481.

Incropera, F.P., DeWitt, D. P. (2000). *Fundamentals of Heat and Mass Transfer.* 4th Ed. New York: Wiley.

Isbin, H. S. et al. (1958). *Two-phase steam-water pressure drops.* Nuclear Science and Engineering Conference, Chicago.

ISO 6976 (1995) *Natural gas - Calculation of calorific values, density, relative density and Wobbe index from composition.* Available: URL http://www.iso.org/iso/catalogue_detail.htm?csnumber=13531. [Accessed: May 2015].

ITER. *Progress in Fusion.* Available: URL http://www.ccfe.ac.uk/JET.aspx. [Accessed: May 2015]

ITER. (2012). *The Tokamak.* Originally available: URL https://www.iter.org/mach. [Accessed: May 2012]

Kaye, G. W. C., Laby, T. H., (1973) *Tables of Physical and Chemical Constants.* 14th Ed. London: Longman Group Ltd.

Kleefeldt, K. (2003). *Thermal-Hydraulic Model of the Helium-Cooled Pebble Bed Test Blanket Module for ITER-FEAT.* Available: URL http://digbib.ubka.uni-karlsruhe.de/volltexte/fzk/6724/6724.pdf. [Accessed: June 2012]

Lin, S. C., Resler, E. L., Kantrowitz, A. (1955). *Electrical Conductivity of Highly Ionized Argon Produced by Shock Waves.* Journal of Applied Physics, 26, 1, pp. 95-109.

Linares, J. I. et al., (2015). *Supercritical CO_2 Brayton power cycles for DEMO fusion reactor based on Helium Cooled Lithium Lead blanket*. Applied Thermal Engineering, 76, pp. 123-133.

Lockhart, R. W., Martinelli, R. C. (1949). *Proposed correlation of data for isothermal two-phase two-component flow in pipes.* Chemical Engineering Progress, 45, 1, pp. 39-48.

Lowden Ltd. *Lens Alloy 136 (58°C).* Available: URL http://www.lowdenlimited.com/LowMelting/LensAlloy136.html. [Accessed: March 2014].

Mackay. D. (2008) *Sustainable Energy – Without the Hot Air*. Cambridge: UIT Cambridge Ltd.

Maisonnier, D. et al., (2004). *The European power plant conceptual study*. Fusion Engineering and Design, 75-79, pp. 1173-1179.

Maisonnier, D. et al., (2007). *Power Plant Conceptual Studies in Europe.* Nuclear Fusion, 47, 11, pp. 1524-1532.

Masonnier et al., (2006). *DEMO and fusion power plant conceptual studies in Europe.* Fusion Engineering and Design, 81, 8-14, pp. 1123-1130.

Martinelli, R. C., Nelson, D. B. (1948). *Prediction of pressure drop during forced circulation boiling of water.* Transactions of ASME, 70, 6, pp. 695-702.

Maxwell, J. C. (1904). *Treatise on Electricity and Magnetism: Volume 1.* 3rd Ed. Oxford: Clarendon Press.

Moir, R. (1977). *Direct Energy Conversion in Fusion Reactors*. In Considine, D. M., Energy Technology Handbook, pp. 150-154. USA: McGraw-Hill.

Moody, L. F. (1944), *Friction factors for pipe flow.* ASME Transactions, 66, 8, pp. 671–684.

Müller-Steinhagen, H., Heck, K. (1986). *A simple Friction Pressure Drop Correlation for Two-Phase Flow in Pipes.* Chemical Engineering Processing: Process Intensification, 20, 6, pp. 297-308.

National Geographic. (April, 2014) *Can Coal Ever Be Clean?.* Available: URL http://ngm.nationalgeographic.com/2014/04/coal/nijhuis-text. [Accessed: Sep 2015].

National Geographic. *Interactive World Energy Mix.* Available: URL http://environment.nationalgeographic.com/environment/energy/great-energy-challenge/world-electricity-mix/. [Accessed: May 2015].

Norajitra, P. et al., (2003). *Conceptual Design of the Dual-Coolant Blanket within the Framework of the EU PPCS Final Report*. Available: URL http://bibliothek.fzk.de/zb/berichte/FZKA6780.pdf. [Accessed: October 2013]

Paschen, F. (1889). *On the potential difference required for spark initiation in air, hydrogen, and carbon dioxide at different pressures.* Annalen der Physik, 273, 5, pp. 69–75.

Petrick, M. et al. (1978). *Experimental Two-phase Liquid Metal MHD Generator Program*. Argonne National Laboratory Annual Report, ANL/MHD-78-2.

Pfalzner, S. (2006). *An Introduction to Inertial Confinement Fusion.* Florida: CRC Press, Taylor & Francis Group.

Premoli, A., Francesco, D., Prina, A. (1970). *An empirical correlation for evaluating two-phase mixture density under adiabatic conditions.* European Two-Phase Flow Group Meeting, Milan.

Ricapito, I. (2010) *Liquid Metal Blankets for Fusion Reactors,* Summer School for Fusion Technology, Karlsruhe, Institute of Technology, Germany.

Richardson, O. W. (1901). *On the Negative Radiation from Hot Platinum.* Proceedings of the Cambridge Philosophical Society, 11, pp. 286-295.

Rogers, G. F. C., Mayhew, Y. R. (1995). *Thermodynamic and Transport Properties of Fluids.* 5th Ed. Oxford: Blackwell Publishing.

Rosi, F. D., Hockings, E. F., Lindenblad, N. E. (1961). *Semiconducting Materials for Thermoelectric Power Generation.* RCA Review, 22, 1, pp 82-121.

RotoMetals. *Fusible Alloys and Ingots.* Available: URL http://www.rotometals.com/Low-Melting-Fusible-Alloys-s/21.htm. [Accessed: March 2014].

Saito, M., Inoue, S., Fujii-e, Y. (1978). *Gas-Liquid Slip Ratio and MHD Pressure Drop in Two-Phase Liquid Metal Flow in Strong Magnetic Field.* Journal of Nuclear Science and Technology, 15, 7, pp. 476-489.

Sardain, P. et al., (2007). *Alternative power conversion cycles for He-cooled fusion reactor concepts*. Proceedings of the 2nd IAEA Technical Meeting on First Generation of Fusion Power Plants: Design & Technology, Vienna, Austria.

Satyamurthy, P., Thiyagarajan, K., Venkatramani, N. (1995). *A conceptual scheme for electrical power generation from nuclear waste heat using liquid metal magnetohydrodynamic energy converter.* Energy Conversion and Management, 36, 10, pp. 975-987.

Schulz, B. (1991). *Thermophysical properties of the alloy Li(17)Pb(83) alloy.* Fusion Engineering and Design, 14, 3-4, pp. 199-205.

Shinohara, Y. et al. (1997). *Thermoelectric Properties of Segmented Pb-Te Systems with Graded Carrier Concentrations*. Thermoelectrics, Proceedings ICT '97. XVI International Conference on, 26-29, pp. 386-389.

Smil, V. (2010) *Energy Transitions*: *History, Requirements, Prospects,* Santa Barbara, California: Praeger.

Smith, S, L. (1969). *Void fraction in two-phase flow: a correlation based upon an equal velocity head model.* Proceedings of the IMechE, 184, 1, pp. 647-664.

Smithells, C. J. (1967). *Metals Reference Book, Vol III*, 4th Ed. London: Butterworths.

Soo, S. L. (1968) *Direct Energy Conversion.* 2nd Ed. Englewood Cliffs, New.Jersey: Prentice-Hall Inc.

Sowa, E. S. (1963). *The Liquid Metal Linear Generator*. AMU-ANL Conference on Direct Energy Conversion, Argonne National Laboratory-6802, pp. 181-185.

Stacey, W. M. (2010) *Fusion: An Introduction to the Physics of Magnetic Confinement Fusion.* Weinheim: Wiley-VCH

Stork, D. (2012). *DEMO.* Presented at the University of York Lectures on Magnetic Confinement Fusion as part of the MSc Plasma Physics Programme.

Sutton, G. W. & Sherman, A. (2006). *Engineering Magnetohydrodynamics.* New York: Dover Publications.

Tanatugu, N., Fujii-e, Y., Suita, T. (1972). *Electrical Conductivity of Liquid Metal Two-Phase Mixture in Bubbly and Slug Flow Regime.* Journal of Nuclear Science and Technology, 9, 12, pp. 753-755.

The World Bank. *Access to electricity (% of population).* Available: URL http://data.worldbank.org/indicator/EG.ELC.ACCS.ZS. [Accessed: May 2015]

The World Bank. *Electric power consumption (kWh per capita).* Available: URL http://data.worldbank.org/indicator/EG.USE.ELEC.KH.PC. [Accessed: May 2015]

Thom, J. R. S. (1964). *Prediction of pressure drop during forced circulation boiling of water.* International Journal of Heat and Mass Transfer, 7, 7, pp. 709-724.

Tribbe, C., Müller-Steinhagen, H. M. (2000). *An Evaluation of the Performance of Phenomenological Models for Predicting Pressure Gradient during Gas-Liquid Flow in Horizontal Pipelines.* International Journal of Multiphase Flow, 26, 6, pp. 1019-1036.

U.S. Energy Information Administration. *World Net Electricity Consumption.* Available: URL http://www.eia.gov/cfapps/ipdbproject/IEDIndex3.cfm?tid=2&pid=2&aid=2 [Accessed: May 2015].

Way, S. (1963). *Lectures on Magnetohydrodynamic Energy Conversion.* Stanford, California: Stanford University. Webster, H.F., (1959). *Calculation of the Performance of a High-Vacuum Thermionic Energy Converter*, J. App. Phys. 30, 4, pp. 488.

Whaley, P. B. (1987). *Boiling, Condensation and Gas-Liquid Flow.* Oxford: Clarendon Press.

Wilhelmy, L. (1850). *The Law by Which the Action of Acids on Cane Sugars Occurs.* Annalen der Physik und Chemie, 81, pp. 413-433.

Wolf, B et al. (1995). *Characteristics of Ion Sources.* In Wolf, B. *Handbook of ion sources*. Florida: CRC Press.

Wong, et al., (2008). *Overview of liquid metal TBM concepts and programs.* Fusion Engineering and Design, 83, 7-9, pp. 850-857.

World Energy Council. *World Energy Scenarios: Composing energy futures to 2050.* Available: URL http://www.worldenergy.org/wp-content/uploads/2013/09/World-Energy-Scenarios_Composing-energy-futures-to-2050_Executive-summary.pdf. [Accessed: May 2015].

World Nuclear Association. *Heat Values of Various Fuels.* Available: URL http://world-nuclear.org/info/Facts-and-Figures/Heat-values-of-various-fuels/. [Accessed: May 2015].

World Nuclear Association. *Nuclear Power Reactors.* Available: URL http://www.world-nuclear.org/info/Nuclear-Fuel-Cycle/Power-Reactors/Nuclear-Power-Reactors/. [Accessed: May 2015]

Wu, Q. et al, (2007). *Feasibility analysis of two-phase MHD energy conversion for liquid metal cooled reactors.* Nuclear Engineering and Design, 237, 20-21, pp. 2114-2119.

Yakhot. A, Branover, H. (1982). *An Analytical Model of a Two-Phase Liquid Metal MHD Generator.* 3rd International Seminar on MHD Flows and Turbulence, Israel.

Yuan, Y., Lee, T. R. (2013). *Contact Angle and Wetting Properties.* In Bracco, G. Holst, B. *Surface Science Techniques.* Berlin: Springer-Verlag.

Zhang, Y., Xu, Z. (1995). *Atomic radii of noble gas elements in condensed phases*. American Mineralogist, 80, 7-8, pp. 670-675.

Zivi, S. M. (1964). *Estimation of steady-state steam void fraction by means of the principle of minimum entropy production.* Journal of Heat Transfer, 86, 2, pp. 247-252.